The molecular imaging suite: applications in nanotechnology, targeted imaging and cell tracking

Alessandro Ruggiero

The molecular imaging suite: applications in nanotechnology, targeted imaging and cell tracking

Molecular Imaging suite: toepassingen in de nanotechnologie, targeted imaging en cell tracking

Proefschrift

ter verkrijging van de graad van doctor aan de
Erasmus Universiteit Rotterdam
op gezag van de
Rector Magnificus

Prof.dr. H.G. Schmidt,

en volgens besluit van het College voor Promoties.

De openbare verdediging zal plaatsvinden op
vrijdag 02 november 2012 om 9.30 uur

Door
Alessandro Ruggiero
geboren te Brindisi

ERASMUS UNIVERSITEIT ROTTERDAM

Promotiecommissie

Promotor: Prof. Dr G.P. Krestin
                Prof. Dr H. Hricak

Copromotor: Dr. Monique Bernsen

Overige leden: Prof. Dr. M. de Jong
                Prof. Dr. CH Bangma
                Prof. Dr S. Aime

to my family

Contents

1

Introduction

Introduction

The blurring of the boundaries between the disciplines of engineering and the biological sciences has revolutionized medicine. Medicine is still a science of decision-making under uncertainty. However, during the past 30 years, this uncertainty gradually diminished thanks to exceptional advancements in many medical specialties, particularly imaging (1). Advancements and refinements in technology have substantially broadened the range of available imaging procedures. Medical imaging has become an essential tool in preclinical research, clinical trials and medical practice.

The recent arrival of molecular imaging research in the radiological community is the result of concomitant developments in cellular and molecular biology, genomics and proteomics, nanotechnologies and increased sophistication of all our imaging technologies, combined with a large diversification in new contrast agents and probes (2, 3). Molecular imaging (MI) is the *in vivo* characterization and measurement of biological processes occurring at a cellular and molecular level at a macroscopic level of resolution (4). This is in contrast to the current conventional, anatomically based radiology. Clinicians rely on radiology to identify the disease localization, size and characteristics. Based on images, diagnostic or surgical procedures can be planned and performed, as well as response to systemic therapy and disease progression can be assessed. In daily clinical routine these questions are being answered through the application of traditional anatomical imaging methods such as US, CT and MRI. Although these methods still represent the mainstay of clinical imaging, it has become clear that the acquisition of molecular and physiological information by nuclear magnetic resonance and optical imaging technologies could vastly enhance our ability to understand and treat different diseases.

The rapidly evolving field of MI promises improvements in specificity and quantitation for screening and early diagnosis, focused and personalized therapy and earlier treatment follow-up. The main advantage of MI is its ability to characterize diseased tissues without invasive biopsies or surgical procedures, and with this information in hand, a more personalized treatment planning regimen can be applied (5). For example, recent advances in the treatment of breast cancer include a multifactorial approach with combinations of drugs targeting oestrogen receptor, epidermal growth factor types I and II (EGFR and HER2), mammalian target of rapamycin (mTor) and many others. HER2 is one of the crucial targets in breast cancer, being HER2-amplified tumors responsive to the monoclonal antibody trastuzumab (6). MI can be used to identify and quantify the molecular marker profile (e.g. EGFR, HER2) of the tumor without the invasiveness of a surgical biopsy and time associated with pathological characterization. The personalized medicine approach is especially important for determining the best care for patients with advanced stage cancers and poor prognosis. In this case, the risk of exposure to unwanted side-effects of therapy may outweigh the quality of remaining life.

The novel "omics" technologies (namely genomics, proteomics, metabolomics) have the potential to change the management of diseases. MI is going to play a pivotal role in this transformation, because it allows the integration of molecular and physiological information specific to each patient with anatomical information obtained by conventional imaging methods.

The main translational goals for MI are:

1. Early detection of diseases.
The detection at the molecular level of pathological alterations that indicate the presence of a certain disease at an early stage is the most challenging aspect of imaging diagnostics. The value of this goal is better understood if we consider that detection of stage I cancers is associated in most cases with a >90% 5-year survival rate, while the detection at an even earlier stage (precancerous) allows a curative treatment (7). Currently radiological techniques (CT and MRI) typically detect cancers at the macroscopical level at which point they might be associated with circulating and microscopic metastatic deposits. MI is expected to reduce the detectability threshold allowing a much more specific and sensitive imaging and monitoring of key molecular targets and host responses associated with early events in carcinogenesis.

2. Accurate and reliable assessment of treatment response
The ability to precisely assess treatment response and adjust therapeutic protocols in real time is crucial in patient management. Evaluation of tumor response to chemotherapy and biological therapies is currently based on one-dimensional (1D) measurements (maximum diameter of target lesion) and their percentage of changes during therapy according to the Response Evaluation Criteria in Solid Tumours (RECIST 1.1) (8), which use anatomical imaging methods such as computed tomography (CT) or magnetic resonance imaging (MRI). However, these changes in size may take considerable time to appear (weeks to months), and overall are not an accurate reflection of therapeutic efficacy in all cases.

MI has the potential to improve therapeutic monitoring by measuring the direct effect of a drug at an earlier time point before overt morphological and anatomical changes become visible on imaging. The advent of ^{18}F-FDG PET has been a step forward in the evaluation of response to treatment, allowing the quantitative and functional assessment of the tumor mass viability and its changes upon therapy. However, there are several limitations inherent to this radiotracer, such as the non-specific uptake (inflammation, infection) and the limited use in certain organs (whereas glucose uptake is physiologically high: brain, kidneys). Therefore, more specific imaging agents able to visualize cell growth or cell death early after treatment are awaited. In this setting the radio-labeled thymidine analogues (^{18}F-FLT; ^{18}F-FMAU) serve as a useful markers of

cell proliferation and have chances to be widespread in clinical practice in the near future.

3. Improve efficiency of drug development.

The development of novel therapeutics is expensive, time-consuming and often requires large numbers of animals or patients. All these factors are crucial in determining the final cost of new therapies and the timing for the approval for clinical use by the regulatory agency. MI can potentially increase the efficiency and cost-effectiveness of drug development processes. Importantly, noninvasive MI techniques and approaches can be used at all phases of the drug development process. Moreover, novel efficacy endpoints can be identified and closely monitored for a better assessment of novel drugs.

Molecular imaging research chain

Choice of a target

The choice of molecular targets drives the entire MI research chain (Fig 1). Ideal molecular targets are present in multiple copies per cell. These are usually protein targets (<100 to 1 million copies per cell) but can also be mRNA (50 to 1.000 copies per cell). DNA is not used because of both its low copy number (which makes it difficult to produce sufficient specific signal) and its limited informative value: only the fact that a gene is present not the expression of the gene.

Clearly, the abundance and specificity of the target for the disease process under study is critical to make the MI assay successful. One fundamental issue for MI is to know which molecular targets are relevant to study for a given set of biological questions or for a given disease management problem. In fact, even if MI was able to interrogate every potential molecular targets and various other events, it would be still difficult to know which events to actually monitor/image. It is currently not possible to highly-multiplex (detect multiple molecular targets of interest simultaneously) and as a result, selection of molecular targets is critical. Multiplexing is currently limited to 3 to 5 maximum molecular targets.

Chemistry

Chemistry is pivotal in the development of novel probes. Small molecules, peptides, aptamers, engineered proteins and even more complex nanoconjugates are suitable MI probes. The development process can often take several months. The ideal MI candidate would allow rapid synthesis of the probe with high purity so that it can be synthesized in laboratories, clinical and research sites that will perform the imaging. For potential human translation, it is important that the synthesis is performed following the good manufacturing practice (GMP) guidelines. A novel aspect inherent to some MI probes
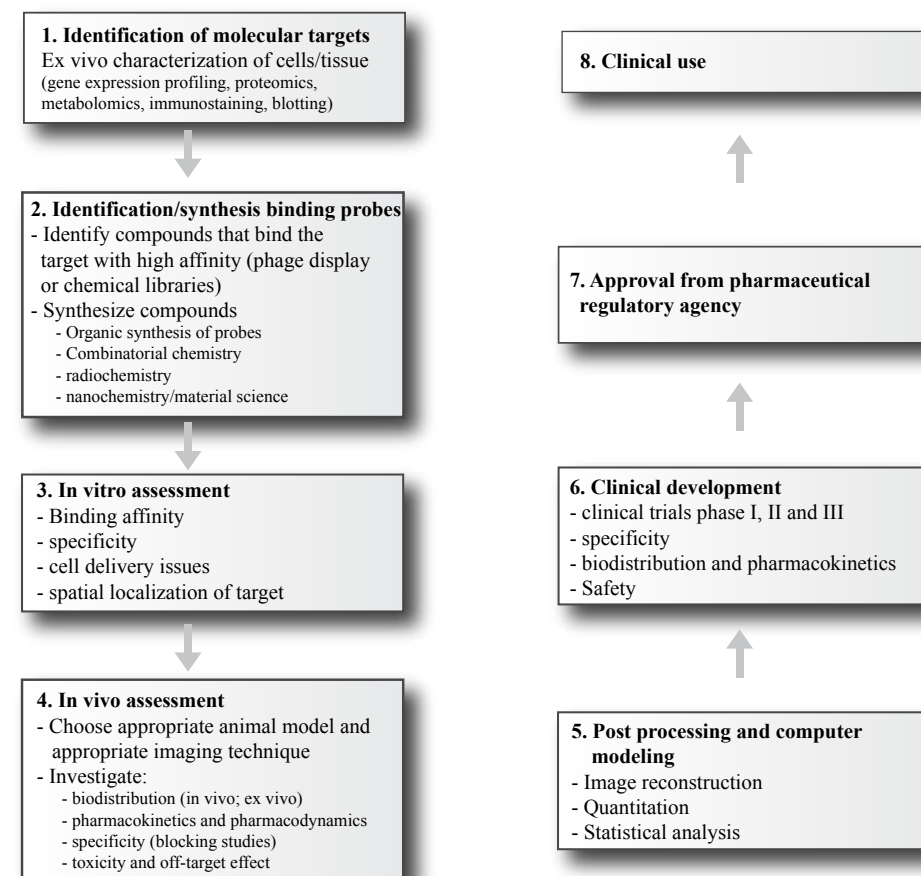
Fig. 1 MI research chain. Adapted from (5).

is the possibility to construct probes that besides the targeting moiety and the imaging component, include a therapeutic moiety, which constitute the "theranostic" agents. Also the development of multimodality probes enables the imaging on multiple imaging platforms (Fig 2).

Testing

MI probes can be tested *in vitro* with cell extracts or intact cells in culture. The latter one helps to better understanding the ability to cross cell membrane, the time involved for targeting and clearance for the cells and also the potential nonspecific binding that may increase background signal. Moreover, by adopting standard molecular biology techniques it is possible to test the relationship between MI probe and the levels of molecular target.

Fig. 2 "Anatomy" of a theranostic probe

Fig. 3 Different MI probes: a) "always on" probes; b) probes activated after being internalized (lisosomes) c) probes activated upon binding to a specific target on the cell surface d) probes selectively activated by agents (enzymes) secreted by the target and present in the extracellular matrix

However, *in vitro* testing does not answer some crucial questions: *a)* how to deliver sufficient amounts of the MI probes to the 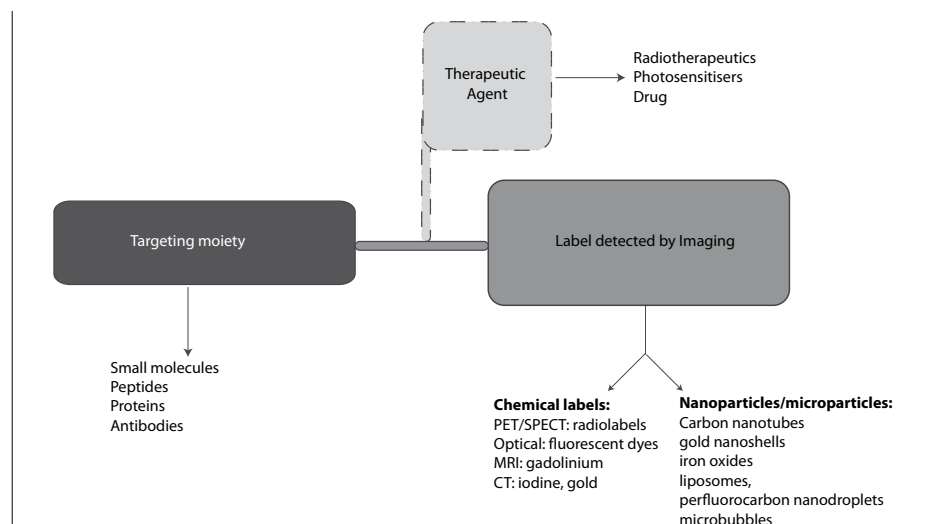cells of interest in the whole body setting; *b)* how the probe is cleared out from the circulation and from the non target sites; *c)* whole body toxicity in the short and long-term. To address these points, *in vivo* testing in animals is required. Small laboratory animals (mostly rodents) are much more convenient to test due to their relatively low cost, high throughput capabilities and ease of handling. The availability of several strains allows to design and use the best animal for the purposes of the study. The molecular targets can be studied in mouse models which spontaneously develop a disease that exhibits the molecular targets or can be exogenously expressed by implanting cells in mice. Alternatively, murine models can be developed by introducing or deleting genes of interest, such as transgenic knock-in and knock-out mice, respectively. However, there are cases in which small animal models cannot properly reflect human disease, therefore large animals have to be adopted as porcine models (cardiovascular studies) or primates (neurological studies). It is obvious that no animal model is fully reflective of the human disease, however the use of animal models is crucial in testing potential toxicities in a living subject prior to translation in human. Another important point is inherent to the radiation dosimetry for those studies involving the use of radioisotopes. Radiation exposure of every organ need to be evaluated, quantified and extrapolated fo human comparison.

The next step is to test the animal with the imaging with the appropriate imaging platform. The ideal technology platform should determine very low levels of molecular target concentration (e.g. picomolar or 10^{-10}-10^{-12} mol/L), have the ability to follow just a few cells, have high spatial resolution (sub-millimeter), high temporal resolution (millisecond), be low-cost, offer high-throughput and be fully quantitative. Also, it should allow the interrogation of the whole body and at all depths throughout the subject and
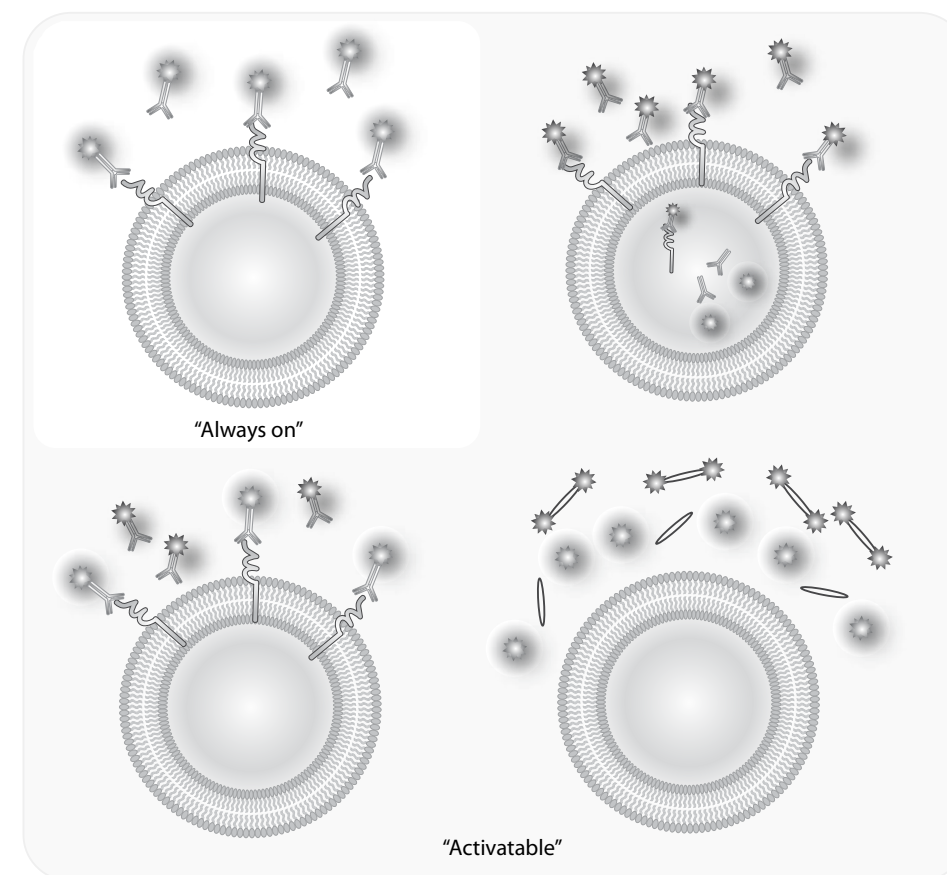
allow measurement of molecular targets located anywhere in the subject and in any location within the cell. Since so perfect platform does not exist, the appropriate technique should be selected according to the biological question. It has become clear that there is no single 'best technique' in MI. Rather there is an array of high sensitivity, high spatial resolution and functional techniques that work best in combination. The next step is to process the imaging data and quantitate the presence of the probe in the site of interest. Usually, serial images are acquired to characterize changes in the locations of the MI probe and produce time/activity curves. The amount of MI probe is quantified at various sites including the target tissues and related the signal to the amount injected (*% Injected dose*). A key issue in every molecular imaging study is the requirement that levels of signal should be able to related back to levels, or even activity (activatable probes) of the molecular target of interest. Table 1 illustrates the "what to image and how to image" with molecular imaging approaches. In many but not all cases, the final steps are to translate the developed MI strategy to clinical application. This requires approval from the regulatory agencies (FDA, EMEA) and the local internal review board.

Table 1. What to image and how to image

Imaging modality	Spatial resolution (mm)	Sensitivity (mol/L)	Imaging agent	What to image	How to image	Advantages	Disadvantages
Fluorescence Imaging	FRI: 2-3; FMT: 1	10^{-9}–10^{-12}	Photoproteins, fluorochromes, Quantum dots, etc.)	Surface marker, secreted proteins (enzymes), intracellular proteins	Direct imaging; at NIR wavelenghts can image deep tissue	Multiplexing, sensitive, quantitative, short acquisition time, inexpensive	Limited depth penetration (<1cm²); low spatial resolution
Bioluminescence Imaging	3-5	10^{-15}–10^{-17}	Cells transduced to express luciferase	Cell tracking Residence, homing, viability, differentiation, quantification	After systemic injection of D-Luciferine or Coelenterazine	Easy, high sensitivity, high-throughput, low cost; assessment of cell viability	Not suitable for clinical translation; surface imaging; low spatial resolution; requires completely dark environment
PET	1-2 (mPET); 6-10 (clinical PET)	10^{-11}–10^{-12}	Radiolabeled small molecules, peptide, antibodies, aptamers	Metabolism, proliferation, hypoxia, apoptosis, surface marker, receptors	Direct imaging	High sensitivity, quantitative, whole body imaging, combined with CT/ MRI	Radiation; expensive, low spatial resolution, long acquisition time
			Cell tracking (direct labeling or cells transduced to express PET reporter genes (HSV1tk)	Residence, homing, differentiation, quantification,	Direct or after systemic injection of correspondent probe (^{18}F-FHBG, ^{18}F-FEAU, etc.)	High sensitivity, long term cell tracking; assessment viability	Radiaton; need to transduce cells; potential immunogenicity
SPECT	0.5-2 (mSPECT); 7-15 (clinical SPECT)	10^{-10}–10^{-11}	Radiolabeled small molecules, peptide, antibodies, aptamers	Metabolism, surface marker, receptors	Direct imaging	High sensitivity, whole body imaging, combined with CT/ MRI	Radiation; expensive, low spatial resolution, long acquisition time
			Cell tracking (direct labeling or cells transduced to express SPECT reporter genes (hNIS)	Residence, homing, viability, differentiation, quantification,	After systemic injection of correspondent radiolabeled probe (^{99m}Tc, etc.)	High sensitivity, long term cell tracking	Radiaton; need to transduce cells; potential immunogenicity
MRI	0.01-0.1 (small animal); 0.5-1.5 (clinical)	10^{-3}–10^{-5}	Paramagnetic agents, superparamagnetic iron oxides, 19F, hyperpolarized molecules	Untargeted probes, Activatable probes, nanoparticles	Direct imaging	No ionizing radiation; Excellent soft-tissue contrast and spatial resolution; functional imaging	Expensive; Long acquisition time (min–hours); Limited sensitivity for detection of molecular contrast agents
			Cells labeled with Iron Oxides; Gd or Mn chelates; perfluorocarbon (^{19}F) or cells expressing MRI reporter genes (transferrin receptor, ferritin, MagA and lysine-rich proteins)	Residence, homing, quantification, migration, differentiation	Direct imaging or after injection of iron oxides (transferrin receptor, ferritin)	High spatial resolution; high soft tissue contrast; functional imaging.	Low sensitivity; need to transduce cells; potential immungenicity

NIR, Near-Infra red imaging; FRI, Fluorescence reflectance imaging; FMT, Fluorescence molecular tomography

Molecular Imaging Probes

A probe should accumulate (by active or passive mechanism) at a specific site of interest and exploit its signal in a way that it is possible to differentiate from the background. Therefore, besides sensitivity and specificity, requirements should also include favorable pharmacokinetic and pharmacodynamic profile. For imaging purposes a probe should quickly reach and accumulate at the target site and should also be quickly cleared out of the circulation (e.g through renal pathway) and without significant modifications or impairment in the physiological functions. The "anatomy" of a MI probe is shown in Figure 2, it is basically composed of a targeting moiety, a signaling component (which can be detected with the corresponding imaging techniques) and a linker between these two (which may or may not be present). MI probes are referred by many names such as imaging agents, radiotracers, radiopharmaceuticals, activatable or "smart" probes, constitutively active probes, reporter genes probes. Although, MI probe does provide "contrast" allowing the depiction of the target site over the background, "contrast agent" is not a preferred term as it is associated to nonspecific agents that have poorly defined molecular targets. MI probes can be broadly categorized as constitutively active probes or activatable probes (Figure 3). The first ones constitutively produce their signal (such as radioactive labels that emit signal associated with radioactive decay). Activatable probes remain in their silent phase until they interact with the specific site of interest, where they get activated leading to a high signal to background ratio.

References

1. Hricak H. Oncologic imaging: a guiding hand of personalized cancer care. Radiology 2011; 259:633-640.
2. Grenier N, Sardanelli F, Becker CD, et al. Development of molecular imaging in the European radiological community. Eur Radiol 2009; 19:533-536.
3. Krestin GP, Bernsen MR. Molecular imaging in radiology: the latest fad or the new frontier? Eur Radiol 2006; 16:2383-2385.
4. Mankoff DA. A definition of molecular imaging. J Nucl Med 2007; 48:18N, 21N.
5. Pysz MA, Gambhir SS, Willmann JK. Molecular imaging: current status and emerging strategies. Clin Radiol; 65:500-516.
6. Wong ST. Emerging treatment combinations: integrating therapy into clinical practice. Am J Health Syst Pharm 2009; 66:S9-S14.
7. American Cancer Society. Cancer Facts & Figures 2011. Atlanta: American Cancer Society; 2011.
8. Eisenhauer EA, Therasse P, Bogaerts J, et al. New response evaluation criteria in solid tumours: revised RECIST guideline (version 1.1). Eur J Cancer 2009; 45:228-247.

2

Thesis motivations and outline

Molecular imaging is developing as a new subspecialty in radiology. The birth in 2012 of the *European Society for Molecular and functional imaging* (ESMOFIR) within the *European Society of Radiology* (ESR) is the most recent proof that clinical MI expertise is required. There are efforts to develop a new "breed" of physicians with training in nuclear medicine and diagnostic radiology, radiochemistry, and molecular biology. Historically, the preclinical development of X-ray, ultrasound, CT and MR imaging was accomplished by engineers and physicists. Radiologists had those tools in their hands for historical reasons and they contributed more in the clinical refinement of the application field than in the preclinical work. The new generation of physicians will need to master the MI potential of all cross-sectional and hybrid imaging modalities—such as PET/CT, PET/MR and optical imaging. They will be able to interact with chemists, physicists, molecular biologists at all stages of a MI probe or technology development from design to preclinical testing to the potential clinical translation.

Understanding the current limitations of imaging techniques, the challenges of current clinical medicine together with a direct understanding of the promises and hurdles of novel imaging platforms and technologies definitely contributes to a step forward in the advancements in the field.

The aims of this thesis was to gain insights in the various opportunities of MI. All the major imaging techniques and potential applications are explored and discussed in **chapters 3, 4** and **5**.

Chapter 3 gives an overview of the role of MI in the assessment of novel probes for imaging and therapy. Nanostructures and targeted probes are gaining importance in biomedical research to further our understanding of both the mechanisms involved in pathological conditions and of the interactions between nanoparticles and the biological milieu. In a more practical sense, filamentous nanomaterials are designed as transporters of therapeutic and/or diagnostic agents with much-wanted control over their *in vivo* tissue navigation, cargo release and clearance profile.

In **chapter 3.1** the mechanisms of elimination of one such type of engineered filamentous nanostructure - functionalized single-walled carbon nanotubes (SWCNTs) is investigated. The SWCNTs are decorated with various ligands (by covalent functionalization) such that renal clearance of the materials in mice can be monitored using three different imaging techniques. The study offers mechanistic explanations, both experimental and theoretical, of how SWCNTs can align with blood flow and be rapidly excreted through the renal filter. These findings have implications for our fundamental understanding of renal physiology and our knowledge of the ability of chemically functionalized SWCNTs to translocate over biological barriers.

In **chapter 3.2**, we further functionalized SWCTs, making them targeted agents (for imaging and therapy) towards the monomeric form of E-cadherin, a molecule involved in the neoangiogenesis. Tumor targeting ability and pharmacokinetic profiles of these constructs were assessed by optical (fluorescence molecular tomography, FMT) and PET imaging in tumor-bearing mice. By labeling targeted SWCT with the a-emitter ^{225}Ac, the effects of the amplification of the specific activity was investigated in a therapy study.

In **chapter 3.3** we developed and tested a novel MI agent for specific PET-based imaging of prostate cancer. The MI probe consisted of a ^{89}Zr-labeled monoclonal antibody targeting the Prostate-Specific Membrane Antigen (PSMA), a prototypical transmembrane marker highly overexpressed in prostate cancer. We investigated the ability of ^{89}Zr-DFO-7E11 to interrogate tumor response to therapy since it binds to the intracellular epitope of PSMA, which becomes available only on membrane disruption in dead or dying cells. *In vitro*, *in vivo* and *ex vivo* findings suggested that ^{89}Zr-DFO-7E11 displays high tumor–to–background tissue contrast in immuno-PET and can be used as a tool to monitor and quantify, with high specificity, tumor response in PSMA-positive prostate cancer.

Chapter 4 explored another important field of MI: cell tracking and its potential for regenerative medicine. **Chapter 4.1 is** an overview of the MI approaches and recent advancements of cell tracking in the heart.

In **chapter 4.2** we discussed one of the limitations of PET based reporter gene imaging, consisting of high radioactivity background related to the sub-optimal pharmacokinetic of probes like ^{18}F-FHBG, ^{18}F-FEAU and ^{124}I-FIAU commonly used for HSV1-tk PET imaging. Our hypothesis was inherent to the potential role of the uptake of the probe by the intestinal bacteria (which express thymidine kinase) which may contribute to the background radioactivity. We also investigated different strategies for reducing the background in PET based reporter gene imaging by increasing the intestinal clearance of these probes.

In **chapter 4.3**, the two main approaches for cell labeling and tracking by MRI were discussed. A thorough *in vitro* and in *vivo* investigation was conducted to delineate the R1, R2 or R2* relaxation rate as a measure of cell viability for mesenchymal stem cells labeled with Gd-liposomes or iron oxide nanoparticles. We assessed the behaviour, advantages and disadvantages of these two labeling approaches. In **chapter 4.4,** by quantitative heart MRI mapping and bioluminescence we investigated *in vivo* the relaxivity changes (R2) associated with proliferation, viability and death of iron-oxide labeled mesenchymal cells implanted in the heart. We investigated whether is possible to predict by relaxivities measurements the changes happening in vivo after cell implantation.

Chapter 5 explored the potentiality of "novel" multimodal approaches addressed by MI techniques. In **Chapter 5.1** we reported on the use of the inherent optical emissions from the decay of radiopharmaceuticals for Cerenkov luminescence imaging (CLI). Briefly, we performed dual optical and immuno-PET imaging of mice bearing tumor by

injecting a radiolabeled probe. Intriguingly, a quantitative correlation among the two techniques was found *in vivo* and ex vivo. These studies represented the first quantitative assessment of CLI for measuring the radiotracer uptake *in vivo*. Many radionuclides common to both nuclear tomographic imaging and radiotherapy have the potential to be used in CLI. The value of CLI lies in its ability to image radionuclides that do not emit either positrons or g-rays and are unsuitable for use with current nuclear imaging modalities.

In **chapter 5.2** we provided the first demonstration of the use of CLI for true image-guided, intraoperative surgical resection of tumors. The results presented strongly support the continued development of CLI as both a preclinical and a clinical tool for use in both molecular imaging and surgical procedures.

The results of this thesis are further discussed and summarized in **chapter 6**.

3.1

Paradoxical glomerular filtration of carbon nanotubes

Ruggiero A, Villa C, Bander E, Rey DA, Bergkvist M, Batt CA, Manova-Todorova K,
Deen WM, Scheinberg DA, McDevitt MR

Abstract

The molecular weight cut-off for glomerular filtration is thought to be 30-50kD. Here we report rapid and efficient filtration of molecules 10-20 times that mass and a model for its mechanism. We conducted multi-modal imaging studies in the mouse to investigate renal clearance of a single-walled carbon nanotubes (SWCNT) construct covalently appended with ligands allowing simultaneous dynamic Positron-Emission Tomography, near-IR fluorescence imaging, and microscopy. These SWCNT have a distribution of lengths ranging from 100 to 500 nm. The average length was determined to be 200-300 nm long which would yield a functionalized construct with molecular weight ~350-500kD. The construct was rapidly ($t_{1/2}$~6 min.) renally cleared intact by glomerular filtration with partial tubular reabsorption and transient translocation into the proximal tubular cell nuclei. Directional absorption was confirmed in vitro using polarized renal cells. Active secretion via transporters was not involved. Mathematical modeling of the rotational diffusivity showed the tendency of flow to orient SWCNT of this size to allow clearance via the glomerular pores. Surprisingly, these results raise questions about the rules for renal filtration, as these large molecules (with aspect ratios ranging from 100-to-500:1, were cleared similarly to small molecules. SCWNT and other novel nanomaterials are being actively investigated for potential biomedical applications and these observations – that high aspect ratio in addition to large molecular size have an impact on glomerular filtration – will allow design of novel nano-scale based therapeutics with unusual pharmacological characteristics.

Introduction

Carbon nanotubes (CNT) have interesting properties and have been proposed as novel components of drugs and devices in pharmaceutical and biomedical applications (1). CNT possess unique intrinsic physical, chemical, electronic, thermal, and optical properties and can be chemically modified (*e.g.*, with targeting ligands, magnetic, radioactive, fluorescent, and chemotherapeutic moieties) to exhibit additional extrinsic properties (2-4). Pharmacokinetic (PK) studies of covalently-functionalized single-wall CNT (SWCNT) (5-9) and multiwall (MWCNT) (10-12) have reported short blood compartment half-life (1-3h), limited tissue (kidneys, liver, and spleen) accumulation and renal excretion. Clearance via renal mechanisms is significant (13) as it provides the opportunity for the host to eliminate SWCNT and this will allow potential therapeutic and diagnostic applications in vivo. The elimination of non-covalently modified SWCNT has been reported to favor the hepatobiliary route with evidence that the renal route has a minor role (14).

Renal clearance of solutes occurs by a combination of the processes of glomerular filtration, active tubular secretion, and passive tubular reabsorption (15). Previously, we reported radioactivity in the renal cortex and in the urine within 1h of administration of radiolabeled SWCNT, but were unable to describe the mechanism (8). Others described glomerular filtration of multi-wall CNT (MWCNT), but did not investigate or comment on the other possible elimination processes (10-12) of secretion or reabsorption. However, skepticism about CNT renal excretion remained (16) because of lack of a complete biologic mechanism and confirmation of the identity of the bulk of the excreted CNT. We designed a covalently functionalized-SWCNT construct, suitable for several different imaging modalities, in order to explore the global and local PK profile in an animal model and performed a series of experiments to investigate the net contributions of renal filtration, secretion and reabsorption to clearance and to comment on the identity of the eliminated SWCNT. Further we explained the experimental data by mathematically modeling the rotational diffusivity of this high aspect ratio, high molecular weight (MW) molecule.

Herein, SWCNT were covalently-functionalized with amino-groups; appended with two fluorescent dyes (AF488 and AF680) and metal-ion chelands (DOTA); radiolabeled with [86]Y and fully characterized before and after injection into mice. The PK of the construct, SWCNT-[(([86]Y]DOTA)(AF488)(AF680)], was determined with dynamic PET of the entire animal, Near-InfraRed (NIR) fluorescence imaging of the kidney and by immunohistochemistry (IHC) and immunofluorescence (IF) imaging of the nephron taking advantage of the different imaging modalities appended to the construct.

Results

Synthesis and characterization of size, charge and composition of multi-functionalized SWCNT.

The high purity HiPco-produced SWCNT (Unidym) have individual tube lengths specified to range between 100 to 1000 nm and diameters to range between 0.8 to 1.2 nm (as measured by AFM). We did not acid oxidize nor sonicate at high power our SWCNT material at any step. Chromatographic, TEM, chemical, spectroscopic, and Raman characterizations were performed as described previously (7-9) and confirmed the identity, stoichiometry and purity of the nano-material (Fig. 1). TEM analyses of our materials showed bundled aggregates of SWCNT with length (mean ± s.d.) of 195 ± 69 nm (n = 644) which spanned a 500 nm range (SI, Fig.S6). Dynamic light scattering (DLS) showed an average hydrodynamic radius of 105±2.9 nm for the construct (range was 90-900 nm). Based on this DLS data (and the assumptions provided in the Materials and Methods) the average SWCNT length was calculated to be ~315 nm (assuming a CNT rod shape with d~1 nm). A z-potential value of -8.9±3.3 mV revealed that the construct had an overall negative charge (SI, Fig. S2). Taking the TEM and DLS data into account would yield a construct with average length of 200-300 nm. The SWCNT-[(DOTA)(AF488)(AF680)] was assayed to contain 0.02 mmol of AF488, 0.04 mmol AF680, and 0.4 mmol DOTA per gram of SWCNT, respectively. Using these values, a representative construct of L~315 nm would have a MW ~500 kD, and have 10 AF488, 20 AF680, and 200 DOTA moieties appended per molecule. Shorter and longer constructs would have proportionally smaller and larger MW. The radiolabeled SWCNT-[([^{86}Y]DOTA)(AF488)(AF680)] had a specific activity of 322 GBq/g (8.7 Ci/g) and was 96% radiochemically pure. Reverse phase radio-HPLC analysis confirmed the identity of the radiolabeled product which contained ^{86}Y activity (> 95%), the characteristic CNT UV-Vis spectral signature, and both fluorophore (488 and 680 nm) absorbance and fluorescence signals (Fig. 1).

High molecular weight CNT constructs were excreted intact via glomerular filtration in the first seconds after injection

After injection of the construct, dynamic PET images showed rapid (< 1 min.) construct accumulation in the kidneys (Fig. 2a, 2c); radioactivity, measured by Region of Interest (ROI), increased rapidly in the first seconds post-injection, representing mainly the renal blood pool activity and reached a peak at approximately 3 minutes post-injection. Radioactivity also rapidly appeared in the bladder immediately post-injection and plateaued after 20 minutes (Fig. 2b, 2d).

The contribution of active secretion to the clearance mechanism was investigated by competitive inhibition studies. Cimetidine, probenecid and gentamicin were administered to block the organic cation (OCT), the organic anion (OAT), or the megalin transport apparatus, respectively (17-19). The time-activity curve data from the kidneys (Fig. 2c) and bladder (Fig. 2d) was not statistically different for all groups. Rapid blood
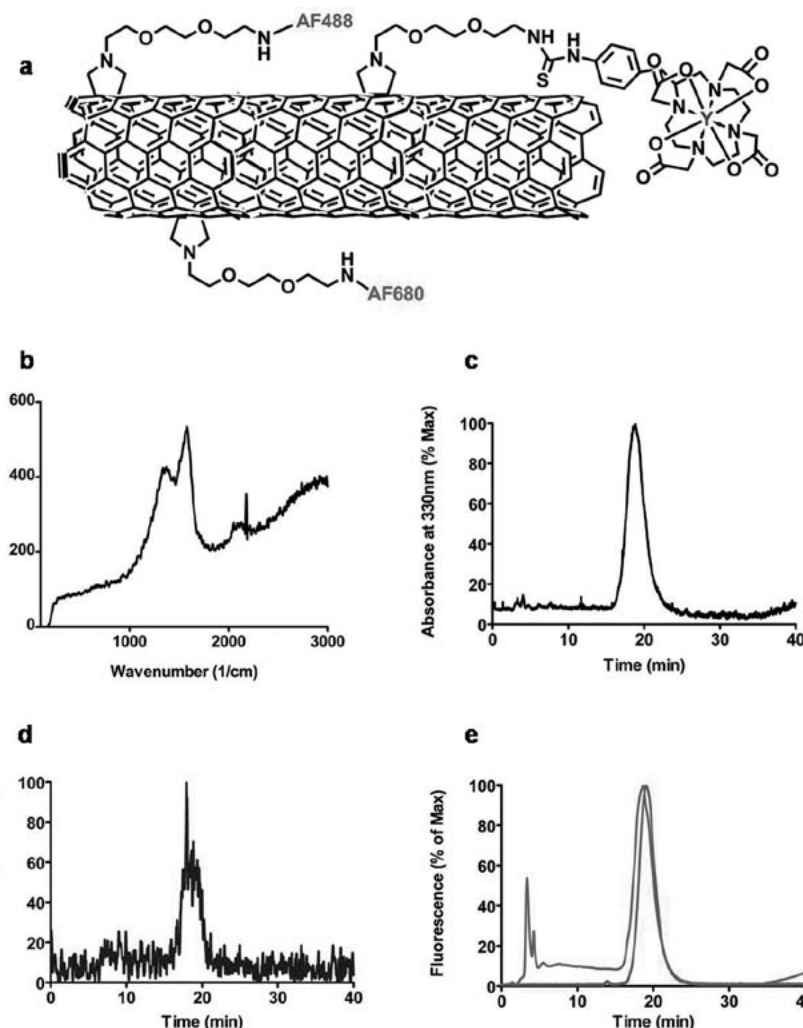
Fig. 1 *Water-soluble CNT covalently-functionalized with DOTA, AF488 and AF680.* (**a**) Schematic representation of the key appended moieties comprising the radiolabeled construct SWCNT-[([^{86}Y]DOTA) (AF488)(AF680)]. (**b**) Raman spectrum of the purified SWCNT-NH$_2$ starting material. Reverse phase HPLC chromatographs of SWCNT-[([^{86}Y]DOTA)(AF488)(AF680)] demonstrating the four major components: (**c**) UV-Vis trace (black) of the absorbance at 330 nm (CNT signature); (**d**) radioactivity trace (blue) of the ^{86}Y; (**e**) the superimposed fluorescence traces of the AF488 (green) and AF680 (red) dye moieties.

clearance was observed as previously reported (6-11). ROI analysis of the dynamic PET images of the heart was employed to yield a t$_{1/2}$ of 6-10 min. for blood compartment clearance while a t$_{1/2}$ of 6 min. was seen for activity in the bladder to plateau. Ex vivo biodistribution at 1 hour post-injection confirmed the PET data. There was no statistically significant difference in the kidney or other harvested tissue between the groups (Fig. 2e). Competitive inhibition of the OAT, OCT, or megalin transport apparatus did not impact the clearance of the construct and thus ruled-out active secretion or reabsorption via these transporters as components of the renal processing and elimination.
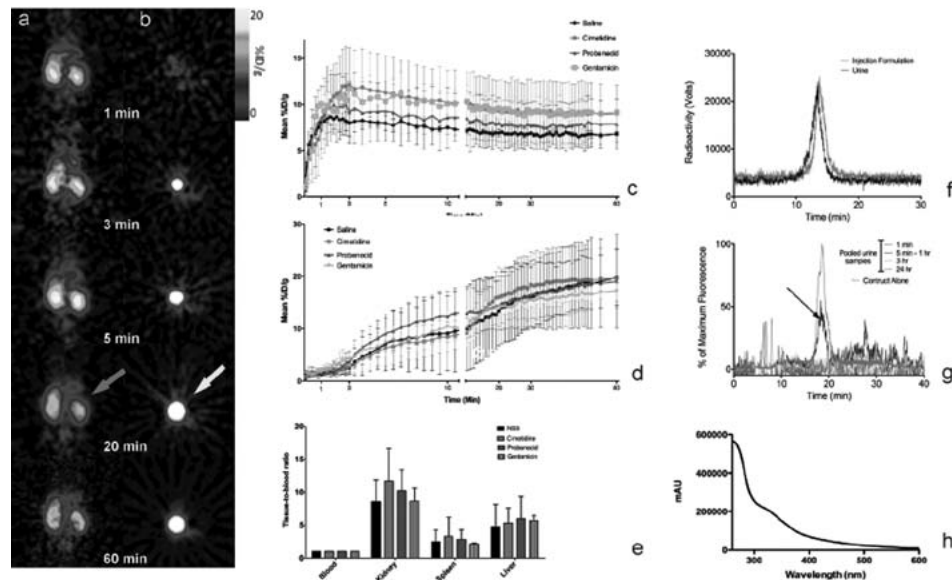
Fig. 2 *Biodistribution data of SWCNT-[([86Y]DOTA)(AF488)(AF680)] in mice.* Dynamic PET images of a representative animal showing the rapid renal clearance: (**a**) kidney coronal sections (green arrow) and (**b**) axial bladder sections (yellow arrow) at different time points. Time activity curve data (mean ± SD) obtained from ROI analysis of PET images of the (**c**) kidneys and (**d**) bladders of mice in the three groups receiving the inhibitors of active secretion and a saline control group. The 3-min. kidney accumulation (mean±s.d.) values were saline 8.0±1.4; cimetidine 12.1±3.9; probenecid 9.1±3.3; gentamicin 11.6±0.9 %ID/g. Bladder accumulated activity at 20-min. were saline 13.3±6.5; cimetidine 16.0±5.6; probenecid 14.4±4.6; gentamicin 14.2±1.2 %ID/g. (**e**) Tissue-to-blood data from the tissue harvest data of the mice in the active secretion study. (**f**) Radioactivity chromatograph of urine sample (black trace) from a mouse that received SWCNT-[([86Y]DOTA)(AF488)(AF680)] overlaid with a sample of the injected construct (red trace). (**g**) Fluorescence chromatograph (black trace) of urine samples collected at 1 min, 5-60 min, 3 hr, and 24 hr from mice that were administered SWCNT-[(DOTA)(AF488)(AF680)] overlaid with a sample of the injected construct (red trace).

The identity of the excreted construct was characterized by HPLC analysis of the urine samples. Chromatographs of the urine of mice that received the radiolabeled construct for PET studies contained a radio-peak that eluted with the same retention time as the injected construct (Fig. 2f). Similarly, chromatographs of the urine of mice that were injected with the construct for NIR imaging, IHC and IF studies contained a fluorescent peak that eluted with the same retention time as the construct (Fig. 2g). The intact construct was found in the urine and assumptions that the imaged signals were associated with the construct were validated. Additional analyses of urine samples from mice that received 6- to 40-fold larger doses of construct showed the characteristic UV-Vis spectrum of the SWCNT in the chromatographic peak attributed to the construct (SI figure S7). The analysis of urine samples from mice that received injections of only the hydrolyzed dyes (SI Fig. S1b) revealed that the unattached dyes eluted earlier and at very different times than the urine samples containing the intact construct.

SWCNT were partially reabsorbed in the proximal tubules and reversibly accumulate in the nuclei.

The nephron distribution of the construct was evaluated as a function of time from 1 minute to 7 days by IF, IHC and NIR imaging (Fig. 3 and SI Fig. S4). There was a strong correlation observed between IHC and IF results (IHC had higher background staining while IF revealed more detailed structure). In the first minute post-injection, SWCNT appeared in the glomerular capillaries as well as in the Bowman capsule and in the tubular system. No significant signal was visualized in the peritubular capillaries or in the baso-lateral compartments, suggesting mainly a first-pass filtration clearance. Noteworthy, the
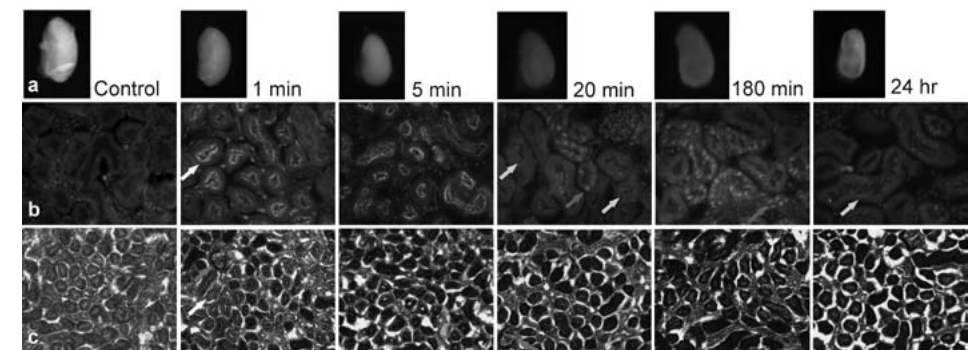

Fig. *3 NIR images of harvested kidneys and correspondent IF and IHC microscopic sections of mice injected with SWCNT-[(DOTA)(AF488)(AF680)].* Time course imaging of kidney of animals injected with SWCNT-[(DOTA)(AF488)(AF680)] by using: (**a**) NIR imaging; (**b**) IF (composite image: DAPI + AF488 + TRITC) and (**c**) IHC techniques. It is reported proximal tubule brush border accumulation (white arrows) glomerulus (red arrows) in the first minutes and progressively cytoplasmic (yellow arrows) and nuclear accumulation (magenta arrows).

highest IF and IHC signal was associated with the luminal side of proximal tubular cells (brush border) rather than distal tubules and collecting ducts. The signal remained in this location and increased in intensity at 3 and 5 minutes. At 20 minutes, the signal was no longer only associated with the brush border, but also with the cytoplasm of proximal tu-bular cells (punctate pattern). Perinuclear and nuclear compartments were also stained in some of the proximal tubular cells. The nuclear/perinuclear staining intensity increased at 60 (Fig 3, Fig 4a and 4b) and 180 minutes, while the cytoplasmic signal diminished. At 24 hours, most of the signal cleared from the nuclei and again appeared cytoplasmic (punctate pattern). After 7 days the construct staining was very weak and only a few tubules were stained. The PK of AF488 dye-alone was acquired at 1 and 60 minutes as a control (see SI Fig. S4). AF488 dye was rapidly and completely filtered with staining apparent only in the tubules in the first minute and no sign of retention at 60 minutes. An in vitro time course study using polarized kidney HK-2 cells (Fig. 4 c-h) showed a similar accumulation of construct by the tubular cells, again with preferential uptake from the luminal side (Fig 4i).
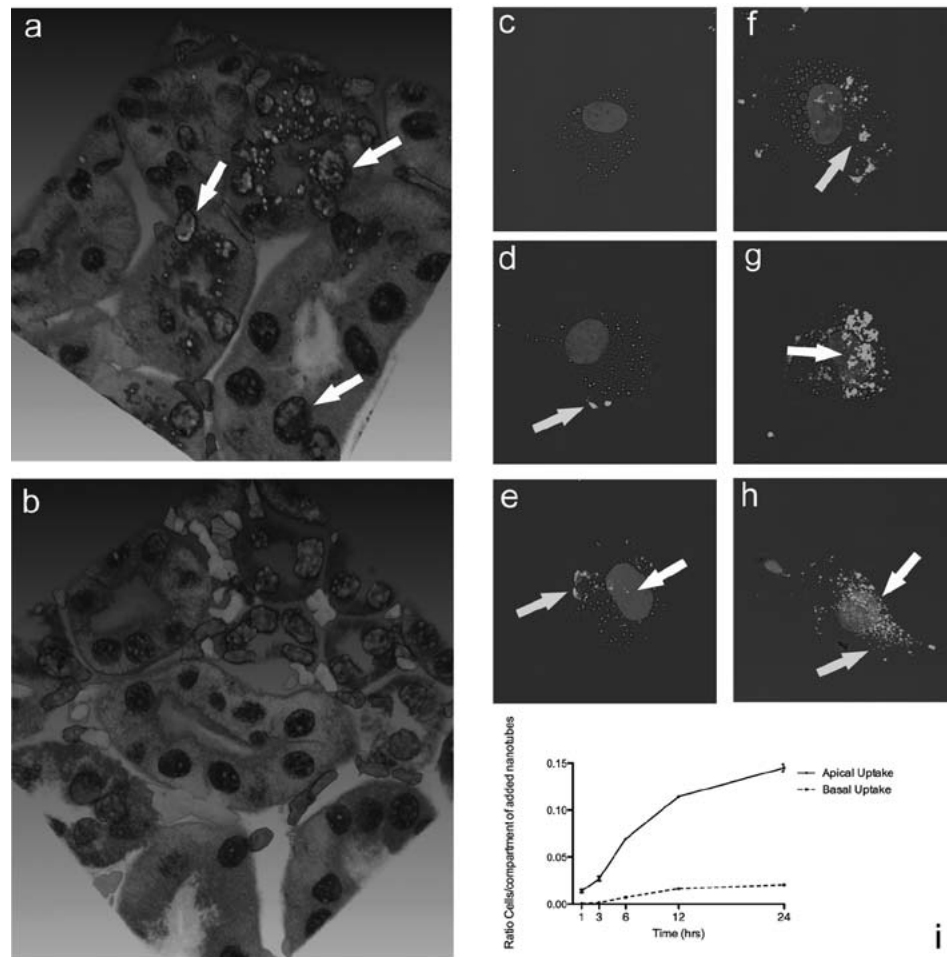
Fig. 4 *In vivo and in vitro kidney cell uptake of SWCNT-[(DOTA)(AF488)(AF680)].* Confocal microscopic 3D reconstructed IF image of the kidney cortex in mice (**a**) injected with SWCNT-[(DOTA)(AF488)(AF680)] at 1h post-administration showing both 'punctate' cytoplasmic and nuclear accumulation and (**b**) control (not-injected) animal. Composite (AF488+DAPI+DIC) confocal images of HK-2 cells (**c**) not exposed and exposed to SWCNT-[(DOTA)(AF488)(AF680)] for (**d**) 30 min, (**e**) 60 min, (**f**) 6 h (**g**) 12 h and (**h**) 24h. Progressive accumulation of the construct in the cytoplasm (yellow arrow) and nuclei (white arrow). (**i**) Differential uptake of SWCNT-[([111In]DOTA)(AF488)(AF680)] by HK-2 cells exposed either on the apical (brush border) side or the basal side by using transwell chamber (see SI).

Mathematical modeling explains how these high aspect ratio molecules align with flow and access the glomerular pores allowing rapid clearance compared to globular molecules.

The lengths of the SWCNT (based on TEM data) used were 100 nm ≤ L ≤500 nm and any individualized construct greatly exceeds the apparent diameter of glomerular capillary pores (~10 nm). Accordingly, to pass through the capillary wall at an appreciable rate during filtration, the CNT must be highly oriented, with the long axis directed toward the openings as shown (Fig. 5a). As with the flow of a dilute suspension of fibers
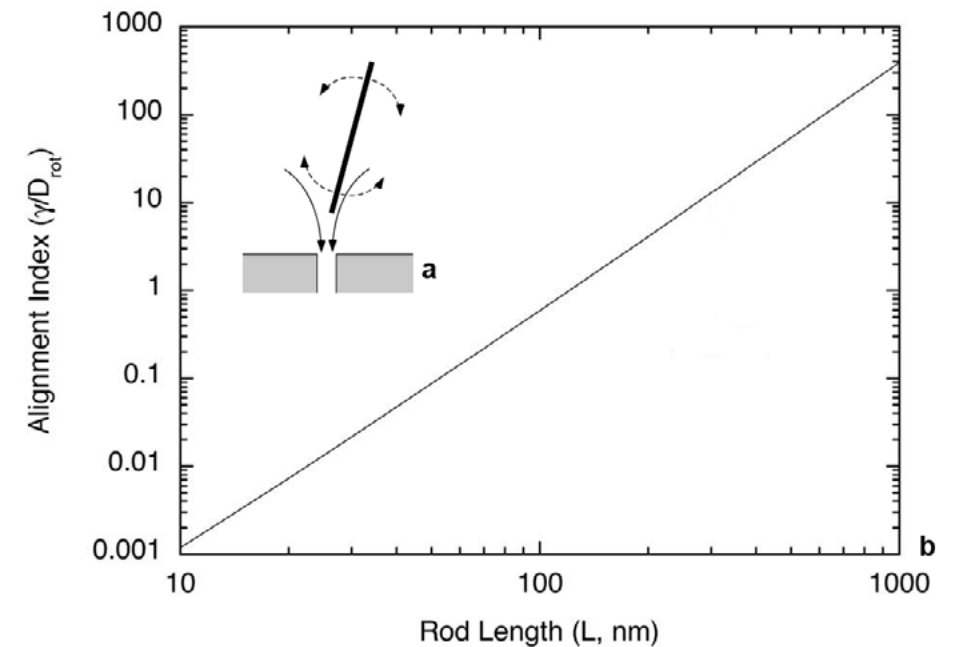

Fig. 5 *Mathematical modeling of the rotational diffusivity showing how the values for g/D_{rot} increase dramatically as the length of the SWCNT decreases.* (**a**) Schematic of a long, rod-like molecule approaching the entrance of a pore in a filtration process. The converging flow (solid curves) tends to align the major axis of the rod with the pore. This is opposed by rotational diffusion (dashed curves), which tends to randomize the rod orientations. If the rod length greatly exceeds the pore diameter (as shown), entry into the pore is probable only if the rotational Brownian motion is weak enough to permit a high degree of alignment. (**b**) Predicted effect of molecular length on the tendency of a rod-like molecule to align end-on at a glomerular pore. The rod diameter is assumed to be 1 nm and the other inputs are as described in the text. Values of g/D_{rot} much larger than unity, as for the SWCNT studied, suggest high degrees of alignment and a greatly increased probability of entering pores in the capillary wall.

toward an orifice, the tendency of the velocity field to create such an end-on orientation will be opposed by Brownian motion. That is, random rotation of the fibers due to thermal motion tends to preclude any preferred orientation. The competition between these processes is embodied in the ratio g/D_{rot}, where g is the rate of strain in the fluid and D_{rot} is the rotational diffusivity of a fiber or molecule. Large values of this ratio (compared to unity) indicate a strong tendency for flow-induced orientation, and small ones suggest nearly random orientations (20). If the mean fluid velocity at an orifice is u and the radius of the opening is r, then a suitable measure of the local rate of strain is $g = 4u/r$ (21). For a rigid rod of length L and diameter d, such that L/d is large, the rotational diffusivity is described by the following equation:

$$D_{rot} = \frac{3k_B T}{\pi \mu L^3} \ln\left(\frac{L}{d}\right) \qquad (1)$$

In equation 1, k_B is Boltzmann's constant, T is temperature, and m is the viscosity of the solvent (21). Using $u = 2 \cdot 10^{-5}$ m/s (average velocity at a fenestral opening) and $r = 5 \cdot 10^{-9}$ m (22), a representative rate of strain for fluid entering a glomerular pore is $g = 1.6$

$\cdot\ 10^4$ s^{-1}. With $k_B = 1.38 \cdot 10^{-23}$ J/K, $T = 310$ K, $m = 7 \cdot 10^{-4}$ Pa·s, $d = 1$ nm, and average $L = 200\text{-}300$ nm, the rotational diffusivity of a SWCNT is estimated as $D_{rot} = 1.1 \cdot 10^3$ s^{-1}. Thus, $g/D_{rot} \cong 9\text{-}15$. (n.b., an avearge range of lengths 200-300 nm was used for this calculation based upon TEM and DLS data.)

Discussion

In this article we describe how large molecules with high molecular weight and high aspect ratio, such as CNT, have unique properties in regards to renal clearance. Their unique pharmacokinetic profile makes them an appealing paradigm to better understand kidney glomerular physiology and to suggest the potential design features (e.g., shape and aspect ratio) of novel constructs with improved clearance properties.

The glomerulus acts as a highly selective filter consisting of the fenestrated endothelium, the glomerular basement membrane (GBM) and the interdigitated foot processes of podocytes. In addition to the heteroporous structure (i.e., many small and a few large pores) of the glomerular filter (23), there are also filtration slits bounded by podocytes with zipper-like structures and openings postulated to have dimensions of 4 nm x 14 nm, corresponding to slit half-width of 2 nm (24).

The immediate appearance of radioactivity in the bladder, within the first minute post-injection, strongly suggested a rapid translocation of SWCNT from the vascular to the urine compartment through glomerular filtration. This finding was surprising since predicting the trans-glomerular passage of a solute entails consideration of the molecular size, net charge, and configuration and in practice, albumin-sized globular proteins (~50kD) are typically not filtered (24, 25). Albumin has a Stokes-Einstein radius of 3.5 nm and is associated with a very low sieving coefficient ($\Theta = 0.0021$) (26). However, elongated molecules, such as bikunin and hyaluronan behave differently, resulting in over 100-fold higher sieving coefficients than albumin, despite similar molecular weights and charges. Moreover, it has to be taken into account that the threshold for the glomerular filtration of polymers is in the range of 30-50 kDa and also depends on charge, molecular conformation and deformability (24, 27). Because of its high aspect-ratio (d~1 nm, $100 \leq L \leq 500$nm), negative charge and high MW (150 to 750 kD), our construct largely exceeds the structural sizes of glomerular pores (at least in the longitudinal dimension) and the size of other molecules used to investigate glomerular filtration. Despite these features, we observed the renal elimination of ~65% of the recovered construct with ~15% of the construct undergoing passive reabsorption in the tubules at 1 hour post-injection.

Lacerda et al. reported transmission electron microscopy (TEM) evidence of several MWCNT molecules translocating via their transverse dimension directly into the Bowman capsule (11). This same group also reported a dynamic single photon emission tomography study to image the rapid clearance of their radiolabeled MWCNT in a mouse model into the urine (10). However, the contribution of secretion and reabsorption to the overall clearance mechanism was not reported.

We provide a theoretical model to suggest that the flow is strong enough to steer the CNT into the pores, and this provides a physical explanation for their rapid clearance into urine. As shown in Fig. 5b, if L were a factor of ten smaller (30 nm), then D_{rot} would increase by three orders of magnitude and the balance would shift toward no preferred orientation. Reducing L further to 10 nm, which is roughly the length of an albumin molecule, would further lessen the tendency toward flow-induced orientation by another order of magnitude. Thus, this mechanism for enhancing the passage of large molecules appears to be unique to entities with dimensions like those of the SWCNT studied.

Noteworthy, DLS measurements of our construct as well as TEM were used to characterize the size, since the latter only evaluates (in a typical sampling size) a non-representative amount of the CNT batch being studied (28). DLS measurements of cylindrical CNT also rely on some assumptions to yield a value for the size. The data provide an average hydrodynamic radius (R_h). We then assume a rod shape to relate R_h to radius of gyration (R_g). R_g for rods depends on the aspect ratio (length/diameter ratios). Our measured average value ranges of L ~ 200-300 nm certainly reflects the specified properties of this SWCNT. The TEM images (SI Fig. S6) show a sampling of the SWCNT with sizes consistent with the DLS predictions.

Our previous PK report on analogous SWCNT constructs demonstrated a slower beta clearance phase from the kidney that can now be explained as the fraction of construct that was transiently taken into the tubule cells by reabsorption and then cleared (7). Presumably, the reabsorbed construct was processed in the tubules and then released back to the blood (which also demonstrated a slower beta clearance phase (8)) for filtration.

The PK profile of different CNT constructs has varied depending on the chemical composition. Pristine SWCNT showed significant Reticulo-Endothelial System (RES) tropism, attributable to the lipophilicity of the carbon atoms (29); non-covalently PEG-functionalized-SWCNT exhibited long blood circulation with RES uptake (14); and covalently-functionalized-SWCNT and -MWCNT demonstrated renal clearance with limited RES uptake (5-12). Pristine CNT, dispersed with surfactants, favor liver accumulation and hepatobiliary excretion over kidney accumulation and renal excretion while covalently-modified CNT favor the converse. The constructs in this study did accumulate about 7% ID in the liver. The PK profiles of these materials were complex but they can be manipulated through the construct design.

Finally, we and others did not observe any glomerular or tubular cell toxicity or modification of the nephron structure nor observed any chronic toxicity with functionalized CNT (6-12, 30-32). The importance of understanding the PK and toxicity of these novel CNT materials is crucial in developing medically useful agents (33). Of course, the PK profile may vary depending upon the stoichiometry and identity of the moieties attached to the CNT. Clearly, the results reported herein demonstrated the surprising ability of an animal model to immediately and efficiently eliminate large, soluble, covalently-functionalized CNT nanomaterials intact by glomerular filtration. The tubular reabsorption component of the mechanism seemed to be transient and the absorbed CNT was released to presumably undergo further rounds of elimination in the slower beta clearance phase (see blood and tissue PK in ref. 8 and 7, respectively). Reversible accumulation of PEGylated-SWCNT in mammalian cell nuclei has been reported (34) only in vitro and is an area of interest that needs to be further addressed. We described progressive and reversible accumulation of the construct in kidney tubular cells in vitro (HK-2) as well as in vivo.

In conclusion, the kidney was able to rapidly and effectively eliminate xenobiotics from the blood compartment without concomitant degradation and this is the most desired clearance route for imaging and therapeutic constructs. Surprisingly, this large molecule, with an aspect ratio of ranging from 100-to-500:1, was cleared similarly to a small molecule. Hence, a better understanding of the biophysics of novel materials within the glomerular filter helps further the design criteria of potentially new medicinally useful constructs.

Materials and Methods

Synthesis and characterization of the SWCNT-[(DOTA)(AF488)(AF680)] construct

Raw HiPCO SWCNT (Unidym) were not acid-treated or sonicated, but were only covalently amine-functionalized as described (2-4,6-9). The SWCNT-NH$_2$ product was purified from carbonaceous impurities using a C18 Seppak (Waters) and analyzed by HPLC, Raman spectroscopy, and transmission electron microscopy (TEM) (Fig. 1 and SI). The amine loading was determined using the Sarin assay and TEM and Raman spectroscopy were performed as described previously (7-9). Details of the SWCNT functionalization with the different fluorophores and radiolabeling procedures are presented in SI.

Size and Charge Characterization

Dynamic light scattering (DLS) and z-potential measurements were performed using a Zetasizer Nano ZS system equipped with a narrow bandwidth filter (Malvern Instruments). The SWCNT construct was diluted 1:10 in 10 mM HEPES pH 7.2 buffer and measurements were carried out in triplicate. Average diameter of SWCNT ($2 \cdot R_h$ (radius of hydration)) was obtained using the non-negative least squares fitting algorithm provided with the DLS software. R_h was converted to the radius of gyration (R_g) for a cylinder ($R_g = 1.732 x R_h$). Approximate length of SWCNT was calculated using the relation: $R_g = (L^2/12 + R^2/2)^{1/2}$ where L is length and R is the radius of a cylinder. z-potential was calculated via the Henry equation using the Smoluchowski approximation $f(K_a)=1.5$ (35).

Dynamic PET Imaging

Dynamic Imaging was performed with the microPET Focus™ 120 (CTI Molecular Imaging). Mice (♂, NCr/nu/nu, Taconic) were maintained under 2% isoflurane/oxygen anesthesia during the scanning. One-hour list-mode acquisitions were initiated at the time of intravenous (IV) injection of 0.008 mg per mouse (initially 2.78 MBq (0.075 mCi)) of CNT-[([^{86}Y]DOTA)(AF488)(AF680)] via a 27G tail vein catheter (Vevo MicroMarker TVA, Visual Sonics) placed in the lateral tail vein (See SI). For all in vivo experiments, housing and care were in accordance with the Animal Welfare Act and the Guide for the Care and Use of Laboratory Animals. The animal protocols were approved by the Institutional Animal Care and Use Committee at MSKCC.

Organic Cationic Transport, Organic Anionic Transport, and Megalin Receptor Competition Studies

Fifteen mice (♂, NCr/nu/nu) were randomly separated into 4 groups. Group I (n=4) received an intraperitoneal (ip) injection of normal saline; Group II (n=4) received an ip injection of cimetidine at 100 mg/Kg; Group III (n=4) received an ip injection of probenecid at 20 mg/Kg; Group IV (n=3) received an ip injection of gentamicin at 40 mg/Kg (17-19). Each competitive inhibitor and the saline control were injected in a volume of 0.4 mL approximately 0.5 h before SWCNT construct administration and imaging was commenced.

HPLC Analysis of Urine Samples

In one experiment, 8 mice (♂, NCr/nu/nu) that received 0.01 mg of SWCNT-[(DOTA)(AF488)(AF680)] in 0.10 mL via retroorbital sinus IV injection and 1 mouse received no construct and served as a control. Mice were sacrificed at 1, 3, 5, 20, 60, 180m, 24h, and 7d and the kidneys harvested for NIR, IHC and IF analyses and the urine collected for HPLC analysis. HPLC analysis (Method II, see SI) was performed using the AF680 NIR fluorescence signal to follow the construct. An aliquot of the construct and a sample of urine from an untreated mouse each served as controls. The data were normalized to a percentage of maximum fluorescence for each run and the background fluorescence from the untreated mouse urine was subtracted from each chromatograph.

Urine was harvested after the mice were euthanized per IACUC protocol, the bladder exposed by incision, and the urine collected with a sterile 1 mL syringe (before any other tissue or blood harvesting was performed) and transferred to a tared 12×75 mm test tube capped and weighed.

In a second experiment, representative urine samples from the 15 ($\male$, NCr/nu/nu) in the 4 Groups that were PET imaged were collected immediately after imaging (1h post-injection of 0.008 mg of SWCNT-[([^{86}Y]DOTA)(AF488)(AF680)]. HPLC analysis (Method I, see SI) was performed using the radioactivity signal to follow the construct. An aliquot of the construct served as control.

Tissue Harvest for g-Counting

Following the dynamic PET imaging study of the 15 mice to investigate biodistribution, clearance, and the effect of competitive inhibition of the active secretion transporters, each animal was sacrificed with CO_2 aspiration. Tissue samples (blood, kidney, liver, spleen) and urine were harvested, weighed, and counted using a g-counter (Packard Instrument Co.) with a 315 to 435 keV energy window. Standards of the injected formulation were counted to determine the percentage injected dose per gram (%ID/g).

Tissue Harvest for IHC and IF Time Course Microscopy

Eight mice ($\male$, NCr/nu/nu) received 0.01 mg of SWCNT-[(DOTA)(AF488)(AF680)] in 0.10 mL via retroorbital sinus IV injection and 1 mouse received no construct and served as a control. Mice were sacrificed at 1, 3, 5, 20, 60, 180m, 24h, and 7d and the kidneys harvested for IHC and IF analyses and the urine collected for HPLC analysis. Kidneys were harvested, washed in ice cold PBS and fixed for 24h in 4% paraformaldehyde, embedded in OCT, frozen at -80°C, and cryo-sectioned to obtain 0.010 mm thick samples. IHC and IF staining was performed as described (See SI).

NIR Fluorescence Imaging of the Construct in Kidney Samples ex vivo

The NIR fluorescence signal of the SWCNT-[(DOTA)(AF488)(AF680)] construct was imaged in the kidneys following tissue harvest for the IHC and IF time course microscopy study. The kidneys were imaged with the Maestro Imaging System (Cri, Woburn MA) by using the 680nm emission/679nm excitation, long pass step 10 filter. The image acquisition time was 500s with binning 2x2.

Human Proximal Renal Tubular Cells (HK-2 cells)

Human proximal renal tubular cells (HK-2 cells) derived from normal kidney were obtained from ATCC. HK-2 cells were cultured in Keratinocyte Free Serum Medium (K-SFM, Invitrogen, Gibco) medium containing 0.05 g/L bovine pituitary extract and 5 ng/mL EGF at 37°C and 5% CO_2. The HK-2 cells were seeded on 24-mm diameter polyester filters (1 × 10^5 cells/well) with a pore size of 0.4 μm (Transwell Clears, Corning-Costar, Cambridge, MA). The cells were cultured for 7d to the allow cells to attach and polarize (36).

Data Analyses

Three-dimensional ROI analysis on PET images was accomplished with AsiPRO VM 5.0 software (Concorde Microsystems) to perform ROI analyses. TEM image analysis was performed using ImageJ software (NIH, http://rsb.info.nih.gov/ij/). Widefield and confocal microscopy images were evaluated using ImageJ, AxioVision LE (Zeiss) and Amira 4.1 (Visage Imaging, Inc.) software. Graphs were constructed and statistical data were evaluated using Graphpad Prism 3.0 (Graphpad Software, Inc.). Statistical comparison between 2 experimental groups was performed using a t test (unpaired comparison); comparison of multiple groups was performed with the 1-way ANOVA using Bonferroni's multiple comparison post hoc analysis. All statistical comparisons were 2-sided, and the level of statistical significance was set at $p<0.05$.

Acknowledgements

References

1. Kostarelos K et al. (2009) Promises, facts and challenges for carbon nanotubes in imaging and therapeutics. (Translated from eng) Nat Nanotechnol 4(10):627-633 (in eng).

2. Georgakilas V, Tagmatarchis N, Pantarotto D, Bianco A, Briand JP, Prato M. Amino Acid Functionalization of Water Soluble Carbon Nanotubes. Chem. Commun. 2002;5:3050-3051.

3. Tasis D, Tagmatarchis N, Bianco A, Prato M. (2006) Chemistry of carbon nanotubes. (Translated from eng) Chem Rev 106(3):1105-1136 (in eng).

4. Singh P et al. Organic functionalisation and characterisation of single-walled carbon nanotubes. Chem Soc Rev (2009) 38(8): 2214-2230.

5. Wang H, et al. (2004) Biodistribution of carbon single-wall carbon nanotubes in mice. (Translated from eng) J Nanosci Nanotechnol 4(8):1019-1024 (in eng).

6. Singh R, et al. (2006) Tissue biodistribution and blood clearance rates of intravenously administered carbon nanotube radiotracers. (Translated from eng) Proc Natl Acad Sci U S A 103(9):3357-3362 (in eng).

7. McDevitt MR, et al. (2007) Tumor targeting with antibody-functionalized, radiolabeled carbon nanotubes. (Translated from eng) J Nucl Med 48(7):1180-1189 (in eng).

8. McDevitt MR, et al. (2007) PET imaging of soluble yttrium-86-labeled carbon nanotubes in mice. (Translated from eng) PLoS One 2(9):e907 (in eng).

9. Villa CH, et al. (2008) Synthesis and Biodistribution of Oligonucleotide-Functionalized, Tumor-Targetable Carbon Nanotubes. (Translated from Eng) Nano Lett 8(12):4221-4228 (in Eng).

10. Lacerda L, Soundararajan A, & Singh R (2008) Dynamic Imaging of functionalized multi-walled carbon nanotube systemic circulation and urinary excretion. Adv. Mater. 20(2):225-230.

11. Lacerda L, et al. (2008) Carbon-nanotube shape and individualization critical for renal excretion. (Translated from eng) Small 4(8):1130-1132 (in eng).

12. Lacerda L, et al. (2008) Tissue histology and physiology following intravenous administration of different types of functionalized multiwalled carbon nanotubes. (Translated from eng) Nanomed 3(2):149-161 (in eng).

13. Longmire M, Choyke PL, & Kobayashi H (2008) Clearance properties of nano-sized particles and molecules as imaging agents: considerations and caveats. (Translated from eng) Nanomed 3(5):703-717 (in eng).

14. Liu Z, et al. (2008) Circulation and long-term fate of functionalized, biocompatible single-walled carbon nanotubes in mice probed by Raman spectroscopy. (Translated from eng) Proc Natl Acad Sci U S A 105(5):1410-1415 (in eng).

15. Birkett D (1992) Clearance of drugs by the kidneys. Australian Prescriber 15(1):16-19.

16. Liu Z, Tabakman S, Welsher K, & Dai H (2009) Carbon nanotubes in biology and medicine: in vitro and in vivo detection, imaging, and drug delivery. Nano Res 2:85-120.

17. Horbelt M, et al. (2007) Organic cation transport in the rat kidney in vivo visualized by time-resolved two-photon microscopy. (Translated from eng) Kidney Int 72(4):422-429 (in eng).

18. Stahl AR, et al. (2007) Renal accumulation of [111In]DOTATOC in rats: influence of inhibitors of the organic ion transport and diuretics. (Translated from eng) Eur J Nucl Med Mol Imaging 34(12):2129-2134 (in eng).

19. Schmitz C, et al. (2002) Megalin deficiency offers protection from renal aminoglycoside accumulation. (Translated from eng) J Biol Chem 277(1):618-622 (in eng).

20. Mongruel A & Cloitre M (2003) Axisymmetric orifice flow for measuring the elongational viscosity of semi-rigid polymer solutions. J. Non-Newtonian Fluid Mech 110:27-43.

21. Broersma S (1960) Rotational Diffusion Constant of a Cylindrical Particle. (Translated from English) Journal of Chemical Physics 32(6):1626-1631 (in English).

22. Deen WM, Lazzara MJ, & Myers BD (2001) Structural determinants of glomerular permeability. (Translated from eng) Am J Physiol Renal Physiol 281(4):F579-596 (in eng).

23. Deen WM, Bridges CR, Brenner BM, & Myers BD (1985) Heteroporous Model of Glomerular Size Selectivity - Application to Normal and Nephrotic Humans. (Translated from English) American Journal of Physiology 249(3):F374-F389 (in English).

24. Haraldsson B, Nystrom J, & Deen WM (2008) Properties of the glomerular barrier and mechanisms of proteinuria. (Translated from eng) Physiol Rev 88(2):451-487 (in eng).

25. Ohlson M, et al. (2001) Effects of filtration rate on the glomerular barrier and clearance of four differently shaped molecules. (Translated from eng) Am J Physiol Renal Physiol 281(1):F103-113 (in eng).

26. Lindstrom KE, Johnsson E, & Haraldsson B (1998) Glomerular charge selectivity for proteins larger than serum albumin as revealed by lactate dehydrogenase isoforms. (Translated from eng) Acta Physiol Scand 162(4):481-488 (in eng).

27. Fox ME, Szoka FC, & Frechet JMJ (2009) Soluble Polymer Carriers for the Treatment of Cancer: The Importance of Molecular Architecture. (Translated from English) Accounts of Chemical Research 42(8):1141-1151 (in English).

28. Itkis ME, Perea DE, Jung R, Niyogi S, & Haddon RC (2005) Comparison of analytical techniques for purity evaluation of single-walled carbon nanotubes. (Translated from English) Journal of the American Chemical Society 127(10):3439-3448 (in English).

29. Cherukuri P, et al. (2006) Mammalian pharmacokinetics of carbon nanotubes using intrinsic near-infrared fluorescence. (Translated from eng) Proc Natl Acad Sci U S A 103(50):18882-18886 (in eng).

30. Schipper ML, et al. (2008) A pilot toxicology study of single-walled carbon nanotubes in a small sample of mice. (Translated from eng) Nat Nanotechnol 3(4):216-221 (in eng).

31. Sayes CM, et al. (2006) Functionalization density dependence of single-walled carbon nanotubes cytotoxicity in vitro. (Translated from eng) Toxicol Lett 161(2):135-142 (in eng).

32. Dumortier H, et al. (2006) Functionalized carbon nanotubes are non-cytotoxic and preserve the functionality of primary immune cells. (Translated from eng) Nano Lett 6(7):1522-1528 (in eng).

33. Kostarelos K (2008) The long and short of carbon nanotube toxicity. (Translated from eng) Nat Biotechnol 26(7):774-776 (in eng).

34. Cheng J, et al. (2008) Reversible accumulation of PEGylated single-walled carbon nanotubes in the mammalian nucleus. (Translated from eng) ACS Nano 2(10):2085-2094 (in eng).

35. Milton K (1997) Scattering of Light & Other Electromagnetic Radiation (Academic Press, New York).

36. Yuan ZX, et al. (2009) Specific Renal Uptake of Randomly 50% N-Acetylated Low Molecular Weight Chitosan. (Translated from English) Molecular Pharmaceutics 6(1):305-314 (in English)

3.2

Imaging and treating tumor vasculature with targeted radiolabeled carbon nanotubes

Ruggiero A, Villa CH, Holland JP, Sprinkle SR, May C, Lewis JS, Scheinberg DA, McDevitt MR

Abstract

Single wall carbon nanotube (SWCNT) constructs were covalently appended with radiometal-ion chelates (1,4,7,10-tetraazacyclododecane-1,4,7,10-tetraacetic acid (DOTA) or desferrioxamine B (DFO)) and the tumor neovascular-targeting antibody E4G10. The E4G10 antibody specifically targeted the monomeric vascular endothelial-al-cadherin (VE-cad) epitope expressed in the tumor angiogenic vessels. The construct specific activity and blood compartment clearance kinetics were significantly improved relative to corresponding antibody-alone constructs. We performed targeted radioimmunotherapy with a SWCNT-([^{225}Ac]DOTA)(E4G10) construct directed at the tumor vasculature in a murine xenograft model of human colon adenocarcinoma (LS174T). The specific construct reduced tumor volume and improved median survival relative to controls. We also performed positron emission tomographic (PET) radioimmunoimaging of the tumor vessels with a SWCNT-([^{89}Zr]DFO)(E4G10) construct in the same murine LS174T xenograft model and compared the results to appropriate controls. Dynamic and longitudinal PET imaging of LS174T tumor bearing mice demonstrated rapid blood clearance (<1 hour) and specific tumor accumulation of the specific construct. Incorporation of the SWCNT scaffold into the construct design permitted us to amplify the specific activity to improve the signal-to-noise ratio without detrimentally impacting the immunoreactivity of the targeting antibody moiety. Furthermore, we were able to exploit the SWCNT pharmacokinetic profile to favorably alter the blood clearance and provide an advantage for rapid imaging. Near-infrared three-dimensional fluorescent-mediated tomography was used to image the LS174T tumor model, collect antibody-alone pharmacokinetic data and calculate the number of copies of VE-cad epitope per cell. All of these studies were performed as a single administration of construct and were found to be safe and well tolerated by the murine model. These data have implications that support further imaging and radiotherapy studies using a SWCNT-based platform and focusing on the tumor's vessels as the target.

Introduction

Advances in cancer diagnosis and therapy require improvements in the agents used to image and treat disease. Valuable modifications include those that enable these agents to specifically target disease, increase signal-to-noise, rapidly clear from the blood, and incorporate multiple imaging and therapeutic modalities. Carbon nanomaterials are being investigated as delivery platforms for diagnostic and therapeutic cargoes to target disease (1,2). Pharmacokinetic (PK) studies of soluble, covalently-functionalized, radiolabeled carbon nanotubes (CNT) have demonstrated rapid blood compartment clearance, high specific activity (S.A.), multi-modal imaging capability, renal elimination, and tumor-specific accumulation *in vivo* (3,6). Implementation of an imaging and therapeutic drug construct that is designed to target, report location, and irradiate the tumor vessels is a key strategic modification that will take advantage of the single wall CNT (SWCNT-) based construct's chemical, radiochemical and PK properties.

Many cancers are characterized by an extensive angiogenic, aberrant vascular network that supports the tumor proliferation and survival. The endothelial vessels in tumors often do not exhibit the same organizational hierarchy of arterioles, capillaries and venules present in normal tissue. Instead, tumor vessels are tortuous and have abnormal component and structural composition. Endothelial cells in these tumors are inefficiently and irregularly joined with holes, gaps and defects; pericytes are absent or loosely associated with vessels; and basement membranes are inefficiently applied relative to typical normal tissues. The pore diameters of tumors typically range between 40 to 80 nm. Large inter-endothelial junctions in cancerous tissue may be as large as 500 nm, whereas in healthy tissue these junctions are approximately 8 nm (7). Angiogenic endothelial cells express the monomeric VE-cadherin (VE-cad) epitope on the cell surface that upon dimerizing with another monomeric copy of VE-cad on an adjoining cell surface leads to the formation of tight adherens junctions between the cells (8-12). The antibody E4G10 binds only to the monomeric VE-cad and not the homodimeric form (the binding region is masked in the homodimers that form the tight cell-cell contacts), thus conferring specificity for targeting angiogenic and poorly joined endothelial cells in vivo while not binding to normal endothelium or the LS174T tumor.

The alpha particle-emitting radionuclide actinium-225 (^{225}Ac; $t_{1/2}$ = 10.0 d) attached to monoclonal antibodies (IgG) has been used as the therapeutic effector moiety in a number of preclinical studies[13-18] and is currently in clinical use (19-21). Alpha particles are charged helium nuclei that travel approximately 50-80 μm, which is similar to the dimensions of vessels within a tumor. The alpha particle track lengths appropriately match the vessel dimensions and a single traversal through a cell of a high linear energy transfer (LET) alpha particle can be acutely cytotoxic (22,23). Typical tumor vasculature is < 100 μm in diameter and smaller vessels are < 10 micrometers. In addition, individual alpha particles are able to kill a target cell due to their deposition of 5-8 MeV in a short ionizing track that is several cell diameters in length (23). This highly concentrated

field of ionizing radiation may also irradiate the cancer stem cell population that can be found in the adjacent perivascular niche of some tumors (24-26). Alpha particles are very potent cytotoxic agents in proximity to the targeted tissue, but will largely spare normal tissue; it is this characteristic that offers clear advantages to other known forms of radiation as a means of selective cell kill. We have previously demonstrated the utility of [225]Ac-radiolabeled E4G10 constructs to target and irradiate tumor vascular endothelium in animal models and improve survival, control tumor growth and normalize the vessels (27) and also the ability of the construct to target and eradicate bone marrow-derived endothelial progenitors (28).

Zirconium-89 ([89]Zr) is now being developed as one of the most promising new immuno-positron emission tomography (PET) agents for in vivo imaging of cancer (29-34). PET is based on coincidence detection of a positron-emitting radionuclide from two coincident 511 keV annihilation photons emitted simultaneously in opposite directions (35). The clinical use of PET has emerged as an important diagnostic imaging modality for humans because it provides extremely sensitive, quantitative, and functional information that is different from that obtainable with other largely anatomical imaging modalities (35). The physical decay properties of [89]Zr ($t_{1/2}$ = 78.41h, electron capture = 76.6%, β^+ = 22.3%) are well suited for use in the design of imaging agents with extended PK profiles. Recently reported improvements in the separation chemistry of [89]Zr from the yttrium-89 ([89]Y) target material have yielded a facile process for production of clinical-grade high S.A. [89]Zr using a small cyclotron (30). This process should lead to more widespread use of this radionuclide. The rationale for using SWCNT as the scaffold in our construct design is the following: SWCNTs are made almost entirely of carbon, are non-immunogenic and can be chemically modified (36-38). The commercially available SWCNTs have a diameter of 1-2 nm, and lengths of 100 nm to 1,000 nm. Thus, SWCNT have extremely high aspect ratios with estimated surface areas of 1,600 m^2/g. On the atomic level, SWCNTs have highly regular structures with defined periodicity. For every 100 nm of length, a SWCNT can have up to 12200 carbon atoms and weighs 150,000 daltons, providing numerous sites (typically 1 in 95 carbons was modified) for chemical modifications and anchoring of chemical, biological and radionuclide moieties (3-6). SWCNT that have been chemically functionalized with sidewall amino groups exhibit aqueous solubility and reactivity towards a variety of reagents under mild bioconjugation conditions (3-6; 36-39). The SWCNT appended with amines and the metal-ion chelate 1,4,7,10-tetraazacyclododecane-1,4,7,10-tetraacetic acid (DOTA) were water soluble (~20 g/L) and studied in vivo in animal models (3-6). Our data showed that these SWCNTs rapidly ($t_{1/2}$< 1 hour) cleared the blood and prototype SWCNT constructs (diameter=~1 nm; length=~300 nm; molecular weight=~500 kD) were predominantly eliminated intact within minutes via glomerular filtration through the renal pathway. Renal excretion was found to be facilitated by the high aspect ratio of SWCNT which confers lower rotational diffusivity and thus the CNT tend to orient with the blood flow allowing easy access to the glomerular pores (6). Other recent work described the enzymatic degradation of functionalized SWCNT *in vitro* and *in vivo*, offering the potential for

metabolic decomposition of CNT drug constructs (40-43). Further, toxicity studies have confirmed the safe in vivo use of functionalized SWCNT (44-47). Taken together, these data on renal elimination, enzymatic degradation and lack of toxicity support continued investigation of SWCNT as a platform in drug development.

We hypothesize that CNT constructs can be covalently multi-functionalized with copies of targeting moieties and different reporting and therapeutic radionuclides and thereby increase signal-to-noise and be used to image tumor vessels and improve the therapeutic index. The underlying rationale for this approach is that we are specifically targeting the aberrant and angiogenic tumor vessels and delivering a dose of short range (1–4 cell diameters), high energy (several million electron volts) cytotoxic alpha particles to the targeted area. In addition we will report the location of the drug construct. This approach is novel because it will examine the attributes of targeted radioimmunotherapy (RIT) with alpha particle generators, sensitive and quantitative PET imaging, and the specificity of the targeting E4G10 antibody in combination with the unique nanomaterial properties of SWCNT.

Materials and methods

LS174T Xenograft model in nude mice

Athymic nude mice (NCr nu/nu, ♂), 4-12 weeks of age were obtained from Taconic, Germantown, NY, USA. For all *in vivo* experiments, housing and care were in accordance with the Animal Welfare Act and the Guide for the Care and Use of Laboratory Animals. The animal use protocols were approved by the Memorial Sloan-Kettering Cancer Center (MSKCC) Institutional Animal Care and Use Committee. Human LS174T cells (human colon adenocarcinoma) were expanded in DME media supplemented with glucose, non-essential amino acids, L-glutamine, and 10% fetal bovine serum in an atmosphere of 5% CO_2 and air at 37°C. Cells were harvested and mixed with Matrigel (BD Biosciences, Palo Alto, CA) and 0.1 mL of 2–3E6 cells were injected subcutaneously into the right hind flank of each animal.

Table 1. Construct nomenclature, designation, study use, and specific activity

Construct nomenclature	Designation	Study	High SA (Ci/g)	Low SA (Ci/g)
SWCNT-([225Ac]DOTA)(E4G10)	Construct I	RIT	23	0.05
SWCNT-([225Ac]DOTA)(anti-KLH)	Control Construct I	RIT	23	N/A
SWCNT-([89Zr]DFO)(E4G10)	Construct II	RII	16	N/A
SWCNT-([89Zr]DFO)(anti-KLH)	Control Construct II	RII	16	N/A

Abbreviations: SA, specific activity; SWCNT, single wall carbon nanotube; DOTA, 1,4,7,10-tetraazacyclododecane-1,4,7,10-tetraacetic acid; RIT, radioimmunotherapy; anti-KLH, anti-keyhole limpet hemocyanin; DFO, desferrioxamine B; RII, radioimmunoimaging.

Construct design and syntheses

SWCNT (Nanolab, Newton, MA) were covalently amine-functionalized as described previously (3-6; 36-39). The SWCNT-NH$_2$ product was purified from carbonaceous impurities using a C18 Sep-Pak (Waters, Milford, MA, USA) and analyzed by high-performance liquid chromatography (HPLC), Raman spectroscopy, and TEM (3-6). Amine loading was determined using the Sarin assay while TEM and Raman spectroscopy were performed as described previously (3-6). Table 1 provides a list of the key drug constructs, the corresponding nomenclature, studies performed, and the SA values for the therapeutic and imaging studies from this work.
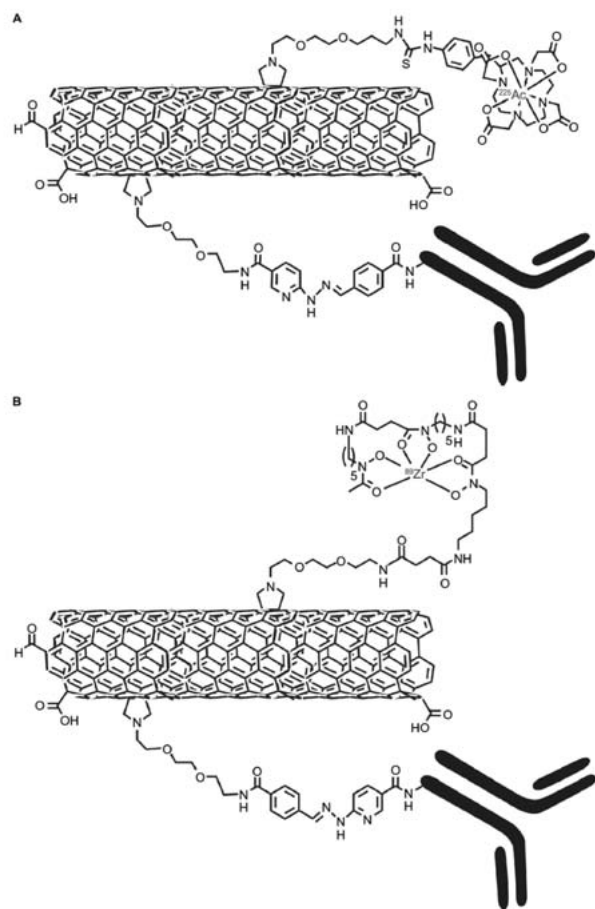

Fig. 1 Graphical representation (not drawn to scale) of the key appended moieties of the water-soluble SWCNT-NH$_2$ by covalent functionalization with radionuclides, DOTA, DFO and antibodies. (a) Radioimmunotherapeutic drug Construct I (SWCNT-([^{225}Ac]DOTA)(E4G10)); and (b) Radioimmunoimaging drug Construct II SWCNT-([^{89}Zr]DFO)(E4G10).

The radioimmunotherapeutic (RIT) drug **Construct I** (Figure 1A) was designed to specifically target the tumor vessels and deliver the potent alpha particle-emitting ^{225}Ac radionuclide generator (13). The key SWCNT-precursor to **Construct I** was assembled by first converting a fraction of the primary amines on the SWCNT-NH$_2$ construct to reactive hydrazinopyridine (HNH) moieties. Briefly, 0.5 g of SWCNT-NH$_2$ was dissolved in 1 mL of 100 mM sodium phosphate (NaH$_2$PO$_4$ and Na$_3$PO$_4$, Sigma-Aldrich, St. Louis MO)/150 mM sodium chloride (NaCl, Sigma-Aldrich), pH 7.8 buffer. Immediately before use, 5.5 mg of succinimidyl 4-hydrazinonicotinate acetone hydrazone (SANH, Solulink Inc., San Diego, CA) was dissolved in 0.2 mL of dry *N,N*-dimethylformamide (DMF, Sigma-Aldrich). An aliquot of SANH/DMF solution was added to the SWCNT-NH$_2$ to achieve a 0.25-fold mole ratio of SANH to primary amine. The reaction proceeded at ambient temperature for 2-3 hours at pH 7.6. The product, SWCNT-(HNH)(NH$_2$), was purified using size exclusion chromatography (SEC) with a 10 DG gel permeation column (BioRad Laboratories, Hercules, CA) as the stationary phase and metal-free water (MFW, Purelab Plus System, U.S. Filter Corp., Lowell, MA) as the mobile phase. The product was lyophilized to yield a solid that was found to be the desired SWCNT-(HNH)(NH$_2$) construct.

The second step entailed covalently appending multiple copies of 2-(*p*-isothiocyanatobenzyl)-1,4,7,10-tetraazacyclododecane-1,4,7,10-tetraacetic acid (DOTA-NCS, Macrocyclics, Inc., Dallas, TX, USA) to the remaining amines on the water soluble SWCNT-(HNH)(NH$_2$) construct, to yield a SWCNT-(DOTA)(HNH) construct in metal-free conditions at pH 9.5 (adjusted with 1 M metal-free carbonate solution) for 40 minutes at room temperature at a stoichiometry of 10:1 (DOTA-NCS to amine) (3-6). The product was purified using a 10 DG gel permeation column with MFW as the mobile phase. The 10 DG column was rendered metal-free by washing with 50 mL of 25 mM ethylenediaminetetraacetic acid (EDTA, Sigma-Aldrich) followed by rinsing with 250 mL of MFW. The product was lyophilized to yield a solid that was found to be the desired SWCNT-(DOTA)(HNH) construct.

$$\text{SWCNT-(DOTA)(HNH)} + {}^{225}\text{Ac} \rightarrow \text{SWCNT-([}^{225}\text{Ac]DOTA)(HNH)} \quad (1)$$

^{225}-Ac radionuclide was obtained from the U.S. Department of Energy's Oak Ridge National Laboratory (ORNL, Oak Ridge, TN, USA). Methods for radiolabeling and purification of a MFW solution of SWCNT-(DOTA)(HNH) with ^{225}Ac at pH 5 are similar to those described previously.[48] Briefly, 0.18 mg of SWCNT-(DOTA)(HNH) in 0.020 mL MFW were reacted with 0.005 mL of ^{225}Ac in 50 mM Optima grade hydrochloric acid (HCl, Fisher Scientific, Pittsburgh, PA) along with 0.020 mL of 150 g/L *l*-ascorbic acid (Sigma-Aldrich) and 0.20 mL of 3M tetramethylammonium acetate (Fisher Scientific) buffer, pH 5.5, at 60°C for 60 min (Reaction 1). Purification was accomplished using SEC with a P6 gel stationary phase and a PBS mobile phase. Chemicals used in the radiolabeling and purification steps were of ACS Reagent grade or higher purity. The labeling solutions were prepared and subsequently rendered metal-free with Chelex→ 100 resin, 200-400 mesh, sodium form, (BioRad Laboratories), and sterile filtered through a 0.22 or 0.45 mm filter device. Solutions of 50 mM diethylenetriaminepentaacetic acid (DTPA, Sigma-Aldrich) were sterile filtered and used to quench the labeling reaction prior to SEC. Human serum albumin (HSA) (Swiss Red Cross, Bern, Switzerland) and

0.9% NaCl (Abbott Laboratories, North Chicago, IL) were used as received. ^{225}-Ac activity was measured with a Squibb CRC-17 Radioisotope Calibrator (or equivalent model) (E.R. Squibb and Sons, Inc., Princeton, NJ) set at 775 and multiplying the displayed activity value by 5 to report the activity.

Instant thin layer chromatography using silica gel impregnated paper (ITLC-SG, Gelman Science Inc., Ann Arbor, MI) was used to determine the labeling efficiency of the reaction mixture and the purity of the product. Briefly, a 0.001 mL aliquot was spotted onto the paper strips and developed using two different mobile phases.[13,23,48] Mobile phase I was 10 mM EDTA and II was 9% NaCl (Sigma-Aldrich)/10 mM sodium hydroxide (NaOH, Sigma-Aldrich). The R_f of the radiolabeled construct was 0 and any free metal species and metal chelates were characterized by R_f of 1.0 in mobile phase I. In mobile phase II, the radiolabeled construct and free metal species were characterized by R_f of 0 and the R_f of the metal chelates were 1.0. The strips were counted intact using a System 400 Imaging Scanner (Bioscan Inc., Washington, DC).

E4G10 + SFB → E4G10-FB   (2)

The next key step (Reaction 2) was the conversion of the VE-cad specific IgG (E4G10, Imclone Systems, New York, NY) or the isotype control anti-Keyhole Limpet Haemocyanin (KLH) IgG (R&D Systems, Minneapolis, MN) to the reactive arylaldehyde modified-IgG precursors. Briefly, immediately before use, 15 mg of succinimidyl 4-formylbenzoate (SFB, Solulink) was dissolved in 0.50 mL DMF. An aliquot of this modification solution was added to 2.5 mg of E4G10 protein (5 g/L) (or the isotype control IgG) to achieve a 10- to 20-fold molar excess of the reagent. The reaction mixture was incubated at 37ºC for 2-3 hours. Purification of the arylaldehyde modified IgG was performed by SEC as described above. The modified proteins were stored at 4°C. The stoichiometry of substitution (moles of FB per mole IgG) was determined first by assaying the protein concentration using the bicinchoninic acid protein assay (BCA) Protein Assay (Pierce, Rockford, IL) and the moles of formylbenzoate per mole IgG using the 2-hydrazinopyridine-dihydrochloride (2-HP, Solulink) quantification assay. Briefly, the addition of a molar excess 2-HP to the FB moiety on E4G10 at pH 4.7 permitted the measurement of the molar substitution ratio by electronic absorption spectroscopy using the arylhydrazone chromophore (Abs$_{max}$ = 350 nm, e = 18,000 M^{-1}cm^{-1}).

SWCNT-([^{225}Ac]DOTA)(HNH) + E4G10-FB → SWCNT-([^{225}Ac]DOTA)(E4G10) (3)
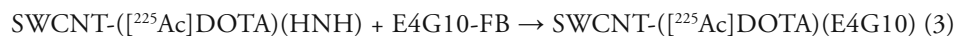
The E4G10-FB antibodies were covalently attached to the SWCNT-([^{225}Ac]DOTA)(HNH) by reaction of 0.05 mg of SWCNT-([^{225}Ac]DOTA)(HNH) with 0.17 mg of E4G10-FB in 1.2 mL of of 100 mM sodium phosphate/150 mM NaCl, pH 5.2 buffer (reaction 3). A similar chemical scheme was used to append several of the anti-KLH-FB moieties to the SWCNT-([^{225}Ac]DOTA)(HNH) precursor to yield the **control Construct I**. The reaction mixture was incubated at 37ºC for several hours and the high

and low S.A. SWCNT-([^{225}Ac]DOTA)(E4G10) (**Construct I**) and isotype **control Construct I** products were stored at 4°C. The products were formulated into 1% HSA for injection.

The radioimmunoimaging (RII) drug **Construct II** (Figure 1B) was designed to specifically target the tumor vessels and deliver the positron-emitting ^{89}Zr radionuclide for PET imaging. The key precursor to **Construct II** was assembled first by appending multiple copies of the reactive arylaldehyde, SFB. Briefly, the SFB was dissolved in 0.100 mL DMF and a volume of this modification solution was added to 0.5 mg of SWCNT-NH$_2$ (3 g/L) to achieve a ratio of 5 SFB per 100 amines. The reaction mixture was incubated at 37°C for 2-3 hours. Purification of the arylaldehyde modified SWCNT was performed by SEC as described above. The stoichiometry of substitution was determined (moles of FB per g SWCNT) using the 2-HP quantification assay as described previously. Next, the remaining amines on the SWCNT-(FB)(NH$_2$) construct were covalently modified by appending the desferrioxamine B (DFO) chelate. The details of preparation of the reactive DFO intermediate reagent are as described below.

The synthesis of *N*-succinylDFO (*N*-succDFO) was performed by the reaction of DFO mesylate (0.508 g, 0.77 mmol, Calbiochem, Spring Valley, CA) dissolved in 7.5 mL of pyridine (Sigma-Aldrich) with excess (1.704 g, 0.017 mol) succinic anhydride (Sigma-Aldrich) at room temperature for 24 h. The resulting white suspension was then poured into an aqueous NaOH solution (120 mL, 0.015 M) and stirred at room temperature for 16 h. The colorless solution was adjusted to pH 2 by the addition of 12 M HCl and cooled with stirring at 4ºC for 2 h. The white precipitate was collected by filtration, washed with copious amounts of 0.01 M HCl and then water and dried *in vacuo* to give the *N*-succinyldesferrioxamine B (*N*-succDFO) as a white microcrystalline solid (0.306 g, 4.75×10^{-4} mol).

The preparation of Fe(DFO-TFP) was performed by reacting the activated ester *N*-succDFO (9.0 mg, 0.014 mmol), suspended in 3.0 mL 0.9% sterile saline and the pH adjusted to 6.5, with 0.050 to 0.075 mL of 0.1 M sodium carbonate (Na$_2$CO$_3$, Sigma-Aldrich). A solution of ferric trichloride hexahydrate (FeCl$_3$•6H$_2$O, Sigma-Aldrich) (4.0 mg, 0.015 mmol, 0.300 mL of 0.1 M HCl) was added to this *N*-succDFO solution. Upon addition of the FeCl$_3$, the reaction mixture changed from colorless to deep orange due to the intense electronic absorption band of Fe(DFO) with a peak at 430 nm (ε_{430} = 2,216 ± 49 M^{-1}cm^{-1}). After stirring the reaction mixture at room temperature for 1 h, a 1.2 M solution of 2,3,5,6-tetrafluorophenol (TFP, 0.300 mL, 0.036 mmol, Sigma-Aldrich) in chelex purified acetonitrile (MeCN, Sigma-Aldrich) was added to the reaction followed by the addition of solid *N*-(3-dimethylaminopropyl)-*N'*-ethylcarbodiimide hydrochloride (EDAC, 120 mg, 0.63 mmol, Sigma Aldrich). The reaction mixture (pH 6.5) was then stirred at room temperature for 1 h before purifying the Fe(DFO-TFP) product using a C18 Light Sep-Pak cartridge (Waters). The reaction mixture was loaded onto a pre-activated (6 mL MeCN, 10 mL H$_2$O) C18 cartridge, washed with copious

amounts of water (>40 mL), and eluted with 1.5 mL MeCN. The final Fe(DFO-TFP) solution had a concentration approximately 9.8 mM. The Fe(DFO-TFP) solution was stored at 4ºC.

The Fe(DFO-TFP) reagent was then reacted with the remaining amines on the SW-CNT-(FB)(NH$_2$) construct to introduce the DFO chelate onto the SWCNT precursor. The Fe was removed by exposing the metallated-precursor to a 10-fold excess of EDTA (0.0674 M, 0.0137 mmol, 0.030 mL) with respect to Fe(N-succDFO-TFP). The reaction was incubated in a water bath at 38ºC for 1 h. The SWCNT-(DFO)(FB) was purified by SEC chromatography to render it Fe-free and was ready to be radiolabeled (Reaction 4).

SWCNT-(DFO)(FB) + ^{89}Zr → SWCNT-([^{89}Zr]DFO)(FB)   (4)
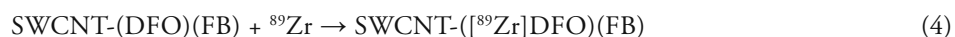
^{89}Zr was produced via the ^{89}Y(p,n)^{89}Zr transmutation reaction on an EBCO TR19/9 variable beam energy cyclotron (EBCO Industries Inc., Richmond, British Columbia, Canada) in accordance with previously reported methods (30). The ^{89}Zr-oxalate was isolated in high radionuclidic and radiochemical purity (RCP) >99.9%, with an effective S.A. of 195–497 TBq/g, (5,280–13,430 Ci/g).[30] Methods for radiolabeling and purification of a 10 g/L solution of SWCNT-(DFO)(FB) in MFW with ^{89}Zr at pH 5 are similar to those described previously.[30] Briefly, 0.10 mg of SWCNT-(DFO)(FB) in 0.020 mL MFW was reacted with 122.5 MBq (3.31 mCi) of ^{89}Zr in 0.005 mL of 1M oxalic acid (Sigma-Aldrich), pH 6.5. The pH was adjusted to 8.1 with the addition of 0.170 mL of 1.0 M Na$_2$CO$_3$. The reaction was heated to 60ºC for 60 min. Purification was accomplished using SEC with a P6 gel stationary phase and a PBS mobile phase. ^{89}Zr activity was measured with a Squibb CRC-17 Radioisotope Calibrator (or equivalent model) set at 465. ITLC-SG was used to determine the labeling efficiency of the reaction mixture and the purity of the product. The strips were counted intact using a System 400 Imaging Scanner (or equivalent).

E4G10+ SANH → E4G10-HNH   (5)

The next key step was the conversion of the E4G10 or the isotype control anti-KLH IgGs to the reactive arylhydrazine modified-IgG precursors (Reaction 5). Briefly, 1 mg of IgG was dissolved in 0.2 mL of 100 mM sodium phosphate/150 mM NaCl, pH 7.6 buffer. Immediately before use, 2.0-4.0 mg of SANH was dissolve in 0.1 mL of dry DMF. A volume of SANH/DMF solution was added to the IgG to achieve a 10- to 20-fold molar excess of the SANH to primary amine. The reaction proceeded at ambient temperature for 2-3 hours at pH 7.6. The product, IgG-HNH, was purified using SEC with a 10 DG gel column as the stationary phase and 100 mM 2-(N-morpholino) enthanesulfonic acid (MES, Sigma-Aldrich)/150 mM NaCl conjugation buffer at pH 5.4 as the mobile phase. The amount of HNH substituent per IgG was determined first by assaying the protein concentration using the BCA Protein Assay and the moles of arylhydrazine (HNH) per

mole IgG using the 4-nitrobenzaldehyde (4-NBA, Solulink)) quantification assay. Addition of a molar excess 4-NBA to the HNH moiety on IgG at pH 4.7 permitted the measurement of the molar substitution ratio of the chromophore (Abs$_{max}$ = 390 nm, e = 24,000 M^{-1}cm^{-1}).

SWCNT-([^{89}Zr]DFO)(FB) + E4G10-HNH → SWCNT-([^{89}Zr]DFO)(E4G10)   (6)

The E4G10-HNH antibodies (or anti-KLH-HNH) were covalently attached to the SWCNT-([^{89}Zr]DFO)(FB) by reaction of 0.1 mg of SWCNT-([^{89}Zr]DFO)(FB) with 0.3 mg of E4G10-HNH in 0.25 mL of 100 mM MES/150 mM NaCl conjugation buffer at pH 4.7 (Reaction 6). The reaction mixture was incubated at 37ºC for several hours. The SWCNT-([^{89}Zr]DFO)(E4G10) (**Construct II**) and isotype **control Construct II** products were stored at 4°C and were formulated into 1% HSA for injection.

Amplification of construct specific activity

A fixed mass of SWCNT-(DOTA)(HNH) precursor was radiolabeled with varying amounts of ^{225}Ac activity to determine the reaction yields and specific activities. In each of 5 radiolabeling reactions, the volume, pH, time, temperature, and reagent concentrations were held constant (see specific conditions described above) while varying only the amount of radionuclide added. Briefly, 0.18 mg of SWCNT-(DOTA)(HNH) was ^{225}Ac-radiolabeled in 0.40 mL at pH 6, at 60ºC for 65 min. in five different reactions. In amplification reaction I, the SWCNT-(DOTA)(HNH) was labeled with 0.444 MBq (0.012 mCi); II used 1.48 MBq (0.040 mCi); III used 2.26 MBq (0.061 mCi); IV used 21.1 MBq (0.570 mCi); and V used 193 MBq (5.21 mCi). An aliquot of each reaction was assayed using ITLC-SG (see above) and then the reaction was quenched with the addition of DTPA. The reaction mixture was then purified by SEC (see above) and the purified product assayed by ITLC-SG and the recovered activity measured.

Data for numerous preclinical radiolableing preparations of ^{225}Ac-E4G10 was also compiled for comparison. The radiolabeling data using our published methods[48] from 11 dose preparations that used 0.75 ± 0.13 mg (mean ± s.d.) of E4G10 and 93.6 ± 51.1 MBq (2.53 ± 1.38 mCi) of ^{225}Ac per dose were used as comparison to the results from the SWCNT-(DOTA)(HNH) labeling study.

As a further demonstration of the consistency of our published 2-step IgG radiolabeling methodology, lintuzumab (Protein Design Labs, Inc., Mountain View, CA), a monoclonal IgG that targets CD33 on leukemia cells was routinely radiolabeled with ^{225}Ac for a Phase I clinical trial to produce ^{225}Ac-lintuzumab. The radiolabeling data from 17 clinical dose preparations that used 1.4 ± 0.5 mg (mean ± s.d.) of lintuzumab and 91.0 ± 55.1 MBq (2.46 ± 1.49 mCi) of ^{225}Ac were also included as comparison to the results from the SWCNT-(DOTA)(HNH) labeling study.

Three-dimensional fluorescent-mediated tomography (FMT) imaging study to assess the PK of E4G10 and determine the number of VE-cad monomer epitopes per cell in vivo

Tridimensional fluorescent-mediated tomography (FMT) experiments were performed by using the FMT-2500, (VisEn Medical, Boston, MA) to determine the PK profile of the of E4G10 (and anti-KLH isotype control) IgGs and to determine the number of binding sites per newly formed vascular endothelial cell in the LS174T xenograft model.

The E4G10 and anti-KLH antibodies were reacted with the succinimidyl ester of Alexa Fluor→ 680 carboxylic acid (AF680, Invitrogen, Carlsbad, CA) per the manufacturer's instructions to prepare two antibody constructs for an in vivo Near Infrared (NIR) FMT imaging study. Briefly, the constructs were prepared by reaction of a 10- to 20-fold mole excess of the succinimidyl ester of the AF680 dye per 1 mg of IgG at pH 8.0 for 2 h at ambient temperature. The dye-labeled constructs were purified by SEC chromatography as described above and characterized by UV-Vis spectroscopy (measured the absorbance at 280 and 679 nm per the manufacturer's instructions) and SEC HPLC. The HPLC system used a Beckman Coulter System Gold Bioessential 125/168 diode array detection system (Beckman Coulter, Fullerton, CA) equipped with an in-line Jasco FP-2020 fluorescence detector (Tokyo, Japan). The stationary phase was a Tosoh Science G3000SWXL column (300 mm x 7.8 mm; 5 micrometer) (Fisher Scientific) and a 20 mM sodium acetate (Sigma-Aldrich), 150 mM NaCl, pH 6.4 mobile phase at 1 mL/min at ambient temperature.

Two groups of 5 nude mice with the LS174T tumor were randomly assembled and each mouse received 0.030 mg of the construct in 0.10 mL in 1% HSA via intravenous (IV) retroorbital sinus injection. NIR FMT imaging was performed every 24-48 hours over a 7 day time period by using the specific 680 channel (Ex/Em: 680 nm/700 nm). The volume of interest (VOI) was drawn over the whole tumor (as visualized by the 3-dimensional photographic image acquisition) and fluorescence uptake was quantified. Mice were maintained on a diet of low fluorescence chow (AIN76A, Harlan Teklad, WI, USA) to minimize background noise. The FMT device was calibrated for use with sample standards of the E4G10-AF680 and anti-KLH-AF680 constructs in accordance with the manufacturer's guidelines. The values obtained from meaurements of these standards of the injected dose were entered into the Truequant software (VisEn Medical) to allow for quantification.

To determine the number of VE-cad epitopes in these tumors, we employed data obtained from Hilmas and Gillette(49) which reported a morphometric analyses of tumor microvasculature during growth. Their data described changes in the tumor's vascular volume, vessel diameter, and mean vessel length and surface area per unit volume of tumor tissue. Further, it was assumed that a VE cell has an area (50) of 1E-3 mm^2 (0.141 mm × 0.007 mm) and that there were 1E9 cells per gram of tumor. The data of Hilmas and Gillette reported that a 500 mm^3 tumor had a vascular surface area per tumor vol-

ume of 13 mm^2/mm^3 and as the tumor volume increased (up to 1,500 mm^3), the ratio of vascular surface area per tumor volume decreased and leveled at 12 mm^2/mm^3.

Radioimmunotherapeutic study to target and irradiate the tumor vasculature (survival and tumor regression)

A RIT study was performed in the LS174T xenograft tumor model with SWCNT-([^{225}Ac]DOTA)(E4G10) versus appropriate controls. Briefly, tumor cells were xenografted 13 days before treatment (the mean ± s.d tumor volumes for the animals in this study were 179 ± 112 mm^3 at the time RIT commenced). Mice were randomly separated into 4 groups prior to treatment and all mice received a single IV dose of drug (or vehicle control) via the retroorbital sinus except one mouse in Group 1 that received a single intraperitoneal injection to investigate tumor targeting by that administration route. Group 1 mice (n=6) each received a single dose of the high S.A. = 851 GBq/g SWCNT (23 Ci/g) **Construct I** containing 16.1 kBq (435 nCi) ^{225}Ac, 19 ng SWCNT, and 29 ng E4G10. Group 2 mice (n=5) each received a single dose of the high S.A. = 851 GBq/g SWCNT (23 Ci/g) isotype **control Construct I** containing 15.2 kBq (410 nCi) ^{225}Ac, 18 ng SWCNT, and 27 ng anti-KLH. Group 3 mice (n=5) each received a single dose of the low S.A. = 1.9 GBq/g SWCNT (0.05 Ci/g) **Construct I** containing 0.037 kBq (1 nCi) ^{225}Ac, 19 ng SWCNT, and 29 ng E4G10. The Group 4 mice (n=4) each received a single dose of normal saline and served as a growth control. Mice were observed daily and tumor volumes measured and recorded. The tumor volumes were assessed using calipers to measure the diameters where *a* was the longest diameter and *b* was the shortest diameter and the volume was calculated as V = *a* x *b*^{2} x 0.52. When tumor volumes reached 1,000 mm^3 or greater, mice were euthanized. Survival was analyzed as a function of time from treatment using Kaplan-Meier analyses.

Radioimmunoimaging study of tumor vasculature

A RII study was performed in the LS174T xenograft tumor model with SWCNT-([^{89}Zr]DFO)(E4G10) vs appropriate controls. Briefly, tumor cells were xenografted 13 days before treatment (the mean ± s.d tumor volumes for the animals in this study were 558 ± 413 mm^3 at the time RII imaging commenced). Mice were randomly separated into three groups prior to treatment and all mice received a single i.v. dose of drug the lateral tail vein. All the SWCNT-([^{89}Zr]DFO)(IgG) constructs were labeled to high S.A. (592 GBq/g SWCNT (16 Ci/g)). Group 1 mice (n=4) received a single dose of **Construct II** containing 4.18 MBq (0.113 mCi) ^{89}Zr, 7,000 ng SWCNT, and 15,700 ng E4G10. Group 2 mice (n=3) received a single i.v. dose 0.800 mg of unlabeled E4G10 (50-fold excess relative to the construct-associated E4G10) 30 min prior to the single dose of **Construct II** containing 4.18 MBq ^{89}Zr, 7,000 ng SWCNT, and 15,700 ng E4G10. This group served as a blocking control. Group 3 mice (n=3) received a single dose of the isotype **control Construct II** containing 3.08 MBq (0.083 mCi) ^{89}Zr, 5,200 ng SWCNT, and 12,100 ng anti-KLH.

The PET study was performed with a microPET Focus™ 120 (CTI Molecular Imaging, Knoxville, TN). Mice were maintained under 2% isoflurane/oxygen anesthesia during the scanning. Images were recorded at various time-points between 0–96 h post-injection. List-mode data were acquired for between 10 and 30 min. using a γ-ray energy window of 350–750 keV, and a coincidence timing window of 6 ns. For all static images, scan time was adjusted to ensure a minimum of 20 million coincident events were recorded. Data were sorted into 2-dimensional histograms by Fourier re-binning, and transverse images were reconstructed by filtered back-projection (FBP) into a 128×128×63 (0.72×0.72×1.3 mm) matrix. The reconstructed spatial resolution for ^{89}Zr was 1.9 mm full-width half maximum (FWHM) at the center of the field-of-view (FOV). The image data were normalized to correct for non-uniformity of response of the PET, dead-time count losses, positron branching ratio, and physical decay to the time of injection but no attenuation, scatter, or partial-volume averaging correction was applied. An empirically determined system calibration factor (in units of (mCi/mL)/(cps/voxel)) for mice was used to convert voxel count rates to activity concentrations. The resulting image data were then normalized to the administered activity to parameterize images in terms of %ID/g. Manually drawn 2-dimensional regions-of-interest (ROIs) or 3-dimensional VOI were used to determined the maximum and mean %ID/g (decay corrected to the time of injection) in various tissues.[6] Images were analyzed by using ASIPro VM™ software (Concorde Microsystems, Knoxville, TN).

Characterization of E4G10 reactivity

LS174T, Chinese hamster ovary (CHO), and CHO cells that stably expressed human VE-cadherin were assessed for VE-cadherin expression by flow cytometry. Cells were stained with E4G10 plus a secondary goat anti–rat IgG phycoerythrin (PE) conjugated antibody (R&D Systems), and then analyzed by flow cytometry (FACSAria, Beckman Coulter). In addition, lysates from these cell lines were tested for VE-cadherin expression by Western blot analysis. The lysates were resolved on a 4–12% NuPAGE Bis–Tris gel (Invitrogen), transferred to a polyvinylidene difluoride membrane, and VE-cadherin was detected using E4G10 plus a goat anti-rat IgG-HRP conjugated antibody (R&D Systems). In addition, glyceraldehyde 3-phosphate dehydrogenase (GAPDH) was included as a loading control and was measured to evaluate protein loading using an anti-GAPDH pAb (R&D Systems).

Data Analyses

Three-dimensional VOI analysis on PET images was accomplished with ASIPro VM™ 5.0 software (Concorde Microsystems). Statistical data were evaluated using Graphpad Prism 5.0 (Graphpad Software, Inc.). Analysis of NIR images used the VisEn FMT-2500 instrument's Truequant software. Statistical comparison between 2 experimental groups was performed using a t test (unpaired comparison); comparison

of multiple groups was performed with the 1-way ANOVA using Bonferroni's multiple comparison post hoc analysis. All statistical comparisons were 2-sided, and the level of statistical significance was set at $P<0.05$.

Results

Construct syntheses and amplification of specific activity

The SWCNT-(DOTA)(HNH) precursor to Construct I was assayed and found to contain 1 mmol DOTA and 0.06 mmol HNH per gram of SWCNT. This precursor was radiolabeled (reaction 1) with 5 different amounts of ^{225}Ac activity, which after SEC purification yielded 96% radiochemically pure SWCNT-([^{225}Ac]DOTA)(HNH). The SA for the 5 reaction products was 2.15, 4.07, 12.1, 108, and 914 GBq/g (0.058, 0.11, 0.326, 2.91, and 24.7 Ci/g, respectively). The 2 antibody components, E4G10-FB and the isotype control anti-KLH-FB, had 5–7 FB reactive groups appended per IgG (reaction 2). These IgG precursors were in turn reacted (reaction 3) in 5-fold excess (per 100 nm of SWCNT) with the SWCNT-([^{225}Ac]DOTA)(HNH) (0.058 and 24.7 Ci/g) precursors to yield the RIT Construct I at two different SA and the nontargeting high-SA isotype control Construct I. Approximately 3 IgG per construct were appended per SWCNT. The starting amount of radioactivity used in the reaction is plotted vs the resultant SA (Figure 2).

The preclinical radiolabeling data for 225Ac-E4G10 yielded SA of 6.7 ± 4.4 GBq/g (0.18 ± 0.12 Ci/g) with RCP of 96.7% ± 2.6%. The radiolabeled clinical IgG, 225Aclintuzumab, yielded SA of 6.7 ± 1.9 GBq/g (0.18 ± 0.05 Ci/g) with RCP of 97.2% ± 2.5%. A comparison of the SWCNT-(DOTA)(HNH) precursor and the IgG construct labeling results demonstrates that the increased amount of DOTA per SWCNT yields almost a 2-log amplification of SA vs the IgG-DOTA constructs (Figure 2).

The N-succDFO product was obtained in 62% yield. High resolution mass spectrometry confirmed the product identity (HRMS-ES+ Calculated for [C29H52 N6O11 + H+] = 661.3772; found 661.3760 ([M + H+] = 100%). The SWCNT-(DFO)(FB) precursor to Construct II was assayed and found to contain 0.4 mmol DFO and 0.3 mmol FB per gram of SWCNT. This precursor was radiolabeled with 89Zr activity, which after SEC purification yielded 97% radiochemically pure SWCNT-([^{89}Zr]DFO)(FB) (reaction 4).

The SA was 592 GBq/g (16 Ci/g). To assemble Construct II, ~11 HNH reactive groups were appended per IgG to yield E4G10-HNH and the isotype control anti-KLH-HNH (reaction 5). These antibody precursors were in turn reacted with the SWCNT-([^{89}Zr]DFO)(FB) precursor in 10-fold excess (to SWCNT) to yield the RII Construct II and the nontargeting isotype control Construct II (reaction 6). Approximately 3 IgG per construct were appended per SWCNT.
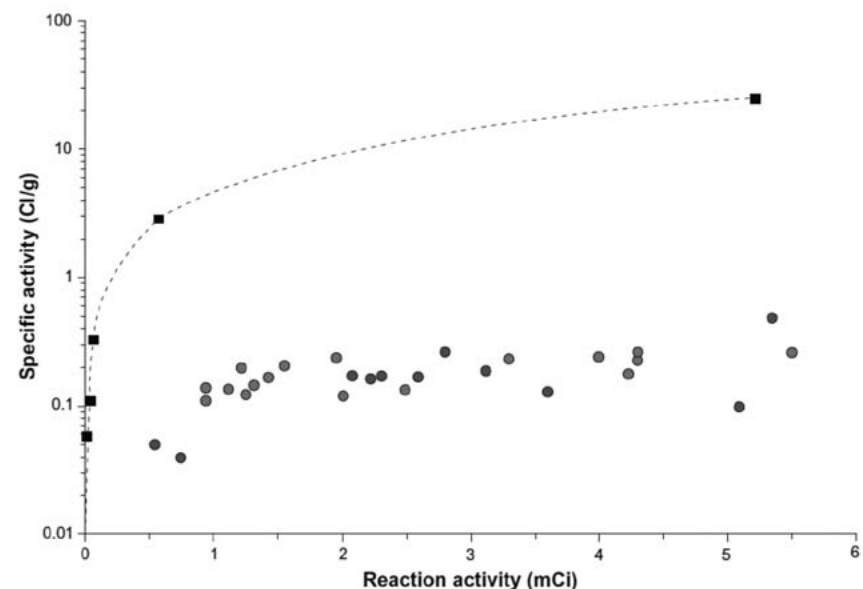
Figure 2. A plot of the starting ^{225}Ac activity used to radiolabel versus the final specific activity. The multiple copies of DOTA chelate covalently appended to the SWCNT-scaffold (filled black squares) permit amplification of the amount of radioactivity that can be loaded onto the targeting construct relative to two different IgG-DOTA constructs (lintuzumab (filled red circles) and E4G10 (filled blue circles)). The non-linear regression fitted curve (dashed black line) is shown for the SWCNT-DOTA labeling data.

Pharmacokinetic profile of E4G10 and the number of VE-cad monomer epitopes per cell

The E4G10-AF680 and anti-KLH-AF680 constructs prepared for the FMT tumor NIR imaging and PK studies were prepared in 75 and 51% yield, respectively. Spectrophotometric analysis revealed that there were 5.5 AF680 appended per E4G10 and 10.2 AF680 per anti-KLH isotype control. Both constructs were 99% pure as determined by HPLC analysis. The amount of dye that accumulated in each tumor was imaged and measured on days 1, 2, 3, 5, 6, and 7 by FMT imaging. NIR FMT images of 2 representative mice demonstrate the differential targeting of the VE-cad epitope in the LS174T tumor vessels with E4G10-AF680 versus a similarly prepared isotype anti-KLH-AF680 non-targeting control construct 7 days post-injection (Figure 3). There was 1.2 ± 1.0 pmol E4G10-AF680 (mean ± s.d.) versus 0.04 ± 0.06 pmol anti-KLH-AF680 per group (n = 5 mice per group) on day 7 representing a 30-fold excess of signal-to-noise at this time.

A kinetic analysis of this data yielded the concentration of IgG-AF680 per tumor per day (Figure 4) which demonstrated a blood compartment clearance time of approximately 3 days. The tumor volumes (mean ± s.d) of the E4G10-AF680 group were 1,208 ± 444 mm³ (n = 5) and the anti-KLH-AF680 group had tumor volumes of 1,022 ± 667
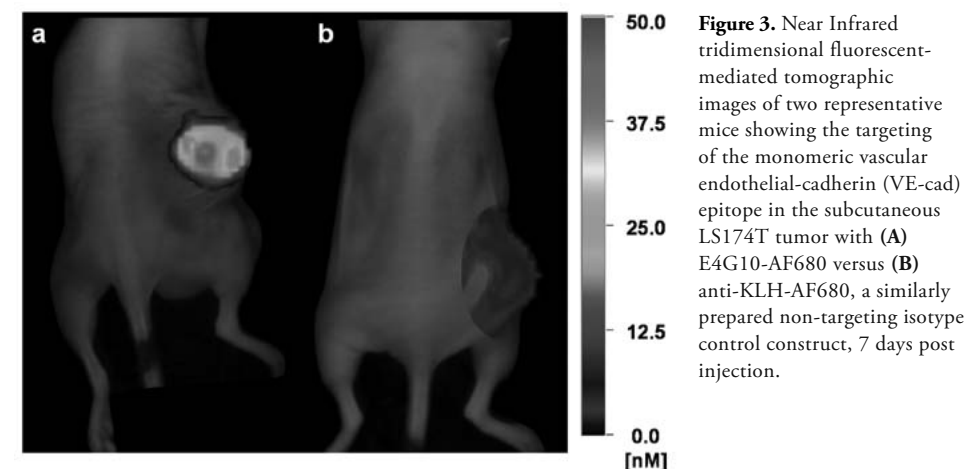
Figure 3. Near Infrared tridimensional fluorescent-mediated tomographic images of two representative mice showing the targeting of the monomeric vascular endothelial-cadherin (VE-cad) epitope in the subcutaneous LS174T tumor with **(A)** E4G10-AF680 versus **(B)** anti-KLH-AF680, a similarly prepared non-targeting isotype control construct, 7 days post injection.

mm³ (n = 5) on the second day of NIR FMT imaging study. This PK data was also used to calculate an estimate of the number of VE-cad per VE cell. In the E4G10-AF680 group, the mean tumor volume was 1,208 mm³ and 3.2 ± 0.08 pmol of E4G10 was ac-
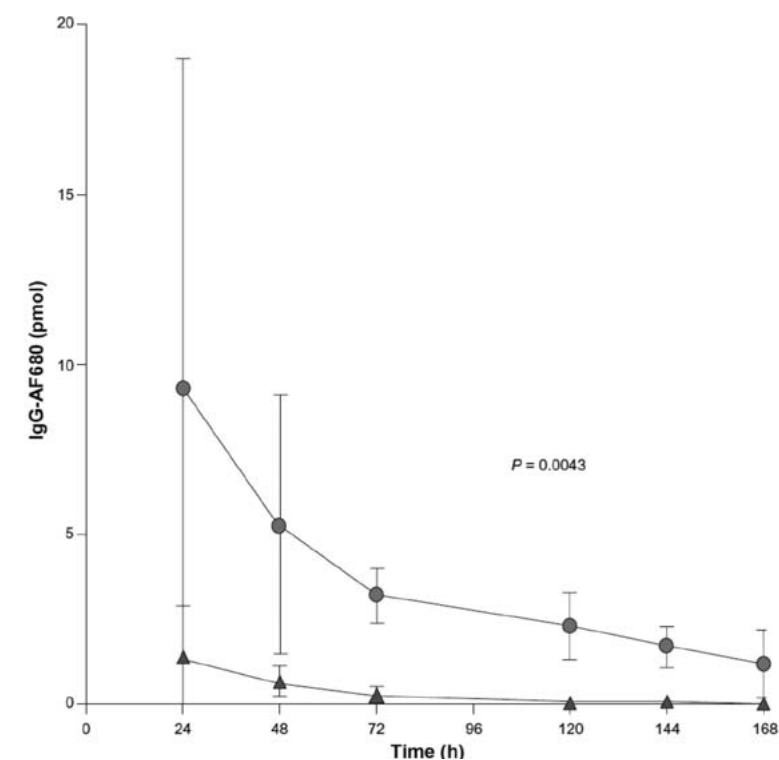
Figure 4. Near Infrared tridimensional fluorescent-mediated tomographic signal (normalized for moles of AF680 dye per IgG) in the LS174T tumor as a function of time post injection. E4G10-AF680 (red circles) versus a similarly prepared isotype anti-KLH-AF680 (blue triangles).

Figure 5. Kaplan-Meier survival plot of the fraction of LS174T-xenografted mice surviving versus time following treatment with **(A)** high S.A. SWCNT-([225Ac]DOTA)(E4G10) (solid green line); high S.A. SWCNT-([225Ac]DOTA)(anti-KLH) (solid red line); low S.A. SWCNT-([225Ac]DOTA)(E4G10) (solid blue line); and untreate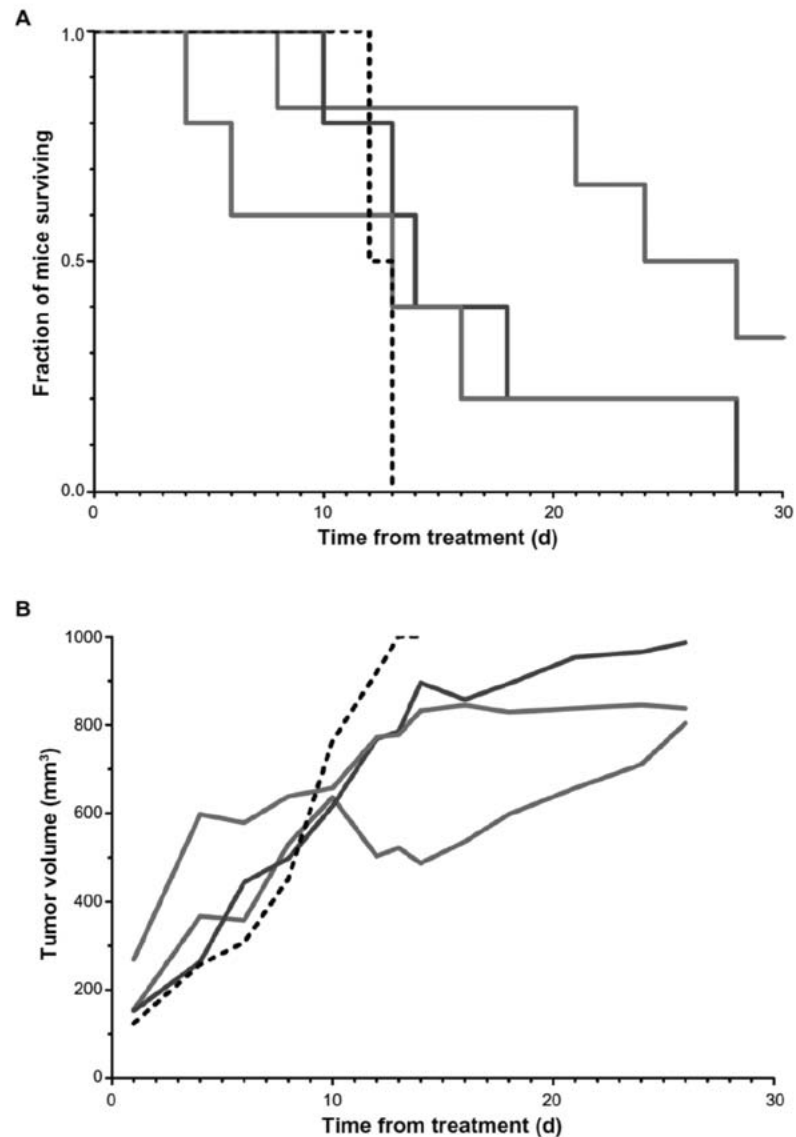d growth control (dashed black line). **(B)** Mean tumor volumes for each treatment group as a function of time from treatment (n.b., the line colors and styles correspond to the data in panel **A**).

cumulated after the blood compartment cleared. Using data from Hilmas and Gillette (49) along with the assumptions stated above, there were 1.44E7 VE cells in the tumor with 1.33E5 VE-cad epitopes per VE cell. (The isotype control group that received the anti-KLH-AF680 had 0.27 ± 0.25 pmol of antibody in the tumor.)
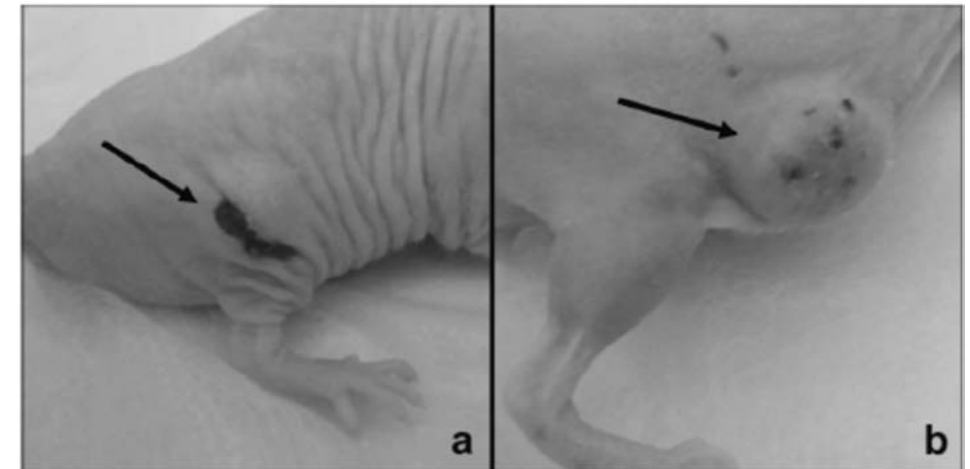

Figure 6. Two representative LS174T-xenografted mice from the radioimmunotherapeutic study 10 days after treatment. (A) A mouse treated with high SA SWCNT-([225Ac]DOTA)(E4G10) and (B) a mouse treated with low SA SWCNT-([225Ac]DOTA)(E4G10).

Radioimmunotherapy targeted to the tumor vessels improved median survival and tumor regression

A single administration of the high S.A. **Construct I** to the RIT Group 1 mice significantly improved the median survival relative to the RIT Group IV mice (the growth controls) (26 days vs 12.5 days, P =0.0334). RIT Group 2 mice received the high SA isotype **control Construct I** and RIT Group 3 mice received the low SA **Construct I** and had median survival times of 13 and 14 days, respectively. The Kaplan-Meier survival plot and the plot of the change in tumor volumes from time of treatment showed the benefit of a single dose high SA **Construct I** relative to controls (Figure 5). It was observed that on day 10 after treatment, there was a noticeable transient decrease in tumor volume in RIT Group 1 mice compared to other groups. Photographic images (Figure 6) of a representative mouse from RIT Group 1 and Group 3 are shown at day 10 from treatment to illustrate the therapeutic effect of the high SA drug construct versus the low SA drug construct control. The tumor volume was significantly less in the RIT Group I mouse with a lesion scar in the center of the tumor area.

Radioimmunoimaging of tumor vasculature

A single i.v. administration of **Construct II** to the RII Group 1 mice via the lateral tail vein showed rapid accumulation by PET ROI analysis of signal in the tumor (~ 0.36 %ID/g at 24 h post injection) (Figure 7A). RII Group 2 mice (n=3) received a single i.v. 0.800 mg dose of unlabeled E4G10 (50-fold excess relative to the construct-associated E4G10) 30 min. prior to a single dose of **Construct II** and did not show accumulation of signal in the tumor (approx. 0.24 %ID/g at 24 h post injection) (Figure 7B). RII Group 3 mice (n=3) received a single dose of the isotype **control Construct II** and did

not show accumulation of signal in the tumor (approx. 0.18 %ID/g at 24 hours post injection) (Figure 7C). Other imaging data (Figure 8A) was taken from dynamic PET measurements in the first hour post-administration and included the rapid blood compartment clearance ($t_{1/2}$ = 15 minutes). The tumor accumulation in a representative RII Group 1 mouse showed that rapid and persistent accumulation of drug was observed, while a representative RII Group 3 control mouse demonstrated decrease of tumor-associated activity in the first 5 minutes that leveled off and appeared as noise. Further PET ROI data (Figure 8B) from a representative mouse from RII Group 1 was plotted as a function of time at 1, 4, 24, and 96 hours and showed a tumor-to-muscle ratio of 1.61, 1.98, 2.95, and 5.08, respectively. The tumor-to-muscle ratios were greatest at 96 hours, but reasonable contrast was apparent between 4 and 24 hours. This demonstrated a significant improvement over E4G10-alone imaging agent that required ∼ 3-4 days for blood compartment activity to clear.
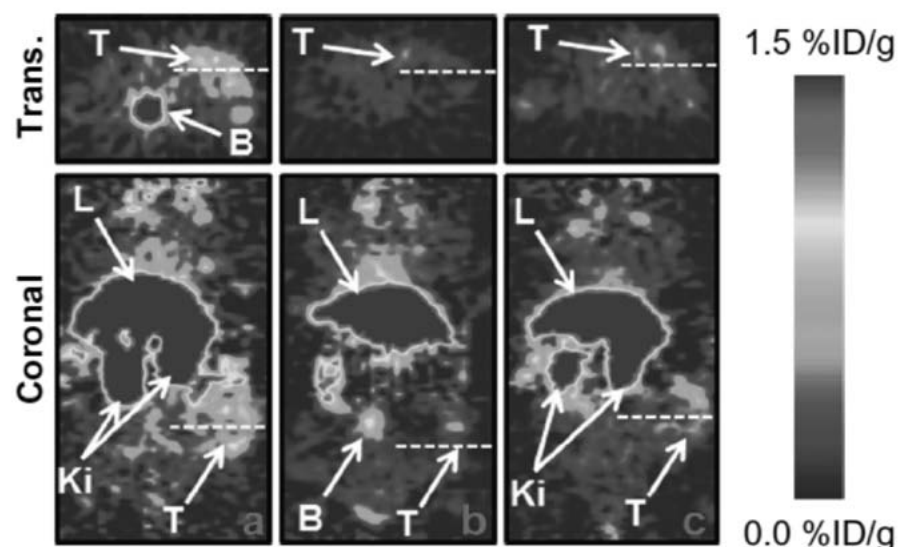
Figure 7. PET images of three representative s.c. LS174T tumored-mice that received an i.v. injection of (A) SWCNT-([^{89}Zr]DFO)(E4G10); (B) low specific-activity ^{89}Zr-DFO-SWCNT-E4G10 (competitive inhibition/blocking control experiment); and (c) non-specific control construct SWCNT-([^{89}Zr]DFO)(anti-KLH) recorded at 24 h post-injection. The top panel is the transverse image and the bottom panel is the coronal image. The notations T, L, Ki, and B indicate the tumor, liver, kidneys, and bladder, respectively.
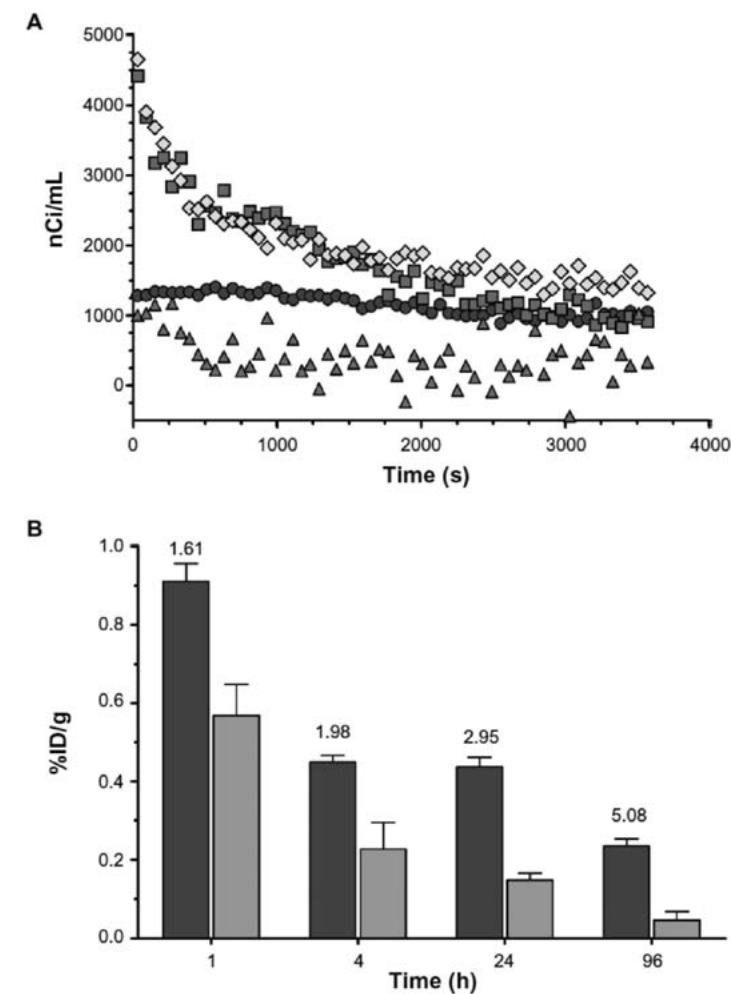
Figure 8. PET data showing tumor accumulation and corresponding blood and muscle clearance of the construct as a function of time. (a) Time activity curves (TAC) from two representative LS174T-xenografted-mice that were dynamically PET imaged immediately after i.v. administration of SWCNT-([^{89}Zr]DFO)(E4G10) and SWCNT-([^{89}Zr]DFO)(E4G10) + excess unlabeled E4G10 (cold blocking control). Tumor accumuation (blue circles) and blood compartment clearance (green squares) were determined by region-of-interest (ROI) analysis for the mouse that received the dose of SWCNT-([^{89}Zr]DFO)(E4G10). Similarly, tumor accumuation (red triangles) and blood compartment clearance (yellow diamonds) were determined by ROI analysis for the mouse that received the blocking dose of excess E4G10 and then the dose of SWCNT-([^{89}Zr]DFO)(E4G10). (b) PET ROI data showing tumor (blue bars) and muscle (orange bars) accumuation (mean ± s.d.) as a function of time for a representative LS174T-xenografted-mouse that received a dose of SWCNT-([^{89}Zr]DFO)(E4G10). The numerical values listed above the tumor data are the tumor-to-muscle ratios.
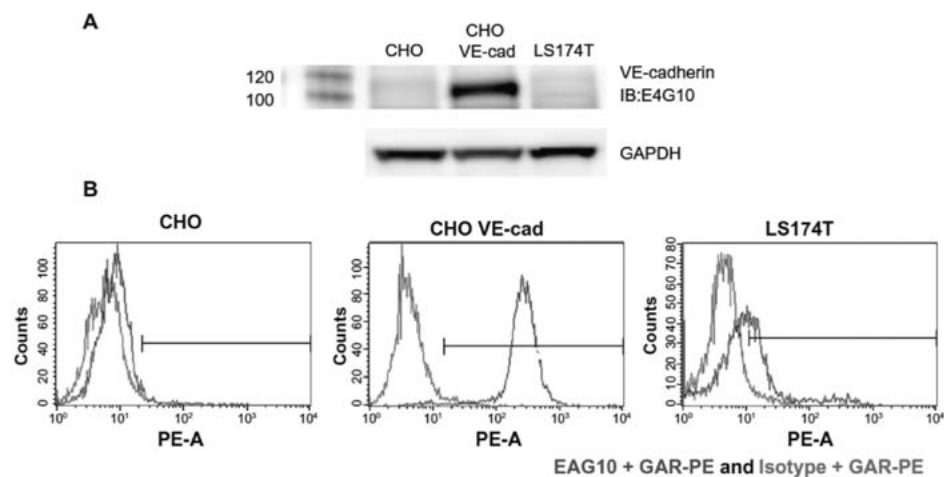
Figure 9. Characterization of E4G10. (a) Western blot analysis of E4G10 binding to cell lysates from the Chinese hamster ovary (CHO), VE-cad-transfected CHO, and LS174T cells. Glyceraldehyde 3-phosphate dehydrogenase (GAPDH) was included as a loading control. (b) Flow cytometric analysis showed the binding characteristics of E4G10 with the CHO, VE-cad-transfected CHO, and LS174T cells. The IgG isotype control was the anti-KLH antibody. The secondary IgG was a goat anti-rat phycoerythrin IgG.

Discussion

The concurrent processes of angiogenesis and tumor cell proliferation are keys to tumor growth and dissemination and are interrelated by a paracrine effect (51). Endothelial cells will expand to produce a tortuous network of vessels that supplies required nutrients, oxygen, cytokines and chemokines to tumor cells. Disrupting and damaging the vascular endothelial architecture associated with tumor tissue has been recognized as a viable therapeutic strategy (51-57). Furthermore, imaging modalities that can specifically target the tumor vessels would be of value in diagnosing disease and following the progression or regression as a function of treatment (58-59).

We hypothesized that novel synthetic structures based on hybrid molecules consisting of targeting biologics, radionuclides and CNT will have emergent anti-cancer properties. These molecular hybrids were designed to amplify the intrinsic targeting, binding, imaging, and therapeutic attributes of a drug construct and should, therefore, improve potency, specificity, and efficacy relative to current drugs. Irradiation of the vessels associated with tumor tissue was effected by specifically targeting the high linear energy transfer (LET) alpha particle emitting ^{225}Ac in high SA to the VE-cad epitope; imaging the tumor vessels was effected by specifically targeting the same epitope with the positron emitting ^{89}Zr in high SA

We previously demonstrated that an alpha particle-emitting, vascular-targeting antibody construct, ^{225}Ac-E4G10, could specifically irradiate prostate carcinoma vascular endothelial cells(27) and also their bone marrow-derived endothelial progenitors (28),
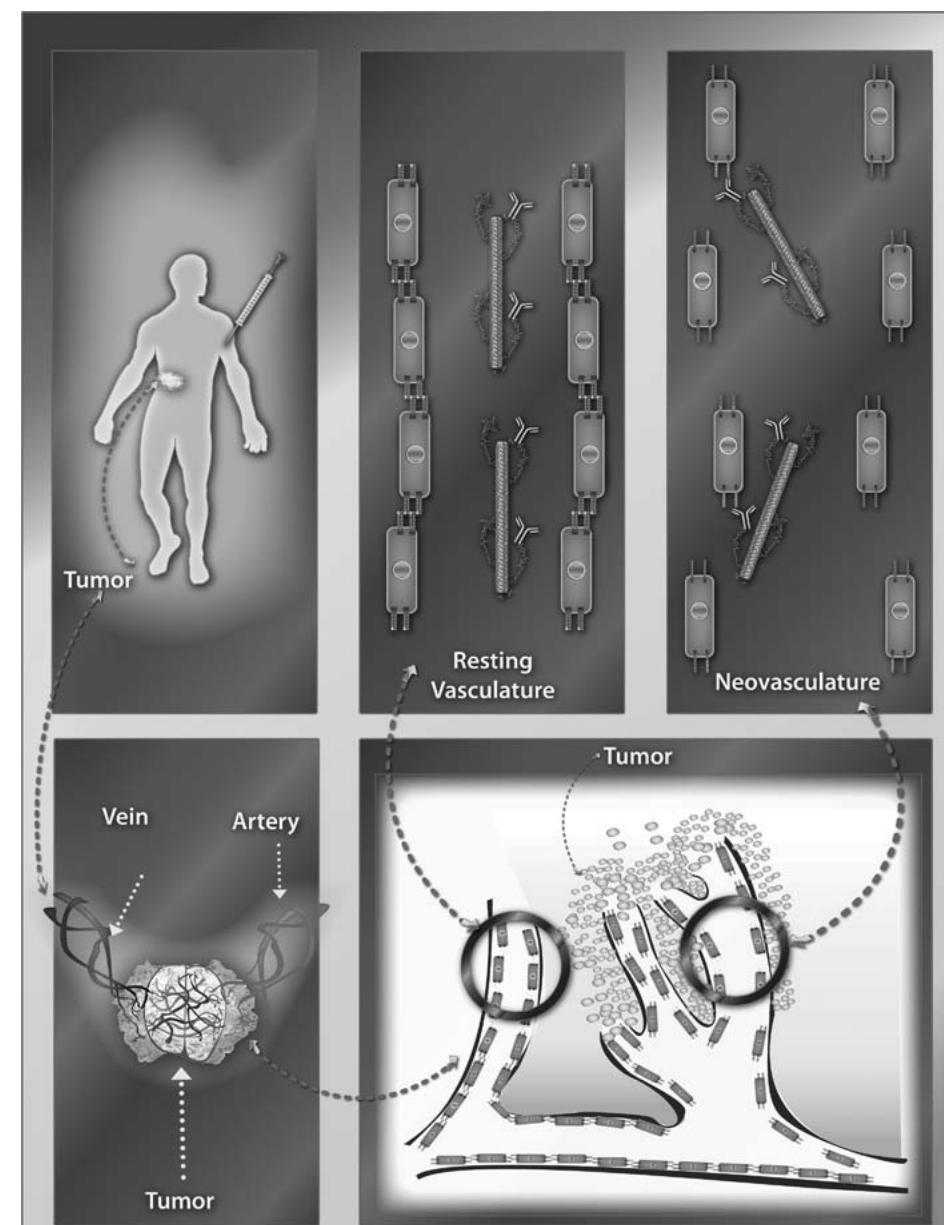
Figure 10. A graphical illustration of the tumor vascular targeting concept using the carbon nanotube constructs. The soluble, covalently-functionalized and radiolabeled constructs are delivered intravenously to the patient with tumor. The construct rapidly accesses the tumor vasculature and then can specifically bind to the monomeric VE-cad that is expressed in the neovasculature, but can not bind to resting vasculature with tight cell-cell contacts at the adherens junctions. (note, Figures are not drawn to scale.)

delaying tumor growth and improving survival. We have also examined ^{225}Ac-E4G10 in vascular targeting strategies to treat animal models of glioblastoma mutiforme (25-26) and the colon carcinoma (LS174T) model of tumor vasculature (60). Others have also

used vascular-targeting, alpha particle-emitting RIT approaches to treat animal models of disease (61-64) or vascular/tumor epitope-targeting RII approaches to PET image tumor (65-67).

Two particular SWCNT properties, the high aspect ratio and periodic structure, have rendered this nanomaterial amenable to being simultaneously appended with multiple copies of reactive primary amines, radiometal-ion chelates (DOTA or DFO) and IgGs. By amplifying the number of chelates per SWCNT, we have demonstrated a 2-log increase of SA of radiolabeling of SWCNT-(DOTA) relative to IgG constructs. Each of these SWCNT molecules had ~100 DOTA or DFO chelates appended per SWCNT. In contrast, an IgG might only accommodate 5-10 DOTA moieties per molecule, before losing the ability to target and bind efficiently (68).

The radiotherapeutic SWCNT-constructs, labeled with ^{225}Ac, were also functionalized with several copies of E4G10 antibody and used to treat LS174T tumors versus low SA control, non-targeting high SA isotype IgG control, and growth control. Survival of animals treated with high SA **Construct I** was doubled after only one treatment relative to the control groups and was significantly better than the growth controls. Tumor growth was also arrested and regressed in the high SA RIT Group I. The mice treated with the high SA, tumor vascular-targeting **Construct I** showed significant tumor regression while the low SA targeting analog did not control tumor growth. The image of the regressed tumor lesion was similar to the images of Nilsson and Neri (69) who targeted the delivery of tissue factor to the ED-B domain of fibronectin, a marker of angiogenesis, and mediated the infarction of solid tumors in mice.

The increased S.A. was also key to achieving a high signal-to-noise ratio for imaging purposes. We have utilized this increased sensitivity with indium-111 (^{111}In) and ^{86}Y labeled SWCNT-(DOTA) constructs for PK studies (3-6). In addition, covalently SWCNT-appended IgG and peptides have conferred biological targeting and binding capabilities to this scaffold and bind to the specific antigen epitope in vitro and in vivo (3-5). We were able to improve the SA of the ^{89}Zr-labeled RII **Construct II** approximately 5-fold relative to ^{89}Zr-labeled IgG-only labeled constructs (30).

Another key SWCNT property that was utilized extensively was the favorable PK profile that featured rapid blood compartment clearance. The RII **Construct II** targeted and bound and then rapidly cleared the blood compartment and the muscle yielding excellent contrast for imaging. The targeting system also favored this profile as the murine VE-cad epitope is expressed in the vessel lumen, and therefore, is readily accessible to the CNT construct. The binding occurred rapidly, precluding any need to diffuse into the solid tumor to target and bind. All of these studies demonstrated that the administered constructs were safe and well tolerated.

The SWCNT-E4G10 construct was tumor-vessel specific and targeted the murine VE-cad. E4G10 did not cross-react with the LS174T tumor cells in flow cytometric or Western blot analyses (Figure 9). Furthermore, the normal, resting vasculature no longer exposes this epitope to the E4G10 IgG for binding (9), thus sparing normal vessels. An illustration of this VE-cad targeting concept using IV delivered soluble, targeting, radiolabeled (for imaging or therapy) constructs in patients with tumor is presented in Figure 10. The construct rapidly accesses the tumor vasculature and then can specifically bind to the monomeric VE-cad that is expressed in the neovasculature, but can not bind to resting vasculature with tight cell-cell contacts at the adherens junctions.

This E4G10/VE-cad targeting system is unlike the arginine-glycine-aspartic acid (RGD)-based agents that target the $\alpha_v\beta_3$ integrin which is often expressed by both the tumor and the vascular network. The RGD/$\alpha_v\beta_3$ integrin system lacks the vascular-specificity that we designed into our constructs. Targeting studies of VEGF-A that is expressed in the LS174T human xenograft model with bevacizumab were complicated not only by the relatively small numbers of copies of epitope per tumor cell (12E3), but by the imaging artifact that was created by the lack of expression of human VEGF-A in a mouse model (66).

The NIR FMT imaging data in vivo yielded an estimate of the number of VE-cad expressed per vascular endothelial cell. Using the measured values of the moles of E4G10 (3.2 pmol) per tumor (1,208 mm³) and published vessel area values per tumor volume (49) and VE cell area (1E-3 mm²) (50), there were 1.4E7 VE cells in the tumor with 1.3E5 VE-cad epitopes per VE cell. The VE-cad epitope was not expressed by the LS174T tumor and is a murine protein in the vessels of a mouse model. Baumgartner and Drenckhahn (70) reported 6E6 VE-cad dimers (12E6 VE-cad monomers) for immortalized mouse microvascular endothelial cells (MyEND) as determined in vitro using affinity chromatography and trypsinization. Our value was 90-fold lower than their value; however, it might be safely assumed that most of the vascular endothelial cells in our tumor were not newly formed angiogenic cells and the thus the epitope was hidden. Since our value was based on total vascular endothelial cells, then if only 10% of the vascular endothelial cells in the tumor were newly formed or had irregular or poorly connected adherens junctions, then our estimate of the number of epitopes per cell would increase 10-fold (1.3E6 VE-cad epitopes per VE cell). If the number of newly formed VE cells was only 1% of the total VE cell population in the tumor, then the value would increase 100-fold (1.3E7 VE-cad epitopes per VE cell). The latter assumption yielded a better correlation with the Baumgartner data.

Conclusion

SWCNT constructs were designed, constructed and used to deliver therapeutic and imaging radionuclide cargoes specifically to the vessels of a solid tumor using a target on VE-cad found only on new vascular endothelium. The goal was to target the neo- and irregular vessels in a tumor with these novel nano-constructs and image accumulation and evaluate therapeutic anti-angiogenic effects. The construct design incorporated 100-fold amplified cargo delivery (relative to the gold standard for targeted therapy – IgG) and were built to be multi-functional and thus have therapeutic or imaging cargo as well as targeting capability conferred by the appended IgG. This proof-of-concept design resulted in a construct with therapeutic efficacy, good image contrast and specificity for the target. This amplified SA may prove important in delivering potent enough therapy and sensitive enough diagnostic signals simultaneously to the tumor. Our data also provided support of the use of nanomaterials in vascular targeting strategies. These SWCNT construct doses were well-tolerated and safe in these animal models. The number of VE-cad epitopes per tumor was measured and extrapolated to estimate a number of bound VE-cad epitopes per cell. These latter results along with the PK profile will be of use in designing more optimized therapeutic and imaging studies with these constructs. Moving forward, it is anticipated that a single construct could be designed to incorporate both the imaging and therapeutic cargoes onto the same platform. Futhermore, since the construct targets an epitope expressed by the tumor vascular network, a single agent could be employed to image or treat a variety of different tumors.

Acknowledgments

References

1. Scheinberg DA, Villa CH, Escorcia FE, McDevitt MR. Conscripts of the infinite armada: systemic cancer therapy using nanomaterials. *Nat Rev Clin Oncol.* 2010;7(5):266-276.

2. Kostarelos K, Bianco A, Prato M. Promises, facts and challenges for carbon nanotubes in imaging and therapeutics. *Nat Nanotechnol.* 2009;4(10):627-633.

3. McDevitt MR, Chattopadhyay D, Kappel BJ, et al. Tumor targeting with antibody-functionalized, radiolabeled carbon nanotubes. *J Nucl Med.* 2007:48(7);1180-1189.

4. McDevitt MR, Chattopadhyay D, Jaggi JS, et al. PET Imaging of Soluble Yttrium-86-labeled Carbon Nanotubes in Mice. *PLoS One.* 2007;2(9):e907.

5. Villa CH, McDevitt MR, Escorcia FE, et al. Synthesis and biodistribution of oligonucleotide-functionalized, tumor-targetable carbon nanotubes. *Nano Lett.* 2008;8(12):4221-4228.

6. Ruggiero A, Villa CH, Bander E, et al. Paradoxical glomerular filtration of carbon nanotubes. *Proc Natl Acad Sci USA.* In press 2010.

7. Fox ME, Szoka FC, Frechet JMJ. Soluble Polymer Carriers for the Treatment of Cancer: The Importance of Molecular Architecture. *Acc Chem Res.* 2009;42(8):1141-1151.

8. Corada M, Liao F, Lindgren M, et al. Monoclonal antibodies directed to different regions of vascular endothelial cadherin extracellular domain affect adhesion and clustering of the protein and modulate endothelial permeability. *Blood.* 2001;97(6):1679-1684.

9. Liao F, Doody JF, Overholser J, et al. Selective targeting of angiogenic tumor vasculature by vascular endothelial-cadherin antibody inhibits tumor growth without affecting vascular permeability. *Cancer Res.* 2002;62(9):2567-2575.

10. Corada M, Zanetta L, Orsenigo F, et al. A monoclonal antibody to vascular endothelial-cadherin inhibits tumor angiogenesis without side effects on endothelial permeability. *Blood.* 2002;100(3):905-911.

11. May C, Doody JF, Abdullah R, et al. Identification of a transiently exposed VE-cadherin epitope that allows for specific targeting of an antibody to the tumor neovasculature. *Blood.* 2005;105(11):4337-4344.

12. Lamszus K, Brockmann MA, Eckerich C, et al. Inhibition of glioblastoma angiogenesis and invasion by combined treatments directed against vascular endothelial growth factor receptor-2, epidermal growth factor receptor, and vascular endothelial-cadherin. *Clin Cancer Res.* 2005;11(13):4934-4940.

13. McDevitt MR, Ma D, Lai LT, et al. Tumor therapy with targeted atomic nano-generators. *Science.* 2001;294(5546):1537-1540.

14. Borchardt PE, Yuan RR, Miederer M, McDevitt MR, Scheinberg DA. Targeted Actinium-225 in vivo generators for therapy of ovarian cancer. *Cancer Res.* 2003;63(16):5084-5090.

15. Miederer M, McDevitt MR, Sgouros G, Kramer K, Cheung NK, Scheinberg DA. Pharmacokinetics, dosimetry and toxicity of the targetable atomic generator, 225Ac-HuM195, in nonhuman primates. *J Nucl Med.* 2004;45(1):129-137.

16. Ballangrud ÅM, Yang WH, Palm S, et al. Alpha-particle Emitting Atomic Generator (Actinium-225)-Labeled Trastuzumab (Herceptin) Targeting of Breast Cancer Spheroids: Efficacy versus HER2/neu Expression. *Clin Cancer Res.* 2004;10(13):4489-4497.

17. Miederer M, McDevitt MR, Borchardt P, et al. Treatment of neuroblastoma meningeal carcinomatosis with intrathecal application of a-emitting atomic nanogenerators targeting disialo-ganglioside GD2. *Clin Cancer Res.* 2004;10(20):6985-6992.

18. Yuan RR, Wong P, McDevitt MR, et al. Targeted deletion of T-cell clones using alpha-emitting suicide MHC tetramers. *Blood.* 2004;10(8):2397-2402.

19. Jurcic JG, McDevitt MR, Divgi CR, et al. Alpha-Particle Immunotherapy for Acute Myeloid Leukemia (AML) with Bismuth-213 and Actinium-225. *Cancer Biother Radiopharm.* 2006;221(4):396.

20. Rosenblat TL, McDevitt MR, Pandit-Taskar N, et al. Phase I Trial of the Targeted Alpha-Particle Nano-Generator Actinium-225 (225Ac)-HuM195 (Anti-CD33) in Acute Myeloid Leukemia (AML). *Blood.* 2007;110(11):277A.

21. Miederer M, Scheinberg DA, McDevitt MR. Realizing the potential of the Actinium-225 radionuclide generator in targeted alpha-particle therapy applications. *Adv Drug Deliv Rev.* 2008;60(12):1371-1382.

22. McDevitt MR, Sgouros G, Finn RD, et al. Radioimmunotherapy with alpha-emitting radionuclides. *Eur J Nucl Med.* 1998;25(9):1341-1351.

23. Nikula TN, McDevitt MR, Finn RD, et al. Alpha-emitting Bismuth Cyclohexylbenzyl DTPA Constructs of Recombinant Humanized Anti-CD33 Antibodies: Pharmacokinetics, Bioactivity, Toxicity and Chemistry. *J Nucl Med.* 1999;40(1):166-176.

24. Calabrese C, Poppleton H, Kocak M, et al. A perivascular niche for brain tumor stem cells. *Cancer Cell.* 2007;11(1):69-82.

25. Hambardzumyan D, Squatrito M, Carbajal E, Holland EC. Glioma formation, cancer stem cells, and akt signaling. *Stem Cell Rev.* 2008;4(3):203-210.

26. Hambardzumyan D, Becher OJ, Rosenblum MK, Pandolfi PP, Manova-Todorova K, Holland EC. PI3K pathway regulates survival of cancer stem cells residing in the perivascular niche following radiation in medulloblastoma in vivo. *Genes Dev.* 2008;22(4):436-448.

27. Jaggi JS, Henke E, Seshan SV, et al. Selective Alpha-Particle Mediated Depletion of Tumor Vasculature with Vascular Normalization. *PLoS One.* 2007;2(3):e267.

28. Nolan DJ, Ciarrocchi A, Mellick AS, et al. Bone marrow-derived endothelial progenitor cells are a major determinant of nascent tumor neovascularization. *Genes Dev.* 2007;21(12):1546-1558.

29. Verel I, Visser GW, Boellaard R, Stigter-van Walsum M, Snow GB, van Dongen GA. 89Zr immuno-PET: Comprehensive Procedures for the production of 89Zr-labeled monoclonal antibodies. *J Nucl Med.* 2003;44(8):1271-1281.

30. Holland JP, Sheh Y, Lewis JS. Standardized methods for the production of high specific-activity zirconium-89. *Nucl Med Biol.* 2009;36(7):729-739.

31. Holland JP, Williamson MJ, Lewis JS. Unconventional nuclides for radiopharmaceuticals. *Mol Imaging.* 2010;9(1):1-20.

32. Holland JP, Caldas-Lopes E, Divilov V, et al. Measuring the pharmacodynamic effects of a novel Hsp90 inhibitor on HER2/neu expression in mice using Zr-DFO-trastuzumab. *PLoS One.* 2010;5(1):e8859.

33. Ruggiero A, Holland JP, Lewis JS, Grimm J. Cerenkov luminescence imaging of medical isotopes. *J Nucl Med.* 2010;51(7):1123-1130.

34. Holland JP, Divilov V, Bander NH, Smith-Jones PM, Larson SM, Lewis JS. 89Zr-DFO-J591 for immunoPET of prostate-specific membrane antigen expression in vivo. *J Nucl Med.* In press 2010.

35. von Schulthess GK, Steinert HC, Hany TF. Integrated PET/CT: Current Applications and Future Directions. *Radiology.* 2006;238(2):405-422.

36. Georgakilas V, Tagmatarchis N, Pantarotto D, Bianco A, Briand JP, Prato M. Amino Acid Functionalization of Water Soluble Carbon Nanotubes. *Chem Commun (Camb).* 2002;(24):3050-3051.

37. Tasis D, Tagmatarchis N, Bianco A, Prato M. Chemistry of carbon nanotubes. *Chem. Rev.* 2006;106(3):1105-1136.

38. Singh P, Campidelli S, Giordani S, Bonifazi D, Bianco A, Prato M. Organic functionalisation and characterisation of single-walled carbon nanotubes. *Chem Soc Rev.* 2009;38(8):2214-2230.

39. Singh R, Pantarotto D, Lacerda L, et al. Tissue biodistribution and blood clearance rates of intravenously administered carbon nanotube radiotracers. *Proc Natl Acad Sci USA.* 2006;103(9):3357-3362.

40. Allen BL, Kichambare PD, Gou P, et al. Biodegradation of single-walled carbon nanotubes through enzymatic catalysis. *Nano Lett.* 2008;8(11):3899-3903.

41. Allen BL, Kotchey GP, Chen Y, et al. Mechanistic investigations of horseradish peroxidase-catalyzed degradation of single-walled carbon nanotubes. *J Am Chem Soc.* 2009;131(47):17194-17205.

42. Konduru NV, Tyurina YY, Feng W, et al. Phosphatidylserine Targets Single-Walled Carbon Nanotubes to Professional Phagocytes In Vitro and In Vivo. *PLoS One.* 2009;4(2):e4398.

43. Kagan VE, Konduru NV, Feng W, et al. Carbon nanotubes degraded by neutrophil myeloperoxidase induce less pulmonary inflammation. *Nat Nanotechnol.* 2010;5(5):354-359.

44. Dumortier H, Lacotte S, Pastorin G, et al. Functionalized carbon nanotubes are non-cytotoxic and preserve the functionality of primary immune cells. *Nano Lett.* 2006;6(7):1522-1528.

45. Sayes CM, Liang F, Hudson J.L, et al. Functionalization density dependence of single-walled carbon nanotubes cytotoxicity in vitro. *Toxicol Lett.* 2006;161(2):135-142.

46. Schipper ML, Nakayama-Ratchford N, Davis CR, et al. A pilot toxicology study of single-walled carbon nanotubes in a small sample of mice. *Nat Nanotechnol.* 2008;3(4):216-221.

47. Kostarelos K. The long and short of carbon nanotube toxicity. *Nat Biotechnol.* 2008;26(7):774-776.

48. McDevitt MR, Ma D, Simon J, Frank RK, Scheinberg DA. Design and synthesis of Actinium-225 radioimmunopharmaceuticals. *Appl Radiat Isot.* 2002;57(6):841-847.

49. Hilmas DE, Gillette EL. Morphometric analyses of the microvasculature of tumors during growth and after x-irradiation. *Cancer.* 1974;33(1):103-110.

50. Haas TL, Duling BR. Morphology Favors an Endothelial Cell Pathway for Longitudinal Conduction within Arterioles. *Microvasc Res.* 1997;53(2):113-120.

51. Folkman J. Tumor angiogenesis and tissue factor. *Nat Med.* 1996;2(2):167-168.

52. Folkman J. Anti-angiogenesis: New concept for therapy of solid tumors. *Ann Surg.* 1972;175(3):409-416.

53. Denekamp J. Endothelial cell proliferation as a novel approach to targeting tumor therapy. *Br J Cancer.* 1982;45(1):136-139.

54. Denekamp J. Review article: angiogenesis, neovascular proliferation and vascular pathophysiology as targets for cancer therapy. *Br J Radiol.* 1993;66(783):181-196.

55. Burrrows FJ, Thorpe PE. Vascular targeting-a new approach to the therapy of solid tumors. *Pharmacol Ther.* 1994;64(1):155-174.

56. Folkman J. Addressing tumor blood vessels. Nat Biotechnol. 1997;15(6):510.

57. Kerbel RS. Antiangiogenic Therapy: A Universal Chemosensitization Strategy for Cancer? *Science.* 2006; 312(5777):1171-1175.

58. Cai W, Chen X. Multimodality molecular imaging of tumor angiogenesis. *J Nucl Med.* 2008;49(Suppl 2):113S-128S.

59. Dobrucki LW, de Muinck ED, Lindner JR, Sinusas AJ. Approaches to Multimodality Imaging of Angiogenesis. *J Nucl Med.* 2010;51(Suppl 1):66S-79S.

60. Leunig M, Yuan F, Menger MD, et al. Angiogenesis, microvascular architecture, microhemodynamics, and interstitial fluid pressure during early growth of human adenocarcinoma LS174T in SCID mice. *Cancer Res.* 1992;52(23):6553-6560.

61. Kennel SJ, Mirzadeh S. Vascular targeted radioimmunotherapy with 213Bi-an alpha-particle emitter. *Nucl Med Biol.* 1998;25(3):241-246.

62. Kennel SJ, Lankford TK, Foote LJ, Davis IA, Boll RA, Mirzadeh S. Combination vascular targeted and tumor targeted radioimmunotherapy. *Cancer Biother Radiopharm.* 1999;14(5):371-379.

63. Kennel SJ, Chappell LL, Dadachova K, et al. Evaluation of ^{225}Ac for vascular targeted radioimmunotherapy of lung tumors. *Cancer Biother Radiopharm.* 2000;15(3):235-244.

64. Kennel SJ, Mirzadeh S, Eckelman WC, et al. Vascular-targeted radioimmunotherapy with the alpha-particle emitter ^{211}At. *Radiat Res.* 2002;157(6):633-641.

65. Nagengast WB, de Vries EG, Hospers GA, et al. In Vivo VEGF Imaging with Radiolabeled Bevacizumab in a Human Ovarian Tumor Xenograft. *J Nucl Med.* 2007;48(8):1313–1319.

66. Stollman TH, Scheer MG, Leenders WP, et al. Specific imaging of VEGF-A expression with radiolabeled anti-VEGF monoclonal antibody. *Int J Cancer.* 2008;122(10):2310–2314.

67. Nayak TK, Garmestani K, Baidoo KE, Milenic DE, Brechbiel MW. PET imaging of tumor angiogenesis in mice with VEGF-A targeted (86)Y-CHX-A"-DTPA-bevacizumab. *Int J Cancer.* In press 2010.

68. Nikula TK, Bocchia M, Curcio MJ, et al. Impact of the high tyrosine fraction in complementarity determining regions: measured and predicted effects of radioiodination on IgG immunoreactivity. *Mol Immunol.* 1995;32(12):865-872.

69. Nilsson F, Kosmehl H, Zardi L, Neri D. Targeted delivery of tissue factor to the ED-B domain of fibronectin, a marker of angiogenesis, mediates the infarction of solid tumors in mice. *Cancer Res.* 2001;61(2):711-716.

70. Baumgartner W, Drenckhahn D. Plasmalemmal concentration and affinity of mouse vascular endothelial cadherin. *Eur Biophys J.* 2002;31(7):532-538.

3.3

Targeting the internal epitope of prostate-specific membrane antigen with 89Zr-7E11 immunoPET imaging

Ruggiero A, Holland JP, Hudolin T, Shenker L, Koulova A, Bander NH, Lewis J, Grimm J

Abstract

The potential of the positron-emitting ^{89}Zr has been recently investigated for the design of radioimmunoconjugates for immuno-positron emission tomography (immunoPET). In this study, we report the preparation and *in vivo* evaluation of ^{89}Zr-desferrioxamine B (DFO)-7E11; a novel ^{89}Zr-labeled monoclonal antibody (mAb) construct for targeted imaging of prostate-specific membrane antigen (PSMA), a prototypical cell surface marker highly overexpressed in prostate cancer (PC). The ability of ^{89}Zr-DFO-7E11 to delineate tumor response to therapy was also investigated, as it binds to the *intracellular epitope* of PSMA which becomes available only upon membrane disruption in dead or dying cells.

Methods: 7E11 as a marker of dying cells was studied by flow cytometry and microscopy of cells after antiandrogen-, radio- and chemotherapy treatment in LNCaP and PC3-PSMA positive cells. The *in vivo* behaviour of ^{89}Zr-DFO-7E11 was characterized in mice bearing subcutaneous LNCaP (PSMA-positive) by biodistribution studies and immunoPET. The potential of assessing tumor response was evaluated *in vivo* after radiotherapy treatment.
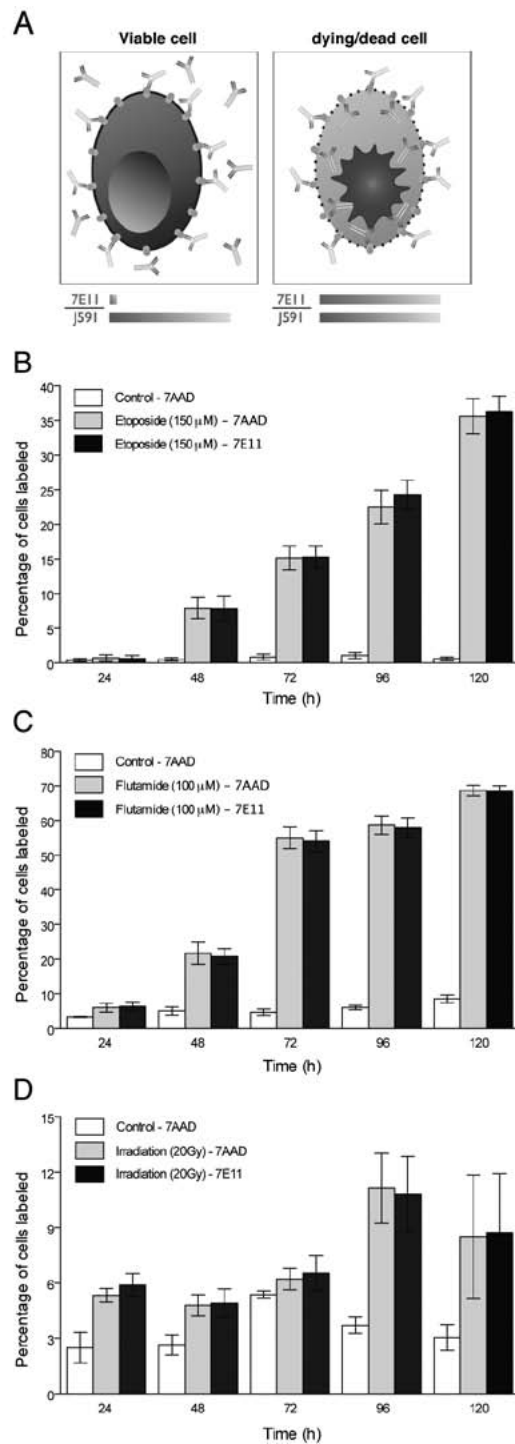
Results: In vitro studies correlated 7E11 binding with markers of apoptosis (7AAD and Caspase-3). *In vivo* biodistribution experiments revealed high, target-specific uptake of ^{89}Zr-DFO-7E11 in LNCaP tumors after 24 h (20.35±7.50%ID/g), 48 h (22.82±3.58%ID/g), 96 h (36.94±6.27%ID/g) and 120 h (25.23±4.82%ID/g). Excellent image contrast was observed with immunoPET. 7E11 uptake was statistically increased in irradiated *versus* control tumor as measured by immunoPET and biodistribution studies. Binding specificity was assessed by effective blocking studies at 48 h. **Conclusion:** These findings suggest that ^{89}Zr-DFO-7E11 displays high tumor–to–background tissue contrast in immunoPET and can be used as a tool to monitor and quantify with high specificity tumor response in PSMA-positive PC.

Introduction

Prostate cancer (PC) accounts for around 25% of cancers in American men as well as 9% of cancer deaths (*1*). Prostate-specific antigen (PSA) testing has led to earlier diagnosis and is used widely in monitoring for recurrence after therapy. Although serum PSA measurement is widely by physicians as a measure of treatment response, no PSA-based endpoint has yet been validated by regulatory agencies as a surrogate marker for survival in trials of new drugs (*2*). Besides the utility of standard imaging techniques (CT, MRI, ultrasound, ^{99m}Tc-based bone scintigraphy and ^{111}In-Capromab Pendetide PET), at present there are no highly accurate non-invasive methods for detection and monitoring of PC therapy (*3*).

^{18}F-FDG PET, the most used PET radiotracer, has been suggested as a useful technique for diagnosis and staging of primary PC with high Gleason score, for the assessment of the extent of metabolically active castrate-resistant disease. However, there are several limitations with ^{18}F-FDG PET e.g. PC uptake can overlap with the one from normal prostatic tissue, benign prostatic hyperplasia, prostatitis and post-radiotherapy changes, and imaging of local PC is frequently obfuscated by adjacent background uptake in the bladder (*3, 4*). In the assessment of therapy response clinical results have been mixed (*5-7*). Molecular targeted agents (such as monoclonal antibodies, peptides, aptamers, and small molecules) functionalized with imaging moieties are currently under investigation for monitoring PC, but despite efforts towards translation, results have been slow to emerge (*8*). Overall, there is an urgent need for the development and clinical translation of novel tools for non-invasive staging and evaluation of the response to treatment in PC.

Prostate-specific membrane antigen (PSMA), a 100-kDa, type II glycoprotein, is an established biomarker of PC, and its expression has been correlated with tumor stage and grade, biochemical recurrence and androgen independence (*9, 10*). 7E11 is a murine monoclonal antibody (mAb) that recognizes a specific epitope located on the intracellular domain of PSMA (*11*). In 1996, the US Food and Drug Administration (US-FDA) approved the use of a radiolabeled form of the 7E11 mAb, ^{111}In-Capromab pendetide or ^{111}In-7E11 (ProstaScint→ Cytogen Corporation, Princeton NJ, USA), for single-photon emission computed tomography (SPECT). Its use is indicated as an imaging agent in newly-diagnosed patients with biopsy-proven PC who are at high risk for pelvic lymph node metastases, and in post-prostatectomy patients with a rising PSA and a negative or equivocal standard metastatic evaluation in whom there is a high clinical suspicion of occult metastatic disease (*12*). In several studies, ^{111}In-7E11 imaging displayed sensitivity of 60%, specificity of 70%, positive predictive value of 60%, and negative predictive value of 70% for PC soft-tissue lesions (*13-16*). However, the use of ^{111}In-7E11 for clinical diagnosis has been considered limited (in comparison to other PSMA antibodies, particularly J591) because its *intracellular* binding site is only accessible upon membrane disruption in dead, dying or apoptotic cells within tumor sites (*17*). In our previous

Fig. 1. PSMA+ cells' responses to different treatments in vitro (A) The monoclonal antibody 7E11 binds to an intracellular epitope of PSMA, labeling apoptotic or already dead cells, whose leaky cell membrane permits access of the antibody to the intracellular domain. The monoclonal antibody J591, recognizes the extracellular domain of PSMA and thus binds to all PSMA-positive cells, regardless of their viability. Higher percentage of 7AAD and 7E11 stained cells is observed over time after treatment compared to control (p<0.05 at all treaments and regimens, with the exception of etoposide treatment at 24 h). Corresponding staining is observed for both 7E11 and 7AAD staining in all experiments (P>0.05). Data are reported as percentage of labeled cells after treatment with (B) etoposide (PC3/PSMA+) (C) flutamide and (D) radiation therapy (LNCap).

work, we sought to overcome both limitations by investigating [89]Zr-DFO-J591, a radioimmunoconjugate for the targeting and PET imaging of the extracellular PSMA in PC viable tissues (*18*).

Herein, given our previous positive experience with the positron-emitting radionuclide [89]Zr (*18, 19*) we developed [89]Zr-labeled 7E11 and report its use as imaging agent for PC immunoPET imaging. Moreover, we envision to make use of the presupposed limitation of 7E11 (i.e. the fact that its epitope only becomes accessible upon membrane disruption, resulting in limited number of available targets) to monitor changes in epitope presentation after treatment by means of PET imaging. Our hypothesis was that the effects of different treatment options available for PC could be monitored by observing the increase in 7E11 uptake with progressing cell

membrane disruption resulting from treatment (Fig. 1A). We also sought to improve upon several imaging limitations associated with ^{111}In for SPECT by taking advantage of the favorable thermodynamic, kinetic and PET imaging characteristics of a [89]Zr-DFO-labeling strategy. Combined, our *in vitro* and *in vivo* studies confirm the effectiveness of this *proof-of-concept* study, demonstrating increasing 7E11 binding upon cell membrane disruptions resulting from different treatments.

Materials and Methods

Antibodies

The murine IgG$_1$ mAb, 7E11 was provided by the institutional Monoclonal Antibody Core Facility (*11*). The mAb, J591 has been described elsewhere (*20, 21*).

Cells lines

Androgen-dependent LNCaP (PSMA-positive) cell lines were obtained from ATCC (Manassas, VA). The retrovirally transduced PC-3 human PSMA cell line (PC-3/PSMA+ [PSMA-positive]) was obtained from Dr. M. Sadelain (MSKCC) (*22*).

Cell membrane permeabilization in vitro studies

Cell permeabilization was achieved by using radiotherapy, chemotherapy (etoposide) and anti-androgen hormonal therapy (flutamide) regimens. 48 h after seeding, PC-3/PSMA+ cells received etoposide (150 µM; Sigma Aldrich, St. Louis, MO). Control cells were treated with the vehicle only (DMSO). LNCaP cells were exposed to 20 Gy by using an XRAD 320 (Precision X-Ray, Inc.) at a dose rate of 117.5 cGy/min. Cells not exposed to radiation therapy were used as a control. In separate experiments, LNCaP cells were treated with flutamide (100 µM; Sigma Aldrich, St. Louis, MO). Control cells were exposed to the vehicle only (ethanol). At 24, 48, 72, 96 and 120 h post-treatment floating dying/dead cells were collected and adherent cells harvested by trypsinization. The two fractions were mixed to reconstitute the total population and prepared for FC or microscopy. Additional dosing regimes and further details are provided in the supplemental materials.

For flow cytometry experiments, cells were stained using J591 labeled with allophyco-cyanin (APC) (Invitrogen, Carlsbad, CA, USA) and 7E11 labeled with Alexa Fluor 488 (AF-488) (Invitrogen, Carlsbad, CA, USA). Cells were incubated for 30 min., washed and 7-amino-actinomycin-D (7AAD; BD Biosciences Bedford, MA) was added to assess cell membrane permeabilization. For fluorescence microscopy experiments, cells were stained for 4',6-diamidino-2-phenylindole (DAPI; Vectashield, Vector Laboratories, Inc Burlingame, CA), 7E11-AF-488 and cleaved Caspase-3 antibody (Cell Signaling Technology Inc., Danvers, MA). Images were obtained with DAPI, TRITC and FITC filter sets.

7E11 antibody radiolabeling

7E11 was conjugated to desferrioxamine B (DFO, Calbiochem, Spring Valley, CA) (*19, 23*). Zirconium-89 was produced *via* the $^{89}Y(p,n)^{89}Zr$ transmutation reaction on a cyclotron (Ebco Industries Inc., Richmond, BC, Canada) (*24*). The ^{89}Zr-7E11 was prepared by complexation of ^{89}Zr-oxalate with DFO-7E11. Radiochemical purity was measured by radio-ITLC and size-exclusion chromatography; stability by incubation in saline for 7 days (37°C) and subsequent radio-ITLC, size-exclusion-chromatography, γ-counting, and cellular-binding assays.

Xenograft models

All animal experiments were conducted in compliance with Institutional Animal Care and Use Committee guidelines. Male SCID mice (6–8 wk old) were obtained from Taconic Farms Inc. (Hudson, NY) and were allowed to acclimatize at the Memorial Sloan-Kettering Cancer Center vivarium for 1 week before tumors were implanted. Mice were provided with food and water *ad libitum*. Bilateral LNCaP tumors were induced on the flanks of male SCID mice (Taconic, Hudson, NY) by subcutaneous (s.c.) injection of 4.0×10^6 in Matrigel (BD Biosciences, Bedford, MA). The tumor volume (*V*/ mm³) was estimated as described previously (*18*). Animals bearing LNCaP xenografts (*n*=5 per group) were sedated with ketamine (100mg/Kg) and xylazine (10mg/Kg) and irradiated (total dose: 20 Gy) using an X-ray unit (XRAD 320; Precision X-Ray, Inc.; 117.5 cGy/min, 50-cm source to skin distance). Only one tumor was exposed; the rest of the animal was shielded by a lead-shielded jig. The contralateral LNCaP tumor not irradiated was used as internal control. Radiolabeled antibodies were injected 36 h after radiation treatment.

Acute biodistribution studies

In vivo biodistribution studies were conducted (*n*=5/group) to evaluate uptake of ^{89}Zr-7E11 in LNCaP xenograft. Mice received ^{89}Zr-7E11 (0.55–0.74 MBq, [15–20 μCi], 3–4 μg of mAb) *via* retro-orbital injection (*t*=0 h). Animals were euthanized at 24, 48, 96 and 120 h post-injection and 11 organs (including the tumors) were removed, rinsed, dried, weighed and counted on a gamma-counter for ^{89}Zr activity.

Competitive inhibition (blocking) studies were performed to investigate the specificity of ^{89}Zr-7E11. Non-radiolabeled 7E11 (0.30 mg/mouse) was added to the ^{89}Zr-7E11 formulations to reduce the specific-activity (60-fold decrease: 3.04 MBq/mg [0.082 mCi/mg]). Biodistribution studies were performed at 48 h post injection.

Small-animal immunoPET imaging

Experiments were conducted on a microPET Focus 120 (Concorde Microsystems, Knoxville, TN). Mice (*n*=5) were administered ^{89}Zr-7E11 (8.8–11.1 MBq, [280–300 μCi], 62–67 μg of mAb) *via* tail-vein injection. Approximately 5 min. prior to recording PET images, mice were anesthetized by inhalation of 1% isoflurane (Baxter Healthcare, Deerfield, IL)/oxygen gas mixture and placed on the scanner bed. PET images were recorded at various time-points between 24–120 h post-injection. Full details of image acquisition, reconstruction and analysis are presented in the supplemental materials.

Autoradiography and histology

LNCaP xenografts were harvested and fixed in 4% paraformaldehyde before embedding in OCT (Sakura, Finetek U.S.A Inc.), then frozen at –80°C, and cryo-sectioned. Sections were exposed on a storage phosphor image plate for 48 h. Digital autoradiography (DAR) images were read using a phosphor plate-reader (Fuji Photo Film Co. Ltd., Tokyo, Japan). Consecutive sections were used for immunostaining. After sections were blocked with albumin, cleaved Caspase-3 antibody (Cell Signaling Technology Inc., Danvers, MA) was applied overnight at 4°C, followed by incubation with biotinylated goat anti-rabbit IgG (Vector Laboratories, Inc., Burlingame, CA) for 1 h (room temperature). Immunohistochemistry was completed using the avidin-biotin method. Counterstain was performed with Hematoxylin. Hematoxylin/Eosin staining (H/E) was performed in consecutive sections.

Statistical analysis

Data were analyzed using the unpaired, two-tailed Student's *t*-test (GraphPad Prism, San Diego, California, USA). Differences at the 95% confidence level (*P*<0.05) were considered statistically significant. Flow cytometry data were analyzed with CellQuest Pro (BD Biosciences, Bedford, MA) and Flow-Jo software (Tree Star, San Carlos, CA), PET data with ASIPro VM™ (Concorde Microsystems, Knoxville, TN).

Results

Flow Cytometry and microscopy evaluation of the response to treatment in PSMA expressing cells

7AAD was used to monitor cell viability at different time points and compared to vehicle-treated or non-irradiated cells as a control (Fig 1). J591, recognizes the extracellular domain of PSMA and thus binds to all PSMA-positive cells, regardless of their viability, therefore was used to provide an internal standard for the total amount of PSMA on the cells. However, a higher variability in the fluorescence intensity was observed in some cells compared to vehicle control. This was mainly related to the morphological changes and/or clustering of cells induced by the treatment (Suppl. Fig. S1). Conversely, disruption of the cell membrane upon treatment makes the intracellular epitope available for 7E11 targeting (Fig. 1 and Suppl. Fig 1). We observed an increase in the percentage of cells stained with 7E11 after all treatment regimens (Fig. 1). In each experiment, 7E11 and 7AAD staining gave similar results; for all therapies the correlation coefficient R^2

between 7AAD and 7E11 was >0.99 (Table S1). For example, at 120 h, etoposide treatment (150µM) resulted in 35.5±2.5% for 7AAD and 36.3±2.2% for 7E11 positive cells *versus* control (0.5±0.2% and 0.61±0.2%, respectively; *P*<0.0001 for both). Flutamide (100µM)-induced disruption of the cell membrane reached a maximum at 120 h after treatment (7AAD: 68.7±1.5% and 7E11: 68.5±1.5% *versus* control 7AAD: 8.5±1.1% and 7E11: 8.79±1.1%; *P*<0.0001 for both). Disruption of cells after radiation therapy peaked at 96 h (7AAD: 11.1±1.8%; 7E11: 10.8±2.0% *versus* control: 7AAD 3.6±0.44% and 7E11: 4.36±1.0%; *P*=0.0003 and *P*=0.0011, respectively).

Next, we demonstrated the effectiveness of 7E11 as a marker of membrane disruption by immunofluorescence staining. PC-3/PSMA+ and LNCaP cells treated with etoposide, flutamide or radiation therapy showed increased 7E11 signal compare to controls over time. Caspase-3 staining performed on the same slides showed higher intensity in the treated samples compared to controls. Co-localization of 7E11 and Caspase-3 staining was observed (Fig. 2, Suppl. Fig 2 and supplemental movie).
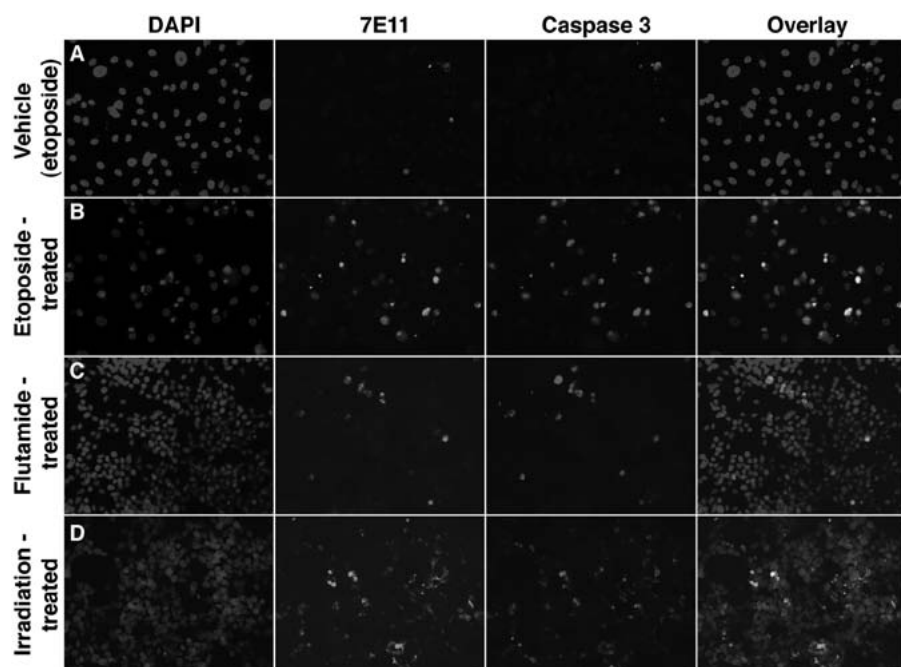

Fig. 2. Immunofluorescence assay of prostate cancer cells stained with DAPI, 7E11 and activated Caspase-3 obtained at 96 h after treatment. (A) PC-3/PSMA+ treated with representative vehicle (control from the etoposide study). Additional controls are in Suppl. Fig. 2. (B) PC-3/PSMA+ cells after treatment with etoposide; (C) LNCaP cells receiving flutamide and (D) LNCaP cells treated with radiation therapy (Magnification: 20 x). In all samples, co-localization of 7E11 and activated Caspase-3 staining was observed

In vivo evaluation of the response to treatment by ^{89}Zr immunoPET

7E11 was functionalized with desferrioxamine B (DFO) and radiolabeled to produce ^{89}Zr-7E11 in high yield, with high radiochemical purity (RCP) and specific activity (*19, 23, 24*). DFO conjugation and purification proceeded in moderate-to-high yield (43±8%) with high purity (>95%). Radiolabeling of DFO-7E11 with ^{89}Zr-oxalate resulted in crude labeling yields >95% (*n*=4). The final radiochemical yield of purified ^{89}Zr-7E11 was 89% with a specific activity of 166.9±1.2 MBq/mg (4.51±0.06 mCi/mg) of mAb (Suppl Fig. 3). Isotopic dilution assays revealed an average of 2.6±0.5 accessible chelates/mAb.

Incubation of ^{89}Zr-7E11 in sterile saline for 7 days at 37ºC revealed a <2% decrease in RCP (*via* demetalation) as shown by radio-ITLC and analytical size-exclusion chromatography. The immunoreactive fraction of the ^{89}Zr-7E11 formulations was measured by specific *in vitro* cellular association assays using sodium azide-treated PC-3/PSMA+ cells prior to each *in vivo* experiment (Suppl Fig. 4). The average immunoreactive fraction of ^{89}Zr-7E11 was 0.89±0.08 (*n*=4) and showed no decrease over 7 days incubation in saline. Control experiments (*n*=4) using PC-3 wild-type (PSMA-negative) cells showed negligible binding, further demonstrating the specificity of ^{89}Zr-7E11 for PSMA (data not shown, JASON CAN YOU PLS CONFIRM THIS ?). Overall, these radiolabeling data are consistent with our previous studies on ^{89}Zr-DFO-labeled mAbs and confirm the suitability of the radiotracer for use *in vivo (18, 19).*

To demonstrate that our approach is applicable to *in vivo* imaging we performed temporal PET imaging of ^{89}Zr-7E11 of mice bearing bilateral LNCaP tumors, with only one tumor receiving radiation therapy (20 Gy). Selectively irradiated tumors showed higher uptake compared to the contralateral (untreated) tumors assigned to increased
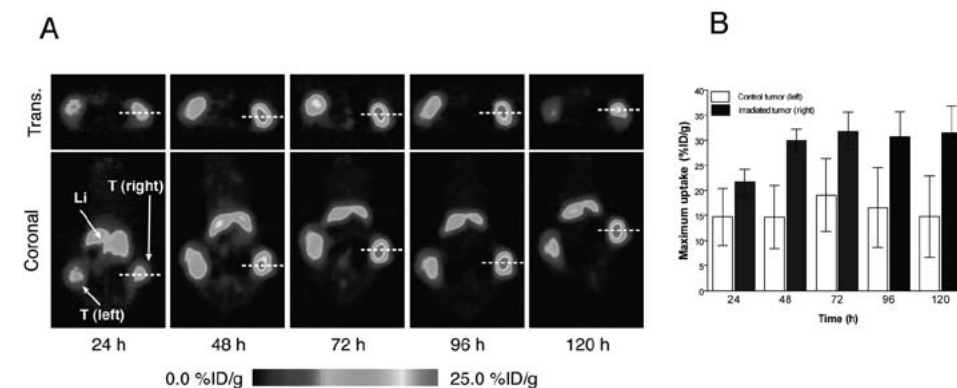
Fig. 3. In vivo imaging of therapy response with ^{89}Zr-7E11 ImmunoPET in xenograft-bearing mice. (A) Representative transverse and coronal ^{89}Zr-7E11 immunoPET images at different time points in a LNCaP xenograft-bearing mouse treated with selective radiation to the right side. Increased uptake of ^{89}Zr-7E11 was observed in the selectively irradiated tumor (right) compared to the control (left). T: Tumor, Li: Liver. The dashed line represents the position of the perpendicularly oriented image. (B) ^{89}Zr-7E11 uptake values (obtained from the PET data as maximum %ID/g) were significantly higher in irradiated than control tumors at 24 h (P=0.0376), 48 h (P=0.0009), 72 h (P=0.0086), 96 h (P=0.01), 120 h (P=0.0075).

target presentation and specific binding to the treatment-exposed intracellular PSMA epitope. Representative PET imaging results are shown in Fig. 3A. Baseline binding on the non-treated LNCaP tumor is expected as some cells are always undergoing cell death or apoptosis in tumors of this size. ^{89}Zr-7E11 uptake values (obtained from the PET data) were significantly higher in irradiated than control tumors at 24 h (21.63±2.53 *versus* 14.72±5.66, p=0.0376), 48 h (29.94±2.3 *versus* 14.65±6.3, p=0.0009), 72 h (31.82±3.84 *versus* 19.07±7.28, p=0.0086), 96 h (30.68±5.01 *versus* 16.56±7.94, p=0.01), 120 h (31.44±5.37 *versus* 14.78 ± 8.11, p=0.0075).

Ex vivo quantitation of the response to treatment

Biodistribution experiments in animals bearing control and irradiated LNCaP xenografts (Fig. 4) revealed increased tumor uptake of ^{89}Zr-7E11 over time in the treated *versus* contralateral control tumors at 24, 48, 96 and 120 h. With the exception of the 24 h time point, all differences between treated and control tumors were statistically significant (Table 1). Competitive inhibition studies using low specific-activity formulations of 7E11 (3.04 MBq/mg [0.082 mCi/mg]) revealed a 6-fold decreased uptake (*P*=0.003) with only 8.8±0.4 %ID/g (versus 52.7±4.8 %ID/g) in treated tumors at 48 h after blocking.

Table 1. Biodistribution data of ^{89}Zr-DFO-7E11, administered intravenously to mice bearing subcutaneous LNCaP tumors.

Organ	24 h (n=5)	48 h (n=5)	96 h (n=5)	120 h (n=5)	Block (300mg of MAb) at 48 h (n=5)
Blood	32.63 ± 4.89	23.82 ± 4.34	12.37 ± 1.88	6.60 ± 2.94	17.21 ± 0.83
Heart	7.33 ± 1.10	4.65 ± 1.63	3.04 ± 0.61	2.95 ± 0.78	3.90 ± 0.58
Lungs	12.84 ± 2.60	7.55 ± 2.43	7.98 ± 1.46	7.79 ± 2.76	6.61 ± 0.68
Liver	53.75 ± 3.83	42.74 ± 3.13	36.08 ± 2.57	32.98 ± 0.65	34.14 ± 1.64
Spleen	28.64 ± 4.44	29.90 ± 4.12	26.48 ± 2.10	31.26 ± 4.04	21.36 ± 2.69
Kidney	27.43 ± 5.13	21.61 ± 2.27	15.84 ± 3.32	15.20 ± 3.38	14.82 ± 2.09
Intestine	3.39 ± 0.66	4.91 ± 2.19	8.18 ± 4.61	1.99 ±0.29	4.56 ± 2.08
Muscle	1.88 ± 0.51	1.02 ± 0.53	1.20 ± 0.76	0.75 ± 0.18	1.24 ± 0.39
Bone	4.10 ± 0.91	6.25 ± 1.32	4.52 ± 0.86	4.93 ± 1.05	4.98 ± 2.19
LNCaP (Irradiated)	24.70 ± 7.24	40.61 ± 7.51	51.79 ± 7.43	52.71 ±11.13	8.84 ± 0.89
LNCaP (Control)	20.35 ± 7.50	22.82 ± 3.58	36.94 ± 6.27	25.23 ± 4.82	5.93 ± 2.11
LNCaP (Irradiated)/blood	0.76 ±0.33	1.8 ± 0.51	4.32 ± 1.21	9.86 ± 5.59	0.51 ± 0.04
LNCaP (Control)/blood	0.62 ± 0.22	0.96 ± 0.21	3.02 ± 0.58	5.21 ± 2.77	0.40 ± 0.03

Biodistribution data of ^{89}Zr-7E11 administered intravenously to mice bearing subcutaneous LNCap tumors (expressed as the percent of injected dose per gram of tissue ;%ID/g± SD).
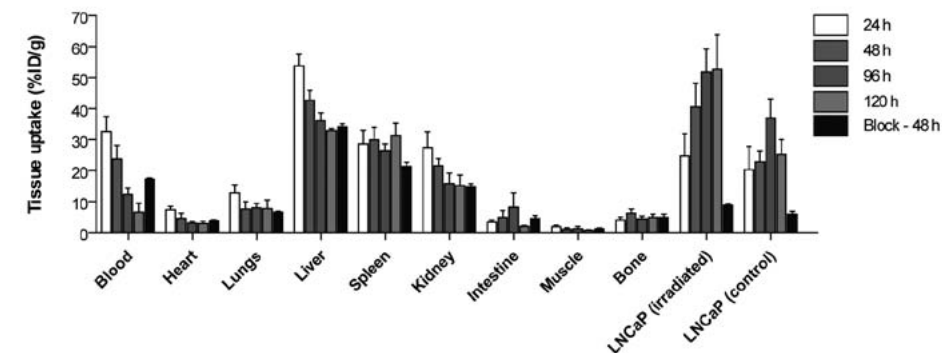
Fig. 4. Biodistribution study with blocking experiment. Bar chart showing selected tissue biodistribution data (%ID/g) for the uptake of ^{89}Zr-7E11 in mice bearing LNCaP xenografts at 24, 48, 72 and 96 h time points. Blocking experiments with non-radiolabeled 7E11 mAb were also conducted at 48 h post-injection. With the exception of the uptake at 24h all data points show a statistically significant difference between irradiated and control tumors (*P<0.012, blocking at 48h P=0.033). Some uptake is observed in the non-irradiated LNCaP tumors since they are PSMA-positive and experience a baseline cell death.

Autoradiography and histology

To correlate the uptake of the 7E11 *in vivo* with actual apoptosis we performed digital autoradiography (DAR) and used consecutive slides to stain for activated Cas
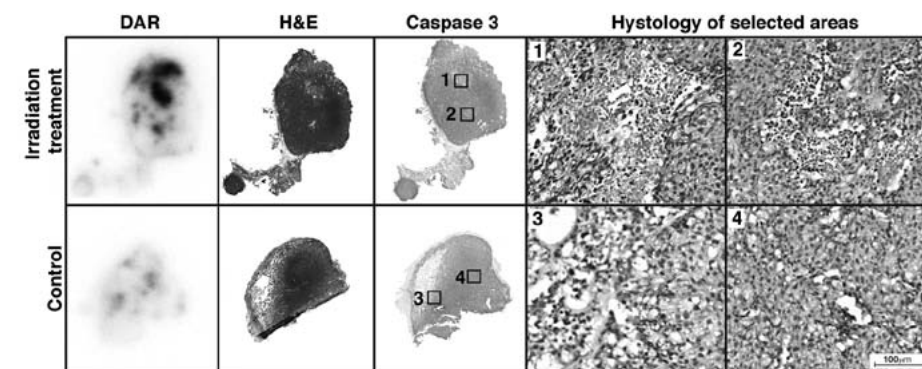
Fig. 5. Autoradiography of the irradiated and control tumor corresponds with activated Caspase-3. Digital autoradiography (DAR), H/E stain and activated caspase-3 staining of the irradiated and the control tumor. Uptake of ^{89}Zr-7E11 was observed in treated tumors; co-localizing with apoptotic/necrotic areas by H/E and Caspase-3 staining as demonstrated by the overlay of DAR and activated caspase-3 staining. The numbered rectangles in the Caspase 3 staining represent the approximate localization of the higher magnification images.

pase-3. DAR demonstrated higher uptake of ^{89}Zr-7E11 in the irradiated tumors than in the control tumors (Fig. 5). Intratumoral distribution of ^{89}Zr-7E11 averaged 40% of cross-sectional area and revealed excellent co-localization with apoptotic/necrotic areas by both Caspase-3 and H/E staining.

Discussion

PET has been regarded as having higher sensitivity (2 to 3 orders of magnitude) and better spatial and temporal resolution than SPECT (*25*), which are critical features especially for radioimmunoimaging. Here, we report the development of the novel radiopharmaceutical ^{89}Zr-7E11 and investigate its use in the PET imaging of PC, thus overcoming several limitations inherent to SPECT imaging and associated with the FDA approved radiotracer (^{111}In-7E11). The ability of ^{89}Zr-7E11 to target PSMA-expressing tissue has been examined using acute biodistribution studies and immunoPET *in vivo* at different time points. Advantages of using ^{89}Zr ($I_{\beta+}$=22.7%, $E_{\beta+}$(mean)= 395.5 keV, $t_{1/2}$=78.4 h) have been discussed elsewhere (*26*) and include high *in vivo* stability, excellent contrast, and high resolution of ^{89}Zr-PET images (*18, 23, 24*). The results demonstrate that ^{89}Zr-7E11 shows high specific uptake in LNCaP (PSMA positive) tumors. In a comparison with earlier work, the absolute tissues uptake of ^{89}Zr-7E11 at the different time points was found to be higher than those observed with ^{111}In-7E11 (*17, 27*). In the same s.c. LNCaP model the tumor-to-blood ratios at 96 h after injection were slightly higher for ^{89}Zr-DFO-7E11 (tumor-to-blood ratio: 5.21) than ^{111}In-7E11 (tumor-to-blood ratio: 2.83) (*17*). As expected, LNCaP tumor uptake was lower with ^{89}Zr-7E11 (tumor-to-blood ratio: 5.21) than with ^{89}Zr-J591 (tumor-to-blood ratio 29.7), as previously reported by our group (*18*).

In vitro cellular and autoradiography studies demonstrated that 7E11 binds only to dead/dying cells (*17, 28*), as the intracellular PSMA epitope for 7E11 becomes accessible only upon membrane disruption (*11*). Therefore, in the present work, we propose the potential use of ^{89}Zr-radiolabeled 7E11 antibody (the mAb for which is a known marker of cell death) as a quantitative, PET imaging tool to evaluate early response to treatment. In the process, we turn the perceived disadvantage of clinical imaging with 7E11 (targeting an intracellular epitope only accessible upon cell membrane disruption) into an advantage.

Thus far, no clinically utilized antibodies have been suggested for imaging treatment response in PC, although other agents have shown some potential (*29*). For example, ^{99m}Tc-Annexin V has been proposed to image early apoptosis in murine tumors after chemotherapy (*30*). The loss of cellular membrane integrity has also been imaged with macromolecules that can be exchanged between the extra- and intracellular compartment, such as ^{99m}Tc-pyrophosphate (*31*) or ^{99m}Tc-Glucarate (*32*). An ^{111}In-labeled murine Fab fragment that binds to myosin has been used to image damage to muscular cells in acute myocardial infarction with non-quantitative SPECT imaging (*33*).

7AAD is a well-established marker of late-stage apoptosis/necrosis after all types of therapy. In our study, 7E11 and 7AAD binding correlated very strongly after each type of treatment. Microscopy showed co-localization of 7E11 with Caspase-3 staining, confirming that 7E11 binding to exposed PSMA indicates the presence of apoptotic/necrot-

ic cells. Further, we noted a time/drug concentration dependency of the 7E11 and 7AAD binding to cells but in all cases, the observed correlation between 7E11 and 7AAD held. Based on these findings we can suggest that ^{89}Zr-7E11 uptake in prostate cancer can be used as a surrogate marker of cell death.

Radiation therapy was administered selectively to LNCaP xenografts, using contralateral (untreated) tumors as control in the same animal. We observed that uptake of ^{89}Zr-7E11 was significantly higher in the selectively treated tumors than in the control tumors. These data suggested a tumor response to therapy resulting in higher availability of the internal epitope of PSMA. Quantitative PET data were confirmed by biodistribution studies (Fig. 4), which showed a statistically significant difference between radiotracer binding in treated *versus* control tumors.

Autoradiography showed an intratumoral distribution of ^{89}Zr-7E11 corresponding to necrotic/apoptotic areas (by Caspase-3 and H/E staining), consistent with previous reports (*17*). In particular, uptake of ^{89}Zr-7E11 (and necrosis/apoptosis) was higher in irradiated tumors than in control tumors, corresponding in the former to approximately 40-50% of the cross-sectional area.

To better evaluate the specificity of ^{89}Zr-7E11 tumor uptake, independent from therapy- induced vascular changes which contribute to tumor uptake by the "enhanced permeability retention" (EPR) effect, we performed biodistribution studies including comparisons with competitive inhibition (blocking) experiments. We found a 6-fold decrease of ^{89}Zr-7E11 specific binding at 48 h in the group that received a blocking dose of non-radiolabeled 7E11. While our data show a relatively high baseline uptake in aggressive untreated LNCaP tumors, the additional increase after therapy is significantly higher and potentially could negate the requirement for a baseline study in order to stratify patient populations as responders or non-responders. Specifically, we believe that, although challenging to first define, suitable standardized uptake value (SUV) thresholds may be applicable to ^{89}Zr-7E11 imaging for defining tumor response to treatment. To the best of our knowledge, the use of SUV thresholds to identify patients responding to chemotherapy has not been tested using immunoPET and, as with for example, ^{64}Cu-ATSM imaging of hypoxia, is worth considering in the design of future clinical trials. Notably, the approach presented here could be applied to other targets using engineered pairs of antibodies recognizing intra- and extracellular epitopes to image therapy effects in other disease models. Importantly, considering that ^{111}In-labeled 7E11 has already received US-FDA approval for the imaging of soft-tissue metastasis in PC, we anticipate that ^{89}Zr-7E11 immunoPET may benefit from rapid translation to the clinic.

Conclusions

Overall our studies demonstrate that [89]Zr-7E11 for immunoPET imaging of changing PSMA levels has the potential to be used in monitoring patient response to therapies including various chemotherapies and radiation therapy. We anticipate that as with 7E11 for prostate cancer, the concept of targeting an intracellular epitope of a molecular protein target may find application in a various other pathologies, particularly those responding to cytotoxic treatment.

Acknowledgements

References

1. Jemal A, Siegel R, Ward E, Hao Y, Xu J, Thun MJ. Cancer statistics, 2009. *CA Cancer J Clin.* Jul-Aug 2009;59(4):225-249.

2. Attard G, de Bono JS. Prostate cancer: PSA as an intermediate end point in clinical trials. *Nat Rev Urol.* Sep 2009;6(9):473-475.

3. Jadvar H. Prostate cancer: PET with 18F-FDG, 18F- or 11C-acetate, and 18F- or 11C-choline. *J Nucl Med.* Jan;52(1):81-89.

4. Liu IJ, Zafar MB, Lai YH, Segall GM, Terris MK. Fluorodeoxyglucose positron emission tomography studies in diagnosis and staging of clinically organ-confined prostate cancer. *Urology.* Jan 2001;57(1):108-111.

5. Oyama N, Akino H, Suzuki Y, et al. FDG PET for evaluating the change of glucose metabolism in prostate cancer after androgen ablation. *Nucl Med Commun.* Sep 2001;22(9):963-969.

6. Haberkorn U, Bellemann ME, Altmann A, et al. PET 2-fluoro-2-deoxyglucose uptake in rat prostate adenocarcinoma during chemotherapy with gemcitabine. *J Nucl Med.* Aug 1997;38(8):1215-1221.

7. Jadvar H. Molecular imaging of prostate cancer with 18F-fluorodeoxyglucose PET. *Nat Rev Urol.* Jun 2009;6(6):317-323.

8. Jadvar H. Molecular imaging of prostate cancer: a concise synopsis. *Mol Imaging.* Mar-Apr 2009;8(2):56-64.

9. Wright GL, Jr., Grob BM, Haley C, et al. Upregulation of prostate-specific membrane antigen after androgen-deprivation therapy. *Urology.* Aug 1996;48(2):326-334.

10. Mannweiler S, Amersdorfer P, Trajanoski S, Terrett JA, King D, Mehes G. Heterogeneity of prostate-specific membrane antigen (PSMA) expression in prostate carcinoma with distant metastasis. *Pathol Oncol Res.* Jun 2009;15(2):167-172.

11. Horoszewicz JS, Kawinski E, Murphy GP. Monoclonal antibodies to a new antigenic marker in epithelial prostatic cells and serum of prostatic cancer patients. *Anticancer Res.* Sep-Oct 1987;7(5B):927-935.

12. Bander NH. Technology insight: monoclonal antibody imaging of prostate cancer. *Nat Clin Pract Urol.* Apr 2006;3(4):216-225.

13. Haseman MK, Reed NL, Rosenthal SA. Monoclonal antibody imaging of occult prostate cancer in patients with elevated prostate-specific antigen. Positron emission tomography and biopsy correlation. *Clin Nucl Med.* Sep 1996;21(9):704-713.

14. Babaian RJ, Sayer J, Podoloff DA, Steelhammer LC, Bhadkamkar VA, Gulfo JV. Radioimmunoscintigraphy of pelvic lymph nodes with 111indium-labeled monoclonal antibody CYT-356. *J Urol.* Dec 1994;152(6 Pt 1):1952-1955.

15. Polascik TJ, Manyak MJ, Haseman MK, et al. Comparison of clinical staging algorithms and 111indium-capromab pendetide immunoscintigraphy in the prediction of lymph node involvement in high risk prostate carcinoma patients. *Cancer.* Apr 1 1999;85(7):1586-1592.

16. Apolo AB, Pandit-Taskar N, Morris MJ. Novel tracers and their development for the imaging of metastatic prostate cancer. *J Nucl Med.* Dec 2008;49(12):2031-2041.

17. Smith-Jones PM, Vallabhajosula S, Navarro V, Bastidas D, Goldsmith SJ, Bander NH. Radiolabeled monoclonal antibodies specific to the extracellular domain of prostate-specific membrane antigen: preclinical studies in nude mice bearing LNCaP human prostate tumor. *J Nucl Med.* Apr 2003;44(4):610-617.

18. Holland JP, Divilov V, Bander NH, Smith-Jones PM, Larson SM, Lewis JS. 89Zr-DFO-J591 for immunoPET imaging of prostate-specific membrane antigen (PSMA) expression in vivo. *J Nucl Med.* 2010;51(8):1293-1300

19. Holland JP, Caldas-Lopes E, Divilov V, et al. Measuring the pharmacodynamic effects of a novel Hsp90 inhibitor on HER2/*neu* expression in mice using 89Zr-DFO-trastuzumab. *PLoS ONE.* 2010;5(1):e8859.

20. Liu H, Moy P, Kim S, et al. Monoclonal antibodies to the extracellular domain of prostate-specific membrane antigen also react with tumor vascular endothelium. *Cancer Res.* Sep 1 1997;57(17):3629-3634.

21. Liu H, Rajasekaran AK, Moy P, et al. Constitutive and antibody-induced internalization of prostate-specific membrane antigen. *Cancer Res.* Sep 15 1998;58(18):4055-4060.

22. Gong MC, Latouche JB, Krause A, Heston WD, Bander NH, Sadelain M. Cancer patient T cells genetically targeted to prostate-specific membrane antigen specifically lyse prostate cancer cells and release cytokines in response to prostate-specific membrane antigen. *Neoplasia.* Jun 1999;1(2):123-127.

23. Verel I, Visser GW, Boellaard R, Stigter-van Walsum M, Snow GB, van Dongen GA. 89Zr immuno-PET: comprehensive procedures for the production of 89Zr-labeled monoclonal antibodies. *J Nucl Med.* Aug 2003;44(8):1271-1281.

24. Holland JP, Sheh Y, Lewis JS. Standardized methods for the production of high specific-activity zirconium-89. *Nucl Med Biol.* Oct 2009;36(7):729-739.

25. Rahmim A, Zaidi H. PET versus SPECT: strengths, limitations and challenges. *Nucl Med Commun.* Mar 2008;29(3):193-207.

26. Holland JP, Williamson MJ, Lewis JS. Unconventional nuclides for radiopharmaceuticals. *Mol Imaging.* 2010;9(1):1-20.

27. Pan MH, Gao DW, Feng J, et al. Biodistributions of 177Lu- and 111In-labeled 7E11 antibodies to prostate-specific membrane antigen in xenograft model of prostate cancer and potential use of 111In-7E11 as a pre-therapeutic agent for 177Lu-7E11 radioimmunotherapy. *Mol Imaging Biol.* May-Jun 2009;11(3):159-166.

28. Smith-Jones PM, Vallabahajosula S, Goldsmith SJ, et al. In vitro characterization of radiolabeled monoclonal antibodies specific for the extracellular domain of prostate-specific membrane antigen. *Cancer Res.* Sep 15 2000;60(18):5237-5243.

29. De Saint-Hubert M, Prinsen K, Mortelmans L, Verbruggen A, Mottaghy FM. Molecular imaging of cell death. *Methods.* Jun 2009;48(2):178-187.

30. Mandl SJ, Mari C, Edinger M, et al. Multi-modality imaging identifies key times for annexin V imaging as an early predictor of therapeutic outcome. *Mol Imaging.* Jan 2004;3(1):1-8.

31. Khaw BA. The current role of infarct avid imaging. *Semin Nucl Med.* Jul 1999;29(3):259-270.

32. Perek N, Sabido O, Le Jeune N, et al. Could 99mTc-glucarate be used to evaluate tumour necrosis? In vitro and in vivo studies in leukaemic tumour cell line U937. *Eur J Nucl Med Mol Imaging.* Jul 2008;35(7):1290-1298.

33. Khaw BA, Fallon JT, Beller GA, Haber E. Specificity of localization of myosin-specific antibody fragments in experimental myocardial infarction. Histologic, histochemical, autoradiographic and scintigraphic studies. *Circulation.* Dec 1979;60(7):1527-1531.

4.1

Cell tracking in cardiac repair: what to image and how to image

Ruggiero A, Thorek DLJ, Guenoun J, Krestin GP, Bernsen

Abstract

Stem cell therapies hold the great promise and interest for cardiac regeneration among scientists, clinicians and patients. However, advancement and distillation of a standard treatment regimen are not yet finalised. Into this breach step recent developments in the imaging biosciences. Thus far, these technical and protocol refinements have played a critical role not only in the evaluation of the recovery of cardiac function but also in providing important insights into the mechanism of action of stem cells. Molecular imaging, in its many forms, has rapidly become a necessary tool for the validation and optimisation of stem cell engrafting strategies in preclinical studies. These include a suite of radionuclide, magnetic resonance and optical imaging strategies to evaluate non-invasively the fate of transplanted cells. In this review, we highlight the state-of-the-art of the various imaging techniques for cardiac stem cell presenting the strengths and limitations of each approach, with a particular focus on clinical applicability.

Introduction

In the last decade a great amount of research and clinical interest has been directed at stem cells (SC) for their potential to regenerate otherwise permanently damaged tissues. Work with these pluripotent cells has begun to be broadly explored, giving new hope for regenerative approaches in the therapy of myocardial infarction (MI).

Early success in preclinical studies demonstrated that stem cell-based therapy holds the potential to limit the functional degradation of cardiac function after MI [1]. This instigated clinical translation at a rapid pace (Table 1). Since the first study in 2002 which showed safety and effectiveness on intracoronary transplantation of autologous SC [2], several randomised, controlled clinical trials have been performed. Due to the absence of standardised protocols (cell number, timing and route of injection, baseline patient characteristics and techniques of evaluating cardiac function), results have been mixed. However, recent meta-analyses have shown that improvement in ejection fraction (EF), ventricular dimension and infarct area, despite being modest, are statistically significant [3-5].

This field clearly benefited from the advancements in imaging sciences as almost all clinical trials involved the use of one or more imaging techniques to evaluate the therapeutic efficacy of stem cell transplantion. Clinically established techniques allow for the evaluation of myocardial contractility, viability and perfusion, but do not provide the direct visualisation of transplanted stem cells, therefore their effective presence and viability can be only presumed. Ideally, transplanted cells in the infarcted myocardium are expected to survive engraftment, be self-renewing and differentiate into cardiac cells (cardiomyocytes, endothelial cells or smooth muscle cells) forming electromechanical junctions with adjacent viable tissues. However, the long-term improvement appears to be most closely related to paracrine effects rather than transdifferentiation of the cell transplant and heart muscle regeneration [6].

Great strides in imaging techniques and technologies have been made that enable the cellular and molecular imaging of transplanted stem cells, their short and long term fate and in some instances their viability and differentiation status.

Table 1. Selected randomised clinical trials (>50 patients) of stem cell transplantation following myocardial infarction

Study	Pts	Cell type	Assessment method	Outcome
REPAIR-AMI [101; 102]	204	Intracoronary BMC vs placebo	LV angiography	At 4 months LVEF increased in BMC vs placebo (mean±SD) increase, (5.5±7.3% vs. 3.0±6.5%; P = 0.01). At 12 months: death, recurrence of myocardial infarction, rehospitalization for heart failure significantly reduced.
ASTAMI [103; 104]	100	Intracoronary BMC vs control	99mTc-SPECT; ECHO MRI	No effect on global left ventricular function at 6 months and 3 years.
BOOST[105; 106]	60	Intracoronary BMC vs control	MRI	At 6 months global LVEF increase (6.7%). No effects at 18 months and 5 years.
Janssens et al. [107]	67	Intracoronary BMC vs placebo	MRI; [11C] acetate PET	At 4 months no effect on LVEF and LV volumes. Reduction of infarct volume (measured by serial contrast-enhanced MRI) was greater in BMC patients than in controls.
TOPCARE-AMI [16]	59	Intracoronary BMC vs CPC	LV angiography; MRI	At 4 months LV angiography showed significant increase of LVEF (50±10% to 58±10%), and significant decrease of end-systolic volumes (54±19 ml to 44±20 ml) without differences between the two cell groups. At 12 months MRI showed reduced infarct size and absence of reactive hypertrophy.
Meluzin et al [108]	60	Intracoronary BMC (high and low doser) vs control	Echo; 99mTc-SPECT; 18F-FDG PET	LVEF improved in the group receiving the highest dose (108 cells) by 6%, 7%, and 7% at months 3, 6, and 12, respectively.
MAGIC[8]	97	SMB vs placebo injected in and around the scar	Echo	No improvement in regional or global LV function at 6 months.
Chen et al[109]	69	Intracoronary BMSC (bone marrow mesenchymal stem cells) vs placebo	18F-FDG; Echo	At 3 months LVEF significantly increased in the BMSC group (67±11%) compared to controls (53±8%) and the same group before implantation (49±9%). No change in LVEF at 6 months versus 3 months.
Dill T et al[110]	204	Intracoronary BMC vs placebo	MRI	In the BMC group, EF increased significantly by 3.2±1.3 absolute percentage points at 4 months, and this increase was sustained at 12 months (+3.4 ± 1.3 absolute percentage points vs baseline). In the placebo group, EF was unchanged (+0.6 ± 1.2 absolute percentage points, at 12 months.

BMC, bone marrow stem cells; CPC, circulating progenitor cells; SMB, skeletal myoblast. Pts, number of patients. LVEF, left ventricular ejection fraction.

Stem cells for cardiac repair

Currently adult stem cells, embryonic stem cells (ESC) and induced pluripotent stem cells (iPS) can be used to regenerate heart tissue. Adult stem cells comprise skeletal myoblasts (SM), mesenchymal stem cells (MSC), bone marrow- derived stem cells (BMC), endothelial (EPC) and cardiac progenitor (CPC) cells. SM were the first option to be used in stem cell transplant as they are available from an autologous source (therefore lacking ethical or immunogenicity issues), and have been demonstrated to provide functional benefit after myocardial infarction in animals [7]. However, in a recent clinical trial no sustained benefit in the global EF was observed and increased number of early postoperative arrhythmic events was reported [8].

BMC transplantation has been shown to improve heart function in animal models [1; 9]. However, others have identified that most of the cells injected adopted a mature haematopoietic transformation and only a small number of cardiomyocytes expressed the genetic markers of the transplanted cells [10; 11]. Mesenchymal stem cells (MSC) constitute the stromal compartment of bone marrow and, importantly, are not hematopoietic. These are able to differentiate into a variety of cell types [12] and improvement in whole heart function has been described in a swine model of myocardial infarction [13]. Visceral and subcutaneous adipose tissue have been shown to contain vascular/adipocyte progenitor cells and adult multipotent mesenchymal cells (adipose tissue-derived stromal cells [14]). ASC have been reported to improve left ventricular function in animal models of myocardial infarction [15]. The circulating endothelial progenitor cells (EPC) represent a more accessible source of autologous SC and have been used in clinical trials [16]. The existence of a subpopulation of resident cardiac SC (RCSC) has been reported that is self-renewing, clonogenic and multipotent, capable of differentiating in myocytes, smooth muscle and endothelial cells [17]. Promising results have been reported in preclinical studies [18], and results of phase I clinical trials, started in 2009, are awaited with interest.

To date, ESC-derived cardiomyocytes [19] and ESC-derived endothelial cells [20] have been successfully used to treat heart disease in animal models. However several problems are related to their use, including immunological incompatibility with the host [21], the tendency to form teratomas [22] and ethical controversies. Several studies have been performed to manipulate the expression of transcription factors with the goal of transforming somatic cells (derived from an autologous source, such as keratinocytes and fat stromal cells) into induced pluripotent stem cells (iPS) [23]. These cells possess the same advantages as ESC, without the associated immunological and ethical complications. Cardiomyocytes have been successfully obtained from iPS in vitro [24] and their transplantation in animal models of infarction resulted in improved myocardial function [25].

To summarise, ESC and iPS have the greater potential for cardiomyogenesis, while the formation of new cardiomyocytes by transdifferentiation of SM and BMC has so far

not been supported with convincing evidence. It should be noted that several studies have reported moderate improvements in whole cardiac function after transplantation of SM and BMC [7; 26]. It has been demonstrated that SCs are responsible for paracrine effects, consisting of the release of various cytokines or growth factors (eg. VEGF, bFGF) that increase collateral perfusion and neoangiogenesis and influence the contractile characteristics of chronically failing myocardium [26].

Imaging of stem cells

The ability to image and monitor the biodistribution, viability and possibly the differentiation status of implanted SCs is of massive clinical and research benefit. All of the pre-clinical and clinical imaging techniques have been leveraged towards this goal; each providing unique advantages and limitations. Fig. 1 illustrates the major paradigms for the labelling of SC for detection by the various imaging approaches. Table 2 reports the most important preclinical studies in the field. Table 3 summarises the most relevant features of each imaging technique.
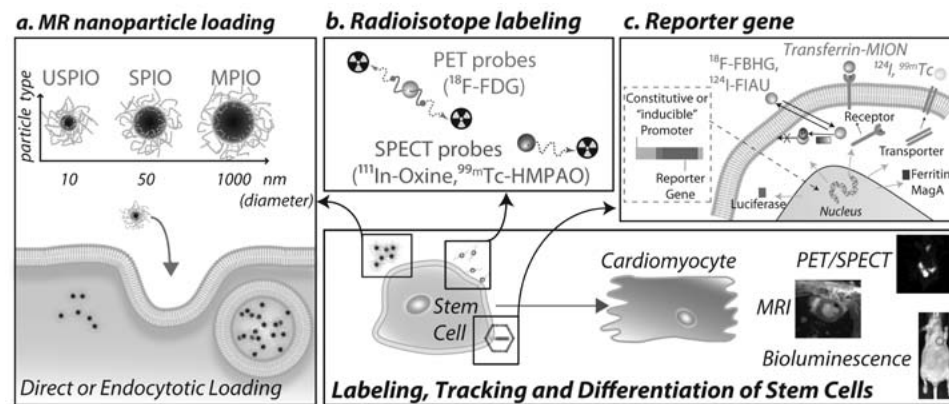

Figure 1
Schematic representation of the current technologies available for stem cell (SC) tracking. Before implantation SC can be passively loaded with: (A) superparamagnetic nanoparticles that allow for the MR detection of labelled cells as areas of signal loss; (B) radiolabelled PET or SPECT probes. (C) Reporter gene approaches consist of the introduction through viral or non-viral-vectors of a reporter gene driven by a constitutive or inducible promoter. The reporter gene undergoes transcription to mRNA, which is translated into a protein that can be: 1) an enzyme (as HSV1-tk or luciferase), 2) a receptor (as transferrin receptor or hSSTR [human somatostatin receptor]) 3) a transporter (hNIS [human sodium iodide symporter]) 4) intracellular iron storage protein (ferritin). When a complementary reporter probe is administered, it concentrates or activates only at the site where the reporter gene is expressed. The level of probe accumulation is proportional to the level of reporter gene expression and can be monitored to evaluate the number of cells or the induction of a specific reporter gene.

Table 1. Selected randomised clinical trials (>50 patients) of stem cell transplantation following myocardial infarction

Study	Pts	Cell type	Assessment method	Outcome
REPAIR-AMI [101; 102]	204	Intracoronary BMC vs placebo	LV angiography	At 4 months LVEF increased in BMC vs placebo (mean±SD) increase, (5.5±7.3% vs. 3.0±6.5%; P = 0.01). At 12 months: death, recurrence of myocardial infarction, rehospitalization for heart failure significantly reduced.
ASTAMI [103; 104]	100	Intracoronary BMC vs control	^{99m}Tc-SPECT; Echo MRI	No effect on global left ventricular function at 6 months and 3 years.
BOOST[105; 106]	60	Intracoronary BMC vs control	MRI	At 6 months global LVEF increase (6.7%). No effects at 18 months and 5 years.
Janssens et al [107]	67	Intracoronary BMC vs placebo	MRI; [11C] acetate PET	At 4 months no effect on LVEF and LV volumes. Reduction of infarct volume (measured by serial contrast-enhanced MRI) was greater in BMC patients than in controls.
TOPCARE-AMI [16]	59	Intracoronary BMC vs CPC	LV angiography; MRI	At 4 months LV angiography showed significant increase of LVEF (50±10% to 58±10%), and significant decrease of end-systolic volumes (54±19 ml to 44±20 ml) without differences between the two cell groups. At 12 months MRI showed reduced infarct size and absence of reactive hypertrophy.
Meluzin et al [108]	60	Intracoronary BMC (high and low doser) vs control	Echo; ^{99m}Tc-SPECT; ^{18}F-FDG PET	LVEF improved in the group receiving the highest dose (10^8 cells) by 6%, 7%, and 7% at months 3, 6, and 12, respectively.
MAGIC[8]	97	SMB vs placebo injected in and around the scar	Echo	No improvement in regional or global LV function at 6 months.
Chen et al [109]	69	Intracoronary BMSC (bone marrow mesenchymal stem cells) vs placebo	^{18}F-FDG; Echo	At 3 months LVEF significantly increased in the BMSC group (67±11%) compared to controls (53±8%) and the same group before implantation (49±9%). No change in LVEF at 6 months versus 3 months.
Dill T et al [110]	204	Intracoronary BMC vs placebo	MRI	In the BMC group, EF increased significantly by 3.2±1.3 absolute percentage points at 4 months, and this increase was sustained at 12 months (+3.4 ± 1.3 absolute percentage points vs baseline). In the placebo group, EF was unchanged (+0.6 ± 1.2 absolute percentage points, at 12 months.

BMC, bone marrow stem cells; CPC, circulating progenitor cells; SMB, skeletal myoblast. Pts, number of patients. LVEF, left ventricular ejection fraction.

Table 2. Selected cell tracking studies of SC

Study	Species	Cell type	Detection method	Delivery	Results
MRI					
Kraitchman et al. [111]	swine	MSC	SPIO	Intramyocardial-percutaneous	Detection of tranplanted cells (25.8%) up to 3 weeks.
Amado et al.[112]	swine	MSC	SPIO	Intramyocardial-percutaneous	Gradual loss of intensity of the SPIO label but retection of tranplanted cells (42.4%±15) at 8 weeks.
Stuckey et al.[113]	rat	BMC	GFP-SPIO	Intramyocardial –direct	No improvement in LEVF. Detection of tranplanted cells up to 16 weeks confirmed by MR and immunofluorescence.
Amsalem et al. [43]	rat	MSC	SPIO	Intramyocardial –direct	At 4 weeks after injection, most of the transplanted labelled MSCs did not survive and their iron content was engulfed by resident macrophages. Injection of labelled or unlabelled cells attenuate ventricular dilatation and dysfunction after MI.
Ebert et al. [114]	mice	mESC	SPIO	Intramyocardial -direct	Detection up to 4 weeks by MRI. LVEF identical between the tranplanted group and control.
Terrovitis et al. [45]	rat	hCDCrCDC	SPIO	Intramyocardial -direct	Signal void persisted after 3 weeks in both syngeneic and xenogeneic cell implantation. Immunohistochemistry identifies the iron containing cells as macrophages.
Radionuclide					
Chin et al. [62]	swine	MSC	^{111}In-oxine	Intravenous	Significant lung activity that obscured the assessment of myocardial cell tracking.
Brenner et al.[63]	rat	HPC-CD34+	^{111}In-oxine	Intracavitary (left ventriculum)	Impairment of cell proliferation and differentiation induced by ^{111}In-oxine. At 96 h only 1% of radioactivity was detected in the heart.
Blackwood et al. [65]	dog	BMC	^{111}In-tropolone	Intramyocardial -direct	Viability at day 6 after intramyocardial injection was calculated to be 75%.
Terrovitis et al. [82]	rat	rCDC	^{18}F-FDG	Intramyocardial -direct	Different retention values were observed at 1h after injection of cells with normal condition (17.8%±7.3), arrested heart (75.8%±18.3), adenosine injection (35.4%±5.3) and adenosine plus fibrin glue (39.3%±11.6).
Mitchell et al. [66]	dog	EPC	^{111}In-tropolone	Intramyocardial-percutaneous	15 days after intramyocardial injection SPECT/CT imaging demonstrated comparable degrees of retention: 57%±15 for the subepicardial injections and 54%±26 for the subendocardial injections.
Multimodal					
Terrovitis et al.	Rat	rCDC	^{99m}Tc, ^{124}I; hNIS	Intramyocardial -direct	Detection up to 6 days after injection and their presence validated by ex vivo imaging and qPCR.
Qiao et al. [98]	rat	mESC	SPIO; HSV1-tk + ^{18}F-FHBG	Intramyocardial -direct	Increasing ^{18}F-FHBG uptake up to 4 weeks. Most of the SPIO were contained in infiltrating macrophages at week 4. Teratoma formation. Increased LVEF. Only <0.5% of the implanted cell were cardiomyocytes.
Chapon et al. [115]	rat	rBMC	SPIO; ^{18}F-FDG	Intramyocardial -direct	MRI detection of SPIO labelled cells grafted in the heart up to 6 weeks, confirmed by hystology. At 1 week increased 18F-FDG uptake in BMC implanted heart vs control. No improvement of heart function.
Higuchi et al. [99]	rat	hEPC	SPIO; NIS +^{124}I	Intramyocardial -direct	Rapid decrease of ^{124}I uptake after day 3. Signal nor detectable at day 7. MRI signal void remained unchanged throughout the follow-up period. Histology confirmed the presence of transplanted cells on day 1 but not on day 7, when iron was contained only in resident macrophages.
Li et al. [116]	rat	RCSC	Fluc + D-Luciferin; ^{18}F-FDG PET; echocardiography; MRI	Intramyocardial -direct	Implanted cells detected up to 7 weeks by bioluminescence. No improvement in cardiac function assessed by ^{18}F-FDG PET, MRI, echocardiogram and invasive hemodynamic pressure volume-analysis.

BMC (bone marrow derived Stem Cells); MSC mesenchymal stem cells; mESC (mouse embryonic stem cells); hCDC (human cardiac derived stem cells), rCDC (rat cardiac derived stem cells); HPC (hematopoietic progenitor cells); hEPC, human Endothelial Progenitor Cells; RCSC (resident cardiac stem cells); NIS (sodium iodide symporter); Fluc (firefly luciferase); hNIS (human sodium-iodide symporter; MI, Myocardial infarction.

Imaging and treating tumor vasculature with targeted radiolabeled carbon nanotubes

Table 3. What to image and how to image

Imaging modality	Spatial resolution (mm)	Sensitivity (mol/L)	Cell Manipulation	What to image	How to image	Advantages	Disadvantages
Fluorescence Imaging	FRI: 2-3 mm; FMT: 1mm	10^{-9}–10^{-12}	Cells labelled with near-infrared probes (fluorochromes, Quantum dots, etc.)	Residence, homing, quantification (FMT)	Direct imaging; at NIR wavelenghts can image deep tissue	Multiplexed imaging	Not suitable for clinical translation; relatively low spatial resolution
Bioluminescence Imaging	3-5	10^{-15}–10^{-17}	Cells transduced to express luciferase	Residence, homing, viability, differentiation, quantification	After systemic injection of D-Luciferine or Coelenterazine	Easy, high sensitivity, high-throughput, low cost; assessment of cell viability	Not suitable for clinical translation; surface imaging; relatively low spatial resolution; requires completely dark environment
PET	1-2 (mPET); 6-10 (clinical PET)	10^{-11}–10^{-12}	Cells loaded with ^{18}F-FDG; ^{64}Cu labelled compounds	Residence, homing, quantification	Direct imaging	High sensitivity, translational	Radiation; only short term cell tracking
			Cells transduced to express PET reporter genes (HSV1tk, HSV1-sr39tk)	Residence, homing, differentiation, quantification,	After systemic injection of correspondent radiolabelled probe (^{18}F-FHBG, ^{18}F-FEAU, etc.)	High sensitivity, long term cell tracking; assessment viability	Radiation; need to transduce cells; potential immunogenicity
SPECT	0.5-2 (mSPECT); 7-15 (clinical SPECT)	10^{-10}–10^{-11}	Cells labelled with ^{99m}Tc, ^{111}In-labelled compounds	Residence, homing, quantification	Direct imaging	High sensitivity, translational; assessment viability	Radiation; only short term cell tracking
			Cells transduced to express reporter genes (hNIS)	Residence, homing, viability, differentiation, quantification,	After systemic injection of correspondent radiolabeled probe (^{99m}Tc, etc.)	High sensitivity, long term cell tracking	Radiation; need to transduce cells; potential immunogenicity
MRI	0.01-0.1 (small animal); 0.5-1.5 (clinical)	10^{-3}–10^{-5}	Cells labelled with Iron Oxides; Gd or Mn chelates; perfluorocarbon (^{19}F)	Residence, homing, migration, quantification	Direct imaging	High spatial resolution; high soft tissue contrast; functional imaging	Relatively low sensitivity; long scanning times; probe dilution upon cell proliferation; persistence of SPIO after cell death (macrophage)
			Cells transduced to express MRI reporter genes β-galactosidase, transferrin receptor, ferritin, MagA and lysine-rich proteins	Residence, homing, quantification, migration, differentiation	Direct imaging or after injection of iron oxides (transferrin receptor, ferritin)	High spatial resolution; high soft tissue contrast; functional imaging; no probe dilution;	Low sensitivity; need to transduce cells; potential immunogenicity

NIR, Near-Infra red imaging; FRI, Fluorescence reflectance imaiging; FMT, Fluorescence molecular tomography

MRI

Magnetic resonance imaging (MRI) is a widely established technique for the evaluation of cardiac anatomy and function, often through the addition of paramagnetic contrast material [27]. Taking advantage of its excellent spatial (10-100 μm [small animal MRI]); 500-1500 μm [clinical]) and temporal resolution SC labelled with superparamagnetic and paramagnetic agents can be visualised [28; 29]. Multispectral non-^{1}H MR imaging (specifically ^{19}F) has also been exploited to enable tracking of transplanted cells.

Superparamagnetic Iron Oxide Nanoparticles

Superparamagnetic iron oxide (SPIO) nanoparticles provide labelled cells with a large magnetic moment and are detectable by MR imaging devices or benchtop relaxometers. SPIO functions by acting as magnetic inhomogeneities, locally disturbing the magnetic field. This leads to enhanced dephasing of protons, resulting in decreased signal intensity on T2-weighted and T2*-weighted images (Figs 2 and 3). These nanoparticles often consist of a core of iron oxide (magnetite and/or maghemite) with a polymeric or polysaccharide coating. They are widely viewed to be biocompatible, have a limited effect on cell function and can be synthesized to be biodegradable. According to their size (diameter), these are classified as ultrasmall paramagnetic iron oxide (USPIO, <10 nm), monocrystalline iron oxide particles (MION, or cross-linked CLIO; 10-30 nm), standard superparamagnetic iron oxide (SPIO; 60-150 nm) and micron-sized iron oxide
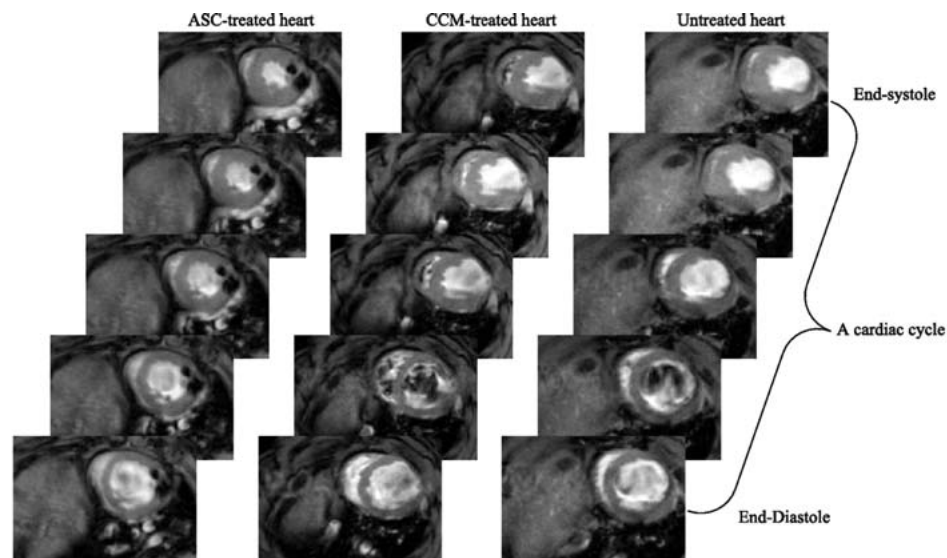
particles (MPIO, 0.7-1.6 μm). Of note, ferucarbotran (Resovist˚; Bayer Schering Pharma, Berlin, Germany) and ferumoxides (Feridex I.V.˚, Advanced Magnetic Industries, Cambridge, Maryland, USA; Endorem˚, Guerbet, Gorinchem, the Netherlands) have been approved by the FDA for contrast enhanced-MRI imaging of liver tumors [30] and metastatic involvement of lymph nodes [31].

Cell uptake is mediated through the size and electrostatic charge conditions of the SPIO [32], schematically illustrated in Fig. 1a. Further, loading can be augmented through the addition of cell penetrating peptides, electroporation or transfection agents [33].

Studies reported that SPIOs do not affect cell viability, proliferation, differentiation or migration [34-38]. However, recent work has raised several concerns, such as decreased MSC migration and colony-formation ability [39], and interference with cell function [40; 41]. A major issue beyond potential cellular effects is the question of contrast specificity to the presence of cells. Namely, the hypointense signal is maintained at a site regardless of cell viability and SPIO are present not necessarily within implanted SC at longer time points [42], but rather in phagocytosing monocytes following SC death [43]. Recently, Winter *et al* reported the absence of any discrimination between healthy

Figure 2. Anatomical and functional MR evaluation after transplantion of adipose-derived stem cell (ASC) and relative controls: cell culture medium (CCM), and untreated hearts. The CCM-treated and untreated hearts showed evident thinning in the anterior wall of the left ventricle. *From Wang, L. et al. Am J Physiol Heart Circ Physiol 297: H1020-H1031 2009 [15] (with permission)*
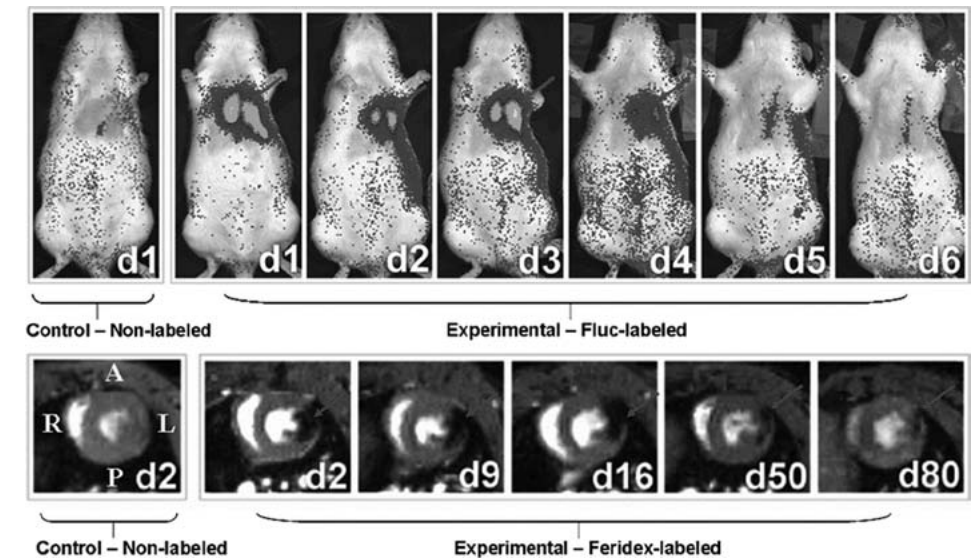
Figure 3. Longitudinal BLI and MRI of H9c2 cells after transplantation. BLI shows a robust distinct heart signal on day 1 (red arrow), compared to no discernable signal in a representative control rat having received non-labelled cells (top panel, left). The signal increases slightly on day 3 but decreases rapidly to near background levels by day 6.
MRI imaging of a representative rat injected with the same amount of cells labelled with Feridex shows a large hypointense signal (red arrow) in the anterolateral wall of the myocardium. The size of the signal decreases slightly over time, and the signal persists for at least 80 days post cell injection. No signal is observed in control rat that received non-labelled cells (bottom panel, left) *Chen, I. Y et al. Mol Imaging Biol. 2009 May-Jun;11(3):178-87. [42] (with permission).*

successfully engrafted SC and dead SC phagocytosed by macrophages within the heart. In particular, no differences in signal voids up to more than 40 days were observed with dead and viable cells recipient with respect to size, number and localisation [44]. Similarly, it has been demonstrated that MRI overestimates the SPIO labelled SC survival after transplantation in the heart [45]. Furthermore, SPIO-induced hypointensity can sometimes be difficult to interpret because it may be obscured by the presence of endogenous blood derivates, such as hemosiderin [46]. The clinical translation of SPIO for cell tracking is further reduced now that ferumoxides (Feridex® or Endorem®) are no longer available in the USA and Europe. However, the use of iron oxides approaches should not be discouraged as they provide very high sensitivities. New compounds with improved tissue clearance properties (therefore higher specificities) are awaited from material sciences research.

Paramagnetic Ions

Cell labelling with "positive contrast" such as gadolinium (Gd) chelates and manganese (Mn) chloride compounds allow the visualisation of SC as hyperintense signal on T1-weighted images. Internalization of Gd can be accomplished by exposure of cells to Gd chelates or through the use of liposomal formulations [33]. MRI sensitivity in the detection of Gd-labelled cells is lower compared to SPIO-labelled cells and is dependent upon contrast behaviour and relaxivity in the cellular compartment (endosomes) in which they are localised [47; 48]. This is a result of the reduced water accessibility to chelated ions following intracellular concentration, resulting in decreased relaxivity. To overcome these issues several approaches have been considered to drive the endosomal escape of paramagnetic compounds [49]. Furthermore, safety issues might be related to the rapid dechelation of compounds at the low pH of lysosomes and endosomes raising concerns related to free Gd^{3+} ions [50].

Sub-millimolar concentrations of Mn chloride ($MnCl_2$) have been sufficient to enable SC labelling and detection for both in vitro and in vivo MR, with no detectable toxicity. Also in the same study the potential of $MnCl_2$ labelling in the assessment of SC viability by T1 and T2 mapping was investigated in *in vitro* studies [51]. Mn-oxide nanoparticles have recently been used to label and track implanted glioma cells. Of considerable interest, the feasibility of successfully tracking two cell populations simultaneously has been suggested, where one is labelled with Mn-Oxide and the other with SPIOs [52]. These and other paramagnetic ion techniques offer the hope that positive contrast approaches will enable sensitive MR tracking of SC in vivo. Novel nanotechnology approaches are becoming available for stem cell tracking such as gadolinium-containing carbon nanocapsules (Gadonanotubes), whose T_1 relaxivity is greater than that of any known material to date (outperforming clinically available Gd-based contrast agents by 40-fold) [53]. They will definitely play a role in the future of imaging sciences as soon as their toxicity profiles, currently under investigation, have been clarified.

19F MR

Similar to the imaging of relaxation of ^1H from water, ^{19}F can be used as the basis of the signal for MR spectroscopy and image formation. While this technique is not implemented widely in the clinic, there are unique advantages to fluorine-MR that make it an attractive option for SC tracking in myocardial applications. ^{19}F is not present naturally in soft tissues therefore its signal is exclusively derived from the exogenous contrast agent applied, be it a perfluorocarbon particle or fluorinated nucleosides [54]. ^{19}F MRI can be used with existing ^1H imaging hardware since ^{19}F and ^1H gyromagnetic ratios differ by only 6%.

Importantly, ^{19}F signal can be overlaid on ^1H-MR anatomical images for a highly selective, high-resolution map of cell transplantation. This technique allows for quantitative determination of the cell population [55]. A perfluorocarbon particle loaded cell scheme has been used to show the unequivocal and unique signature for SC, enabling spatial cell localization via ^{19}F- MRI and quantitation via ^{19}F-spectroscopy [56]. Perfluorocarbons have been extensively studied and used as blood substitutes, therefore their toxicity profiles are known. ^{19}F cell tracking has attracted interest, but is still at an early stage of development. It should be noted that this method does suffer from the drawback of lower sensitivity requiring longer imaging times. Efforts are underway to address these deficits including imaging hardware, imaging sequences, and label improvement and ^{19}F MR imaging is expected to play a role in cell tracking in the future [54].

Radionuclide Imaging

Imaging of SC has also taken advantage of the high sensitivity ($10^{-10} – 10^{-12}$ mol/L vs $10^{-3} – 10^{-5}$ mol/L of MRI) and quantitative (acute cell retention as a percentage of the net injected dose per weight, [%ID/g]) characteristics of radionuclide imaging [57]. However, PET and particularly SPECT have inferior spatial resolution (1-2 mm) compared with MRI. Moreover, radionuclide-labelled cells can only be visualised as long as the radioactivity is still detectable (e.g. ^{18}F: 110 min; ^{111}In: 2.8 days; ^{99m}Tc: 6 hours). This sets an appreciable limitation on the radioisotopes direct labelling value for medium- and long-term SC transplant monitoring. SPECT has been largely used to investigate the short-term fate of transplanted cells labelled with radioactive compounds such as ^{111}In-oxine [58-63], ^{99m}Tc-hexamethylprophylene amine oxine (HMPAO) [64] or ^{111}In-tropolone [65; 66]. A persistent limitation for deployment of SPECT is that in order to generate useful (quantitative) images within a reasonable time frame, the administration of relatively large doses of radioactivity are required. This poses the concern of inherent radiation damage (reduced viability and proliferation). In the case of ^{111}In, Auger electrons are also emitted leading to adverse biological effects in very short distances (from the nm to μm range). Brenner *et al.,* demonstrated that despite the homing of progenitor cells into the infarction area, cell labelling with ^{111}In-oxine impairs significantly the viability, proliferation and differentiation at 48 h after implantation [63]. Similar results were observed after exposure of murine haematopoietic progenitor cells at even much

lower levels of radioactivity [67]. The use of other compounds, such as ^{111}In-tropolone, inhibited cell proliferation 3 days after labeling [68]. To abrogate these effects, it has been suggested that only a fraction of the SC population be labelled [69]. Regardless of the method used, very few studies have reported the absence of any cell function impairment [58; 62]. These studies underline the need for further in vitro studies considering different SC, exposed to different activities and importantly following the same labelling protocol.

Positron emission tomography (PET) has been regarded as having higher sensitivity (2 to 3 orders of magnitude) and better spatial and temporal resolution than SPECT [70]. ^{18}F-Fluorodeoxyglucose ([18]F –FDG) has been used for cell labelling and short term imaging in preclinical [71] and clinical settings (Fig. 4) [72; 73]. After intracoronary injection all stem cells showed poor engraftment regardless of cell type and number of implanted cells [61; 72; 73]. In all cases intravenous injection of SC did not show detectable homing of cells to the myocardium [72; 73].
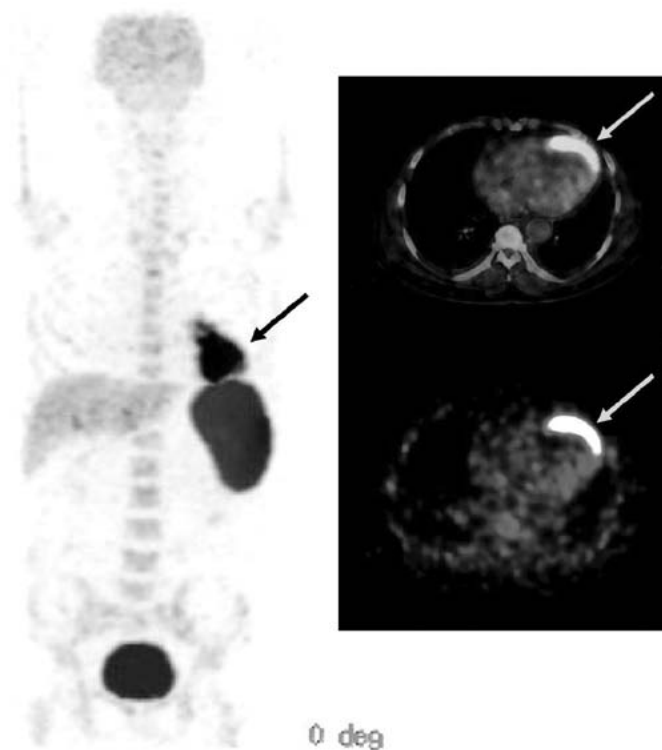

Figure 4. PET/CT images of a patient with hystory of anterior wall infarction. After percutaneous intervention 18F-FDG labelled cells were implanted via intracoronary catheter and images obtained at 2 hrs after the procedure. Total amount of SC at the injection site was measured (2.1% of injected dose). From *Kang et al. J Nucl Med 2006; 47:1295-1301.* [73] (with permission).

Augmenting the higher sensitivity, the wider availability of hybrid PET-CT systems allows for a combination of anatomical non-invasive coronary angiography and cell tracking. This multimodal imaging capability and clinical availability are tempered somewhat by the the short half life of [18]F. Isotopes with longer half life, such as [64]Cu

(12.7 hours) have been suggested [74]. However, with radionuclide based techniques pursued so far, only the immediate fate of transplanted stem cells can be interrogated.

Reporter genes

Reporter gene approaches have significant potential to reveal insights into the mechanisms and fate of SC therapies. The reporter gene paradigm requires often the appropriate combination of reporter transgene and a reporter probe, such that the reporter gene product has to interact with an imaging probe (optical, nuclear, magnetic) and when this event occurs the signal may be detected and quantified with the corresponding imaging technique (Fig. 1c).

Several advantages of reporter gene approaches have been described [75]. Namely, this system identifies with exquisite specificity only viable cells (which actively contain the gene product) and allows long term tracking of transduced SC (circumventing issues of probe dilution with cellular proliferation). Reporter genes can be designed as "constitutive" whose signal is "always turned on" (suitable for the evaluation of transplantation, migration and proliferation of stably transduced SC) or "inducible" reporter gene which is activated and regulated by specific endogenous transcription factors and promoters [75; 76] providing a non-invasive readout of information regarding SC differentiation.

The most widely used reporter gene for radiotracer based imaging is HSV1-*tk* (Herpes simplex virus type 1 thymidine kinase) and its mutant, the HSV1-sr39tk. Unlike mammalian TK1, this enzyme efficiently phosphorylates purine and pyrimidine analogues which results in trapping and accumulation of these ligands. It has been successfully used in association with ^{18}F or [124]I -2'-deoxy-2'-fluoro-5-iodo-1-[β]-D-arabinofuranosyluracil (^{18}F-FIAU and [124]I-FIAU), [18]F 2'-fluoro-5-ethyl-1-[β]-D-arabinofuranosyluracil (^{18}F-FEAU), and 9-(4-[^{18}F]fluoro-3-hydroxymethylbutyl)guanine (^{18}F-FHBG) [75; 77].

Wu *et al.,* pioneered the reporter gene approach in the heart by imaging *in vivo* transplanted cells (expressing luciferase or HSV1-sr39tk) up to 2 weeks by ^{18}F-FHBG PET imaging or BLI [78]. Furthermore, Cao *et al.,* reported survival and proliferation (through increasing signal up to 4 weeks) of murine ES stably transduced with a triple fusion reporter gene, enabling simultaneous PET, bioluminescence and fluorescence imaging [79].

Despite the advantage of signal amplification (through probe phosphorylation and accumulation within cells) of HSV-*tk* based approaches, its immunogenicity might limit use in humans [80]. To overcome this limitation, the human mitochondrial thymidine kinase type 2 (hTK2) have been proposed [81]. An alternative is the sodium iodide symporter [51] as a PET and SPECT reporter gene used in conjunction with [124]I or [99m]Tc (pertechnetate), respectively [75; 82]. Here, despite the lack of probe/signal amplification observed in receptor- and transporter-based techniques (as [124]I or ^{99m}Tc are

free to diffuse out of the cells), hNIS is not immunogenic (since it is expressed in the thyroid, stomach salivary gland, choroid plexus but not in the heart) and does not require complex radiosynthesis of the probes. Nevertheless, in reporter gene approach for the imaging of SC-based cardiac therapy several important issues remain. First, the non-physiological expression of reporter gene proteins may perturb the critical SC cellular and therapeutic functions. To be fully reliable, this system has to guarantee the long term expression of the reporter gene in the proliferating population. Adenoviral transfection is hampered by episomal gene expression (the reporter gene is not integrated in the chromatin, and because they are not replicating, they become diluted with cell proliferation) and by immunogenicity (leakiness of immunogenic adenoviral proteins that can lead to an immune response) [83]. On the other hand, lentiviral vectors accomplish the integration of the reporter gene in the host cell chromatin allowing stable expression in dividing cells [84] and circumventing immunogenicity [85]. Even when lentiviral vectors are used however, transgene expression can be silenced by DNA methylation especially when strong promoters, such as CMV, are used to drive the expression of the reporter gene [86]. The integration of the reporter gene within the genome has raised concerns about the risk of mutagenesis and potential oncogenicity [87].

The imaging of differentiation in vivo was recently investigated by Kammili *et al.,* by employing a novel dual-reporter mouse embryonic SC line. Here, enhanced yellow fluorescent protein (EYFP) was used as a "constitutive reporter", and the firefly luciferase reporter as an "inducible reporter". This latter gene was under the control of the cardiac sodium-calcium exchanger 1 (Ncx1) promoter which showed increased activity upon differentiation of SC into beating cardiomyocytes [76].

Several candidates have been proposed as MRI reporter genes such as β-galactosidase, transferrin receptor, ferritin, MagA and lysine-rich proteins [88; 89]. Recently, SM engineered to express ferritin have been transplanted in infarcted heart and detected (as decreased signal up to 25%) up to 3 weeks [90]. Several studies have been reported with the application of MR reporters, however, none of these strategies have led to a significant number of follow-up studies. This is due to the low sensitivity of MRI for imaging of gene activity in vivo.

Optical imaging
BLI

In contrast to the immediate clinical impact of magnetic and nuclear tomographic imaging, optical imaging techniques such as bioluminescence, planar and fluorescence-mediated tomography have been largely restricted to use in preclinical models. Bioluminescence imaging is commonly used for cell tracking in SC transplantation studies [78; 79; 91] (Figs. 3 and 5). SC are transduced with a luciferase gene and implanted in the recipient animal. Following injection, the probe (D-Luciferin) is oxidized only in the cells expressing luciferase in presence of ATP, O_2 and Mg^{2+} resulting in light photons being
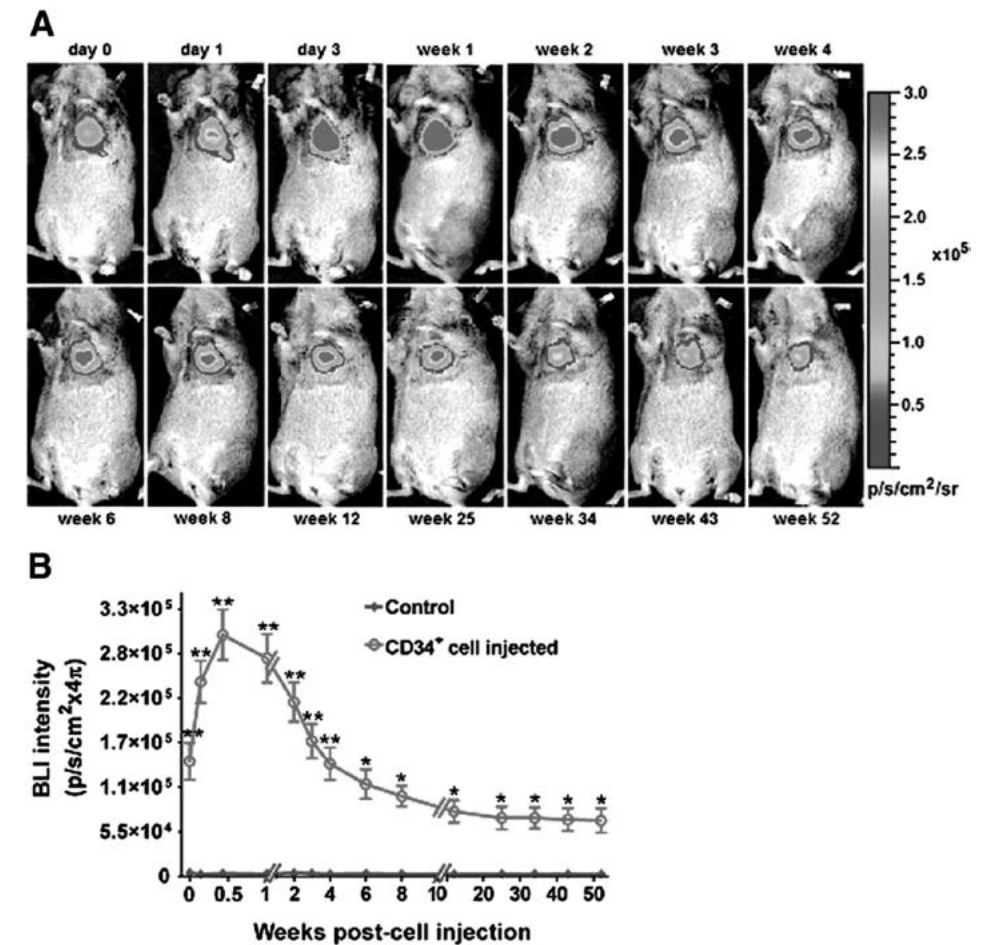
Figure 5. Bioluminescence imaging of CD34+ cells expressing the TGL gene (HSV1-*tk*, e-GFP, f-luc) and implanted in the heart of a SCID mouse. Systemically administered luciferin is activated (oxidized by luciferase) in the injected cells. Here we see follow-up of implanted cells up to 52 weeks post-implantation. Measurement of emitted light in CD34+ implants is higher than in controls (PBS injection). *From Wang, J. et al. Circ Res 2010;106:1904-1911. [91] (with permission).*

emitted (which can be detected by ultrasensitive charge-coupled device [CCD] cameras). BLI has many advantages: it is highly sensitive, quantitative, simple and inexpensive. However, the barrier to clinical translation lies in the inherent limitations imposed by poor tissue penetration (1-2cm) (allowing only surface imaging), high rates of scattering of visible wavelength photons on the human scale and low resolution (3-5mm) (which hamper the exact evaluation of the exact location of the cells) [57].

Fluorescence

Direct labelling of SC with fluorescent probes for visualisation *in vitro* and *in vivo* has been fueled by the availability of near infrared (NIR) probes, as their spectral properties are matched to lower tissue attenuation in the so-called NIR-window. This provides greater signal penetration of tissue through reduced light absorption and tissue scattering. Therefore they have clinical potential, however limited to near-surface or intraoperative imaging stem cell tracking.

Near infrared imaging provides high sensitivity as well as tomographic capabilities and there is no evidence at present that dyes released after cell death are taken up by macrophages. Intracoronary delivery of MSC labelled with the NIR dye IR-786 has been successfully tracked in a swine model of myocardial infarction and sensitivity of 10.000 cells has been reported [92].

Quantum dots (QD) are a class of inorganic, fluorescent nanoparticles that have been successfully used to label SC. Biocompatibility of QD at low concentrations has been demonstrated in vitro in MSC cultures [93] and the absence of adverse effects on cell viability, proliferation or differentiation reported [94]. One of the most attractive qualities of these nanoparticles is their capacity for multiplexed imaging. The tracking of different cell populations is concurrently achieved by labelling cells with different QDs. Multiplex optical imaging of QD-labelled embryonic stem cells have been reported up to 14 days from injection in mice [94]. Moreover, it has been shown that single QD-MSC can be detected in histological sections for at least 8 weeks after delivery [95]. The long-term effects on SC functionality are still unknown, however concerns are related to their metallic core include its exposure or dissolution which may result in toxicity, particularly from heavy metals such as Pb, Cd and Se [96; 97]

Multimodal imaging

The possibility of complementing the sensitivity of radionuclide or optical techniques with the high-resolution anatomical information from MRI is a key player in the clinical and research future of SC tracking. To date, the most interesting approach has been to develop transgenic cells that carry an optical/nuclear imaging reporter together with passive labelling with MRI contrast agents before administration. Qiao *et al.* assessed the survival and proliferation of SPIO-labelled murine ESC transduced with HSV1-sr39tk longitudinally (4 weeks) following injection into the healthy or infarcted myocardium. ESCs grafted and underwent proliferation, as shown by increasing uptake of ^{18}F-FHBG in PET (Fig. 6) and decreasing the size of MR hypointense areas due to SPIO dilution. Interestingly at week 4 the majority of SPIO labels (released upon cell death) were phagocytized and contained in infiltrating macrophages rather than the ESC. Despite teratoma formation, a slight increase in left ventricular ejection fraction in ESC-treated animals was observed, mainly as a result of paracrine effects, as cardiac differentiation of implanted ESC was less than 0.5% [98]. In a similar study human EPC derived from CD34+ mononuclear cells of umbilical cord blood were transduced with NIS reporter
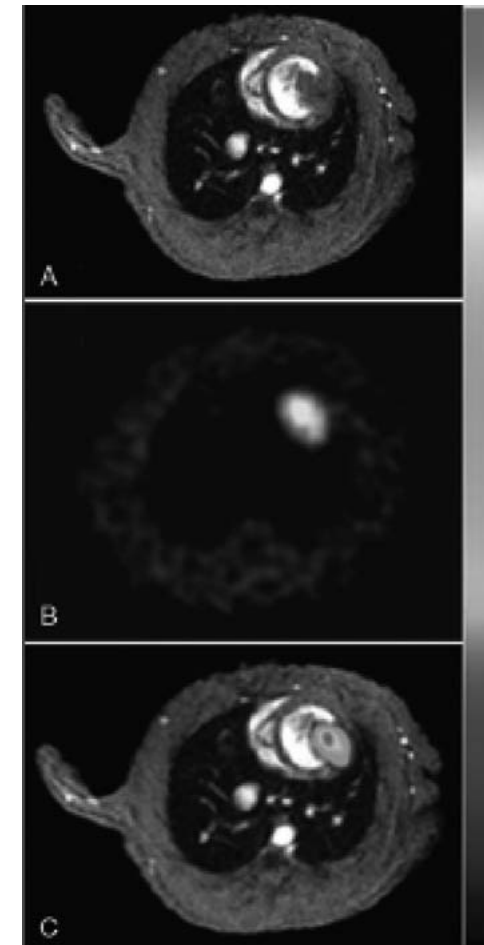
Figure 6. Co-registration of MRI (A) and ^{18}F-FHBG PET (B) of murine ESC transduced with HSV1-*sr39tk* and passively labelled with SPIO. Images depict the presence and tracking of SC 14 days after transplantation. This hybrid imaging (C) approach leverages the advantages of each technique; the fine anatomical resolution of MR and the specificity of nuclear imaging. *From Qiao et al Radiology 250:3, 821-829. [98] (with permission).*

gene and labelled with SPIOs. Rapid loss of viable grafted cells was observed, as ^{124}I PET accumulation decreased below detection limit at 3 days after transplant. However, MRI signal void resulting from SPIO persisted, corresponding to retention of SPIOs within macrophages after graft cells' death (Fig. 7) [99]. Triple fusion reporter gene have been widely applied for multimodality fluorescence, bioluminescence and nuclear imaging approaches [100]. Recently, in a quad-modal optical, PET, CT and MRI coregistration approach CD34+ cells were transduced with a triple fusion reporter gene (e-GFP, f-Luc and HSV1-*tk*). Bioluminescence imaging revealed that cells persisted in the heart up to 12 months and MRI studies reported improvement in the left ventricular ejection fraction was preserved up to 6 months (Fig. 5) [91].

Figure 7. (A) MRI (upper row), [124]I-PET (middle row), and fusion images ^{13}N-NH$_3$ (gray scale)/ [124]I (colour scale) (bottom row) of rat heart 1 day after injection of EPC labelled with iron (left), NIS only (middle), or both iron and NIS (right). Signal void of iron-labeled HEPCs is observed by MRI whereas HEPCs expressing NIS showed focal [124]I accumulation by PET.
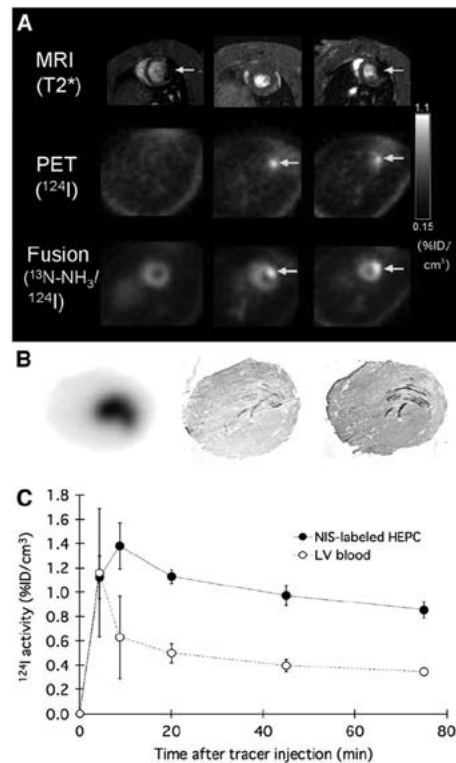(B) Consecutive myocardial sections showing the presence of transplanted cells: autoradiography for [124]I uptake mediated by NIS reporter (left), X-galactosidase staining for LacZ gene expression of graft cells (middle), and Prussian blue staining for iron particle detection (right). (C) Mean±SD time–activity curves after [124]I administration of transplanted cell and left ventricular blood measured by PET. From *Higuchi T et al J Nucl Med, 50(7):1088-1094.* [99] (with *permission*)

Conclusion

Many of the approaches to image stem cells are promising but further work is required before a wide clinical translation becomes reality. Beyond the unresolved safety and ethical issues, crucial questions: "What is the best route for cell delivery ?" "What kind and how many cells ?" and "When to inject ?" remain.

It has become clear that there is no single 'best method' in cell tracking. Rather there is an array of high sensitivity, high spatial resolution and functional techniques that work best in combination. The persistent trends in molecular imaging are: to focus on the development of novel MR-compatible probes able to monitor and track with sufficient sensitivity and specificity the fate of transplanted cells, new PET/SPECT reporter genes with lessened immunogenicity and oncogenicity issues, and the application of related radioprobes with better pharmacokinetic profiles.

References

1   Orlic D, Kajstura J, Chimenti S, et al. (2001) Bone marrow cells regenerate infarcted myocardium. Nature, 410(6829):701-705.

2   Strauer BE, Brehm M, Zeus T, et al. (2002) Repair of infarcted myocardium by autologous intracoronary mononuclear bone marrow cell transplantation in humans. Circulation, 106(15):1913-1918.

3   Abdel-Latif A, Bolli R, Tleyjeh IM, et al. (2007) Adult bone marrow-derived cells for cardiac repair: a systematic review and meta-analysis. Arch Intern Med, 167(10):989-997.

4   Lipinski MJ, Biondi-Zoccai GG, Abbate A, et al. (2007) Impact of intracoronary cell therapy on left ventricular function in the setting of acute myocardial infarction: a collaborative systematic review and meta-analysis of controlled clinical trials. J Am Coll Cardiol, 50(18):1761-1767. doi: S0735-1097(07)02495-3 [pii] 10.1016/j.jacc.2007.07.041

5   Martin-Rendon E, Brunskill SJ, Hyde CJ, Stanworth SJ, Mathur A, Watt SM (2008) Autologous bone marrow stem cells to treat acute myocardial infarction: a systematic review. Eur Heart J, 29(15):1807-1818. doi: ehn220 [pii] 10.1093/eurheartj/ehn220

6   Korf-Klingebiel M, Kempf T, Sauer T, et al. (2008) Bone marrow cells are a rich source of growth factors and cytokines: implications for cell therapy trials after myocardial infarction. Eur Heart J, 29(23):2851-2858. doi: ehn456 [pii] 10.1093/eurheartj/ehn456

7   Taylor DA, Atkins BZ, Hungspreugs P, et al. (1998) Regenerating functional myocardium: improved performance after skeletal myoblast transplantation. Nat Med, 4(8):929-933.

8   Menasche P, Alfieri O, Janssens S, et al. (2008) The Myoblast Autologous Grafting in Ischemic Cardiomyopathy (MAGIC) trial: first randomized placebo-controlled study of myoblast transplantation. Circulation, 117(9):1189-1200. doi: CIRCULATIONAHA.107.734103 [pii] 10.1161/CIRCULATIONAHA.107.734103

9   Yoon YS, Wecker A, Heyd L, et al. (2005) Clonally expanded novel multipotent stem cells from human bone marrow regenerate myocardium after myocardial infarction. J Clin Invest, 115(2):326-338. doi: 10.1172/JCI22326

10 Balsam LB, Wagers AJ, Christensen JL, Kofidis T, Weissman IL, Robbins RC (2004) Haematopoietic stem cells adopt mature haematopoietic fates in ischaemic myocardium. Nature, 428(6983):668-673. doi: 10.1038/nature02460 nature02460 [pii]

11 Murry CE, Soonpaa MH, Reinecke H, et al. (2004) Haematopoietic stem cells do not transdifferentiate into cardiac myocytes in myocardial infarcts. Nature, 428(6983):664-668. doi: 10.1038/nature02446 nature02446 [pii]

12   Ferrari G, Cusella-De Angelis G, Coletta M, et al. (1998) Muscle regeneration by bone marrow-derived myogenic progenitors. Science, 279(5356):1528-1530.

13   Quevedo HC, Hatzistergos KE, Oskouei BN, et al. (2009) Allogeneic mesenchymal stem cells restore cardiac function in chronic ischemic cardiomyopathy via trilineage differentiating capacity. Proc Natl Acad Sci U S A, 106(33):14022-14027. doi: 0903201106 [pii] 10.1073/pnas.0903201106

14   Polascik TJ, Manyak MJ, Haseman MK, et al. (1999) Comparison of clinical staging algorithms and 111indium-capromab pendetide immunoscintigraphy in the prediction of lymph node involvement in high risk prostate carcinoma patients. Cancer, 85(7):1586-1592. doi: 10.1002/(SICI)1097-0142(19990401)85:7<1586::AID-CNCR21>3.0.CO;2-F [pii]

15   Wang L, Deng J, Tian W, et al. (2009) Adipose-derived stem cells are an effective cell candidate for treatment of heart failure: an MR imaging study of rat hearts. Am J Physiol Heart Circ Physiol, 297(3):H1020-1031. doi: 01082.2008 [pii] 10.1152/ajpheart.01082.2008

16   Schachinger V, Assmus B, Britten MB, et al. (2004) Transplantation of progenitor cells and regeneration enhancement in acute myocardial infarction: final one-year results of the TOPCARE-AMI Trial. J Am Coll Cardiol, 44(8):1690-1699. doi: S0735-1097(04)01629-8 [pii] 10.1016/j.jacc.2004.08.014

17   Beltrami AP, Barlucchi L, Torella D, et al. (2003) Adult cardiac stem cells are multipotent and support myocardial regeneration. Cell, 114(6):763-776. doi: S0092867403006871 [pii]

18   Dawn B, Stein AB, Urbanek K, et al. (2005) Cardiac stem cells delivered intravascularly traverse the vessel barrier, regenerate infarcted myocardium, and improve cardiac function. Proc Natl Acad Sci U S A, 102(10):3766-3771. doi: 0405957102 [pii] 10.1073/pnas.0405957102

19   Laflamme MA, Chen KY, Naumova AV, et al. (2007) Cardiomyocytes derived from human embryonic stem cells in pro-survival factors enhance function of infarcted rat hearts. Nat Biotechnol, 25(9):1015-1024. doi: nbt1327 [pii] 10.1038/nbt1327

20   Li Z, Wu JC, Sheikh AY, et al. (2007) Differentiation, survival, and function of embryonic stem cell derived endothelial cells for ischemic heart disease. Circulation, 116(11 Suppl):I46-54. doi: 116/11_suppl/I-46 [pii] 10.1161/CIRCULATIONAHA.106.680561

21   Swijnenburg RJ, Schrepfer S, Cao F, et al. (2008) In vivo imaging of embryonic stem cells reveals patterns of survival and immune rejection following transplantation. Stem Cells Dev, 17(6):1023-1029. doi: 10.1089/scd.2008.0091

22   Nussbaum J, Minami E, Laflamme MA, et al. (2007) Transplantation of undifferentiated murine embryonic stem cells in the heart: teratoma formation and immune response. FASEB J, 21(7):1345-1357. doi: fj.06-6769com [pii] 10.1096/fj.06-6769com

23   Yu J, Vodyanik MA, Smuga-Otto K, et al. (2007) Induced pluripotent stem cell lines derived from human somatic cells. Science, 318(5858):1917-1920. doi: 1151526 [pii] 10.1126/science.1151526

24   Zwi L, Caspi O, Arbel G, et al. (2009) Cardiomyocyte differentiation of human induced pluripotent stem cells. Circulation, 120(15):1513-1523. doi: CIRCULATIONAHA.109.868885 [pii] 10.1161/CIRCULATIONAHA.109.868885

25   Nelson TJ, Martinez-Fernandez A, Yamada S, Perez-Terzic C, Ikeda Y, Terzic A (2009) Repair of acute myocardial infarction by human stemness factors induced pluripotent stem cells. Circulation, 120(5):408-416. doi: CIRCULATIONAHA.109.865154 [pii] 10.1161/CIRCULATIONAHA.109.865154

26   Kocher AA, Schuster MD, Szabolcs MJ, et al. (2001) Neovascularization of ischemic myocardium by human bone-marrow-derived angioblasts prevents cardiomyocyte apoptosis, reduces remodeling and improves cardiac function. Nat Med, 7(4):430-436. doi: 10.1038/86498 86498 [pii]

27   Karamitsos TD, Francis JM, Myerson S, Selvanayagam JB, Neubauer S (2009) The role of cardiovascular magnetic resonance imaging in heart failure. J Am Coll Cardiol, 54(15):1407-1424. doi: S0735-1097(09)02372-9 [pii] 10.1016/j.jacc.2009.04.094

28   Chen IY, Wu JC Cardiovascular molecular imaging: focus on clinical translation. Circulation, 123(4):425-443. doi: 123/4/425 [pii] 10.1161/CIRCULATIONAHA.109.916338

29   Kiessling F (2008) Noninvasive cell tracking. Handb Exp Pharmacol(185 Pt 2):305-321. doi: 10.1007/978-3-540-77496-9_13

30   Semelka RC, Helmberger TK (2001) Contrast agents for MR imaging of the liver. Radiology, 218(1):27-38.

31   Harisinghani MG, Barentsz J, Hahn PF, et al. (2003) Noninvasive detection of clinically occult lymph-node metastases in prostate cancer. N Engl J Med, 348(25):2491-2499. doi: 10.1056/NEJMoa022749 348/25/2491 [pii]

32   Thorek DLJ, Tsourkas A (2008) Size, charge and concentration dependent uptake of iron oxide particles by non-phagocytic cells. Biomaterials, 29(26):3583-3590.

33   Bernsen MR, Moelker AD, Wielopolski PA, van Tiel ST, Krestin GP Labelling of mammalian cells for visualisation by MRI. Eur Radiol, 20(2):255-274. doi: 10.1007/s00330-009-1540-1

34   Arbab AS, Pandit SD, Anderson SA, et al. (2006) Magnetic resonance imaging and confocal microscopy studies of magnetically labeled endothelial progenitor cells trafficking to sites of tumor angiogenesis. Stem Cells, 24(3):671-678. doi: 2005-0017 [pii] 10.1634/stemcells.2005-0017

35   Hsiao JK, Chu HH, Wang YH, et al. (2008) Macrophage physiological function after superparamagnetic iron oxide labeling. NMR Biomed, 21(8):820-829. doi: 10.1002/nbm.1260

36   Delcroix GJ, Jacquart M, Lemaire L, et al. (2009) Mesenchymal and neural stem cells labeled with HEDP-coated SPIO nanoparticles: in vitro characterization and migration potential in rat brain. Brain Res, 1255:18-31. doi: S0006-8993(08)02907-7 [pii] 10.1016/j.brainres.2008.12.013

37   Farrell E, Wielopolski P, Pavljasevic P, et al. (2009) Cell labelling with superparamagnetic iron oxide has no effect on chondrocyte behaviour. Osteoarthritis and Cartilage, 17(7):961-967.

38   Magnitsky S, Walton RM, Wolfe JH, Poptani H (2008) Magnetic resonance imaging detects differences in migration between primary and immortalized neural stem cells. Acad Radiol, 15(10):1269-1281. doi: S1076-6332(08)00278-X [pii] 10.1016/j.acra.2008.05.003

39   Schafer R, Kehlbach R, Muller M, et al. (2009) Labeling of human mesenchymal stromal cells with superparamagnetic iron oxide leads to a decrease in migration capacity and colony formation ability. Cytotherapy, 11(1):68-78. doi: 908442636 [pii] 10.1080/14653240802666043

40   Yang J-X, Tang W-L, Wang X-X (2010) Superparamagnetic iron oxide nanoparticles may affect endothelial progenitor cell migration ability and adhesion capacity. Cytotherapy, 12:251-259.

41   Kostura L, Kraitchman DL, Mackay AM, Pittenger MF, Bulte JWM (2004) Feridex labeling of mesenchymal stem cells inhibits chondrogenesis but not adipogenesis or osteogenesis. NMR in Biomedicine, 17(7):513-517.

42   Chen I, Greve J, Gheysens O, et al. (2009) Comparison of Optical Bioluminescence Reporter Gene and Superparamagnetic Iron Oxide MR Contrast Agent as Cell Markers for Noninvasive Imaging of Cardiac Cell Transplantation. Molecular Imaging and Biology, 11(3):178-187.

43   Amsalem Y, Mardor Y, Feinberg MS, et al. (2007) Iron-Oxide Labeling and Outcome of Transplanted Mesenchymal Stem Cells in the Infarcted Myocardium. Circulation, 116(11_suppl):I-38-45. doi: 10.1161/circulationaha.106.680231

44   Winter EM, Hogers B, van der Graaf LM, Gittenberger-de Groot AC, Poelmann RE, van der Weerd L Cell tracking using iron oxide fails to distinguish dead from living transplanted cells in the infarcted heart. Magn Reson Med, 63(3):817-821. doi: 10.1002/mrm.22094

45   Terrovitis J, Stuber M, Youssef A, et al. (2008) Magnetic resonance imaging overestimates ferumoxide-labeled stem cell survival after transplantation in the heart. Circulation, 117(12):1555-1562. doi: CIRCULATIONAHA.107.732073 [pii] 10.1161/CIRCULATIONAHA.107.732073

46   van den Bos EJ, Baks T, Moelker AD, et al. (2006) Magnetic resonance imaging of haemorrhage within reperfused myocardial infarcts: possible interference with iron oxide-labelled cell tracking? Eur Heart J, 27(13):1620-1626. doi: ehl059 [pii] 10.1093/eurheartj/ehl059

47   Brekke C, Morgan SC, Lowe AS, et al. (2007) The in vitro effects of a bimodal contrast agent on cellular functions and relaxometry. NMR Biomed, 20(2):77-89. doi: 10.1002/nbm.1077

48   Aime S, Castelli DD, Crich SG, Gianolio E, Terreno E (2009) Pushing the sensitivity envelope of lanthanide-based magnetic resonance imaging (MRI) contrast agents for molecular imaging applications. Acc Chem Res, 42(7):822-831. doi: 10.1021/ar800192p

49   Gianolio E, Arena F, Strijkers GJ, Nicolay K, Hogset A, Aime S Photochemical activation of endosomal escape of MRI-Gd-agents in tumor cells. Magn Reson Med. doi: 10.1002/mrm.22586

50   Bulte JW (2009) In vivo MRI cell tracking: clinical studies. AJR Am J Roentgenol, 193(2):314-325. doi: 193/2/314 [pii] 10.2214/AJR.09.3107

51   Yamada M, Gurney PT, Chung J, et al. (2009) Manganese-guided cellular MRI of human embryonic stem cell and human bone marrow stromal cell viability. Magnetic Resonance in Medicine, 62(4):1047-1054.

52   Gilad AA, Walczak P, McMahon MT, et al. (2008) MR tracking of transplanted cells with "positive contrast" using manganese oxide nanoparticles. Magn Reson Med, 60(1):1-7.

53   Tran LA, Krishnamurthy R, Muthupillai R, et al. Gadonanotubes as magnetic nanolabels for stem cell detection. Biomaterials, 31(36):9482-9491.

54   Srinivas M, Heerschap A, Ahrens ET, Figdor CG, de Vries IJ (19) F MRI for quantitative in vivo cell tracking. Trends Biotechnol, 28(7):363-370. doi: S0167-7799(10)00057-0 [pii] 10.1016/j.tibtech.2010.04.002

55   Srinivas M, Morel PA, Ernst LA, Laidlaw DH, Ahrens ET (2007) Fluorine-19 MRI for visualization and quantification of cell migration in a diabetes model. Magnetic Resonance in Medicine, 58(4):725-734.

56   Partlow KC, Chen J, Brant JA, et al. (2007) 19F magnetic resonance imaging for stem/progenitor cell tracking with multiple unique perfluorocarbon nanobeacons. FASEB J, 21(8):1647-1654. doi: fj.06-6505com [pii] 10.1096/fj.06-6505com

57   Massoud TF, Gambhir SS (2003) Molecular imaging in living
      subjects: seeing fundamental biological processes in a new light.
      Genes Dev, 17(5):545-580. doi: 10.1101/gad.1047403

58   Aicher A, Brenner W, Zuhayra M, et al. (2003) Assessment
      of the tissue distribution of transplanted human endothelial
      progenitor cells by radioactive labeling. Circulation, 107(16):2134-
      2139. doi: 10.1161/01.CIR.0000062649.63838.C9
      01.CIR.0000062649.63838.C9 [pii]

59   Barbash IM, Chouraqui P, Baron J, et al. (2003) Systemic delivery
      of bone marrow-derived mesenchymal stem cells to the infarcted
      myocardium: feasibility, cell migration, and body distribution. Circulation,
      108(7):863-868. doi: 10.1161/01.CIR.0000084828.50310.6A
      01.CIR.0000084828.50310.6A [pii]

60   Hou D, Youssef EA, Brinton TJ, et al. (2005) Radiolabeled cell
      distribution after intramyocardial, intracoronary, and interstitial
      retrograde coronary venous delivery: implications for current clinical trials.
      Circulation, 112(9 Suppl):I150-156. doi: 112/9_suppl/I-150 [pii]
      10.1161/CIRCULATIONAHA.104.526749

61   Schachinger V, Aicher A, Dobert N, et al. (2008) Pilot trial on determinants of
      progenitor cell recruitment to the infarcted human myocardium. Circulation,
      118(14):1425-1432. doi: CIRCULATIONAHA.108.777102 [pii]
      10.1161/CIRCULATIONAHA.108.777102

62   Chin BB, Nakamoto Y, Bulte JW, Pittenger MF, Wahl R, Kraitchman
      DL (2003) 111In oxine labelled mesenchymal stem cell SPECT after
      intravenous administration in myocardial infarction. Nucl Med Commun,
      24(11):1149-1154. doi: 10.1097/01.mnm.0000101606.64255.03

63   Brenner W, Aicher A, Eckey T, et al. (2004) 111In-labeled CD34+ hematopoietic
      progenitor cells in a rat myocardial infarction model. J Nucl Med, 45(3):512-518.

64   Penicka M, Lang O, Widimsky P, et al. (2007) One-day kinetics of
      myocardial engraftment after intracoronary injection of bone marrow
      mononuclear cells in patients with acute and chronic myocardial
      infarction. Heart, 93(7):837-841. doi: hrt.2006.091934 [pii]
      10.1136/hrt.2006.091934

65   Blackwood KJ, Lewden B, Wells RG, et al. (2009) In vivo SPECT quantification
      of transplanted cell survival after engraftment using (111)In-tropolone in
      infarcted canine myocardium. J Nucl Med, 50(6):927-935. doi: 50/6/927 [pii]
      10.2967/jnumed.108.058966

66   Mitchell AJ, Sabondjian E, Sykes J, et al. Comparison of initial cell
      retention and clearance kinetics after subendocardial or subepicardial
      injections of endothelial progenitor cells in a canine myocardial infarction
      model. J Nucl Med, 51(3):413-417. doi: jnumed.109.069732 [pii]
      10.2967/jnumed.109.069732

67   Nowak B, Weber C, Schober A, et al. (2007) Indium-111 oxine labelling
      affects the cellular integrity of haematopoietic progenitor cells. Eur J Nucl
      Med Mol Imaging, 34(5):715-721. doi: 10.1007/s00259-006-0275-3

68   Yoon JK, Park BN, Shim WY, Shin JY, Lee G, Ahn YH In vivo tracking of
      111In-labeled bone marrow mesenchymal stem cells in acute brain trauma
      model. Nucl Med Biol, 37(3):381-388. doi: S0969-8051(09)00290-X [pii]
      10.1016/j.nucmedbio.2009.12.001

69   Gholamrezanezhad A, Mirpour S, Ardekani JM, et al. (2009) Cytotoxicity of
      111In-oxine on mesenchymal stem cells: a time-dependent adverse effect. Nucl
      Med Commun, 30(3):210-216. doi: 10.1097/MNM.0b013e328318b328

70   Rahmim A, Zaidi H (2008) PET versus SPECT: strengths,
      limitations and challenges. Nucl Med Commun, 29(3):193-
      207. doi: 10.1097/MNM.0b013e3282f3a515
      00006231-200803000-00002 [pii]

71   Doyle B, Kemp BJ, Chareonthaitawee P, et al. (2007) Dynamic tracking during
      intracoronary injection of 18F-FDG-labeled progenitor cell therapy for acute
      myocardial infarction. J Nucl Med, 48(10):1708-1714. doi: 48/10/1708 [pii]
      10.2967/jnumed.107.042838

72   Hofmann M, Wollert KC, Meyer GP, et al. (2005) Monitoring of bone
      marrow cell homing into the infarcted human myocardium. Circulation,
      111(17):2198-2202. doi: 01.CIR.0000163546.27639.AA [pii]
      10.1161/01.CIR.0000163546.27639.AA

73   Kang WJ, Kang HJ, Kim HS, Chung JK, Lee MC, Lee DS (2006)
      Tissue distribution of 18F-FDG-labeled peripheral hematopoietic stem
      cells after intracoronary administration in patients with myocardial
      infarction. J Nucl Med, 47(8):1295-1301. doi: 47/8/1295 [pii]

74   Adonai N, Nguyen KN, Walsh J, et al. (2002) Ex vivo cell labeling with
      64Cu-pyruvaldehyde-bis(N4-methylthiosemicarbazone) for imaging
      cell trafficking in mice with positron-emission tomography. Proc Natl
      Acad Sci U S A, 99(5):3030-3035. doi: 10.1073/pnas.052709599
      052709599 [pii]

75   Serganova I, Mayer-Kukuck P, Huang R, Blasberg R (2008) Molecular
      imaging: reporter gene imaging. Handb Exp Pharmacol(185
      Pt 2):167-223. doi: 10.1007/978-3-540-77496-9_8

76   Kammili RK, Taylor DG, Xia J, et al. Generation of novel reporter stem cells and
      their application for non-invasive molecular imaging of cardiac-differentiated
      stem cells *in vivo*. Stem Cells Dev. doi: 10.1089/scd.2009.0308

77   Ruggiero A, Brader P, Serganova I, et al. Different strategies for reducing
      intestinal background radioactivity associated with imaging HSV1-tk expression
      using established radionucleoside probes. Mol Imaging, 9(1):47-58.

78　Wu JC, Chen IY, Sundaresan G, et al. (2003) Molecular imaging of cardiac cell transplantation in living animals using optical bioluminescence and positron emission tomography. Circulation, 108(11):1302-1305. doi: 10.1161/01.CIR.0000091252.20010.6E 01.CIR.0000091252.20010.6E [pii]

79　Cao F, Lin S, Xie X, et al. (2006) In vivo visualization of embryonic stem cell survival, proliferation, and migration after cardiac delivery. Circulation, 113(7):1005-1014. doi: CIRCULATIONAHA.105.588954 [pii] 10.1161/CIRCULATIONAHA.105.588954

80　Berger C, Flowers ME, Warren EH, Riddell SR (2006) Analysis of transgene-specific immune responses that limit the in vivo persistence of adoptively transferred HSV-TK-modified donor T cells after allogeneic hematopoietic cell transplantation. Blood, 107(6):2294-2302. doi: 2005-08-3503 [pii] 10.1182/blood-2005-08-3503

81　Ponomarev V, Doubrovin M, Shavrin A, et al. (2007) A human-derived reporter gene for noninvasive imaging in humans: mitochondrial thymidine kinase type 2. J Nucl Med, 48(5):819-826. doi: jnumed.106.036962 [pii] 10.2967/jnumed.106.036962

82　Terrovitis J, Kwok KF, Lautamaki R, et al. (2008) Ectopic expression of the sodium-iodide symporter enables imaging of transplanted cardiac stem cells in vivo by single-photon emission computed tomography or positron emission tomography. J Am Coll Cardiol, 52(20):1652-1660. doi: S0735-1097(08)02880-5 [pii] 10.1016/j.jacc.2008.06.051

83　Gray SJ, Samulski RJ (2008) Optimizing gene delivery vectors for the treatment of heart disease. Expert Opin Biol Ther, 8(7):911-922. doi: 10.1517/14712598.8.7.911

84　Ma Y, Ramezani A, Lewis R, Hawley RG, Thomson JA (2003) High-level sustained transgene expression in human embryonic stem cells using lentiviral vectors. Stem Cells, 21(1):111-117. doi: 10.1634/stemcells.21-1-111

85　Toelen J, Deroose CM, Gijsbers R, et al. (2007) Fetal gene transfer with lentiviral vectors: long-term in vivo follow-up evaluation in a rat model. Am J Obstet Gynecol, 196(4):352 e351-356. doi: S0002-9378(07)00151-2 [pii] 10.1016/j.ajog.2007.01.038

86　Krishnan M, Park JM, Cao F, et al. (2006) Effects of epigenetic modulation on reporter gene expression: implications for stem cell imaging. FASEB J, 20(1):106-108. doi: 05-4551fje [pii] 10.1096/fj.05-4551fje

87　Mikkers H, Berns A (2003) Retroviral insertional mutagenesis: tagging cancer pathways. Adv Cancer Res, 88:53-99.

88　Zurkiya O, Chan AW, Hu X (2008) MagA is sufficient for producing magnetic nanoparticles in mammalian cells, making it an MRI reporter. Magn Reson Med, 59(6):1225-1231. doi: 10.1002/mrm.21606

89　Gilad AA, McMahon MT, Walczak P, et al. (2007) Artificial reporter gene providing MRI contrast based on proton exchange. Nat Biotechnol, 25(2):217-219. doi: nbt1277 [pii] 10.1038/nbt1277

90　Naumova AV, Reinecke H, Yarnykh V, Deem J, Yuan C, Charles EM Ferritin overexpression for noninvasive magnetic resonance imaging-based tracking of stem cells transplanted into the heart. Mol Imaging, 9(4):201-210.

91　Wang J, Zhang S, Rabinovich B, et al. Human CD34+ cells in experimental myocardial infarction: long-term survival, sustained functional improvement, and mechanism of action. Circ Res, 106(12):1904-1911. doi: CIRCRESAHA.110.221762 [pii] 10.1161/CIRCRESAHA.110.221762

92　Ly HQ, Hoshino K, Pomerantseva I, et al. (2009) In vivo myocardial distribution of multipotent progenitor cells following intracoronary delivery in a swine model of myocardial infarction. Eur Heart J, 30(23):2861-2868. doi: ehp322 [pii] 10.1093/eurheartj/ehp322

93　Muller-Borer BJ, Collins MC, Gunst PR, Cascio WE, Kypson AP (2007) Quantum dot labeling of mesenchymal stem cells. J Nanobiotechnology, 5:9. doi: 1477-3155-5-9 [pii] 10.1186/1477-3155-5-9

94　Lin S, Xie X, Patel MR, et al. (2007) Quantum dot imaging for embryonic stem cells. BMC Biotechnol, 7:67. doi: 1472-6750-7-67 [pii] 10.1186/1472-6750-7-67

95　Rosen AB, Kelly DJ, Schuldt AJ, et al. (2007) Finding fluorescent needles in the cardiac haystack: tracking human mesenchymal stem cells labeled with quantum dots for quantitative in vivo three-dimensional fluorescence analysis. Stem Cells, 25(8):2128-2138. doi: 2006-0722 [pii] 10.1634/stemcells.2006-0722

96　Hardman R (2006) A toxicologic review of quantum dots: toxicity depends on physicochemical and environmental factors. Environ Health Perspect, 114(2):165-172.

97　Lovric J, Bazzi HS, Cuie Y, Fortin GR, Winnik FM, Maysinger D (2005) Differences in subcellular distribution and toxicity of green and red emitting CdTe quantum dots. J Mol Med, 83(5):377-385. doi: 10.1007/s00109-004-0629-x

98　Qiao H, Zhang H, Zheng Y, et al. (2009) Embryonic stem cell grafting in normal and infarcted myocardium: serial assessment with MR imaging and PET dual detection. Radiology, 250(3):821-829. doi: 250/3/821 [pii] 10.1148/radiol.2503080205

99　Higuchi T, Anton M, Dumler K, et al. (2009) Combined reporter gene PET and iron oxide MRI for monitoring survival and localization of transplanted cells in the rat heart. J Nucl Med, 50(7):1088-1094. doi: jnumed.108.060665 [pii] 10.2967/jnumed.108.060665

100   Ray P, De A, Min JJ, Tsien RY, Gambhir SS (2004)
      Imaging tri-fusion multimodality reporter gene expression
      in living subjects. Cancer Res, 64(4):1323-1330.

101   Schachinger V, Erbs S, Elsasser A, et al. (2006) Intracoronary bone
      marrow-derived progenitor cells in acute myocardial infarction. N
      Engl J Med, 355(12):1210-1221. doi: 355/12/1210 [pii]
      10.1056/NEJMoa060186

102   Schachinger V, Erbs S, Elsasser A, et al. (2006) Improved clinical outcome
      after intracoronary administration of bone-marrow-derived progenitor
      cells in acute myocardial infarction: final 1-year results of the REPAIR-
      AMI trial. Eur Heart J, 27(23):2775-2783. doi: ehl388 [pii]
      10.1093/eurheartj/ehl388

103   Beitnes JO, Hopp E, Lunde K, et al. (2009) Long-term results after
      intracoronary injection of autologous mononuclear bone marrow cells
      in acute myocardial infarction: the ASTAMI randomised, controlled
      study. Heart, 95(24):1983-1989. doi: hrt.2009.178913 [pii]
      10.1136/hrt.2009.178913

104   Lunde K, Solheim S, Aakhus S, et al. (2006) Intracoronary injection
      of mononuclear bone marrow cells in acute myocardial infarction.
      N Engl J Med, 355(12):1199-1209. doi: 355/12/1199 [pii]
      10.1056/NEJMoa055706

105   Wollert KC, Meyer GP, Lotz J, et al. (2004) Intracoronary
      autologous bone-marrow cell transfer after myocardial infarction:
      the BOOST randomised controlled clinical trial. Lancet,
      364(9429):141-148. doi: 10.1016/S0140-6736(04)16626-9
      S0140673604166269 [pii]

106   Meyer GP, Wollert KC, Lotz J, et al. (2009) Intracoronary bone marrow cell
      transfer after myocardial infarction: 5-year follow-up from the randomized-
      controlled BOOST trial. Eur Heart J, 30(24):2978-2984. doi: ehp374 [pii]
      10.1093/eurheartj/ehp374

107   Janssens S, Dubois C, Bogaert J, et al. (2006) Autologous bone marrow-
      derived stem-cell transfer in patients with ST-segment elevation
      myocardial infarction: double-blind, randomised controlled trial.
      Lancet, 367(9505):113-121. doi: S0140-6736(05)67861-0 [pii]
      10.1016/S0140-6736(05)67861-0

108   Meluzin J, Janousek S, Mayer J, et al. (2008) Three-, 6-, and
      12-month results of autologous transplantation of mononuclear
      bone marrow cells in patients with acute myocardial infarction. Int
      J Cardiol, 128(2):185-192. doi: S0167-5273(07)01090-X [pii]
      10.1016/j.ijcard.2007.04.098

109   Chen SL, Fang WW, Ye F, et al. (2004) Effect on left ventricular
      function of intracoronary transplantation of autologous bone marrow
      mesenchymal stem cell in patients with acute myocardial infarction.
      Am J Cardiol, 94(1):92-95. doi: 10.1016/j.amjcard.2004.03.034
      S0002914904004485 [pii]

110   Dill T, Schachinger V, Rolf A, et al. (2009) Intracoronary administration
      of bone marrow-derived progenitor cells improves left ventricular
      function in patients at risk for adverse remodeling after acute ST-segment
      elevation myocardial infarction: results of the Reinfusion of Enriched
      Progenitor cells And Infarct Remodeling in Acute Myocardial Infarction
      study (REPAIR-AMI) cardiac magnetic resonance imaging substudy.
      Am Heart J, 157(3):541-547. doi: S0002-8703(08)01029-6 [pii]
      10.1016/j.ahj.2008.11.011

111   Kraitchman DL, Heldman AW, Atalar E, et al. (2003) In vivo magnetic
      resonance imaging of mesenchymal stem cells in myocardial infarction.
      Circulation, 107(18):2290-2293. doi: 10.1161/01.CIR.0000070931.62772.4E
      01.CIR.0000070931.62772.4E [pii]

112   Amado LC, Saliaris AP, Schuleri KH, et al. (2005) Cardiac
      repair with intramyocardial injection of allogeneic mesenchymal
      stem cells after myocardial infarction. Proc Natl Acad Sci U
      S A, 102(32):11474-11479. doi: 0504388102 [pii]
      10.1073/pnas.0504388102

113   Stuckey DJ, Carr CA, Martin-Rendon E, et al. (2006) Iron
      particles for noninvasive monitoring of bone marrow stromal cell
      engraftment into, and isolation of viable engrafted donor cells from,
      the heart. Stem Cells, 24(8):1968-1975. doi: 2006-0074 [pii]
      10.1634/stemcells.2006-0074

114   Ebert SN, Taylor DG, Nguyen HL, et al. (2007) Noninvasive tracking of
      cardiac embryonic stem cells in vivo using magnetic resonance imaging
      techniques. Stem Cells, 25(11):2936-2944. doi: 2007-0216 [pii]
      10.1634/stemcells.2007-0216

115   Chapon C, Jackson JS, Aboagye EO, Herlihy AH, Jones WA, Bhakoo
      KK (2009) An in vivo multimodal imaging study using MRI and PET
      of stem cell transplantation after myocardial infarction in rats. Mol
      Imaging Biol, 11(1):31-38. doi: 10.1007/s11307-008-0174-z

116   Li Z, Lee A, Huang M, et al. (2009) Imaging survival and function of
      transplanted cardiac resident stem cells. J Am Coll Cardiol, 53(14):1229-1240.

4.2

Different strategies for reducing intestinal background radioactivity associated with imaging HSV1-tk expression using established radionucleoside probes

Ruggiero A, Brader P, Serganova I, Zanzonico P, Hricak H, Lipman N, Blasberg RG

Chapter 4.2

Different strategies for reducing intestinal background radioactivity associated with imaging HSV1-tk expression using established radionucleoside probes

Abstract

One limitation of HSV1-*tk* reporter PET imaging with nucleoside analogues is the high background radioactivity in the intestine. We hypothesized that endogenous expression of thymidine kinase in bacterial flora could phosphorylate and trap such radiotracers, contributing to the high radioactivity levels in the bowel and therefore explored different strategies to increase fecal elimination of radiotracer.

Methods: Intestinal radioactivity was assessed by *in vivo* microPET imaging and *ex vivo* tissue sampling following intravenous injection of ^{18}F-FEAU, ^{124}I-FIAU or ^{18}F-FHBG in a germ-free mouse strain. We also explored the use of an osmotic laxative agent and/or a 100% enzymatically hydrolyzed liquid diet.

Results: No significant differences in intestinal radioactivity were observed between germ-free and normal mice. ^{18}F-FHBG-derived intestinal radioactivity levels were higher than those of ^{18}F-FEAU and ^{124}I-FIAU; the intestine-to-blood ratio was more than 20-fold higher for ^{18}F-FHBG than for ^{18}F-FEAU and ^{124}I-FIAU. The combination of Peptamen and Nulytely lowered intestinal radioactivity levels and increased (2.2-fold) the HSV1-*tk* transduced xenograft-to-intestine ratio for ^{18}F-FEAU.

Conclusions: Intestinal bacteria in germ-free mice do not contribute to the high intestinal levels of radioactivity following injection of radionucleoside analogs. The combination of Peptamen and Nulytely increased radiotracer elimination by increasing bowel motility without inducing dehydration.

Introduction

Monitoring adoptive cell-based therapies and viral vector tracking in gene therapy are challenging, yet they are currently the most clinically relevant applications of reporter gene imaging. The herpes simplex virus type 1 thymidine kinase gene (HSV1-*tk*), either wild type or the *sr39tk* mutant, currently is the most commonly used radiotracer-based reporter gene used in positron emission tomography (PET) studies[1]. HSV1-*tk* gene expression can be effectively imaged using radiolabeled substrates that are selectively phosphorylated by the HSV1-TK enzyme and the phosphorylated substrate is unable to cross the cell membrane; thus, the phosphorylated substrate is essentially trapped within the HSV1-*tk* transduced cell [2]. The two most commonly used substrates are [^{124}I]-2'-fluoro-1-h-D-arabino-furanosyl-5-iodo-uracil (^{124}I-FIAU) for HSV1-*tk* and 9-(4-fluoro-3-hydroxymethylbutyl)guanine (^{18}F-FHBG) for HSV1-*sr39tk* [3, 4]. More recently [^{18}F]-2'-Fluoro-2'deoxy-1h-D-arabionofuranosyl-5-ethyl-uracil (^{18}F-FEAU) has been shown to be a very effective substrate for both wild-type and the sr39 variant of HSV1-*tk* [5]. These substrates are minimally (if at all) phosphorylated by endogenous mammalian thymidine kinase (TK) and, therefore, the local accumulation of radiotracer is frequently used as a measure of reporter gene expression. However, background radioactivity is often problematic in organs (e.g. the intestine) involved in the clearance of radiolabeled nucleosides and their metabolites from the body and adjacent tissues.

The characteristics of a good substrate for reporter-gene imaging studies *in vivo* include not only high selectivity and sensitivity for the gene product, but also a favorable pharmacokinetic clearance profile. The level of background radioactivity must be low and not obscure the specific signal in the anatomic site of interest. The most notable levels of background radioactivity following injection of radiolabeled nucleosides is observed in the abdomen, due to both renal and hepato-biliary clearance of such agents. High levels of radioactivity are initially seen throughout the renal tract, but at later times (1-4 hours) they are largely confined to the bladder [4, 5]. The hepato-biliary-intestinal clearance presents a greater problem, resulting in a high and heterogenous pattern of background radioactivity throughout the abdomen [3, 5, 6], that remains high over several hours, often obscuring specific structures of interest [7].

Nimmagadda et al. demonstrated in dogs that the time-activity profile of ^{18}F-FIAU in the gallbladder begin to increase 10 minutes after intravenous (IV) injection and continues to increase over 60 minutes, as the tracer is cleared from the blood [8]. Yaghoubi et al. reported that background radioactivity in the intestine in humans, following IV injection of ^{18}F-FHBG was high (almost 10%ID/g) 25 minutes after injection, with a further slight increase over time [9]. Several other HSV1-*tk* probes have been developed and tested both *in vitro* and *in vivo* and their advantages and disadvantages have been extensively discussed in the literature [4, 10]. ^{18}F-FHBG, Owing to its lipophilic structure, has been associated with higher hepato-biliary secretion and higher intestinal background activity compared to ^{18}F-FEAU [11]. However, to our knowledge no studies

Chapter 4.2

Different strategies for reducing intestinal background radioactivity associated with imaging HSV1-tk expression using established radionucleoside probes

have investigated mechanisms other than hepato-biliary clearance to explain the rapid and diffuse uptake of the radioactivity throughout the whole intestine. Also, no strategy has been suggested in the literature to reduce the abdominal background, particularly the intestinal component.

Similarities between HSV1-*tk* and prokaryotic *tk* genes have been described. Bettegowda and colleagues demonstrated that endogenous bacterial TKs are sufficiently similar to that of viral TKs to permit bacteria to be imaged in mammalian hosts using the same radiolabeled nucleosides analogues [12]. Prokaryotic *tk* genes in a wide range of bacteria allowed the detection and imaging of these bacteria with ^{125}I-FIAU in experimentally created infections. This approach has also been successfully tested for visualizing musculoskeletal bacterial infections using [124]I-FIAU-PET-Computed Tomography (CT) in a small number of patients [13]. We previously reported that a probiotic bacterial strain of *Escherichia Coli Nissle 1917*, which endogenously expresses HSV1-TK, trafficked to a subcutaneous (SC) breast tumor xenograft following i.v. administration and that the tumor-targeting bacteria could be visualized by ^{18}F-FEAU and [124]I-FIAU microPET. Given that SC tumors were located in the shoulders of the host mice, the renal-hepato-biliary clearance of the radiotracers did not interfere with measurements of the tumor uptake. Furthermore, it was also shown that the level of tumor radioactivity could be used as an indicator of the number of bacteria present in the target tissue [14].

The role of commensal intestinal flora in the gut and the clearance of radiolabeled nucleoside analogs from the body has not been investigated previously. This commensal population, composed of anaerobic, aerobic and facultative aerobic bacteria, represents a heterogeneous microbial ecosystem containing approximately 10^{14} bacteria, forming a natural protective barrier and exerting numerous protective, structural and metabolic effects on the intestinal epithelium [15, 16].

In this study, we tested the hypothesis that radionucleoside analogs can translocate from the bloodstream to the intestinal mucosa, where they can be taken up, phosporylated and trapped by the commensal intestinal flora contributing in this manner to the high and early intestinal background observed in radionucleoside imaging. We determined whether abdominal background activities of three different radionucleoside analogs (^{18}F-FEAU, ^{18}F-FHBG and [124]I-FIAU) are substantially different in germ-free mice raised in a sterile vivarium environment compared to animals with normal bacterial flora raised in a normal vivarium environment. We evaluated organ-specific activities by both *in vivo* microPET imaging and by *ex vivo* tissue sampling. In addition, we evaluated different strategies to reduce the intestinal background by increasing intestinal motility and radiotracer fecal excretion in nude mice bearing an HSV1-TK expressing xenograft.

Materials and Methods

^{18}F-FEAU, ^{18}F-FHBG and [124]I-FIAU Syntheses

[18]F was produced on the Memorial Sloan-Kettering Cancer Center (MSKCC) cyclotron. ^{18}F-FEAU was synthesized by coupling the radiolabeled fluoro sugar with the silylated pyrimidine derivatives following a procedure previously reported by Serganova and colleagues [17]. The specific activity of the ^{18}F-FEAU was ~37GBq/µmol (~1 Ci/µmol) and the radiochemical purity >95% after purification by high-performance liquid chromatography (HPLC). The product was formulated in 0.9 NaCl containing 5% ethanol and terminally sterilized by filtration.

^{18}F-FHBG was synthesized using ^{18}F in the form of potassium fluoride in aqueous solution as previously described [18]. The specific activity of the final product was ~70GBq/µmol (~1.9 Ci/µmol) and radiochemical purity > 96% by HPLC.

[124]I-FIAU was synthesized by reacting the precursor of 5-trimethyl-stannyl-1-(2-deoxy-2-fluoro-β-D-arabinofuranosyl)uracil (FTAU) with carrier-free [[124]I]NaI. [124]I was produced on the Memorial Sloan-Kettering cyclotron using the $^{124}Te(p,n)$ ^{124}I nuclear reaction on an enriched $^{124}TeO_2/Al_2O_3$ solid target. Radiosynthesis was done as previously described [4, 18] with minor modifications. The specific activity of the product was >1,000 GBq/µmol (>27 Ci/µmol); radiochemical purity >95% as determined by thin-layer chromatography (TLC) (Rf 0.7) using silica gel plates and a mobile phase of ethyl acetate/acetone/water (14:8:1, v/v/v).

Cell lines

The RG2 rat glioma cell line was obtained from American Type Culture Collection (Manassas, VA, USA). RG2 cells were transduced with the recombinant replication-deficient STK retrovirus containing the NeoR gene and HSV1-*tk* gene. The transduced cell line, RG2-*tk*, has been characterized previously [19].

Experimental Groups of Animals

Animal studies were performed in compliance with all applicable policies, procedures, and regulatory requirements of the Institutional Animal Care and Use Committee, the Research Animal Resource Center of Memorial Sloan Kettering Cancer Center, and the NIH Guide for the Care and Use of Laboratory Animals.

Three groups of five germ-free (defined as a gnotobiote - free of all demonstrable microbial association) Swiss Webster mice 6-to-8 weeks-old raised in a sterile environment (Taconic Farms, Inc., Germantown, N.Y.) were shipped in a sterile container with sterile food, and kept under sterile conditions until imaging. Experiments were conducted on three consecutive days after shipment. Each day a single cage of 5 animals was carefully

Chapter 4.2

Different strategies for reducing intestinal background radioactivity associated with imaging HSV1-tk expression using established radionucleoside probes

removed using sterile technique to preserve the sterility of the container and of the remaining cages. Fecal pellets were collected in each cage and microbiologically evaluated to confirm the germ-free status of the animals. Three groups (n=5 per group) of bacteria associated Swiss Webster mice 6-to-8 weeks-old (Taconic Farms, Inc., Germantown, NY) raised in a normal vivarium environment were used as controls. Fecal pellets were also collected from the control animals and evaluated for bacteria in the same manner.

Three- to 4-weeks-old athymic *nu/nu* mice (CrTac:NCr-*Foxn1^{nu}* Taconic Farms, Inc.) were used in a second set of experiment involving tumor implantation. Twenty mice, divided into four groups (control, Nulytely [Braintree Laboratories, Braintree, MA], Peptamen [Nestlé, Vevey, Switzerland,], combination of Peptamen and Nulytely; n=5/group) were studied with two tumor xenografts produced in each animal. Transduced RG2 HSV1-*tk* cells (test) and wild-type RG2 cells (control) were removed by trypsinization, washed in phosphate buffered saline (PBS), and 1.0×10^6 cells (resuspended in 50 µL Matrigel®) were implanted SC into the right and left shoulders, respectively, of each animal in all four groups. Mice were monitored for tumor growth by daily measurements of the tumor size and of the animal's weight. Animals were studied when the SC xenografts reached a diameter of 12-15 mm, 14-21 days after s.c. implantation of the RG2 and RG2-HSV1-*tk* cells. The *in vivo* growth rate and macroscopic appearance were similar in the HSV1-*tk* transduced and wild-type SC xenografts.

All animal procedures were performed under inhalation of 2% isoflurane anesthesia. After the studies, all animals were sacrificed by CO_2 inhalation.

Different strategies to increase radionucleoside excretion

We compared three strategies to increase intestinal motility and reduce fecal mass relative to those for standard diet. To reduce the intestinal content we used a complete peptide-based elemental nutritional diet (Peptamen) formulated for the dietary management of patients with inflammatory bowel disease, pancreatic insufficiency, short-bowel syndrome, radiation enteritis and chronic diarrhea. It provides high-energy nutrition (10 kcal/mL; caloric distribution in % of kcal: Protein 16%; Carbohydrate 51%; Fat 33%) without formation of feces. A vanilla-flavored Peptamen (enzymatically hydrolyzed whey protein) was chosen to improve the taste of the solution to stimulate feeding. A ~1:2 dilution in water was placed in a regular 450 ml water bottle.

To increase bowel motility and obtain a faster excretion of the radiotracer, an isosmotic laxative agent (Nulytely; PEG-3350, sodium chloride, sodium bicarbonate and potassium chloride for oral administration) was used. Nulytely is given orally to patients for bowel cleansing prior to colonoscopy. According to the vendor, it is solubilized in water to obtain a solution containing PEG-3350 31.3 mmol/L, sodium 65 mmol/L, chloride 53 mmol/L, bicarbonate 17 mmol/L and potassium 5 mmol/L. The final product was placed in a cage water bottle.

The control group was fed with a standard diet and water ad libitum for 21 days after tumor implantation. For the Nulytely group, regular solid food and water were provided for the first 18 days after tumor implantation; solid food was then discontinued and Nulytely was substituted 36 hours before imaging and sacrifice. For the Peptamen group, a regular diet was provided for 7 days after tumor implantation and then a Peptamen diet for 14 days prior to imaging. The fourth "combination" group received a normal diet for 7 days after tumor implantation followed by Peptamen for 14 days and Nulytely for 36 hours before imaging and sacrifice. Animals determined to be dehydrated were administered fluids intraperitoneally as described in the institutional guidelines for maintaining fluid homeostasis.

MicroPET imaging

^{18}F-FEAU. Five germ-free Swiss Webster mice and five bacteria-associated Swiss Webster mice were injected retro-orbitally with 9.25 MBq (250 µCi) of ^{18}F-FEAU and imaged sequentially. A separate cohort of 20 nude mice divided into four groups (control, Nulytely , Peptamen, combination of Peptamen and Nulytely) were injected retro-orbitally with 9.25 MBq (250 µCi) of ^{18}F-FEAU. MicroPET imaging was performed 2 hours after tracer administration using a 10-min list-mode acquisition.

^{18}F-FHBG. Five germ-free Swiss Webster mice and five bacteria-associated Swiss Webster mice were injected retro-orbitally with 9.25MBq (250 µCi) of ^{18}F-FHBG. MicroPET imaging was performed 2 hours after tracer administration using a 10-min list-mode acquisition.

^{124}I-FIAU. Five germ-free Swiss Webster mice and five bacteria-associated Swiss Webster mice were injected retro-orbitally with 29.6 MBq (800 µCi) of ^{124}I-FIAU. MicroPET imaging was performed 2 and 24 hours after tracer administration using a 10-min and 30-min list-mode acquisitions, respectively.

Germ-free animals were injected and handled under sterile conditions. The pre-anesthesia box, nose cone and microPET table were rinsed with 100% ethanol and measures to avoid contamination was implemented. After tracer administration and before imaging, animals were allowed to recover from anesthesia in their sterile cages and thus to maintain their germ-free status. Imaging was done using a Focus 120 microPET dedicated small-animal PET scanner (Concorde Microsystems, Inc.). Mice were maintained under 2% isoflurane anesthesia with an oxygen flow rate of 2 L/min during the entire scanning period. Three-dimensional list-mode data were acquired using an energy window of 350 to 700 keV for ^{18}F and 410 to 580 keV for ^{124}-I and a coincidence timing window of 6 ns. Data were sorted into two-dimensional histograms by Fourier rebinning, reconstructed and normalized as previously described (14).

Chapter 4.2

Different strategies for reducing intestinal background radioactivity associated with imaging HSV1-tk expression using established radionucleoside probes

MicroPET image analysis was performed using *ASIPro* software (Concorde Microsystems, Inc.). For each microPET scan, the intestine was identified and ROIs were manually drawn in the anterior abdominal compartment. ROIs were also placed over the RG2 wild-type and RG2 HSV1-TK xenografts. Reconstructed images were parameterized in terms of %ID/g and the maximum and total voxel values were recorded for each tissue; the tumor-to-organ radioactivity concentrations ratios were also calculated.

Radioactivity quantification of tissue samples

Euthanized mice were rinsed with 100% ethanol before tissue removal. Large and small intestines were removed "en-bloc" with their fecal content liver, gallbladder, kidneys, heart, skeletal muscle and blood were sampled and weighed before radioactivity measurement. Tissue harvesting of germ-free mice was performed under sterile surgical conditions and organs collected in sterile scintillation vials. ^{18}F-FEAU, ^{18}F-FHBG and [124]I-FIAU derived radioactivity (%ID/g) in the tissue samples was measured in a Wizard 1470 gamma counter (Perkin-Elmer, Waltham, USA) and the tissue to blood ratios calculated. The correlation between microPET and scintillation counter radioactivity values was assessed.

Bacterial evaluation of intestinal samples

Microbiologic analysis was performed both on the fecal pellets (collected from the cage before injection and imaging) and on both small and large intestinal contents from germ-free and control mice. Post-mortem intestinal samples were collected under sterile conditions. The fecal pellets and intestinal samples were homogenized in 1 ml PBS and dilutions (1:10, 1:100 and 1:1000) were plated on blood agar plates.

Statistics

One-way analyses of variance were applied using Prism Software (GraphPad® Software Inc. San Diego, CA, USA) to determine the statistical significance among the experimental groups. Statistical significance was set at $p<0.05$. Results were reported as Mean ± SD.

Results

Comparison of radiotracer distributions and clearance in germ-free and control mice

^{18}F-FEAU and ^{18}F-FHBG radioactivity (%ID/g) was imaged/measured in different organs/tissues of germ-free and control mice two hours after IV administration, whereas [124]I-FIAU was imaged/measured at 24 hours in the same animal cohorts (Figure 1). The absence of enteric bacterial growth from fecal pellets and intestinal samples from the germ-free mice compared to control mice (Figure 2A) confirmed the germ-free status of these mice during the ^{18}F-FEAU and ^{18}F-FHBG study. It should be noted that all visceral contents were included in the *ex vivo* measurements of tissue radioactivity.
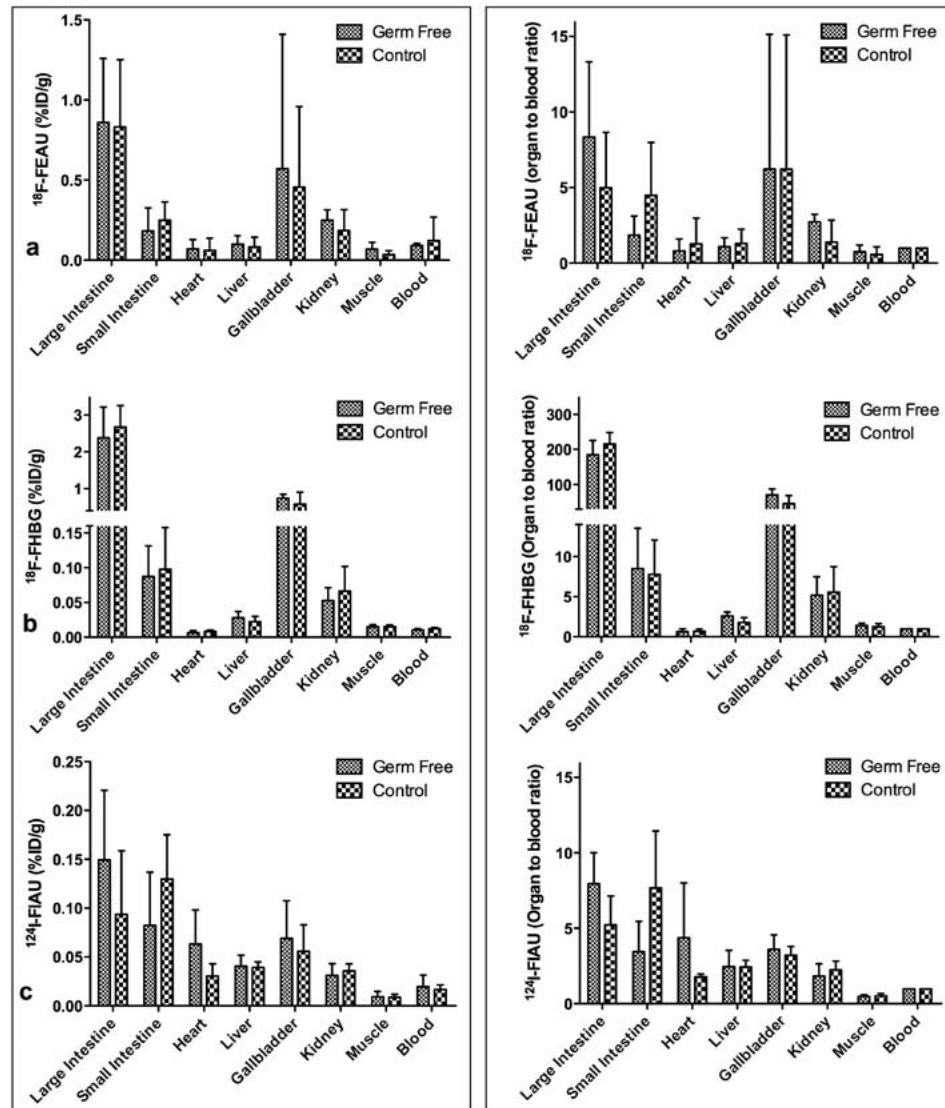
No difference in organ activities were observed between germ-free and control mice, including the large intestine and its contents: ^{18}F-FHBG (2.38±0.84 vs 2.67±0.58 %ID/g), ^{18}F-FEAU (0.86±0.40 vs 0.83±0.42 %ID/g) and [124]I-FIAU (0.15±0.07 vs 0.09±0.07 %ID/g), respectively. Although the radioactivity levels in the small intestine were slightly lower in germ-free than in control animals for each radiotracer, these differences were not statistically significant. The highest radioactivity levels were observed with ^{18}F-FHBG in the large intestine and gallbladder. Normalizing intestinal radioactivity to that in blood yielded intestine-to-blood ratios of 201±37 for ^{18}F-FHBG and 6.9±4.5 for ^{18}F-FEAU at 2 hours, and 6.4±2.3 for [124]I-FIAU at 24 hours.

The microPET images were consistent with the tissue sampling results; no difference in the pattern of abdominal and total body radioactivity distributions was observed between germ-free and control animals (Figure 2B). Specifically, quantitative analysis of the anterior abdominal compartment of the microPET images, based on maximum voxel and total radioactivity values (%ID/g), yielded no statistically significant differences between germ-free and control mice (Figure 2C). The highest maximum-voxel and abdominal radioactivity values (%ID/g) were observed for ^{18}F-FHBG; they were 6.7- and 6.6-fold higher than ^{18}F-FEAU ($p<0.05$) and more than 50- and 13-fold higher than [124]I-FIAU ($p<0.001$), respectively. Importantly, by setting a higher threshold for ^{18}F-FHBG compared to ^{18}F-FEAU and [124]I-FIAU, only the higher activity in the gut was visible (see Figure 2B).

### Strategies to reduce 18F-FEAU background-intestinal radioactivity levels

We developed and tested several different bowel-cleansing regimens to increase abdominal clearance of ^{18}F-FEAU during the study, including an osmotic agent (Nulytely), a peptide-based elemental nutrition regimen (Peptamen), and a combination of Peptamen and Nulytely (Figure 3). Only the combination of Peptamen and Nulytely resulted in a significant decrease in large- intestine radioactivity levels compared to that in controls (Figure 3A). Due to dehydration resulting in a 14±0.5 % weight loss in the Nulytely group of animals (Figure 3C), renal excretion of ^{18}F-FEAU was reduced and high tissue

Chapter 4.2

Different strategies for reducing intestinal background radioactivity associated with imaging HSV1-tk expression using established radionucleoside probes

Figure 1

***Ex Vivo* Biodistribution of ^{18}F-FEAU, ^{18}F-FHBG and ^{124}I-FIAU in germ-free and control mice.** *Ex vivo* biodistribution (%ID/g) (left panel) and normalized to blood data (right panel) in mice following injection of **(A)** ^{18}F-FEAU, **(B)** ^{18}F-FHBG and **(C)** ^{124}I-FIAU in germ-free and control mice. No statistically significant difference in large intestine radioactivity (%ID/g) was observed between the germ-free and control animals. Radioactivity measured in the small intestine was slightly lower in germ-free animal than control for each radiotracer, although not statistically significant. ^{18}F-FHBG was associated with higher large intestine radioactivity (2.9-fold compared to ^{18}F-FEAU and 18-fold compared to ^{124}I-FIAU, p<0.001). The lowest levels were observed with ^{124}I-FIAU at 24 hours. The intestine-to-blood ratio for ^{18}F-FHBG (201±37) was very high compared to that for ^{18}F-FEAU (6.9±4.5) at 2 hours and ^{124}I-FIAU (6.4±2.3) at 24 hours.
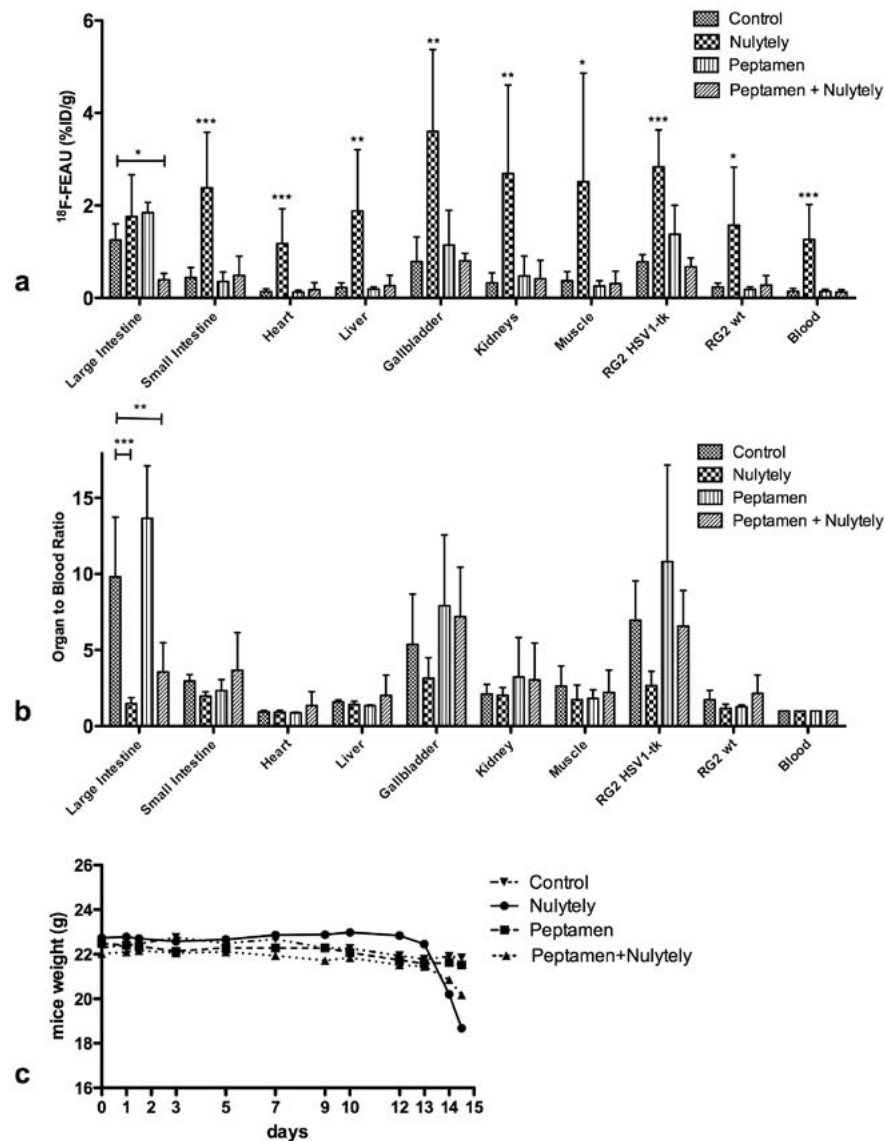
Figure 2
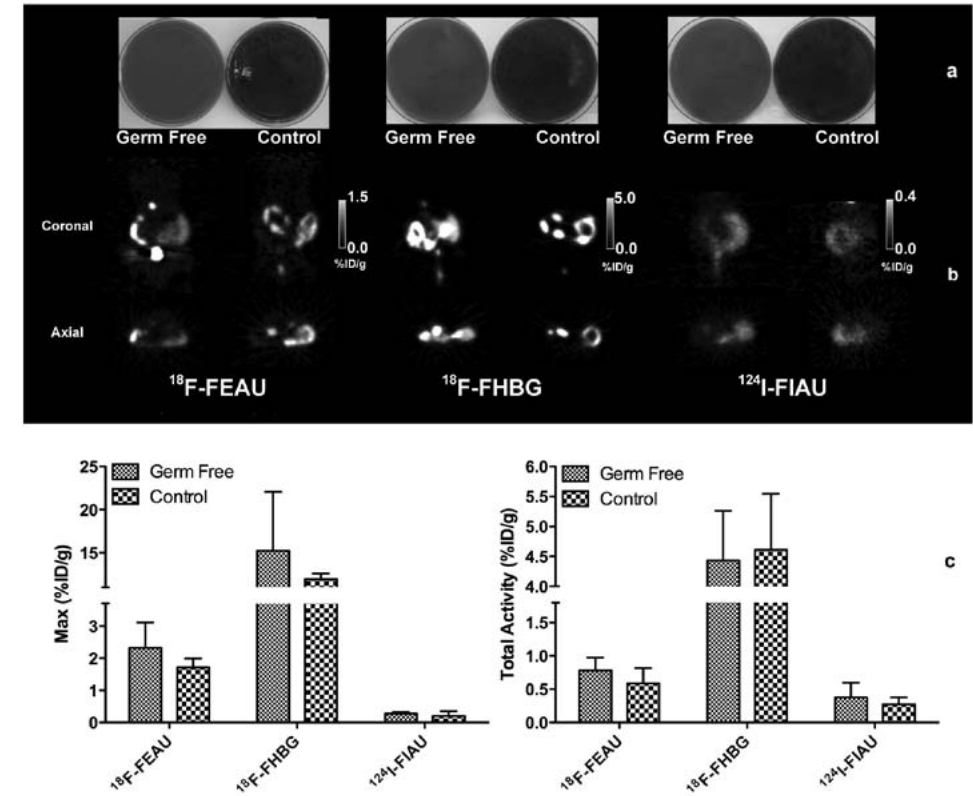
^{18}F-FEAU, ^{18}F-FHBG and ^{124}I-FIAU microPET imaging in germ-free and control mice. (A) Pictures of the blood agar plates where homogenized samples of the fecal pellet were placed (1:10 dilutions) to confirm the germ-free status versus control groups of animals. The red-to-brown color shift indicates the presence of metabolic activity, corresponding the growth of bacteria. Bacterial colonies were visible in the brown (control) plates, but not in the plates from the germ-free animals. **(B)** Coronal and axial PET images of germ-free versus control mice at 2 hours after injection of ^{18}F-FEAU, ^{18}F-FHBG and 24 hours after injection of ^{124}I-FIAU. ^{18}F-FHBG is associated with the highest abdominal radioactivity compared to ^{18}F-FEAU and ^{124}I-FIAU; note the higher threshold of the intensity bar (5% ID/g) for ^{18}F-FHBG. No difference is observed in the PET images between germ-free and control animals in each radionucleoside group. **(C)** Comparison of the intestinal uptake of ^{18}F-FEAU, ^{18}F-FHBG and ^{124}I-FIAU in germ-free versus control mice, calculated from multiple intestinal ROIs drawn on the whole intestine on the axial plane. Values of the *Maximum Pixel Value* (Max %ID/g) and *Total Activity* (%ID/g) are illustrated. The highest values were observed for ^{18}F-FHBG; Maximum pixel (%ID/g) intestinal background was ~6.7-fold higher than that for ^{18}F-FEAU (p<0.05) and more than 50-fold higher than that for ^{124}I-FIAU (p<0.001).

and blood values were measured at 2 hours post-injection. Dehydration occurred in the Nulytely-treated group despite i.p. hydration, whereas only a slight weight loss (6±1 %) was noted in the Peptamen plus Nulytely treatment group. No change in animal weight was observed with Peptamen treatment alone. Hydration status and radiotracer retention has to be taken into consideration in order to meaningfully compare the different bowel-cleansing strategies. Normalizing the 2 hour tissue data to that of blood, yielded significantly lower large intestine-to-blood ratios for the Nulytely (86% decrease;

Chapter 4.2

Different strategies for reducing intestinal background radioactivity associated with imaging HSV1-tk expression using established radionucleoside probes

Different strategies in increasing radionucleoside excretion and ¹⁸F-FEAU biodistribution. Biodistribution of ¹⁸F-FEAU in tumor bearing nude mice at 2 hours after injection, treated with Nulytely (36 hours), Peptamen (14 days) and a combination of Peptamen (14 days) and Nulytely (36 hours) versus control (regular diet and water ad libitum). Values are expressed in **(A)** %ID/g and **(B)** organ-to-blood normalized data. (*p<0.05;**p<0.01; ***p<0.001). Asterisks in (a) indicate the statistically significant difference between the Nulytely group and the control. The highest values (1.5-to-8 fold higher compared to control group) were observed in the Nulytely group. The normalization of tissue (organ) radioactivity to that in blood takes into consideration the hydration status of the mice. **(C)** Different intestinal cleansing strategies and their effect on animal weight. A 14±0.5% weight loss was observed after 36 hours of Nulytely treatment alone, due to dehydration and food deprivation. The combination of Nulytely and Peptamen resulted in only 6±1% weight loss during the same period of treatment.

p<0.001) and the combination (Peptamen plus Nulytely) treatment groups (65% decrease, p<0.005) compared to control animals (Figure 3B).

Optimizing HSV1-tk reporter imaging by reducing intestinal background radioactivity

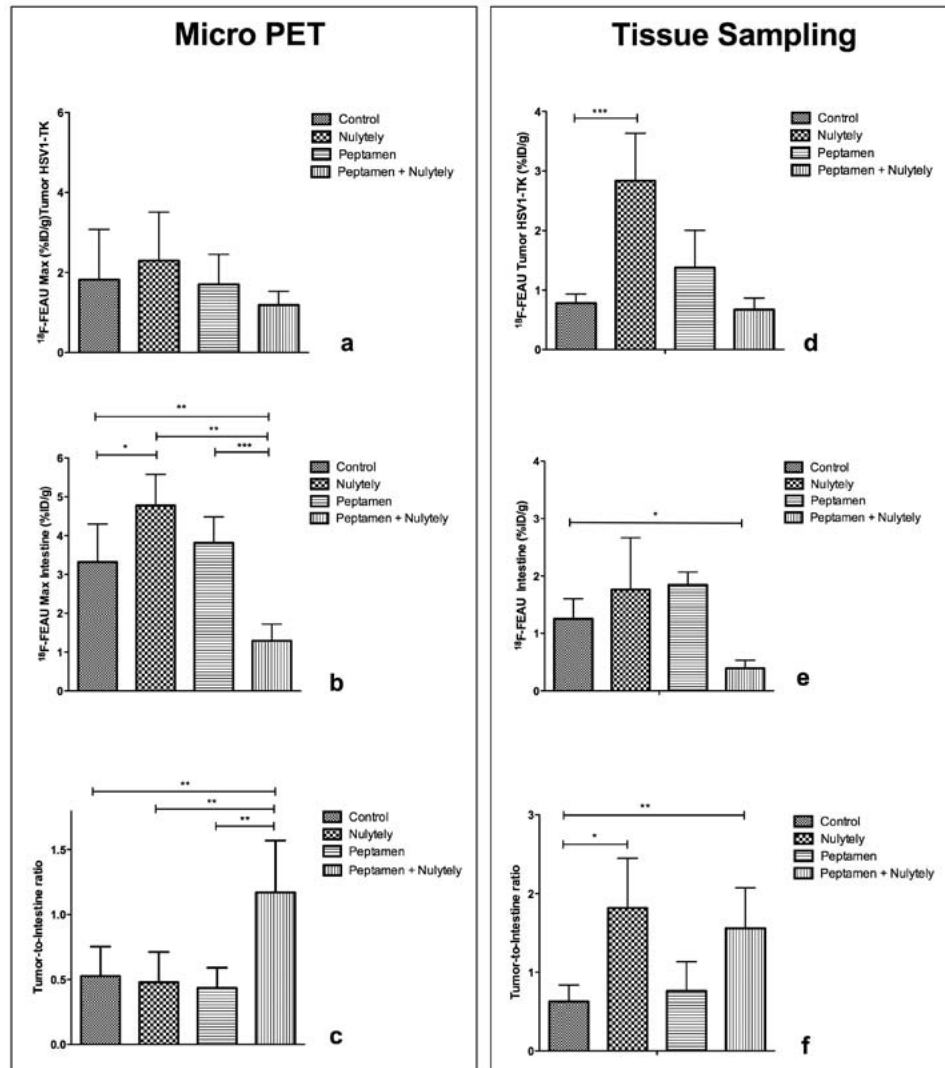The visualization of the RG2 HSV1-*tk* xenografts with ¹⁸F-FEAU relative to background intestinal radioactivity was optimized in the animals treated with the combination of Peptamen and Nulytely, compared to the control and the other treatment groups (Figure 4). The measured ¹⁸F-FEAU radioactivity profile comparing the different treatment groups, using either microPET or tissue- sampling measurements of RG2 HSV1-*tk* xenograft and large-intestine radioactivity, was similar (see Figure 4). Intestinal radioactivity measured by microPET (Figure 5) and by tissue sampling in animals treated with the combination of Peptamen and Nulytely was significantly lower (62% and 69% decrease, respectively) compared to control and to the other treatment groups.

The tumor-to-intestine ratios measured by microPET and by tissue sampling (see Figure 4C) were similar and significantly higher (2.2- (p<0.01) and 2.5-fold (p<0.05), respectively) for the Peptamen plus Nulytely combination treatment compared to the controls. No significant differences were observed between the other treatment groups and the controls. Importantly, the HSV1-*tk* transduced-to-wild type tumor ratios did not changed significantly between treatment groups and control animals.

Discussion

In the current study we investigated whether normal enteric bacterial flora contributes to the intestinal accumulation of radiolabeled nucleoside analogs that are commonly used to image HSV1-*tk* expression. It has been shown that bacteria can transport and phosphorylate nucleoside analogs [12-14]. It has also been shown that radiolabeled nucleoside analogs can be used to image bacterial infection and to image bacteria that target tumors [14, 20]. We hypothesized that the high levels of intestinal radioactivity imaged in HSV1-*tk* reporter-gene studies within 1-2 hours after injection could reflect not only the hepatobiliary excretion but also the translocation of the radionucleoside analogs from the bloodstream to the intestinal mucosa and consequent uptake of the radiopharmaceutical by normal intestinal flora. Although it is well known that radiolabeled nucleoside analogs are actively secreted into the small intestine through the hepato-biliary system, there is no evidence for direct secretion of nucleosides in the large intestine. The transport of radionucleoside analogues (such as ¹⁸F-FEAU, ¹²⁴I-FIAU, ¹⁸F-FHBG) by the intestinal epithelium has never been investigated, although plasma membrane carriers are known to transport nucleosides and nucleobase analogues [21, 22]. Nevertheless, the localization of radioactivity to the large bowel suggested that enteric bacteria could play a role [5, 14]. To assess whether enteric bacteria contribute to high intestinal background

Chapter 4.2

Different strategies for reducing intestinal background radioactivity associated with imaging HSV1-tk expression using established radionucleoside probes

Figure 4

Quantitative PET analysis and tissue sampling data. Comparison of microPET data (*left panel*) and tissue sampling data (*right panel*) for intestinal and tumor (HSV1-TK) ^{18}F-FEAU – derived radioactivity (%ID/g) in nude mice bearing HSV1-TK transduced and wild type RG2 xenografts, treated with different bowel cleansing agents. In the left panel the values of Maximum (%ID/g) for **(a)** tumor RG2 (HSV1-TK) **(b)** intestine (calculated by drawing multiple intestinal on the whole intestine on the axial plane) and **(c)** the calculated tumor-to-large intestine ratio are graphed. Similar graphs are presented for the tissue sampling results **(d)**, **(e)**, **(f)**. Significant differences between treatment groups are indicated (*p<0.05; **p<0.01; ***p<0.001).

Figure 5
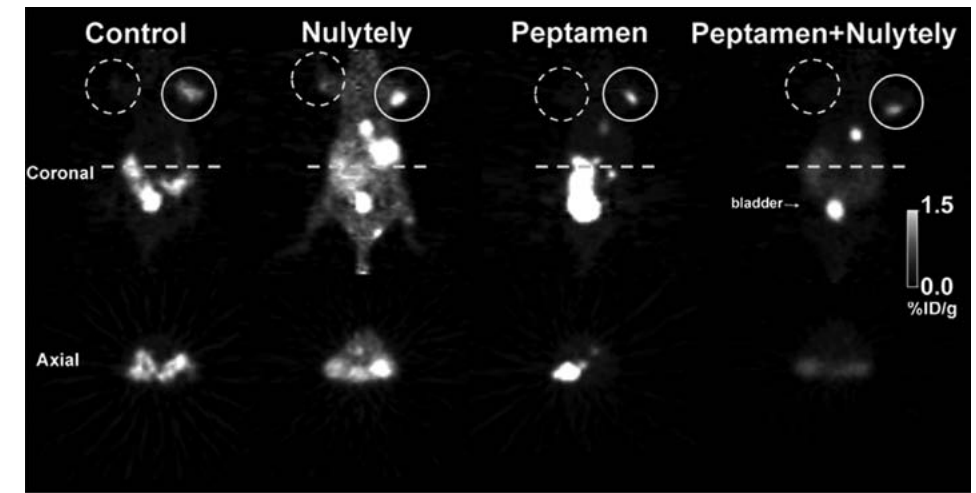
Different strategies and their effect in mice. Coronal and axial ^{18}F-FEAU PET images of nude mice bearing a RG2 HSV1-TK xenograft in the right shoulder (circle) and a RG2 wild-type xenografts in the left shoulder (dotted circle). Coronal images are shown through the mid-abdomen. Axial images are shown for a section through the abdomen indicated by the orange dotted line. Note that the high intestinal background observed with the laxative agent alone (Nulytely) is due to dehydration and high radioactivity retention.

in rodents, we studied the biodistribution of three radiolabeled nucleoside analogs in germ-free Swiss Webster mice and in the same strain of Swiss Webster mice exposed to a normal (non-sterile) vivarium environment.

To our knowledge this is the first study to analyze the differences in intestinal background radioactivity among the three most commonly used radionucleoside analogs for imaging HSV1-*tk* or HSV1-*sr39tk*. The ^{18}F-FEAU, ^{18}F-FHBG and [124]I-FIAU biodistribution data are consistent, in that the clearance of radioactivity from all organs, except for the intestine, is fairly rapid. At 2 hours large-intestine radioactivity levels are substantially higher than that in the small intestine; whereas with [124]I-FIAU at 24 hours, both large- and small-intestine radioactivity levels are low. We demonstrated that the presence or absence of bacteria in the intestinal lumen does not affect intestinal background radioactivity. No statistically significant differences were observed in germ-free mice compared to control animals following injection of ^{18}F-FEAU, ^{18}F-FHBG or [124]I-FIAU. It is known that germ-free mice have distinctive characteristics other than the absence of bacteria, such as greater susceptibility to infection, reduced intestinal vascularity, digestive enzyme activity and muscle wall thickness, and fewer intraepithelial lymphocytes [23]. None of these factors appeared to have influenced our results. Our experimental design excluded bacteria as a major contributor to the high levels of intestinal background radioactivity, but it remains unknown whether a small, perhaps undetectable amount of radiotracer can be excreted by the intestinal epithelium and trapped by bacteria. The commensal flora is composed of aerobic, anaerobic and facultative aerobic bacteria. It

Chapter 4.2

Different strategies for reducing intestinal background radioactivity associated with imaging HSV1-tk expression using established radionucleoside probes

is known that the anaerobic proportion gradually increases from the proximal to distal regions of the intestine, reaching 99% of the inhabitants of the large intestine [24]. We demonstrated that differential accumulation of the radiotracer in the distal compared to proximal part of the intestine is not related to a different bacterial population, but rather to water reabsorption occurring in the distal sections of the intestine, thereby concentrating the radiotracer in the stool and reducing the intestinal progression and elimination of the radionucleoside.

Our biodistribution data for all the radiotracers were comparable to those reported in the literature for ^{18}F-FHBG [4, 7, 25] and ^{18}F-FIAU [4], except for the intestine. We observed intestine radioactivity (%ID/g) values for ^{18}F-FHBG that were almost 15-fold higher compared to that reported in nude mice by Allaudin and colleagues [7, 25], and more than 20-fold higher than that reported in rats by Tjuvajev and colleagues [4]. Despite the differences in animal strain and species in these studies, the common denominator for this discrepancy is the technique used for harvesting and counting intestine samples; namely, intact intestine (containing feces) versus intestinal wall (cleansed of feces). It should be noted that a close correspondence was observed between the tissue sampling and microPET ROI radioactivity measurements (Figure 4). This is also in accordance with our unpublished data, where the majority of intestinal radioactivity was found to reside in the stool, and not in the intestinal wall. Lower levels of abdominal-intestinal background is one advantage for imaging HSV1-tk expression in target cells or tissue with ^{18}F-FEAU and ^{124}I-FIAU compared to ^{18}F-FHBG.

A strategy to increase the intestinal motility to facilitate the progression of stool and hepato-biliary excreted radionucleoside through the intestine was investigated. For this study, we selected a single agent, ^{18}F-FEAU, because it has the best HSV1-tk imaging characteristics and it is likely that ^{18}F-FEAU will be used to image HSV1-tk reporter gene expression more extensively in the future. It is also likely that these bowel-cleansing strategies will be more effective in experiments involving radionucleoside probes with higher intestinal background activity, such as ^{18}F-FHBG. A laxative agent was successfully used in mice by Pickhardt et al. to cleanse the bowel prior to virtual CT colonoscopy [26]. We attempted a similar approach, by increasing bowel motility with Nulytely and food deprivation. Despite the strict monitoring of the animals for signs and symptoms of dehydration, according to the institutional guidelines, the prolonged laxative treatment resulted in dehydration (14% weight loss) and systemic retention of radioactivity due to decreased urine output. The effects of dehydration were reflected in higher blood and tissue radioactivity levels and a higher background visualized on microPET imaging compared to that in control animals. Given that the intestine has a highly branched and developed vascular system, we suggest that the majority of radioactivity observed in the large and small intestine samples of the Nulytely-treated animals is attributed to the blood (compare panels A and B in Figure 3). This does not appear to be the case for the control and Peptamen-treated animals. Therefore, normalization of tissue radioactivity to blood values is a better reflection of biodistribution differences between animal

groups. Moreover, the higher levels of radioactivity obtained in the PET ROIs measurements compared to the tissue sampling measurements (%ID/g), may reflect the analysis of the whole intestinal compartment without precise discrimination between intestine and abdominal vessels (blood pool). Food deprivation and feces loss induced by the PEG-based laxative also contributed to the weight loss. Nulytely® was most effective in cleansing the intestine of radioactive stool compared to the other treatment groups, as measured by the normalized tissue to blood ratio data (see Figure 3). At necropsy, macroscopic viewing of the large and small intestine revealed the near total absence of stool.

Peptamen has been used successfully by Cottart and colleagues as an alternative to laxative agents, in cystic fibrosis transgenic mice to prevent intestinal obstruction [27]. A therapeutic benefit with prolonged survival was described for animals fed with Peptamen for more than 60 days. In our experiments, animals tolerated the Peptamen feeding well for 14 days, without any significant weight loss compared to control animals. Surprisingly, although the liquid diet was thought to transit the gastrointestinal tract more rapidly, the intestinal/abdominal level of radioactivity in the Peptamen® group was not statistically different compared to control animals. Despite the higher lipid content of Peptamen, compared to standard pelleted diet A03 (Safe, Augy, France) (lipids g/100kcal: 3.7 vs 1.6) [27], it has been reported that an amino acid-containing diet may not adequately stimulate cholecystokinin (CCK) release [28]. The known effect of CCK in stimulating the contraction of the gallbladder, the lower esophageal sphincter and the sphincter of Oddi, as well as its role in increasing the motility of the stomach and intestine was reduced during Peptamen® treatment. This probably explains the slightly higher values (although not statistically significant) observed in the Peptamen® group compared to control. Moreover, the high variability in the gallbladder data and the small number of animals per group (n=5) preclude resolution of this issue.

The disadvantages of two of the strategies were reduced by combining them (Peptamen® plus Nulytely®). The combination resulted in only a modest weight loss (6%) compared to control animals, most probably due to the reduction of intestinal contents and fecal mass. Importantly, the continuous feeding with Peptamen® during Nulytely® administration allowed us to partially overcome the dehydration issue. We did not observe signs of dehydration and therefore supplemental fluid administration was not needed. The combined treatment gave a 62% and 69% decrease in large intestine (with feces) radioactivity, respectively, for tissue sampling and microPET measurements compared to controls.

Our final goal was to optimize the visualization of HSV1-*tk* reporter expression in tumor bearing mice. This was assessed by comparing radioactivity measurements in HSV1-tk expressing (transduced) xenografts to background activity measured in wild-type (non-transduced) xenografts and in the abdomen/large intestine. The microPET ROI analysis of the images showed an improvement of 2.2-fold (p<0.001) in the HSV1-tk bearing tumor-to-abdominal ratio for the Peptamen® plus Nulytely® group compared to

Chapter 4.2

Different strategies for reducing intestinal background radioactivity associated with imaging HSV1-tk expression using established radionucleoside probes

the control group. In contrast, there was no change in the transduced-to-wild-type RG2 tumor ratio between the treatment groups. A more complete evaluation of the utility of the combination Nulytely® - Peptamen® treatment should be performed using different HSV1-*tk* transduced models, such as monitoring lymphocyte trafficking or metastatic bone disease, where abdominal/intestinal background radioactivity could be a greater problem and obscure visualization of HSV1-*tk* expression in abdominal structures.

Acknowledgements

References

1. Serganova I, Ponomarev V, Blasberg R. Human reporter genes: potential use in clinical studies. Nucl Med Biol. 2007;34:791-807.

2. Eriksson S, Munch-Petersen B, Johansson K, et al. Structure and function of cellular deoxyribonucleoside kinases. Cell Mol Life Sci. 2002;59:1327-46.

3. Alauddin MM, Shahinian A, Park R, et al. In vivo evaluation of 2'-deoxy-2'-[(18)F]fluoro-5-iodo-1-beta-D-arabinofuranosyluracil ([18F]FIAU) and 2'-deoxy-2'-[18F]fluoro-5-ethyl-1-beta-D-arabinofuranosyluracil ([18F]FEAU) as markers for suicide gene expression. Eur J Nucl Med Mol Imaging. 2007;34:822-9.

4. Tjuvajev JG, Doubrovin M, Akhurst T, et al. Comparison of radiolabeled nucleoside probes (FIAU, FHBG, and FHPG) for PET imaging of HSV1-tk gene expression. J Nucl Med. 2002;43:1072-83.

5. Miyagawa T, Gogiberidze G, Serganova I, et al. Imaging of HSV-tk Reporter gene expression: comparison between [18F]FEAU, [18F]FFEAU, and other imaging probes. J Nucl Med. 2008;49:637-48.

6. Penuelas I, Mazzolini G, Boan JF, et al. Positron emission tomography imaging of adenoviral-mediated transgene expression in liver cancer patients. Gastroenterology. 2005;128:1787-95.

7. Alauddin MM, Shahinian A, Gordon EM, et al. Direct comparison of radiolabeled probes FMAU, FHBG, and FHPG as PET imaging agents for HSV1-tk expression in a human breast cancer model. Mol Imaging. 2004;3:76-84.

8. Nimmagadda S, Mangner TJ, Douglas KA, et al. Biodistribution, PET, and radiation dosimetry estimates of HSV-tk gene expression imaging agent 1-(2'-Deoxy-2'-18F-Fluoro-beta-D-arabinofuranosyl)-5-iodouracil in normal dogs. J Nucl Med. 2007;48:655-60.

9. Yaghoubi S, Barrio JR, Dahlbom M, et al. Human pharmacokinetic and dosimetry studies of [(18)F]FHBG: a reporter probe for imaging herpes simplex virus type-1 thymidine kinase reporter gene expression. J Nucl Med. 2001;42:1225-34.

10. Min JJ, Iyer M, Gambhir SS. Comparison of [18F]FHBG and [14C]FIAU for imaging of HSV1-tk reporter gene expression: adenoviral infection vs stable transfection. Eur J Nucl Med Mol Imaging. 2003;30:1547-60.

11. Chin FT, Namavari M, Levi J, et al. Semiautomated radiosynthesis and biological evaluation of [18F]FEAU: a novel PET imaging agent for HSV1-tk/sr39tk reporter gene expression. Mol Imaging Biol. 2008;10:82-91.

12. Bettegowda C, Foss CA, Cheong I, et al. Imaging bacterial infections with radiolabeled 1-(2'-deoxy-2'-fluoro-beta-D-arabinofuranosyl)-5-iodouracil. Proc Natl Acad Sci U S A. 2005;102:1145-50.

13. Diaz LA, Jr., Foss CA, Thornton K, et al. Imaging of musculoskeletal bacterial infections by [124I]FIAU-PET/CT. PLoS ONE. 2007;2:e1007.

Chapter 4.2 HSV1-

Different strategies for reducing intestinal background radioactivity associated with imaging HSV1-
tk expression using established radionucleoside probes

14. Brader P, Stritzker J, Riedl CC, et al. Escherichia coli Nissle 1917 facilitates tumor detection by positron emission tomography and optical imaging. Clin Cancer Res. 2008;14:2295-302.

15. Berg RD. The indigenous gastrointestinal microflora. Trends Microbiol. 1996;4:430-5.

16. O'Hara AM, Shanahan F. The gut flora as a forgotten organ. EMBO Rep. 2006;7:688-93.

17. Serganova I, Doubrovin M, Vider J, et al. Molecular imaging of temporal dynamics and spatial heterogeneity of hypoxia-inducible factor-1 signal transduction activity in tumors in living mice. Cancer Res. 2004;64:6101-8.

18. Tjuvajev JG, Avril N, Oku T, et al. Imaging herpes virus thymidine kinase gene transfer and expression by positron emission tomography. Cancer Res. 1998;58:4333-41.

19. Tjuvajev JG, Stockhammer G, Desai R, et al. Imaging the expression of transfected genes in vivo. Cancer Res. 1995;55:6126-32.

20. Soghomonyan SA, Doubrovin M, Pike J, et al. Positron emission tomography (PET) imaging of tumor-localized Salmonella expressing HSV1-TK. Cancer Gene Ther. 2005;12:101-8.

21. Lu H, Chen C, Klaassen C. Tissue distribution of concentrative and equilibrative nucleoside transporters in male and female rats and mice. Drug Metab Dispos. 2004;32:1455-61.

22. Pastor-Anglada M, Cano-Soldado P, Molina-Arcas M, et al. Cell entry and export of nucleoside analogues. Virus Res. 2005;107:151-64.

23. Shanahan F. The host-microbe interface within the gut. Best Pract Res Clin Gastroenterol. 2002;16:915-31.

24. Magalhaes JG, Tattoli I, Girardin SE. The intestinal epithelial barrier: how to distinguish between the microbial flora and pathogens. Semin Immunol. 2007;19:106-15.

25. Alauddin MM, Shahinian A, Gordon EM, et al. Preclinical evaluation of the penciclovir analog 9-(4-[(18)F]fluoro-3-hydroxymethylbutyl)guanine for in vivo measurement of suicide gene expression with PET. J Nucl Med. 2001;42:1682-90.

26. Pickhardt PJ, Halberg RB, Taylor AJ, et al. Microcomputed tomography colonography for polyp detection in an in vivo mouse tumor model. Proc Natl Acad Sci U S A. 2005;102:3419-22.

27. Cottart CH, Bonvin E, Rey C, et al. Impact of nutrition on phenotype in CFTR-deficient mice. Pediatr Res. 2007;62:528-32.

28. Borowitz D, Durie PR, Clarke LL, et al. Gastrointestinal outcomes and confounders in cystic fibrosis. J Pediatr Gastroenterol Nutr. 2005;41:273-85.

4.3

In vivo quantitative assessment of cell viability of Gadolinium or iron-labeled cells using MRI and BLI

Guenoun J*, **Ruggiero A**, Doeswijk G, Janssens RC,
Koning GA, Kotek G, KrestinGP, Monique R. Bernsen
*Both authors contributed equally to this work

Abstract

In cell therapy, non-invasive monitoring of *in vivo* cell fate is challenging. In this study we investigated possible differences in R1, R2 or R2* relaxation rate as a measure of cell viability for mesenchymal stem cells labeled with Gd-liposomes (Gd-MSCs) or iron oxide nanoparticles (SPIO-MSCs). Cells were also transduced with a luciferase vector, facilitating a correlation between MRI findings and cell viability using bioluminescence imaging (BLI). Viable Gd-MSCs were clearly distinguishable from non-viable Gd-MSCs under both *in vitro* and *in vivo* conditions, clearly differing quantitatively (ΔR1 and ΔR2) as well as by visual appearance (hypo- or hyperintense contrast). Immediately post-injection, viable Gd-MSCs caused a substantially larger ΔR2 and lower ΔR1 effect compared to non-viable MSCs. With time, the ΔR1 and ΔR2 relaxation rate showed a good negative correlation with the increasing cell number following proliferation. Upon injection, no substantial quantitative or visual differences between viable and non-viable SPIO-MSCs were detected. Moreover, non-viable SPIO-MSCs caused a persisting signal void *in vivo*, compromising the specificity of this contrast agent. *In vivo* persistence of SPIO particles was also confirmed by histological staining. A large difference was found between SPIO- and Gd-labeled cells in the accuracy of MR relaxometry to assess the cell viability status. Gd-liposomes provide a more accurate and specific assessment of cell viability than SPIO-particles. Viable Gd-cells can be differentiated from non-viable Gd-cells even by visual interpretation. These findings clearly indicate towards Gd as the favourable contrast agent in qualitative and quantitative evaluation of labeled cell fate in future cell therapy experiments.

Introduction

In recent years, cell transplantation has evolved to a promising treatment option for a variety of diseases and disorders such as cancer, cardiovascular disease, neurodegenerative diseases, and musculoskeletal disorders. This field clearly benefited from the technological advancements in imaging sciences as the majority of clinical trials involved the use of one or more imaging modalities to evaluate therapeutic efficacy of stem cell transplants (1-4). Molecular imaging techniques enable a complete assessment of the implanted stem cells (viability, proliferation, migration, differentiation) and contribute to important insights into the mechanism of action of stem cells (5-6). However, not all preclinical visualization tools can be easily translated to clinical applications. One of the critical issues to address in cell transplantation is the noninvasive assessment of cell engraftment and survival in the long term. In pre-clinical research, investigation of cell viability usually requires the use of laborious *ex vivo* histological techniques. As histology provides only a snap-shot at a certain time point, an intra-individual longitudinal assessment of stem cell fate needs a different approach. The ability to non-invasively deduce basic functional information from cell transplants, would provide a powerful tool for evaluating therapy effect and initiate progress towards translational research.

MRI is a favourable imaging modality due to its high spatial resolution, lack of use of ionizing radiation, excellent soft tissue visualization and functional information. Visualization of transplanted cells with MRI can be relatively easily accomplished by labeling the cells with MRI contrast agents (7). Until now, iron-oxide based T2 contrast agents (CAs) (8-11) were considered the CA of choice, mainly given their high sensitivity. However, their use carries some serious limitations. Iron particles released from apoptotic cells will undergo re-uptake by locally attracted macrophages (12-18), causing a false-positive MRI signal. This is a relevant issue in imaging of cell transplants. For example, in cell grafting for repair of myocardial infarction, over 90% cell death occurs in the first 24 hours post-transplantation (19-21). Furthermore, once iron particles have been cleared by macrophages, the magnetic label can be transferred to other cells of the monocyte/macrophage system and presumably also to many other cell types (22). This further complicates the iron clearance pathway, deteriorating the specificity of the MRI signal even more and clearly illustrating the difficulties in unambiguous identification of transplanted SPIO labeled cells.

The use of the T1 CA Gd-DTPA might overcome these limitations. As macrophage endocytosis is mainly size-dependent (13), it is hypothesized that the low molecular weight (500Da) Gd-DTPA molecule can escape macrophage re-uptake. Following labeled cell death, the swift diffusion of Gd will therefore increase the specificity of MRI signal read-out. Previously, it was shown that labeling with Gd-liposomes produces excellent MR visibility of mesenchymal stem cells (23). Remarkably, several studies reported a reduced longitudinal relaxivity following cellular internalization of Gd *in vitro* (24-27). This 'quenching' is mainly caused by the decreased accessibility of H_2O to

compartmentalized Gd (28-29). To our knowledge, the 'quenching' of Gd has not been studied *in vivo* up to now. We hypothesize that cell death, and the subsequent release and decompartmentalization of Gd will result in an increased T1 shortening *in vivo*.

The aim of this study was to assess whether the contrast characteristics of Gd-liposomes can be used to distinguish between viable and non-viable cells in vivo in comparison to SPIO-labeled cells. For validation of MRI findings cells transduced with the luciferase gene were used for additional bioluminescence imaging (BLI) as well. As the activity of the luciferase enzyme is dependent on Mg^{2+}, ATP and O_2, it will be active in viable cells only, thus providing an excellent validation tool for cell viability assessment (30).

Results

In vitro contrast behaviour

The actual death rate of cells, rendered non-viable by repeated freeze thawing, was shown to be 99% by a Trypan Blue exclusion test (fig. 1). Non-viable cells remained largely intact. In addition, to confirm the specificity of BLI for viable cells, photon emission by dead cells was shown to be absent (fig. 2a,b). Linear regression analysis showed the amount of emitted photons and the number of viable cells to be linearly proportional (fig. 2b). These findings supported the use of BLI as a validation tool for our MR results.

Heavily concentrated samples of viable Gd-MSCs generated a signal void (hypointensity) on MR images, an effect which is known as 'quenching' (fig 3a). In contrast, similar concentrations of non-viable Gd-MSCs generated a bright signal (hyperintensity) allowing them to be visually distinguished from viable Gd-MSCs.

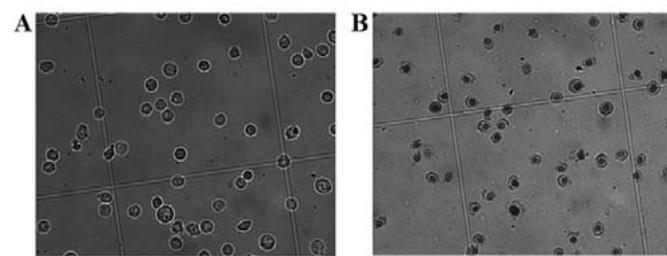The ΔR1 (fig. 4a) and ΔR2 (fig. 4b) relaxation rate were found to be linearly pro-

Fig. 1 Light microscopy image showing Trypan Blue exclusion test on Gd-liposome labeled MSCs prior to transplantation. Viable Gd-MSCs (a) exclude the Trypane Blue dye, whereas nonviable MSCs (b) stain blue due to membrane disintegrity.

portional to the Gd-labeled cell amount across the entire range of cell numbers studied, thus allowing the measurement of the relaxivity per cell. The r1 and r2 cellular relaxivities (r1$^\emptyset$ resp. r2$^\emptyset$) were determined from the slopes of the regression lines of the R1 and R2 relaxation rates against cell number. For viable Gd-cells this yielded a r1$^\emptyset$ of 2 x 10^{-7} s^{-1} cell^{-1} and r2$^\emptyset$ of 4 x 10^{-6} s^{-1} cell^{-1}. For non-viable Gd-cells r1$^\emptyset$ and r2$^\emptyset$ were 5 x 10^{-7} s^{-1} cell^{-1} and 1 x 10^{-6} s^{-1} cell^{-1}, respectively. As both viable and non-viable SPIO-MSCs (fig. 3b) generated a signal void, a viability assessment based on mere visual distinction was
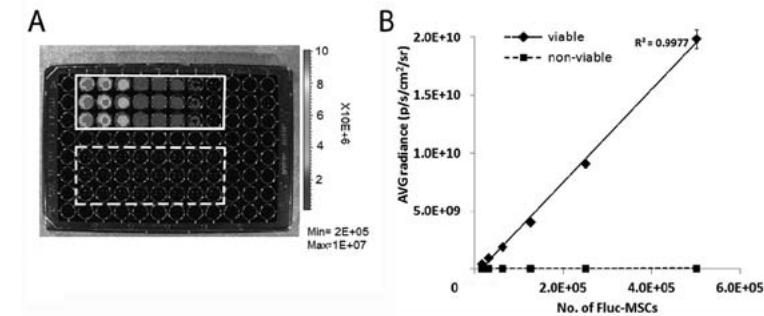
Fig. 2 Bioluminescence imaging of a 1:1 serial dilution of a stock of 5*10^5 unlabeled Fluc-MSCs. BLI image showing signal from viable MSCs (rectangular box) and the absence of signal from non-viable MSCs (dashed rectangular box) (a). Total amount of captured photons was linearly proportional to MSC concentration (b).

not possible. Moreover, T2 and T2* measurements showed no substantial difference in the ΔR2 (fig. 4c) or ΔR2* (fig. 4d) relaxation rate between viable and non-viable SPIO-MSCs. For both viable and non-viable SPIO-MSCs r2$^\emptyset$ was assessed to be 2 x 10^{-4} s^{-1} cell^{-1}. The r2*$^\emptyset$ relaxivity for viable SPIO-MSCs was 9 x 10^{-6} s^{-1} cell^{-1} and for non-viable cells 0.1 x 10^{-6} s^{-1} cell^{-1}.
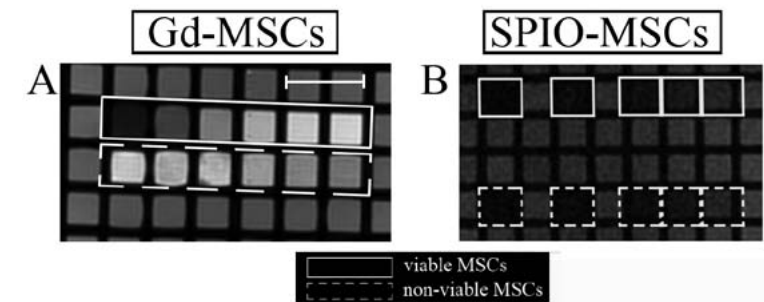
Fig. 3 MR-imaging of in vitro dilution series of viable vs non-viable labeled MSCs at 3.0T. T1-weighted image of Gd-liposomes labeled MSCs (a) and T2-weighted image of SPIO-labeled MSCS (b). The viable cell serial dilution series is demarcated by the undashed rectangular box, non-viable cells by the dashed rectangular box. Cell concentrations from left to right: 1.65*10^5, 8.3*10^4, 4.1*10^4, 2.1*10^4, 1.0*10^4 and 5.1*10^3 MSCs µl^{-1} Ficoll. Scale bar represents 10 mm and applies to both (a) and (b).

Longitudinal in vivo contrast behavior

As expected, non-viable MSCs from both groups did not generate bioluminescent signal *in vivo* (fig. 5a,b). All injected cell grafts were clearly visualized on MRI following injection (fig. 5a,b). Optimized T1, T2 and T2*-weighted sequences were used to cover the entire range of cell visibility during the follow-up time and cell division. SPIO-MSCs caused a signal void (hypointensity), regardless of the cell viability (fig. 5a). In the acute post-transplantation stage, no substantial differences in visual appearance or R2 and R2*
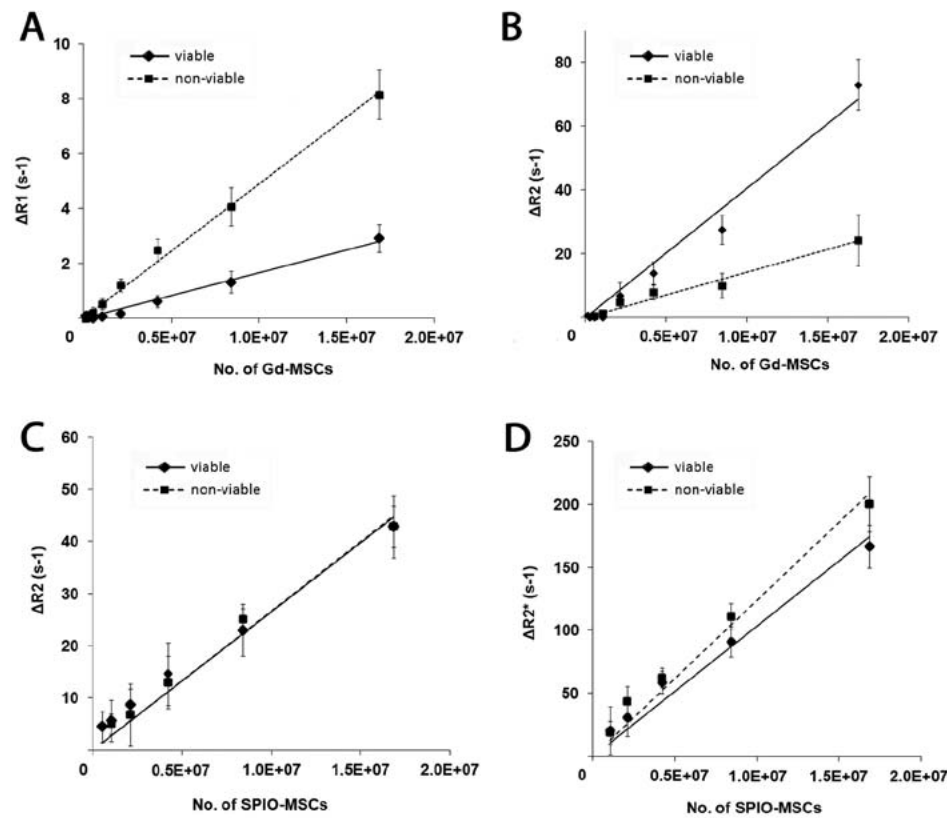
Fig. 4 ΔR1 (a), ΔR2 (b,c) and R2* (d) as a function of Gd or SPIO labeled cell density. The longitudinal r1 (a) and transverse cellular r2 relaxivity (b,c) were obtained by a linear fit of the data. Data are presented as mean ± SD (n=3 different samples, SD refers to intersample SD).
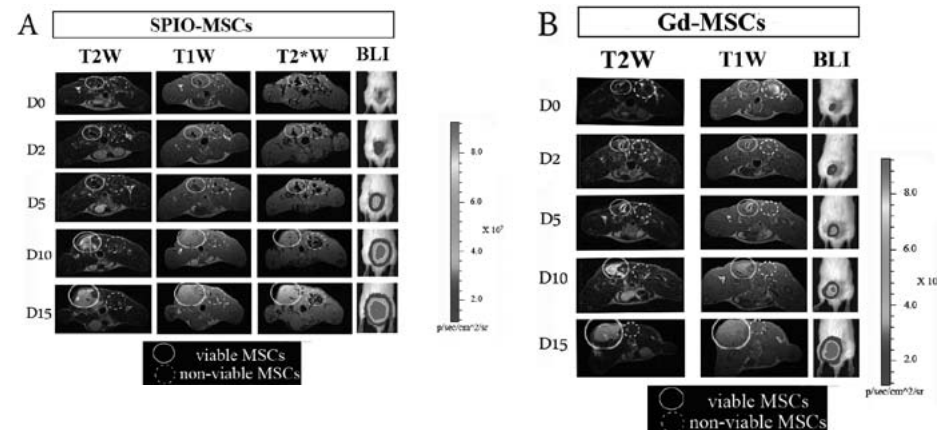

Fig. 5 Dual modality longitudinal imaging of MSCs transplanted in the lower back muscle. Imaging of SPIO-MSCs (a) and Gd-MSCs (b) on T2-weighted FSE (TE 120 ms, TR 3000, NEX 4) T1-weighted SE (TE 10 ms, TR 1200 ms) and T2*-weighted GRE (TE 8 ms, TR 50 ms, α 16º) images. BLI shows considerable viable cell proliferation, visible on MRI as a gradual decrease (Gd-MSCs) and increase (SPIO-MSCs) in signal intensity.
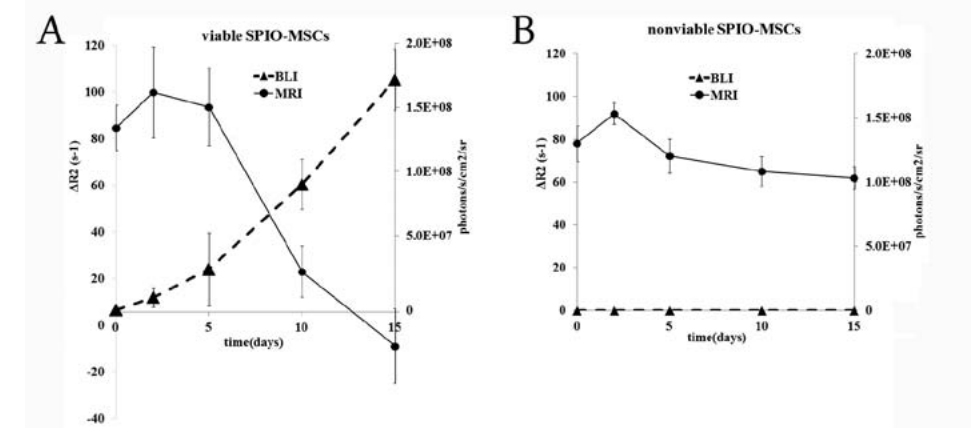

Fig. 6 In vivo measurement of the ΔR2 and ΔR2* relaxation rate of SPIO-MSCs. The ΔR2 effect from viable SPIO-MSCs gradually decreased over time, accompanied by an increasing BLI signal. Non-viable cells displayed a marginal decrease in ΔR2 over time. Data are presented as mean ± SD (n=6 rats, SD refers to inter animal SD).

values were detected between viable and non-viable SPIO-MSCs (fig. 6a,b). Over time, the number of detected photons increased at the site of viable cells injection (fig. 5, 6). In parallel, a substantial drop in ΔR2 relaxation rate from viable SPIO-MSCs (23±11 s^{-1}) occurred from day 5 onwards (fig. 6a), whereas ΔR2 from non-viable cells was virtually unchanged (65±7 s^{-1} at day 14 vs 78±8 s^{-1} at day 0) (fig. 6b). Due to gradual dilution, signal void from viable SPIO-MSCs was barely visible on T2-weighted scans at day 15, except for a small hypointense core on T2*-weighted scans (fig. 5a).

Viable Gd-MSCs showed a remarkable dynamic signal behavior. Immediately post transplantation, they were consistently detected as a hypointense area on T1-weighted scans ('quenched signal intensity'), whereas a similar density of non-viable Gd-MSCs resulted in increased signal intensity (hyperintensity) at the injection site (fig. 5b). In contrast to SPIO-MSCs, hyperintense signal from non-viable Gd-MSCs resolved already after 2 h post-transplantation (data not shown). Quantitatively, this distinction was reflected by substantial differences in R1 and R2 relaxation rates between viable and non-viable Gd-MSCs (fig. 7). At day 0, the ΔR1 effect (0.5±0.2 s^{-1};fig. 7a) of viable Gd-MSCs was nearly half of the ΔR1 from non-viable MSCs (0.9±0.3 s^{-1};fig. 7b), while causing a substantially larger ΔR2 effect (66±26 s^{-1};fig. 7c) compared to non-viable MSCs (0.6±2.9 s^{-1};fig. 7d). Both the ΔR1 and ΔR2 relaxation rate correlated very well with the increasing cell number following proliferation (Spearman r correlation coefficient 0.89 and 0.90 respectively, p<0.05). T1$_{ref}$ and T2$_{ref}$ (the T1 resp. T2 of normal muscle tissue) were assessed to be 1500±91 ms and 36±7.0 ms respectively.
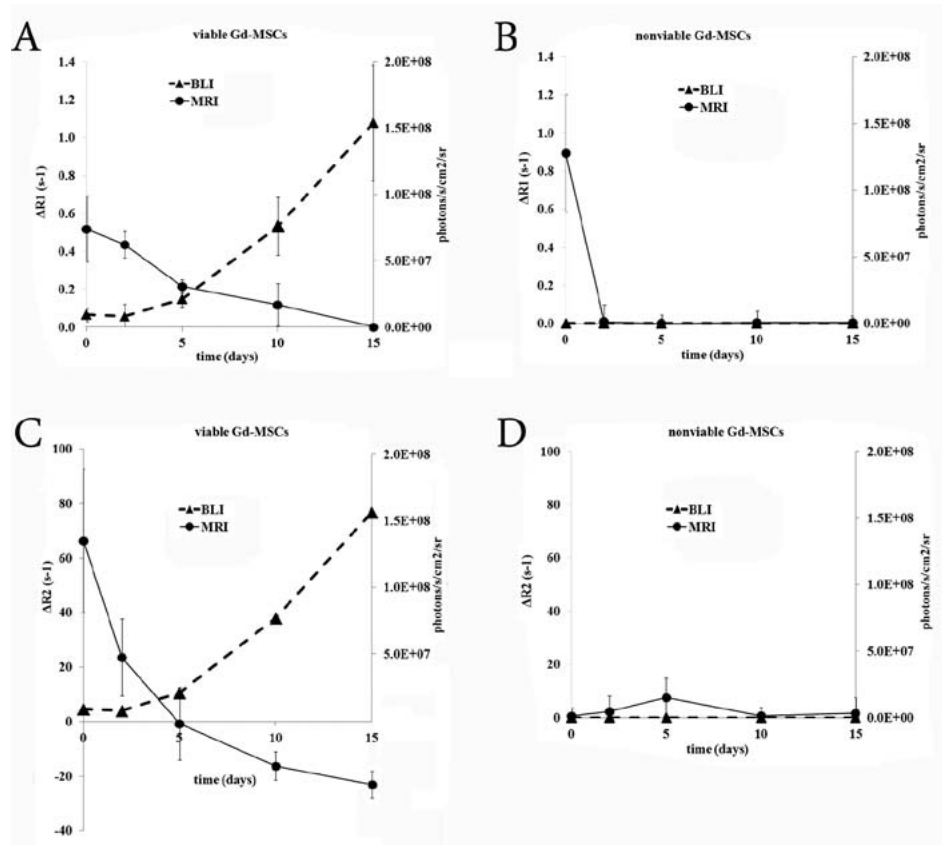
Retention of contrast agent Gd

Fig. 7 In vivo measurement of R1 R2 and relaxation rate of Gd-MSCs. Upon injection, viable Gd-MSCs cause a substantially larger ΔR2 but smaller ΔR1 effect than non-viable Gd-MSCs. ΔR1 and ΔR2 relaxation rate correlated well with the increasing cell number (Spearman r correlation coefficient 0.89 and 0.90 respectively, p<0.05). Data are presented as mean ± SD (n=6 rats, SD refers to inter animal SD).

Fig. 8 Histological detection of cells labeled with rhodamine containing Gd-liposomes, in skeletal muscle tissue (day 15 post-transplantation). Red fluorescence from the rhodamine-liposomes is clearly visible as is the blue nuclear dye Hoechst, added to the cells in culture prior to injection. Inset shows a 10x magnification of the area indicated by the rectangle.

Table 1

	Injected total Gd amount at day 0 (μg)	Retrieved Gd amount at day 14 (μg)	Retrieved Gd amount (%)
Viable Gd-MSCs	145±12	123±14	84±10
Non-viable Gd- MSCs	137±9	12±3	9±2

The retrieved amount of Gd from viable cells was 84±10% of the injected amount, whereas only 9±2% of the initially injected Gd amount was retrieved at sites of transplanted non-viable cells (Table 1). Red fluorescent signal from Gd-liposomes was not detectable at sites where non-viable Gd-MSCs had been injected, suggesting an efficient elimination. Viable transplanted Gd-MSCs however were clearly idientified at the site of transplantation at day 15 by the blue Hoechst dye and the perinuclear red dye from liposomes (fig. 8). At sites of injection with non-viable SPIO-MSCs, iron was shown to be still present (fig. 9), in close proximity to post-injection hemorrhages.
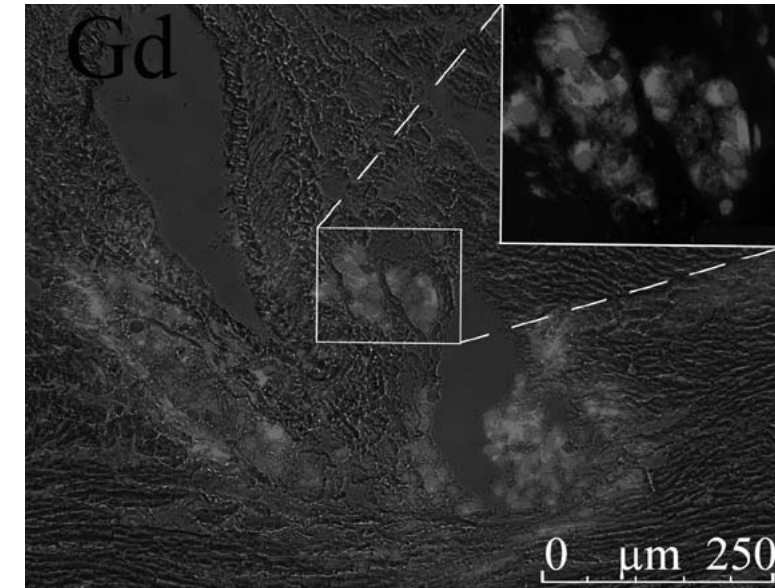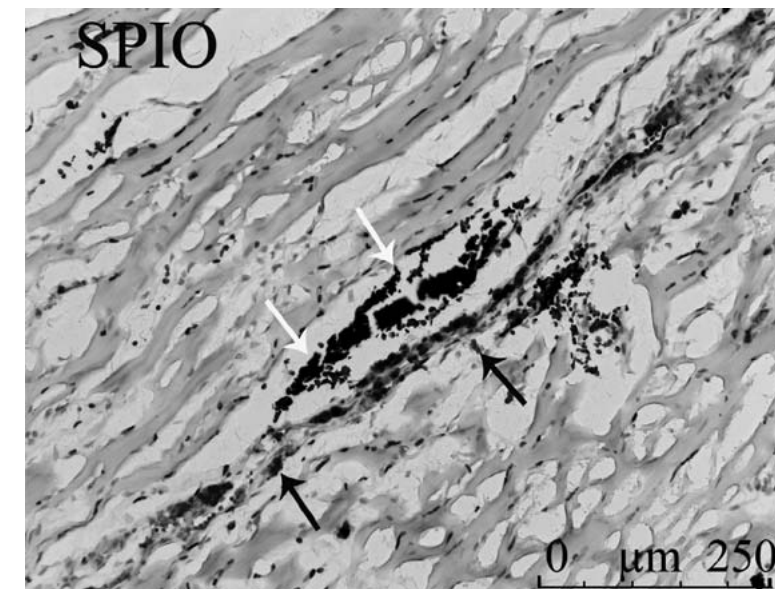

Fig. 9 Histological detection of skeletal muscle tissue (day 15 post-transplantation), priorly transplanted with non-viable SPIO-MSCs. Perl's iron stain shows iron (black arrows) to be still present, in close proximity of erythrocytes (white arrows).

Discussion

Molecular imaging has rapidly become a necessary tool for the validation and optimization of stem cell engrafting strategies in preclinical and clinical studies. One of the most critical and unresolved issues is the non-invasive assessment of the survival and proliferation of cells after implantation. Several available approaches using reporter genes allow the in vivo monitoring of cell survival, monitored by either MRI (31-32), bioluminescence (30) or nuclear techniques such as PET/SPECT (33-34). The reporter gene technique however, being quite invasive, cannot be easily translated to the clinical arena. Therefore we sought to investigate a minimally invasive labeling technique which reflects the actual viability of labeled cells, and validated it by BLI.

A future translation of MRI-based cell tracking to clinical medicine will require an excellent sensitivity and specificity of the contrast probe or an acceptable trade-off between these two requirements, depending on the application. High sensitivity might be essential to investigate the long term fate of implanted stem cells, since probe dilution upon cell proliferation might reduce the detection capabilities. Alternatively, a high specificity is demanded by applications such as cellular transplantation, to detect cell graft rejection at an early stage.

In the current study we have shown Gd to be more specific than SPIO nanoparticles. Irrelevant signal from non-viable Gd-MSCs resolved already 2 h post-transplantation (data not shown) while at the original injection site of non-viable SPIO-MSCs hypointense MRI signal persisted for at least 15 days. In a recent study by Baligand et al., it was reported that even 95 days post-transplantation, false-positive SPIO signal was still detectable in immunorejected grafts (35). Terrovitis et al. concluded that MRI of iron oxide-labeled stem cells is not a reliable technique for quantifying engraftment in the heart because of the considerable residual signals generated by the persistence of iron-laden tissue macrophages after cell death (17). Reuptake by macrophages of previously released SPIO seems to play a major role in this phenomenon (12-16). Specificity is a very important issue, especially in direct injections, involving high cell mortality rates; it would lead to massive release SPIO followed by macrophage uptake, thereby severely increasing the amount of false positives (decreased specificity). In contrast, as a result of its biological short half-life and low molecular weight (36-37), the vast majority of extracellular complexed Gd will diffuse out fast to end up intravascularly, followed by renal excretion (38). Theoretically it is thus less likely that complexed Gd released by injected dead cells undergoes reuptake by surrounding phagocytic cells. This is in line with our observations that only a fraction of the initially injected Gd quantity, contained in non-viable MSCs, was retrieved at the site of injection at day 15 (Table 1).

The intrinsic lower sensitivity of Gd, in comparison with SPIO, has been one of the main reasons of its limited use for cell tracking purposes (39). We observed that viable Gd-MSCs still generated sufficient hyperintense contrast up to at least 10 days post-

transplantation. At day 10 viable SPIO-MSCs no longer caused a pronounced signal loss. However, a small hypointense core remained, that contributed to a still significant $\Delta R2$ value of the whole cell cluster area. Loss of hypointensity (increase in signal intensity) is known to be caused by dilution due to cell proliferation. An additional disadvantage of SPIO was reported in a study by Walczak et al. (40), stating that accelerated SPIO dilution occurs in highly proliferating cells as a result of iron metabolism in the physiological cellular pathways (41). This effect has very likely played a role in the current study as well. The fact that Gd is not metabolized intracellularly can therefore be a major incentive to use Gd instead of SPIO, especially for highly proliferating cells. Baligand et al. reported the detection of Gd-myoblasts up to 2 weeks (35). In that study however, the amount of Gd retained intramuscularly was not reported and no correlation was made with cell death or cell proliferation. Hence it was not clear whether Gd signal decay was due to either the effective elimination of released Gd from dying cells (high specificity) or proliferation-induced Gd-dilution (low sensitivity) or a combination of both.

Several reports exist on the quantitative differentiation of cell-bound SPIO from free SPIO (as may occur after cell death), making use of either the R2 and/or R2* transverse relaxation rate. According to Kuhlpeter et al. compartmentalized, cell bound-SPIO causes a larger R2* than free SPIO (42). The opposite effect was described in a recent study by Henning et al. (43), reporting a statistically significant difference in T2 transverse relaxation time between viable and non-viable lysed cells, but not in T2*. In the latter study however, differences were reported only in vitro and could not be reproduced in vivo in arthritic joints. These differences in quantification results can be attributed to the somewhat complex nature of SPIO quantification. Quantification of SPIO-labeled cells is not straightforward. R2 relaxation rate is not only dominated by the iron content but also by the distribution of iron within a voxel (44-46). Quantification of the R2* relaxation rate on the other hand can be hindered by macroscopic susceptibility artefacts arising from air-tissue interfaces (47). Supposing that free SPIO can indeed be differentiated quantitatively from intracellular incorporated SPIO, this feature will be useless to distinguish between viable and non-viable cells as soon as bystander macrophages enter the transplantation site to engulf the free SPIO particles, released by non-viable cells. In the current study, our T2 measurements showed no substantial difference in the $\Delta R2$ relaxation rate between viable and non-viable SPIO-MSCs. This was not unexpected as changes in T2 are governed for a large part by decompartmentalization of SPIO particles. Although cells had been freeze-thaw multiple times, they remained relatively intact. As SPIO particles are significantly larger than low molecular weight Gd, it seems unlikely that early in the cell death process SPIO particles will diffuse out. In later stages of cell death with concurrent cell fragmentation, SPIO particle decompartmentalization will start to affect R2 and/or R2*.

In this study we showed that Gd-MSCs exhibit a distinct relaxivity as a direct result of the cell viability both *in vitro* and *in vivo*, non-viable Gd-MSCs having a virtually absent R1 and R2 relaxation rate. Recalling that Gd-MSCs $\Delta R1$ and $\Delta R2$ relaxation rate

correlated very well with the increasing cell number following proliferation (r 0.89 and 0.90 respectively, p<0.05), Gd labeling of MSCs can thus very well be used as a tool to track cell fate in vivo.

Viable Gd-MSCs showed a remarkable hypointensity ('signal quenching') directly post-transplantation. This allowed for a clear visual distinction of viable from non-viable cells, making this a valuable qualitative tool for fast read-out of cell fate. This quenching occurred in vitro as well, but at a higher cell density. This is believed to be due in part to differences in water availability, diffusivity and concentration effects in vivo. Even when cells are being transplanted at a similar concentration as in vitro, the density of grafted cells *in vivo* will increase because of tissue pressure, resistance and liquid resorption, resulting in an increased Gd load per voxel. Proliferation will inevitably result in cellular Gd dilution and thus a decreased Gd load per voxel, referred to as 'dequenching'. In the current study this was observed as a hypointense quenched cell graft core, with peripheral hyperintensity. As for the striking contrast difference between viable and non-viable Gd-MSCs a plausible explanation is the following. Gd exerts its T1-shortening effect (i.e. R1 increase) by interacting with surrounding water molecules. It can thus be understood that it will be challenging for water to reach Gd which resides in endosomes inside viable cells with an intact membrane. Furthermore, efflux of Gd from viable cells will be highly unlikely. This 'quenching' effect as a result of cellular Gd compartmentalization was reported previously by Terreno et al. (27). Similarly, in another study by Biancone et al. (48) an initial increase in signal intensity of endosomally contained Gd-HPDO3A was reported. This was explained to occur as a result of intracellular redistribution after endosomal degradation. We mimicked the compartmentalization effects in vitro (fig. 4), comparing viable intact cells with non-viable leaky cells. Interestingly, our measurements confirmed that both $\Delta R1$ (decrease; fig. 4a) *and* $\Delta R2$ (increase; fig. 4b) are affected by compartmentalization, causing the typical Gd signal 'quenching' in viable cells. 'Quenching' by viable Gd-cells can thus be explained by a decrease in the $\Delta R1/\Delta R2$ ratio. Non-viable cells however, allowing both an efflux of Gd and/or influx of water molecules more easily, will exhibit an increased $\Delta R1/\Delta R2$ ratio.

Quantification methods based on T1 or T2 may provide a valuable but laborious and time-consuming tool, both on the data acquisition side as well as on the data processing side. Clearly, this is not a relevant disadvantage for research applications. However, for a successful translation to clinical practice, where time-efficiency is of utmost importance, a qualitative, fast and visually interpretable tool is key.

In this paper, we made use of Gd to allow for a non-ambiguous distinction between cell death and viability. A combined interpretation of the quantitative ($\Delta R2/\Delta R1$) and qualitative findings (contrast changes) may present an important non-invasive tool to track the actual cell fate of transplanted cells in real time, using mere MRI. Summarizing, in practice this means that a visible hypointense signal reflects viable cells; 'dequenching' (hypointense to hyperintense contrast) indicating cell proliferation; the persistent visibility of hyperintense signal indicating ongoing presence of viable cells; quick disappearance of hyperintense signal indicating cell death; slow disappearance of hyperintense signal indicating ongoing cell proliferation. These may be considered as rough rules of thumb. For a more detailed cell fate evaluation a correlation to R1 and R2 values remains essential. Nevertheless, as a result of the high specificity, these rules of thumbs may prove beneficial in a clinical setting, e.g. when immediate monitoring of cell graft rejection is needed. To our knowledge, our study is the first to report the Gd quenching effect as an easy to interpret qualitative tool for cell viability assessment.

Material and Methods

Preparation and characterization of liposomes

Gd-DTPA was incorporated in cationic liposomes using the lipid-film hydration technique, as described before (23). Briefly, a 100 µmol mixture of 1,2-dipalmitoyl-*sn*-glycero-3-phosphocholine (DPPC; Lipoid GmbH, Ludwigshafen, Germany), cholesterol (Sigma-Aldrich, St. Louis, MO, USA), 1,2-dioleoyl-3-trimethylammonium-propane (chloride salt) (DOTAP; Avanti Polar lipids, Alabaster, AL, USA) and rhodamine-PE (Avanti Polar lipids) in the molar ratio 47:33:20:0.1 was dissolved in chloroform/methanol, evaporated and hydrated in Gd-DTPA (Magnevist; Bayer Schering Pharma AG, Berlin, Germany). Following extrusion through 200nm and 100nm filters and ultracentrifugation to separate non-encapsulated from encapsulated Gd, the liposome pellet was resuspended in 2 ml HEPES.

Liposomal size was determined by dynamic light scattering (DLS) using a Zetasizer Nano (Malvern Instruments, Worcestershire, UK). The mean resultant size of Gd-DTPA liposomes was 101 nm with a polydispersity index (PDI) of 0.07. The zeta potential was 43±7.0 mV.

Liposomal phosphate content was assessed by spectrophotometric analysis according to Rouser (49). Relative Gd content was determined by Inductively Coupled Plasma-Optical Emission Spectroscopy (ICP-OES; Optima 4300DV, Perkin Elmer, Norwalk, CT) operating at a wavelength of 342 nm.) and was 66±4 µg Gd/µmol total lipid.

Virus construction and production

A self-inactivating lentivirus was prepared by transient transfection of HEK293T cells in 6x19cm dishes. Briefly, pND-Cag-Luc (60µg/dish) was cotransfected into HEK293T cells with a mixture of pMDLg/pRRE (30µg/dish), pMD2.G (15µg/dish) and pRSV-Rev (15µg/dish) packaging plasmids using polyethylemine.

Lentiviral supernatant was collected at 48 h and 72 h, filtered (0.45µm) and concentrated by ultracentrifugation with a Beckman 45Ti rotor at 20K (4 ºC, 2 hours). The

pellet was then resuspended in 1ml PBS. Mesenchymal stem cells (MSCs; Millipore, Billerica, MA, USA) were grown to 50% confluency in a 24 well plate in DMEM/F10, 10% FCS, P/S and infected with 50 µl lenti-viral stock, resulting in luciferase expressing MSCs.

Cell labeling and preparation

Fluc-MSCs of passage 2 or 3 were used for all experiments at 70% subconfluency. MSCs were cultured in Dulbecco's modified Eagle medium (Invitrogen; Carlsbad, CA, USA) supplemented with 2% FBS (Lonza; Basel, Switzerland), 2% penicillin/strepto-mycin (Invitrogen), 2% L-glutamine (Invitrogen), 1% MEM essential vitamin mixture (Lonza), 1% NEAA (Sigma-Aldrich; St. Louis, MO) and 0.5% glutamax (Invitrogen). Following two washing steps with PBS (Invitrogen, Breda, The Netherlands), the cul-ture medium was replaced by Optimem (Invitrogen). Cells were then labeled for 24h with SPIO (Endorem™; Guerbet S.A., Paris, France) containing 100 µg Fe/ml culture medium (50) or with 125 µM Gd-liposomes for 4h (23). Following labeling, cells were harvested by trypsinization, washed 3 times in PBS and centrifuged at 300 G for 5 min-utes to discard of unincorporated contrast agent.

After centrifugation, cells were equally divided over two separate tubes and further processed to use as either viable cells or dead cells. Non-viable cells were obtained by re-peated freeze thawing of one final suspension in liquid nitrogen. Cell death was assessed by Trypane Blue assay. For *in vitro* experiments, cell pellets were each suspended in Ficoll solution with a density of 1.07 g/mL, to prevent cell sedimentation during imaging (51). For *in vivo* experiments, the cell pellet was suspended in PBS.

MRI and BLI Phantom studies

From the same stock of cells serial dilutions containing live or dead cells were sus-pended in 50µl Ficoll and transferred to a 96 well plate (BLI phantom). Surrounding wells were filled with water to prevent susceptibility artefacts due to air and/or very con-centrated samples. MRI data were acquired by using a 3T clinical scanner (Signa Excite; GE Medical Systems, Milwaukee IL, USA) with unmodified gradients and custom made surface coils (inner diameter of 5 cm). Spin echo (SE) sequences with multiple TR (100-2800 ms; TE10 ms) and multiple TE (10-100 ms; TR 600 ms) were used to obtain T1 longitudinal relaxation times and T2 transverse relaxation times, respectively. T2* trans-verse relaxation times were obtained with a 3D GRE sequence (matrix = 234 x 234, slice thickness = 0.7 mm and NEX = 2, using lower TEs (3-36 ms). Sequences were acquired with a field of view (FOV) = 5.0 x 5.0 cm², matrix = 160 x 160, slice thickness = 1.4 mm and NEX = 2. An in-house developed algorithm script for Matlab (version R2007b) as well as Image J with the MRI analysis calculator (by Karl Schmidt) T1, T2 and T2* times were calculated. The MRI analysis calculator has been used previously by other authors (52-53). Relaxation times were calculated as follows:

$$(1) \qquad \Delta R1_{cells} = \frac{1}{T1_{cells}} - \frac{1}{T1_{ref}}$$

In which $T1_{cells}$, represents the T1 of the cell cluster (both *in vitro* and *in vivo*) and $T1_{ref}$ the T1 of the surrounding wells containing Ficoll (*in vitro*) or of normal muscle (*in vivo*). The same formula was applied to derive the $\Delta R2$ and $\Delta R2^*$ using T2 and T2*, respectively. $T1_{ref}$ and $T2_{ref}$ *in vitro* were assessed to be 3100±120 ms and 167±18 ms respectively. $T1_{ref}$ and $T2_{ref}$ *in vivo* were assessed to be 1500±91 ms and 36±7.0 ms respectively. A voxel-by-voxel linear least squares fit of the natural logarithm of the sig-nal amplitude versus at least 6 echo times (TE) was performed to construct R2 and R2* maps. For R1 maps at least 6 repetition times (TR) were used.

For BLI phantoms, luciferase activity of Fluc-MSCs was measured by using the Xe-nogen IVIS Spectrum (Caliper LS, Hopkington, MA, USA) 10 min after the addition of D-Luciferine at a final concentration of 50 µg/µl (integration time, 10, 20, 30, 40,50, and 60 s; f/stop,1; binning, medium; field of view, B). Optical intensity is reported as photons/second/area/steradian (p/s/cm²/sr). Data were analyzed with the software Living Image vers. 3.2 (Caliper LS).

Cell transplantation and in vivo imaging

All animal experiments were conducted in compliance with dutch law and approval of the Institutional Animal Welfare Committee. Animals were provided with food and water *ad libitum*. All animal procedures were performed under anaesthesia by inhalation of 2% isoflurane (Baxter Healthcare, Deerfield, IL)/oxygen mixture. Wistar rats (4-6 weeks) were obtained from Harlan (Horst, the Netherlands) and were allowed to accli-matize at the Erasmus MC vivarium for 1 week prior to cell injection.

Viable or dead Fluc-MSCs (5 x 10⁶) labeled with Gd-liposome or SPIO were admin-istered in the lower back by intramuscular injection (50 µl). The location of injection was properly marked on the skin.

In vivo studies

For T1, T2 and T2* mapping purposes the same sequences were used as *in vitro*. For-mula (1) was applied, except that T1, T2 and T2* values from healthy spinal muscle were used as reference instead of Ficoll. BLI was performed from 5 minutes after intraperito-neal (i.p.) injection of D-Luciferine (Promega) for 1h. Animals were scanned repeatedly over a two-week period at days 0, 2, 5, 10 and 15.

Immunohistochemistry

At end of follow up, muscular tissue at the injection site was carefully resected. In-jection sites were identified by the markings on the skin.BLI imaging and macroscopic

visual examination were further used to confirm the site of injection. Briefly, tissue was transferred to 4% paraformaldehyde, transferred to 30% sucrose for 1 day, followed by immersion in OCT (Tissue-TEK). Tissue was cryo-sectioned to obtain 10 μm-thick samples. Sections were stained for iron using Perl's iron stain (Klinipath BVBA, Duiven, the Netherlands) and counterstained with haematoxylin (Sigma-Aldrich).

Gd and SPIO in vitro and ex vivo measurements

The total amount of cellular internalized SPIO or Gd content was measured by ICP-OES in three 20 μl aliquots of a SPIO-labeled and Gd-labeled MSC stock solution, respectively. Aliquots were suspended in 4 ml. Triton X-100 2% (St. Louis, MO), heated up at 55 °C and mixed for 30 min. at 6 g to induce cellular and liposomal lysis. Cellular content of the contrast agent (CA) was calculated as:

$$(2) \qquad CA_{cellular} = \frac{CA_{pellet}}{N_{cells}}$$

To measure the amount of retained Gd in the injected muscle, ICP was performed on the ipsi- and contralateral muscle as well. For this purpose, muscle was dissected in small pieces, and crushed in a microdismembrator. Crushed tissue was resuspended in 1% Triton/PBS, lyophilized and finally digested using $HNO3$ and H_2O_2 at 110 °C.

Data analysis

All values are presented as mean±SD from at least triplicate samples and expressed in relation to unlabeled cells. For correlation assessment Spearman r coefficient was determined (Graphpad InStat 3.06; Graphpad Software Inc., San Diego, CA, USA). The degree of significance is given when appropriate (*$p < 0.05$; **$p < 0.01$; ***$p < 0.001$).

Acknowledgements

References

1. Bolli R, Chugh AR, D'Amario D, Loughran JH, Stoddard MF, Ikram S, Beache GM, Wagner SG, Leri A, Hosoda T, Sanada F, Elmore JB, Goichberg P, Cappetta D, Solankhi NK, Fahsah I, Rokosh DG, Slaughter MS, Kajstura J, Anversa P. Cardiac stem cells in patients with ischaemic cardiomyopathy (SCIPIO): initial results of a randomised phase 1 trial. Lancet 2011;378(9806):1847-1857.

2. Hopp E, Lunde K, Solheim S, Aakhus S, Arnesen H, Forfang K, Edvardsen T, Smith HJ. Regional myocardial function after intracoronary bone marrow cell injection in reperfused anterior wall infarction - a cardiovascular magnetic resonance tagging study. J Cardiovasc Magn Reson 2011;13:22.

3. Connick P, Kolappan M, Patani R, Scott MA, Crawley C, He XL, Richardson K, Barber K, Webber DJ, Wheeler-Kingshott CA, Tozer DJ, Samson RS, Thomas DL, Du MQ, Luan SL, Michell AW, Altmann DR, Thompson AJ, Miller DH, Compston A, Chandran S. The mesenchymal stem cells in multiple sclerosis (MSCIMS) trial protocol and baseline cohort characteristics: an open-label pre-test: post-test study with blinded outcome assessments. Trials 2011;12:62.

4. Leistner DM, Fischer-Rasokat U, Honold J, Seeger FH, Schachinger V, Lehmann R, Martin H, Burck I, Urbich C, Dimmeler S, Zeiher AM, Assmus B. Transplantation of progenitor cells and regeneration enhancement in acute myocardial infarction (TOPCARE-AMI): final 5-year results suggest long-term safety and efficacy. Clin Res Cardiol 2011;100(10):925-934.

5. Lee Z, Dennis JE, Gerson SL. Imaging stem cell implant for cellular-based therapies. Exp Biol Med (Maywood) 2008;233(8):930-940.

6. Magnitsky S, Walton RM, Wolfe JH, Poptani H. Magnetic resonance imaging as a tool for monitoring stem cell migration. Neurodegener Dis 2007;4(4):314-321.

7. Bernsen MR, Moelker AD, Wielopolski PA, van Tiel ST, Krestin GP. Labelling of mammalian cells for visualisation by MRI. Eur Radiol 2010;20(2):255-274.

8. Bulte JW, Kraitchman DL. Monitoring cell therapy using iron oxide MR contrast agents. Curr Pharm Biotechnol 2004;5(6):567-584.

9. Frank JA, Miller BR, Arbab AS, Zywicke HA, Jordan EK, Lewis BK, Bryant LH, Jr., Bulte JW. Clinically applicable labeling of mammalian and stem cells by combining superparamagnetic iron oxides and transfection agents. Radiology 2003;228(2):480-487.

10. Hoehn M, Kustermann E, Blunk J, Wiedermann D, Trapp T, Wecker S, Focking M, Arnold H, Hescheler J, Fleischmann BK, Schwindt W, Buhrle C. Monitoring of implanted stem cell migration in vivo: a highly resolved in vivo magnetic resonance imaging investigation of experimental stroke in rat. Proc Natl Acad Sci U S A 2002;99(25):16267-16272.

11. Matuszewski L, Persigehl T, Wall A, Schwindt W, Tombach B, Fobker M, Poremba C, Ebert W, Heindel W, Bremer C. Cell tagging with clinically approved iron oxides: feasibility and effect of lipofection, particle size, and surface coating on labeling efficiency. Radiology 2005;235(1):155-161.

12. Amsalem Y, Mardor Y, Feinberg MS, Landa N, Miller L, Daniels D, Ocherashvilli A, Holbova R, Yosef O, Barbash IM, Leor J. Iron-oxide labeling and outcome of transplanted mesenchymal stem cells in the infarcted myocardium. Circulation 2007;116(11 Suppl):I38-45.

13. Berman SC, Galpoththawela C, Gilad AA, Bulte JW, Walczak P. Long-term MR cell tracking of neural stem cells grafted in immunocompetent versus immunodeficient mice reveals distinct differences in contrast between live and dead cells. Magn Reson Med 2011;65(2):564-574.

14. Cahill KS, Gaidosh G, Huard J, Silver X, Byrne BJ, Walter GA. Noninvasive monitoring and tracking of muscle stem cell transplants. Transplantation 2004;78(11):1626-1633.

15. Pawelczyk E, Jordan EK, Balakumaran A, Chaudhry A, Gormley N, Smith M, Lewis BK, Childs R, Robey PG, Frank JA. In vivo transfer of intracellular labels from locally implanted bone marrow stromal cells to resident tissue macrophages. PLoS One 2009;4(8):e6712.

16. Raynal I, Prigent P, Peyramaure S, Najid A, Rebuzzi C, Corot C. Macrophage endocytosis of superparamagnetic iron oxide nanoparticles: mechanisms and comparison of ferumoxides and ferumoxtran-10. Invest Radiol 2004;39(1):56-63.

17. Terrovitis J, Stuber M, Youssef A, Preece S, Leppo M, Kizana E, Schar M, Gerstenblith G, Weiss RG, Marban E, Abraham MR. Magnetic resonance imaging overestimates ferumoxide-labeled stem cell survival after transplantation in the heart. Circulation 2008;117(12):1555-1562.

18. van Buul GM, Kotek G, Wielopolski PA, Farrell E, Bos PK, Weinans H, Grohnert AU, Jahr H, Verhaar JA, Krestin GP, van Osch GJ, Bernsen MR. Clinically translatable cell tracking and quantification by MRI in cartilage repair using superparamagnetic iron oxides. PLoS One 2011;6(2):e17001.

19. Azarnoush K, Maurel A, Sebbah L, Carrion C, Bissery A, Mandet C, Pouly J, Bruneval P, Hagege AA, Menasche P. Enhancement of the functional benefits of skeletal myoblast transplantation by means of coadministration of hypoxia-inducible factor 1alpha. J Thorac Cardiovasc Surg 2005;130(1):173-179.

20. Jackson KA, Majka SM, Wang H, Pocius J, Hartley CJ, Majesky MW, Entman ML, Michael LH, Hirschi KK, Goodell MA. Regeneration of ischemic cardiac muscle and vascular endothelium by adult stem cells. J Clin Invest 2001;107(11):1395-1402.

21. Zhang M, Methot D, Poppa V, Fujio Y, Walsh K, Murry CE. Cardiomyocyte grafting for cardiac repair: graft cell death and anti-death strategies. J Mol Cell Cardiol 2001;33(5):907-921.

22. Luciani N, Wilhelm C, Gazeau F. The role of cell-released microvesicles in the intercellular transfer of magnetic nanoparticles in the monocyte/macrophage system. Biomaterials 2010;31(27):7061-7069.

23. Guenoun J, Koning GA, Doeswijk G, Bosman L, Wielopolski PA, Krestin GP, Bernsen MR. Cationic Gd-DTPA liposomes for highly efficient labeling of mesenchymal stem cells and cell tracking with MRI. Cell Transplant 2011.

24. Brekke C, Morgan SC, Lowe AS, Meade TJ, Price J, Williams SC, Modo M. The in vitro effects of a bimodal contrast agent on cellular functions and relaxometry. NMR Biomed 2007;20(2):77-89.

25. Kobayashi H, Kawamoto S, Saga T, Sato N, Ishimori T, Konishi J, Ono K, Togashi K, Brechbiel MW. Avidin-dendrimer-(1B4M-Gd) (254): a tumor-targeting therapeutic agent for gadolinium neutron capture therapy of intraperitoneal disseminated tumor which can be monitored by MRI. Bioconjug Chem 2001;12(4):587-593.

26. Lewin M, Clement O, Belguise-Valladier P, Tran L, Cuenod CA, Siauve N, Frija G. Hepatocyte targeting with Gd-EOB-DTPA: potential application for gene therapy. Invest Radiol 2001;36(1):9-14.

27. Terreno E, Geninatti Crich S, Belfiore S, Biancone L, Cabella C, Esposito G, Manazza AD, Aime S. Effect of the intracellular localization of a Gd-based imaging probe on the relaxation enhancement of water protons. Magn Reson Med 2006;55(3):491-497.

28. Strijkers GJ, Mulder WJ, van Heeswijk RB, Frederik PM, Bomans P, Magusin PC, Nicolay K. Relaxivity of liposomal paramagnetic MRI contrast agents. MAGMA 2005;18(4):186-192.

29. Terreno E, Sanino A, Carrera C, Castelli DD, Giovenzana GB, Lombardi A, Mazzon R, Milone L, Visigalli M, Aime S. Determination of water permeability of paramagnetic liposomes of interest in MRI field. J Inorg Biochem 2008;102(5-6):1112-1119.

30. Muller-Taubenberger A. Application of fluorescent protein tags as reporters in live-cell imaging studies. Methods Mol Biol 2006;346:229-246.

31. Gilad AA, Winnard PT, Jr., van Zijl PC, Bulte JW. Developing MR reporter genes: promises and pitfalls. NMR Biomed 2007;20(3):275-290.

32. Louie AY, Huber MM, Ahrens ET, Rothbacher U, Moats R, Jacobs RE, Fraser SE, Meade TJ. In vivo visualization of gene expression using magnetic resonance imaging. Nat Biotechnol 2000;18(3):321-325.

33. Gambhir SS, Barrio JR, Phelps ME, Iyer M, Namavari M, Satyamurthy N, Wu L, Green LA, Bauer E, MacLaren DC, Nguyen K, Berk AJ, Cherry SR, Herschman HR. Imaging adenoviral-directed reporter gene expression in living animals with positron emission tomography. Proc Natl Acad Sci U S A 1999;96(5):2333-2338.

34. Tjuvajev JG, Stockhammer G, Desai R, Uehara H, Watanabe K, Gansbacher B, Blasberg RG. Imaging the expression of transfected genes in vivo. Cancer Res 1995;55(24):6126-6132.

35. Baligand C, Vauchez K, Fiszman M, Vilquin JT, Carlier PG. Discrepancies between the fate of myoblast xenograft in mouse leg muscle and NMR label persistency after loading with Gd-DTPA or SPIOs. Gene Ther 2009;16(6):734-745.

36. Lin SP, Brown JJ. MR contrast agents: physical and pharmacologic basics. J Magn Reson Imaging 2007;25(5):884-899.

37. Oksendal AN, Hals PA. Biodistribution and toxicity of MR imaging contrast media. J Magn Reson Imaging 1993;3(1):157-165.

38. Aime S, Caravan P. Biodistribution of gadolinium-based contrast agents, including gadolinium deposition. J Magn Reson Imaging 2009;30(6):1259-1267.

39. Chemaly ER, Yoneyama R, Frangioni JV, Hajjar RJ. Tracking stem cells in the cardiovascular system. Trends Cardiovasc Med 2005;15(8):297-302.

40. Walczak P, Kedziorek DA, Gilad AA, Barnett BP, Bulte JW. Applicability and limitations of MR tracking of neural stem cells with asymmetric cell division and rapid turnover: the case of the shiverer dysmyelinated mouse brain. Magn Reson Med 2007;58(2):261-269.

41. Weissleder R, Stark DD, Engelstad BL, Bacon BR, Compton CC, White DL, Jacobs P, Lewis J. Superparamagnetic iron oxide: pharmacokinetics and toxicity. AJR Am J Roentgenol 1989;152(1):167-173.

42. Kuhlpeter R, Dahnke H, Matuszewski L, Persigehl T, von Wallbrunn A, Allkemper T, Heindel WL, Schaeffter T, Bremer C. R2 and R2* mapping for sensing cell-bound superparamagnetic nanoparticles: in vitro and murine in vivo testing. Radiology 2007;245(2):449-457.

43. Henning TD, Wendland MF, Golovko D, Sutton EJ, Sennino B, Malek F, Bauer JS, McDonald DM, Daldrup-Link H. Relaxation effects of ferucarbotran-labeled mesenchymal stem cells at 1.5T and 3T: discrimination of viable from lysed cells. Magn Reson Med 2009;62(2):325-332.

44. Bowen CV, Zhang X, Saab G, Gareau PJ, Rutt BK. Application of the static dephasing regime theory to superparamagnetic iron-oxide loaded cells. Magn Reson Med 2002;48(1):52-61.

45. Rad AM, Arbab AS, Iskander AS, Jiang Q, Soltanian-Zadeh H. Quantification of superparamagnetic iron oxide (SPIO)-labeled cells using MRI. J Magn Reson Imaging 2007;26(2):366-374.

46. Kotek G, van Tiel ST, Wielopolski PA, Houston GC, Krestin GP, Bernsen MR. Cell quantification: evolution of compartmentalization and distribution of iron-oxide particles and labeled cells. Contrast Media Mol Imaging 2012;7(2):195-203.

47. Arbab AS, Janic B, Haller J, Pawelczyk E, Liu W, Frank JA. In Vivo Cellular Imaging for Translational Medical Research. Curr Med Imaging Rev 2009;5(1):19-38.

48. Biancone L, Crich SG, Cantaluppi V, Romanazzi GM, Russo S, Scalabrino E, Esposito G, Figliolini F, Beltramo S, Perin PC, Segoloni GP, Aime S, Camussi G. Magnetic resonance imaging of gadolinium-labeled pancreatic islets for experimental transplantation. NMR Biomed 2007;20(1):40-48.

49. Rouser G, Fkeischer S, Yamamoto A. Two dimensional then layer chromatographic separation of polar lipids and determination of phospholipids by phosphorus analysis of spots. Lipids 1970;5(5):494-496.

50. Van Tiel ST, Wielopolski PA, Houston GC, Krestin GP, Bernsen MR. Variations in labeling protocol influence incorporation, distribution and retention of iron oxide nanoparticles into human umbilical vein endothelial cells. Contrast Media Mol Imaging 2010.

51. Sutton EJ, Henning TD, Boddington S, Demos S, Krug C, Meier R, Kornak J, Zhao S, Baehner R, Sharifi S, Daldrup-Link H. In vivo magnetic resonance imaging and optical imaging comparison of viable and nonviable mesenchymal stem cells with a bifunctional label. Mol Imaging 2010;9(5):278-290.

52. Jacobs S, Ruusuvuori E, Sipila ST, Haapanen A, Damkier HH, Kurth I, Hentschke M, Schweizer M, Rudhard Y, Laatikainen LM, Tyynela J, Praetorius J, Voipio J, Hubner CA. Mice with targeted Slc4a10 gene disruption have small brain ventricles and show reduced neuronal excitability. Proc Natl Acad Sci U S A 2008;105(1):311-316.

53. Cotrim AP, Hyodo F, Matsumoto K, Sowers AL, Cook JA, Baum BJ, Krishna MC, Mitchell JB. Differential radiation protection of salivary glands versus tumor by Tempol with accompanying tissue assessment of Tempol by magnetic resonance imaging. Clin Cancer Res 2007;13(16):4928-4933.

4.4

In vivo mapping of iron oxide labeled mesenchymal stem cells implanted in the heart with bioluminescence validation

Ruggiero A, Guenoun J, Doeswijk GN, Houston GC, Krestin GP, Kotek G, Bernsen MR

Abstract

Background: In various stem cell therapy approaches poor cell survival has been recognized as an important factor limiting therapeutic efficacy. Therefore non-invasive monitoring of cell fate is warranted for developing clinically effective stem cell therapy approaches. In this study we investigated the feasibility of the use of voxel-based R2 mapping as a tool to monitor the in vivo stem cell fate in myocardium when the cells are labeled with iron oxide particles (SPIO).

Materials and methods: Single cardiac phase with cardiac triggered double inversion black blood 2D fast Spin echo (BBFSE) images were acquired on the short axis of hearts. Reproducibility studies were performed in normal rats (n=4) imaged in different sessions. A double cell labeling approach was used in which mesenchymal stem cells were transduced with the luciferase gene and subsequently labeled with ferumoxide particles (SPIO). Living labeled cells were injected in the myocardium of healthy Wistar rats (n=9). For control purposes animals were also injected with dead, labeled cells (n=5) or saline (n=3). Cell fate was monitored over a period of 8 weeks by bioluminescence imaging following injection of D-Luciferine and quantitative magnetic resonance imaging, using a black blood FSE sequence with multiple echo times (between 4.4 and 26.4 ms).

Results: Bioluminescence imaging revealed a significant increase of cell number during the first week (peak day 7) with a steep decrease of cell numbers to undetectable levels during the second week. MR imaging showed a sharp increase of R2 values shortly after injection at the injection site (peak day 5), followed by a very gradual decrease of R2 over a period of 8 weeks. No difference in appearance on R2-weighted images or in R2-values was observed between living and dead cells over the entire time period studied.

Conclusion: No significant correlation between the bioluminscence optical data and R2 values were observed. Quantitative MR imaging by means of R2-mapping is not suitable for the in vivo assessment of stem cell fate in rat myocardium as validated by bioluminescence imaging. These results do not follow previous *in vitro* reports where it was proposed that based on the difference in r2 relaxivity between intra-cellular and extra-cellular SPIO, living cells may be distinguished from death cells based on their R2 profile. Cell proliferation, cell migration, cell death, extracellular SPIO dispersion or aggregation exhibit different relaxivities. In vivo these processes happen simultanously making quantification very complex, if not impossible

Introduction

Regenerative approaches in the treatment of myocardial infarction have been widely investigated in the past few years fuelling new hopes for patients and scientists. Preclinical evidences that stem-cell-based-therapy has the potential to limit the degradation of cardiac function after myocardial infarction, led to the rapid development of several clinical trials (1). Recent meta-analyses reported a modest, but statistically significant improvement in the ejection fraction, ventricular dimension and infarct area (2, 3). One or more imaging techniques were greatly exploited in these clinical trials, however only indirect indications of the efficacy of stem cell transplantation was provided by the evaluation of myocardial contractility, viability and perfusion. While these results depict a promising picture of the stem cell-based therapy, questions have been raised regarding actual grafting, transformation and proliferation of stem cells in the host tissue (therefore recovery of the physiological functions of the organ) or whether or not the transplanted cells simply exert paracrine effects (which can induce the recovery of the host tissue) (4).

Molecular imaging (MI) techniques allow the direct visualization of stem cells, their short and long term fate and eventually their viability (5). Two cell labeling approaches are generally used for these purposes: reporter genes or chemical-based contrast agents (5). The former requires the introduction of a reporter gene into the cells of interest, through viral or non-viral-vectors. The reporter gene encodes for a protein (enzymes, receptor, transporter) able to interact with a correspondent reporter probe which is activated or concentrated only in the cells expressing the reporter gene. Probe accumulation is proportional to the expression level of the reporter gene therefore the number of living cells or the induction of a specific reporter gene can be quantified. Passive loading of cells with radioactive agents (^{18}F-FDG, ^{111}In-Oxine, etc.) for positron emission tomography (PET)/single photon emission (SPECT) or contrast agents (iron oxides, Gadolinium, Manganese) for Magnetic resonance imaging (MRI) is another approach commonly used for cell tracking (5, 6).

Labeling with superparamagnetic iron oxide (SPIO) nanoparticles has been extensively studied as they act as magnetic inhomogeneities, locally disturbing the magnetic field, inducing a significant decrease of T2- and T2*-relaxation rates (hypointense signal). Studies reported that SPIOs do not affect cell viability, proliferation, differentiation or migration (7-10). However, a major drawback is related to the persistence of the hypointense signal at the site of transplant regardless of labeled cell viability. In fact, at longer time points SPIO-induced signal loss is not necessarily associated with implanted cells but rather with phagocytosing monocytes (11, 12). Intriguingly, SPIO induced relaxivities have been shown to be dependent on their location; i.e. the relaxivities are different when SPIOs are compartmentalized within the intracellular space or dispersed in the extracellular space (13, 14). Indeed, decreased T2 values have been reported in lysed versus viable SPIO-labeled cells, this effect is related to limited SPIO-proton interaction in the intracellular compartment compared to unlimited proton interactions of SPIO released from disrupted cells (15, 16).

The majority of cell tracking studies in the heart have focused on the potential of SPIO labeling and MRI longitudinal follow-up of implanted cells, relying on a semi-quantitative approach based on signal intensity (signal-to-noise measurements). A quantitative approach, has already been used for the evaluation of SPIO labeled cells *in vivo* (17), but it has never been exploited to assess SPIO labeled cells implanted in the heart. In this work, we aimed:1) to perform quantitative R2 mapping of the heart at 7T 2) to assess reproducibility and robustness of the technique 3) to assess longitudinally in vivo the R2 changes related to cell proliferation and death evaluated by bioluminescence.

Materials and Methods

Rat mesenchymal stem cells expressing firefly luciferase

The plasmid pND-Cag-Fluc was co-transfected into 293T cells with a mixture of Endofree Maxi-kit (Quiagen, Hilden Germany), VSVG (45μg/dish), pMD and pRev using polyethylenimine (Sigma Aldrich, St Louis, MO, USA). Lentivirus supernatant was collected at 48 h and 72 h, filtered (0.45μm) and concentrated by sediment centrifugation. The pellet was then resuspended in 1 ml phospate buffered saline (PBS). Rat mesenchymal stem cells (rMSC; Millipore, Billerica, MA, USA) were grown to 50% confluency in a 24 well plate in Dulbecco's modified Eagle medium (DMEM) /F10 (Invitrogen; Carlsbad, CA, USA), 10% fetal calf serum (FCS) and infected with 50 μl lenti-viral stock. Viral titer was assessed on concentrated supernatant by HIV-p24 ELISA (Dupont, Wilmington, DE, USA). Transduced rMSC (rMSC-Fluc) were expanded and plated at low densities. The expression of Fluc was evaluated by using a luminometer and clones with the highest expression of Fluc were selected and expanded.

Cell labelling with SPIO

rMSC-Fluc were cultured in DMEM supplemented with 2% FBS (Lonza; Basel, Switzerland), 1% MEM essential vitamin mixture (Lonza), 1% NEAA (Sigma-Aldrich; St. Louis, MO) 2% v/v penicillin/streptomycin, 2% v/v L-glutamine, and 0.5% v/v glutamax (Invitrogen). Cells were grown at 80% confluency and incubated with a mixture of ferumoxide-protamine sulfate. Cells were labeled as previously described (18, 19). Briefly, ferumoxides (Endorem, Guerbet S.A., Paris, France; hydrodynamic diameter of 120-180 nm) was diluted in serum free DMEM to a final concentration of 100ug/ml; protamine sulfate was added to a final concentration of 5 ug/ml. After 5 minutes of intermitted shaking the solution was added to the cells. 24 hours later cells were washed three times with 10U/ml heparinized PBS, harvested by trypsinization, put through a 40 μm cell-strainer and counted. Non-viable cells were obtained by repeated freeze/thawing and brief sonication of the injection solution.

Viability assessment of labeled cells

To assess any potential effect of cell labeling on cell viability or proliferation we labeled cells (wild type and expressing luciferase) with SPIO (triplicate samples), harvested cells at different days, and counted the number of cells on an automatic cell counter. Doubling time was estimated assuming a exponential growth model: $A_t = A_o 2^{t/t_d}$ (At, cell number at time t; A0, cell number at time 0; t time; t_d, doubling time) (20). Inductively coupled plasma Optical Emission Spectroscopy (ICP-OES; Optima 4300DV, Perkin Elmer, Norwalk, CT) was used to quantify the intracellular uptake of iron.

Cell transplantation and in vivo imaging

All animal experiments were conducted in compliance with the Institutional Animal Welfare Committee. For assessing the reproducibility of R2 mapping by MR Imaging techniques, rats (Wistar; Harlan; Horst, the Netherlands) (n=4) underwent anesthesia and MRI imaging for a total of 4 sessions each (different days).

For experiments regarding MRI tracking of implanted cells, rats (Wistar; Harlan; Horst, the Netherlands) received intra-myocardial injections. Briefly, animals were induced with 2% isoflurane (Baxter Healthcare, Deerfield, IL)/oxygen mixture, and kept under anesthesia by the intraperitoneal administration of a combination of Fentanyl (300 ug/kg) and Medetomidine (300 ug/kg). Animals were orotracheally intubated and ventilated and left thoracotomy performed. After intra-myocardial injection, the chest was closed, pneumothorax reduced and buprenorfine (0.1 mg/kg) subcutaneously administered. Group 1 (n=9) received 1.5 x10^{6} viable rMSC SPIO-labeled cells; group 2 (n=5) received 1.5 x10^{6} non-viable SPIO-labeled cells; group 3 (n=3) received PBS injection (sham experiment).

Imaging studies

BIOLUMINESCENCE

Optical bioluminescence was performed by using the charged coupled camera device Xenogen IVIS Spectrum (Caliper Life Sciences, Hopkington, MA, USA), 5 minutes after intraperitoneal administration of 150 mg/Kg of D-Luciferine (Promega). Each rat was imaged up to 30 minutes (integration time, 30, 60, 120 s and 180s; f/stop,1; binning, medium; field of view, B) to follow the pharmacokinetic profile of luciferin activation. Optical intensity was quantified in units of photons/second/cm²/steradian. Regions of interest were used to calculate the optical peak value at the level of the implanted cells in the heat. Data were analyzed with the software Living Image 2.6 (Caliper LS, Perkin Elmer).

MAGNETIC RESONANCE IMAGING AND IMAGE PROCESSING

MRI data were acquired by using a 7T scanner (Agilent-GE Discovery MR901 scanner, Milwaukee IL, USA) with with 300 mT/m max gradient. A 150mm diameter quadrature coil was used for transmit and 4ch Rx surface coil array for receive purposes (Rapid Biomedical. Würzburg, Germany).

All animals underwent longitudinal MRI imaging. Every exam started with routine cine sequences (2-chamber view and 4-chamber view) and 3D PDW axial sequence, to allow the proper positioning on the heart axial plane and the selection of the most representative section. The overall time required for slice positioning and scanning was 20 min

Single cardiac phase with cardiac triggered double inversion black blood 2D fast Spin echo (BBFSE) images were acquired on the short axis of hearts. The effective echo times of the separate scans were TE= 4.4, 8.8, 13.2, 17.6, 22, 26.4 ms, the repetition time was ~ TR= 600 ms. The resolution of images was: FOV= 50x50 mm, matrix= 256x256, in-plane voxel size = 0.20x0.20 mm, slice thickness 1.8 mm. The scan time for all TE images was ~ 5 minutes. The triggering was provided by peripheral pulse oxygenation level monitoring on the hind leg of the rats (SA Instruments, Stony Brook, NY, USA). The echo train length was 8, the echo spacing was 4.2 ms, optimized to achieve the required span of available TE values, and yet making sure that the echo train does not extend beyond the cardiac resting phase.

Image processing and analysis

For reproducibility experiments, the inner and outer boundary of the myocardium were manually drawn on the short axis image with the shortest TE, which has the highest signal-to-noise ratio (SNR). To correct for motion artifacts the image set was registered to the images with the shortest TE using a two-step approach. Five anatomical landmarks of the myocardium were manually selected to enable a point based rigid registration, which was used as an initialization for an intensity based mutual information based rigid registration. The myocardium region was divided into standard sectors (21) and the 6 mid-ventricular regions were considered. The mean T2 and the standard deviation were calculated for each region and each day.

For the quantification of SPIO-labeled rMSC, a region-of-interest (ROI) was manually drawn on the short axis image at the level of the signal void (site of injection).

A T2 map was then generated using a Maximum Likelihood (ML) estimator approach which takes the Rician noise distribution of the magnitude MR images into account. This ML formulation also yields the Cramer-Rao Lower Bounds (CRLB) on the precision of the fits. The square root of the CRLB (srCRLB) is a lower bound on the standard deviation of the T2 and can therefore be used as an error estimate in ms. For

reproducibility experiments, to correct for motion artifacts the images were registered to the images with the shortest TE using a two-step approach. Five anatomical landmarks of the myocardium were manually selected to enable a point based rigid registration, which was used as an initialization for an intensity based mutual information based rigid registration. The myocardium region was divided into standard sectors (21) and the 6 mid-ventricular regions were considered. The mean T2 and the standard deviation were calculated for each region and each day.

Hystology

For histological evaluation, hearts were harvested at 2 day and 15 days after injection were, washed in ice-cold PBS, and fixed for 24 h in 4% paraformaldehyde, embedded in Tissue-TEK OCT compound (Sakura, Finetek U.S.A Inc.), frozen at −80 °C, and cryosectioned to obtain 10-μm-thick samples. Slides were stained for iron by using the Accustain kit (Iron stain; Sigma-Aldrich) and imaged by light microscopy.

Statistics

Statistical data were evaluated using Graphpad Prism 5.0 (Graphpad Software). Statistical comparisons between two experimental groups were performed using t- tests (unpaired comparisons); comparison of multiple groups was performed with two-way ANOVA using Bonferroni's multiple comparison post hoc analysis. All statistical comparisons were two-sided, and the level of statistical significance was set at $P < 0.05$. Unless differently specified, all values were reported as Mean ± SEM.

Results

Viability assessment

Analysis of iron content by ICP measurements revealed 7.58 ± 0.09 iron pg/cell (rMSC) and 7.67 ± 0.14 iron pg/cell (rMSC-Fluc) after the labeling procedure. The difference was not statistically significant. In order to assess whether the cell manipulation (Fluc transduction) or cell labeling could affect cell viability, cell proliferation studies were performed (Figure 1). The presence of the Fluc gene in these cells reduced proliferation rate compared to the wild type as lower cell counts were observed in the MSC-Fluc compared to the MSC at all time points (P<0.05). Lower cell counts were observed with MSC-SPIO labeled cells compared to control cells, only on day 7 (P<0.05). SPIO labeling of rMSC-Fluc cells did not have any statistically significant effect on cell proliferation compared to unlabeled control. Doubling times (expressed in days) were calculated to be: 1.85 (MSC unlabeled), 1.86 (MSC labeled with SPIO), 2.02 (MSC-Fluc unlabeled), 2.05 (MSC-Fluc labeled with SPIO). Importantly, doubling time of MSC-Fluc was statistically different from MSC at all time points (P<0.05).
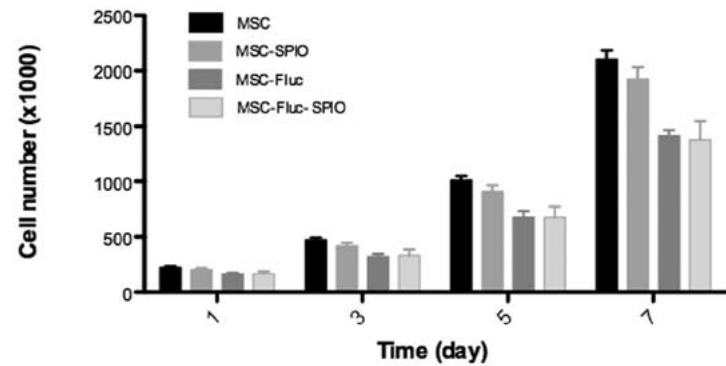
Fig. 1 Assessment of the cell labeling on growth profile. MSC and MSC-Fluc were labeled with SPIO, cultured up to 7 days and cells were counted at different time points. A lower cell count was observed in the MSC-Fluc (doubling time: 2.02 days) compared to the MSC (doubling time: 1.85 days) at all time points (P<0.05). A lower cell count was observed with MSC-SPIO labeled cells compared to control cells (MSC) only on day 7 (P<0.05). SPIO labeling of rMSC-Fluc cell did not have any statistically significant effect on cell proliferation compared to unlabeled control.
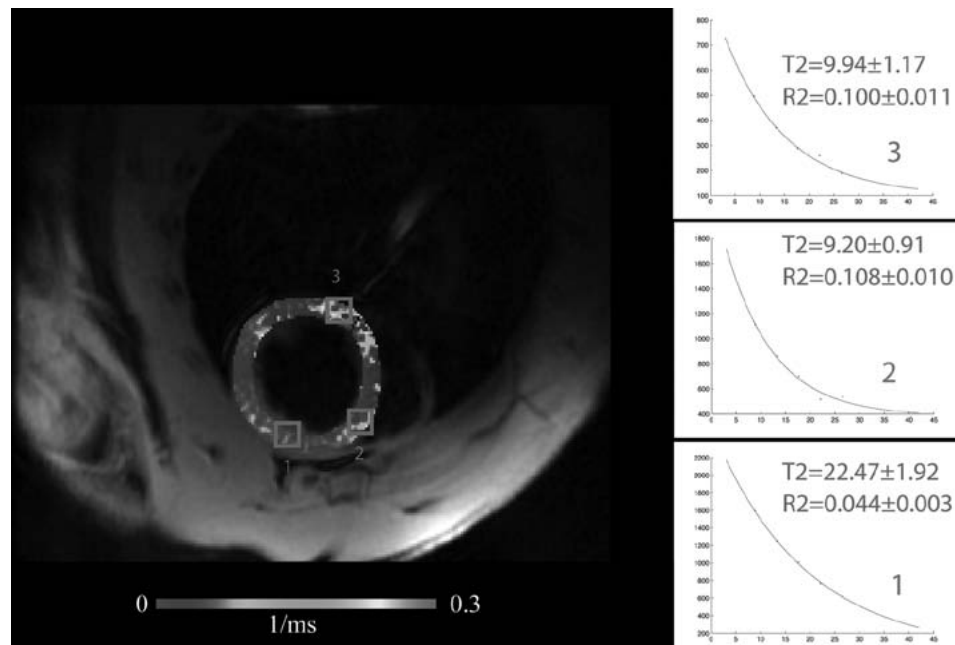
Fig. 2 R2 MRI Mapping approach. Representative image depicting an axial slice of a healthy rat heart with super-imposed R2 values measured by using a BBFSE based mapping approach. The exponential curve of the signal decay is optimal and calculated errors (mean ±SD) are reported. The signal is quite homogenous in the area corresponding to the preferred cell injection site in this paper (anterior and anterolateral segment). However some regions such as the septal region and the inferolateral region are affected by movement artifacts (breathing, blood flow) and are associated with not reliable curve fitting.

Reproducibility study

Using a BBFSE-based mapping approach, reproducibility of myocardial R2 value measurement was performed 4 animals scanned 4 times each to assess the robustness of the technique. Figure 2 shows a representative axial slice of a healthy rat heart (no injection). The exponential of the signal decay was optimal and calculated errors were relatively small. The signal was quite homogenous with T2 values (22.47±1.92 ms) in the preferred area for cell injection (anterior and anterolateral segment). However, some regions such as the septal and the inferolateral region were more prone to movement artifacts (e.g. breathing) and were associated with a less reliable curve fitting.
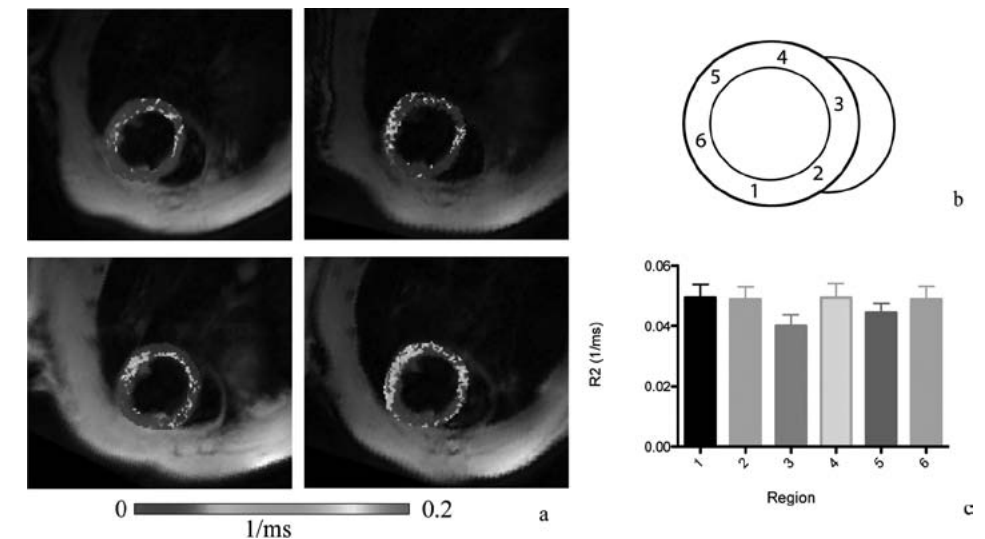

Fig. 3 Reproducibility study. This figure shows a representative BBFSE image with super-imposed R2 mapping values, of an animal imaged in 4 separate sessions (a). Schematic drawing of the region distribution. Region 1: anterior; Region 2: antero-septal; Region 3: inferoseptal; Region 4: inferior; region 5: inferolateral; region 6: anterolateral (b). The graph illustrates the variability of R2 values (mean ± SEM) observed in the different heart regions. (c)

Reproducibility studies were performed in 4 animals scanned 4 times each to assess the robustness of the technique (Fig 3). Regarding repeated measures of T2/R2 in subsequent imaging sessions following variability was observed: anterior, region 1 (21.72 ms ±1.49); antero-septal, region 2 (22.68 ms ± 1.7), region 3 (26.17 ms ± 2.13), region 4 (22.62 ms ± 1.68), region 5 (25.99 ms ± 2.49), region 6 (21.54 ms ± 1.86) (Fig 3).. 1-way ANOVA was used to test spatial variability of R2 and T2 values of the six different heart segments of 4 animals. We did not observe a statistically significant difference among the segments (P=0.67).

Imaging cell fate

The viability and proliferation of implanted cells was assessed longitudinally *in vivo* by both bioluminescence imaging and MR imaging. We observed an increase in optical signal over days 3-7 (3.21-fold and 15.37-fold increase at day 5 and 7 respectively compared to day 3) upon injection of viable cells, most probably related to cell proliferation in the implantation site. On day 10 the signal had declined substantially (0.7-fold reduction compared to highest peak at day 7) and reached background levels on day 15.
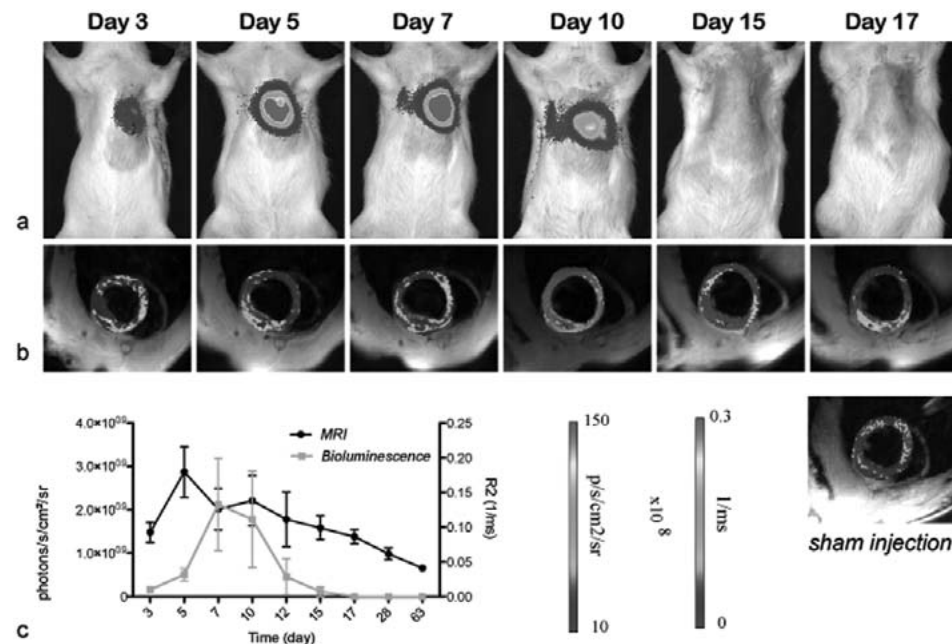

Fig. 4 Longitudinal imaging of cell fate by Bioluminescence and MRI. A. Representative images showing the evolution over time of bioluminescent signal emitted by rMSC-Luc-SPIO cells, transplanted intra-myocardially according to the colorscale provided. b. Representative images showing evolution of R2 values super-imposed on a BBFSE image of a short axis slice of a rat heart at the level of injection with rMSC-Luc-SPIO cells intra-myocardially, over time according to the colorscale provided.. Bottom right image represents data observed in sham-operated animals. C. Graph showing evolution of bioluminescent signal values and R2 values of rat hearts following intra-myocardial injection of rMSC-Luc-SPIO cells (mean ±SEM).

In MR images, large areas of hypointensity, generated by iron labeled cells, were clearly visible in the MRI scans of the injected hearts. Importantly, no difference was observed in terms of size, number and distribution of these signal voids between live and non-viable cells. Longitudinal MRI scans were performed to assess the changes in relaxivities over time. related to iron oxides dilution upon cell proliferation or potential decompartimentalization related to cell death. Quantification of the signal revealed a 2-fold significant increase ($P < 0.05$) in R2 between day 3 and 5 after injection (Fig 4). This was probably related to the early reabsorption of the injection volume with distri-

bution of the cells in the implantation site. From day 5 onwards, R2 values decreased. In sham injected animals, no changes in the R2 values were observed at the site of the presumed injection.

No statistical correlation with the proliferation or viability profile monitored by bioluminescence was observed ($P = 0.1$).

We investigated whether the relaxivity changes associated with the decompartmentalization of iron oxides might be quantified by MRI. We injected a solution of SPIO labeled MSC-Fluc no longer viable (as an effect of repeated freeze/thawing cycles and brief sonication), therefore containing the same amount of SPIO of viable cells but dispersed in the extracellular compartment. No difference was observed in terms of size, number and distribution of the generated signal voids between live and non-viable cells on weighted images. Higher R2 values were associated with dead compared to the viable ones, however the difference was statistically significant only on day 3, probably related to the presence of SPIO in the extracellular matrix and potential macrophage uptake (see discussion). The dead cells showed a similar trend to viable cells, consisting in an increase in R2 on day 5 followed by a decrease

Histological analysis of cryo-sections of hearts revealed that injections with non-viable SPIO-labeled cells were associated with a more puntiform appearance of the iron stain (due to the extracellular release of SPIO in the injection solution). Conversely the iron staining of viable SPIO-labeled cells depicted larger aggregates.
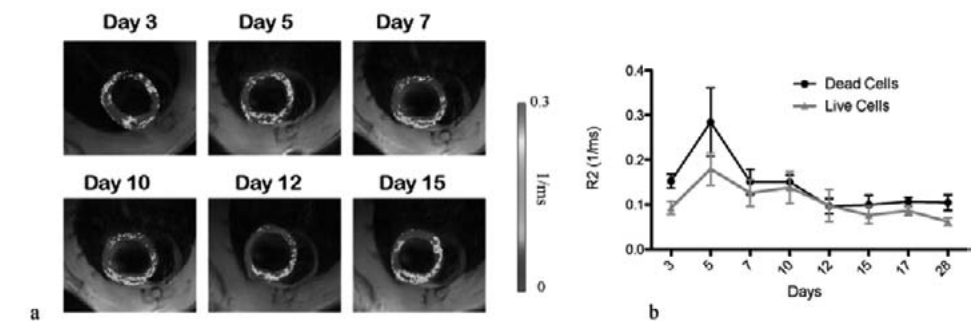

Fig. 5 R2 MRI mapping in viable and non-viable cells. A. Representative images showing evolution of R2 values super-imposed on a BBFSE image of a short axis slice of a rat heart at the level of injection with non-viable rMSC-Luc-SPIO cells intra-myocardially, over time according to the colorscale provided. B. Graph showing evolution of R2 values of rat hearts at the site of injection of living and dead rMSC-Luc-SPIO cells. SPIO labeled MSC-Fluc no longer viable (as an effect of repeated freeze/thawing cycles and brief sonication), containing the same amount of iron of viable cells but decompartmentalized were injected in the heart (a). As an effect of decompartmentalization of SPIO, the implantation of non-viable cells is associated with higher R2 values compared to viable cells. However, this difference is statistically significant only at day 3 after implantation. In the following days despite a trend is clearly visible the difference is not statistically significant and it is probably related to the changes related to free SPIO in the extracellular matrix (uptake from endogenous cells).
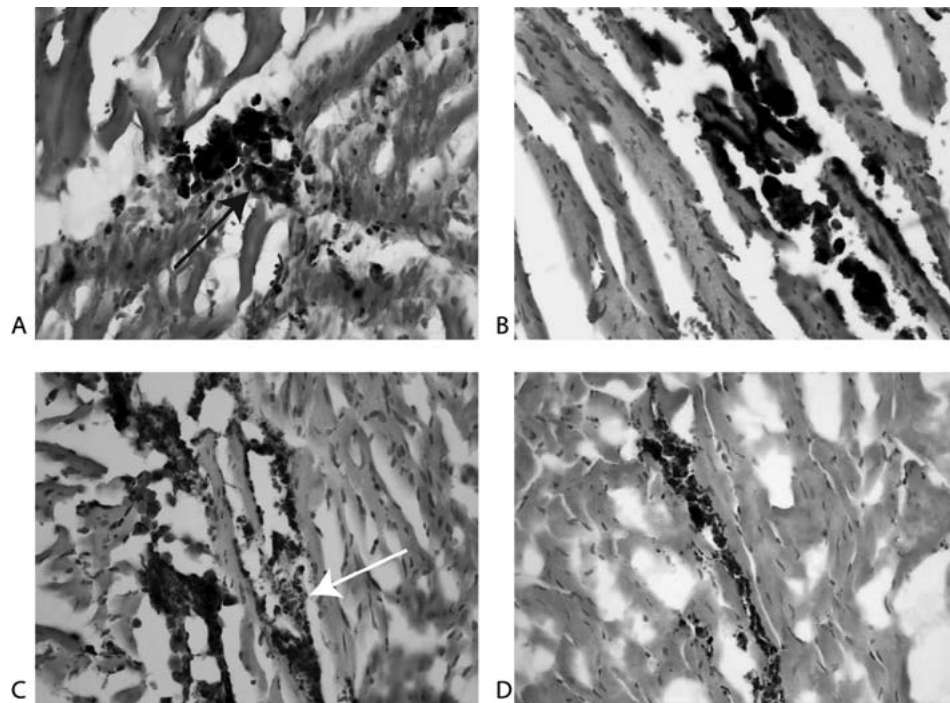
Fig. 6 Representative histological sections of rat hearts injected with viable (upper panel) and non-viable (lower panel) SPIO-labeled cells harvested at 2 days (A, C) and 15 days (B, D) after injection. Iron staining (blue) depicts the presence of iron which is associated with larger aggregates in the viable cells (black arrow) compared to non-viable cells, which present a more puntiform appearance (white arrow) due to extracellular release of SPIO in the injection solution.

Discussion

The ability to monitor the localisation, viability, proliferation and possibly the differentiation status of implanted stem cells provides massive benefit in clinical and research regenerative medicine approaches. All of the pre-clinical and clinical imaging techniques have been leveraged towards this goal; each providing unique advantages and limitations (5). MRI is a widely established technique for the evaluation of cardiac anatomy and function. Taking advantage of its excellent spatial resolution (10–100 µm [preclinical]); 500–1500 µm [clinical]), stem cells labelled with superparamagnetic and paramagnetic agents can be visualised (22, 23). The choice of a proper labeling marker is however a crucial aspect in cell tracking by MRI. High sensitivity allows the long term evaluation of implanted stem cells, since probe dilution upon cell proliferation reduces the detection capabilities. Also, high specificity is demanded to investigate potential cell graft rejection at an early stage.

In this study, luciferase expressing MSC labeled with SPIO were implanted in the heart and longitudinally monitored by quantitative MRI mapping and bioluminescence

imaging. A vast amount of work has been performed on longitudinal imaging of implanted cells in the heart by MRI; SPIO-labeling and assessment of cell fate by means of (loss of) signal intensities on T2-weighted images being the most used approach. As noted before, the detection of low signal intensity areas proves to be an insufficient method as it is associated with some limitations such as: a) inhomogeneity in the coil sensitivity (phased-array coils determine regional myocardial signal variations that may give an inaccurate interpretation); b) artefacts due to motion and flow; c) the inherent qualitative aspect of this approach, whose evaluation relies on regional differences in signal intensity, which strongly depend on the parameters of the sequences used (TR, TE, slice thickness, etc) (24).

To overcome these limitations, the alternative approach consists of the direct quantification of the T2 values of the myocardium. This allows the detection of subtle T2 differences in tissues, reducing the subjective interpretation of signal voids (and their dependence from parameters) and minimizing flow or motion dependent artefacts (24). Many *in vivo* studies on T2 mapping of the heart have been performed in humans in the last two decades, mainly based on spin echo acquisitions. Novel approaches based on T2 prepared steady-state free precession (24), hybrid sequences (25), bright blood approaches (26) or additional adiabatic prepulses (27) have also been suggested recently. It is an area of active investigation for quantitative assessment of myocardial edema and iron overload. However, the use of quantitative mapping for quantification of SPIO-labeled cells implanted in the heart has been quite limited. A few studies suggested R2 (1/T2) and R2* (1/T2*) parametric mapping as a reliable and reproducible quantification method of SPIO or SPIO labeled cells per voxel (14, 28, 29). Importantly, variation of R2 and R2* according to SPIO compartmentalization have been described. Phantom studies demonstrated that with identical iron concentration, cell bound SPIO show higher R2* values compared to free SPIO. Conversely, R2 measurements are higher for free iron than for intra-cellular iron (13, 14).

We sought to use R2 mapping as a means to detect in vivo, changes associated with probe dilution and potential decompartmentalization of SPIO as a result of cell proliferation and cell death, respectively. We employed a double inversion recovery BBFSE sequence and tested its robustness in a reproducibility experiment. The signal was quite homogenous in the preferred regions for cell injection in these experiments such as the anterior and anterolateral segments with T2 values of 22.47±1.92 ms and 21.54±1.86 ms (prior to injection), respectively (Fig 2 and Fig 3). As expected, regions associated with higher cardiac motion such as the septal and the inferolateral segment) corresponded on R2 maps to unreliable curve fitting. However, this limitation did not interfere with the longitudinal assessment of the relaxivity of the injected cells. Overall, the difference in R2 and T2 values among the six different segments was not statistically significant.

In the longitudinal assessment of implanted cells, bioluminescence showed an initial increase of the optical signal (peak on day 7), most probably related to cell proliferation,

followed by a decrease in signal strength. Limited persistence of bioluminescent signal has been observed previously (30) and the explanation of the signal decrease is not univocal. Cell manipulation impairs cell proliferative ability (Fig 1) and may induce further phenotypical changes that may lead to an immunogenic response by the host. Chen et al. reported *in vivo* by bioluminescence a half-life of Fluc labeled cells of 2.65 days, with an optical signal showing an increase within the first 3 days and further decrease with background levels on day 6. Our observations are in agreement with these and other findings, in which the majority (more than 70%)of cells implanted in the heart were reported to die within the first week of injection in immunocompetent animals (30-32). The decreasing signal might also result from epigenetic silencing of reporter gene expression which complicates the overall quantification (33). This phenomenon does not seem likely in our study, since identically generated rMSC-Luc-SPIO cells were also injected in other anatomical locations in rats within our group (data not shown), without a corresponding quick loss of bioluminescent signal.

By using MRI to monitor cell proliferation, we and others previously reported that under *in vitro* conditions, cell proliferation/division is associated with a R2 decrease (T2 increase) (13, 16). On MRI, we observed a 2-fold significant R2 increase from day 3 to 5 after injection, which corresponded to the increasing optical bioluminescence signal (cell proliferation) (Fig 4).

Conversely, when cells die and spread their content to the extracellular matrix an increase of the R2 of SPIO labeled cells has been investigated only in *in vitro* studies and results have been consistent and reproducible. In fact, Simon *et al.* reported a statistically significant difference in R2 relaxation times between viable and non-viable lysed cells (15). Similarly, Nedopil *et al.* reported on ferumoxides-labeled human mesenchymal stem cells implanted in *ex vivo* joints and showed on T2-w images a markedly lower signal (thus shorter T2) of apoptotic compared to viable cells (34). To our knowledge, this is the first attempt to investigate the quantitative approach in an *in vivo* setting. We observed that R2 values already decrease from day 5 onwards, while bioluminescence data still suggest proliferation.. Overall we found no significant correlation between bioluminescent signal profiles and MRI signal evolution (P=0.1). Moreover, we mimicked the release of SPIO content in the injection solution by inducing the death of SPIO-labeled MSC before implantion in the heart. As expected, higher R2 values were associated with the injection of non-viable versus viable cells. However, the difference was statistically significant only on day 3 (Fig 5 and Fig 6).

We argued that the processes happening *in vivo* (such as cell redistribution in the injection site or the re-absorption of the injection medium with further changes in the interactions of the SPIO particles) might obscure the detection of potential changes associated with probe dilution and cell death, making the overall quantitative assessment complicated.

In addition to the above mentioned physiological processes, endogenous cells (e.g. macrophages) might be involved in the potential uptake of the SPIO released in the extracellular matrix or phagocytosis of dead cells may intervene in the later days after injection hampering the detection of the difference in the later days. Chen et al. reported a change in the histological pattern of ferumoxides injected in the myocardium, from dispersed (day 2) to focal (day 9), suggesting the involvement of macrophages in scavenging and concentrating SPIO (30). This is a common issue in the use of SPIO as a labeling marker, Winter *et al.* reported (by means of signal intensit of the void) the absence of any discrimination between healthy successfully engrafted and dead SPIO labeled cells phagocytosed by macrophages within the heart. Particularly, no differences in signal voids up to more than 40 days were observed between dead and viable cells recipients with respect to size, number and localisation. Therefore, just signal loss in T2-w MR Images overestimates SPIO-labelled stem cells survival after transplantation in the heart (12). Similarly, by performing quantitative MRI mapping we were able to depict a slow decrease of the R2 values of the injected cells which remained higher than the relaxivity values of the normal myocardium for the length of our investigation. These findings confirmed for the first time by MRI mapping that SPIO is not a suitable probe for the longitudinal follow-up of the in vivo fate of implanted cells. We are currently implementing novel approaches based on Gd-labeling and optimized T1 mapping, exploiting the increase in T1 relaxivity upon cell death and a more favourable clearance profile of Gd from tissues.

It is worth to observe that one limitation of this study was related to a quantitative MRI approach based only on R2 and not also R2* measurements. First, because R2* values are more sensitive to changes from the intracellular to the extracellular space (decrease) and second because a calculated R2' (R2*-R2) would probably have been more sensitive in depicting subtle changes. R2* measurements have been attempted, however we found this approach difficult to achieve at 7T, since the MR signal saturates at very short echo time, making impractical R2* curve fitting.

Cell proliferation, cell migration, cell death, extracellular SPIO dispersion or aggregation exhibit different relaxivities. Unless, there is only one well defined process happening in a restricted volume of interest *in vivo* quantification is very complex, as previously investigated in *vitro* by our previous study (13).

In conclusion, many of the techniques to image stem cells are promising but further work is required before a wide clinical translation becomes reality. From the review of the current literature it seems that there is "no single best method", rather an array of different techniques, each one with peculiar advantages in terms of spatial resolution, sensitivity and specificity. Reporter gene imaging, considered as the most reliable approach in the quantitative short and long term evaluation of engraftment and survival, is still associated with unsolved issues such as gene silencing, immunogenicity and debated safety. MRI offers great spatial resolution and quantitative capabilities; however cur-

rently available probes are sub-optimal. The development of hybrid techniques (MRI/PET) together with improved reporter genes would certainly play a role in the quantitative assessment of cell transplantation in longitudinal studies.

Acknowledgements

References

1. Orlic D, Kajstura J, Chimenti S, et al. Bone marrow cells regenerate infarcted myocardium. Nature 2001; 410:701-705.

2. Lipinski MJ, Biondi-Zoccai GG, Abbate A, et al. Impact of intracoronary cell therapy on left ventricular function in the setting of acute myocardial infarction: a collaborative systematic review and meta-analysis of controlled clinical trials. J Am Coll Cardiol 2007; 50:1761-1767.

3. Martin-Rendon E, Brunskill SJ, Hyde CJ, Stanworth SJ, Mathur A, Watt SM. Autologous bone marrow stem cells to treat acute myocardial infarction: a systematic review. Eur Heart J 2008; 29:1807-1818.

4. Korf-Klingebiel M, Kempf T, Sauer T, et al. Bone marrow cells are a rich source of growth factors and cytokines: implications for cell therapy trials after myocardial infarction. Eur Heart J 2008; 29:2851-2858.

5. Ruggiero A, Thorek DL, Guenoun J, Krestin GP, Bernsen MR. Cell tracking in cardiac repair: what to image and how to image. Eur Radiol.

6. Bernsen MR, Moelker AD, Wielopolski PA, van Tiel ST, Krestin GP. Labelling of mammalian cells for visualisation by MRI. Eur Radiol; 20:255-274.

7. Arbab AS, Pandit SD, Anderson SA, et al. Magnetic resonance imaging and confocal microscopy studies of magnetically labeled endothelial progenitor cells trafficking to sites of tumor angiogenesis. Stem Cells 2006; 24:671-678.

8. Delcroix GJ, Jacquart M, Lemaire L, et al. Mesenchymal and neural stem cells labeled with HEDP-coated SPIO nanoparticles: in vitro characterization and migration potential in rat brain. Brain Res 2009; 1255:18-31.

9. Farrell E, Wielopolski P, Pavljasevic P, et al. Cell labelling with superparamagnetic iron oxide has no effect on chondrocyte behaviour. Osteoarthritis Cartilage 2009; 17:961-967.

10. van Tiel ST, Wielopolski PA, Houston GC, Krestin GP, Bernsen MR. Variations in labeling protocol influence incorporation, distribution and retention of iron oxide nanoparticles into human umbilical vein endothelial cells. Contrast Media Mol Imaging; 5:247-257.

11. Amsalem Y, Mardor Y, Feinberg MS, et al. Iron-oxide labeling and outcome of transplanted mesenchymal stem cells in the infarcted myocardium. Circulation 2007; 116:I38-45.

12. Winter EM, Hogers B, van der Graaf LM, Gittenberger-de Groot AC, Poelmann RE, van der Weerd L. Cell tracking using iron oxide fails to distinguish dead from living transplanted cells in the infarcted heart. Magn Reson Med; 63:817-821.

13. Kotek G, van Tiel ST, Wielopolski PA, Houston GC, Krestin GP, Bernsen MR. Cell quantification: evolution of compartmentalization and distribution of iron-oxide particles and labeled cells. Contrast Media Mol Imaging; 7:195-203.

14. Kuhlpeter R, Dahnke H, Matuszewski L, et al. R2 and R2* mapping for sensing cell-bound superparamagnetic nanoparticles: in vitro and murine in vivo testing. Radiology 2007; 245:449-457.

15. Simon GH, Bauer J, Saborovski O, et al. T1 and T2 relaxivity
    of intracellular and extracellular USPIO at 1.5T and 3T
    clinical MR scanning. Eur Radiol 2006; 16:738-745.

16. Henning TD, Wendland MF, Golovko D, et al. Relaxation effects of
    ferucarbotran-labeled mesenchymal stem cells at 1.5T and 3T: discrimination
    of viable from lysed cells. Magn Reson Med 2009; 62:325-332.

17. Rad AM, Arbab AS, Iskander AS, Jiang Q, Soltanian-Zadeh H.
    Quantification of superparamagnetic iron oxide (SPIO)-labeled
    cells using MRI. J Magn Reson Imaging 2007; 26:366-374.

18. van Buul GM, Farrell E, Kops N, et al. Ferumoxides-protamine sulfate is more
    effective than ferucarbotran for cell labeling: implications for clinically applicable
    cell tracking using MRI. Contrast Media Mol Imaging 2009; 4:230-236.

19. van Buul GM, Kotek G, Wielopolski PA, et al. Clinically translatable
    cell tracking and quantification by MRI in cartilage repair using
    superparamagnetic iron oxides. PLoS One; 6:e17001.

20. Roth V. http://www.doubling-time.com/compute.php. In, 2006.

21. Cerqueira MD, Weissman NJ, Dilsizian V, et al. Standardized
    myocardial segmentation and nomenclature for tomographic imaging
    of the heart: a statement for healthcare professionals from the Cardiac
    Imaging Committee of the Council on Clinical Cardiology of the
    American Heart Association. Circulation 2002; 105:539-542.

22. Karamitsos TD, Francis JM, Myerson S, Selvanayagam JB,
    Neubauer S. The role of cardiovascular magnetic resonance imaging
    in heart failure. J Am Coll Cardiol 2009; 54:1407-1424.

23. Chen IY, Wu JC. Cardiovascular molecular imaging: focus
    on clinical translation. Circulation; 123:425-443.

24. Giri S, Chung YC, Merchant A, et al. T2 quantification for improved
    detection of myocardial edema. J Cardiovasc Magn Reson 2009; 11:56.

25. Aletras AH, Kellman P, Derbyshire JA, Arai AE. ACUT2E TSE-
    SSFP: a hybrid method for T2-weighted imaging of edema
    in the heart. Magn Reson Med 2008; 59:229-235.

26. Payne AR, Casey M, McClure J, et al. Bright-blood T2-weighted MRI has
    higher diagnostic accuracy than dark-blood short tau inversion recovery MRI
    for detection of acute myocardial infarction and for assessment of the ischemic
    area at risk and myocardial salvage. Circ Cardiovasc Imaging; 4:210-219.

27. Cocker MS, Shea SM, Strohm O, Green J, Abdel-Aty H, Friedrich
    MG. A new approach towards improved visualization of myocardial
    edema using T2-weighted imaging: a cardiovascular magnetic
    resonance (CMR) study. J Magn Reson Imaging; 34:286-292.

28. Boutry S, Forge D, Burtea C, et al. How to quantify
    iron in an aqueous or biological matrix: a technical note.
    Contrast Media Mol Imaging 2009; 4:299-304.

29. Peldschus K, Schultze A, Nollau P, et al. Quantitative MR imaging
    of targeted SPIO particles on the cell surface and comparison
    to flow cytometry. Magn Reson Imaging; 28:599-606.

30. Chen IY, Greve JM, Gheysens O, et al. Comparison of optical
    bioluminescence reporter gene and superparamagnetic iron oxide
    MR contrast agent as cell markers for noninvasive imaging of cardiac
    cell transplantation. Mol Imaging Biol 2009; 11:178-187.

31. Muller-Ehmsen J, Whittaker P, Kloner RA, et al. Survival and
    development of neonatal rat cardiomyocytes transplanted into
    adult myocardium. J Mol Cell Cardiol 2002; 34:107-116.

32. Nakamura Y, Yasuda T, Weisel RD, Li RK. Enhanced cell transplantation:
    preventing apoptosis increases cell survival and ventricular function.
    Am J Physiol Heart Circ Physiol 2006; 291:H939-947.

33. Krishnan M, Park JM, Cao F, et al. Effects of epigenetic modulation on reporter
    gene expression: implications for stem cell imaging. FASEB J 2006; 20:106-108.

34. Nedopil A, Klenk C, Kim C, et al. MR signal characteristics of viable and
    apoptotic human mesenchymal stem cells in matrix-associated stem cell
    implants for treatment of osteoarthritis. Invest Radiol; 45:634-640.

5.1

Cerenkov luminescence imaging of medical isotopes

Ruggiero A, Holland JP, Lewis JS, Grimm J

Abstract

The development of novel multimodality imaging agents and techniques represents the current frontier of research in the field of medical imaging science. However, the combination of nuclear tomography with optical techniques has yet to be established.

Here, we report the use of the inherent optical emissions from the decay of radio-pharmaceuticals for Cerenkov luminescence imaging (CLI) of tumors in vivo and correlate the results with those obtained from concordant immuno-PET studies.

Methods: In vitro phantom studies were used to validate the visible light emission observed from a range of radionuclides including the positron emitters ^{18}F, ^{64}Cu, ^{89}Zr, and ^{124}I; β-emitter ^{131}I; and α-particle emitter ^{225}Ac for potential use in CLI. The novel radio-labeled monoclonal antibody ^{89}Zr-desferrioxamine B-[DFO-J591 for immuno-PET of prostate-specific membrane antigen (PSMA) expression was used to coregister and correlate the CLI signal observed with the immuno-PET images and biodistribution studies.

Results: Phantom studies confirmed that Cerenkov radiation can be observed from a range of positron-, β-, and α-emitting radionuclides using standard optical imaging devices. The change in light emission intensity versus time was concordant with radionu-clide decay and was also found to correlate linearly with both the activity concentration and the measured PET signal (percentage injected dose per gram). In vivo studies conducted in male severe combined immune deficient mice bearing PSMA-positive, sub-cutaneous LNCaP tumors demonstrated that tumor-specific uptake of ^{89}Zr-DFO-J591 could be visualized by both immuno-PET and CLI. Optical and immuno-PET signal intensities were found to increase over time from 24 to 96 h, and biodistribution studies were found to correlate well with both imaging modalities.

Conclusion: These studies represent the first, to our knowledge, quantitative assess-ment of CLI for measuring radiotracer uptake in vivo. Many radionuclides common to both nuclear tomographic imaging and radiotherapy have the potential to be used in CLI. The value of CLI lies in its ability to image radionuclides that do not emit either positrons or γ-rays and are, thus, unsuitable for use with current nuclear imaging mo-dalities. Optical imaging of Cerenkov radiation emission shows excellent promise as a potential new imaging modality for the rapid, high-throughput screening of radiophar-maceuticals.

Introduction

In the field of medical imaging science, the concept of multimodality is providing the driving force for the development of the next generation of imaging techniques. The latest hybrid systems such as PET/CTand PET/MRI are transforming the clinical man-agement of cancer patients by consolidating the noninvasive localization and temporal quantification of changes in tissue function and physiology available from PET, with the high-resolution anatomic maps provided by CT or MRI (1,2).

In contrast to the immediate clinical impact of nuclear tomographic imaging, optical methods such fluorescence-mediated tomography and bioluminescence imaging have been largely restricted to use in preclinical models. Reasons for the limited clinical trans-lation of optical modalities lie in the inherent limitations imposed by high rates of scat-tering and poor tissue penetration at the human scale. Each of these limitations leads to increased difficulty in providing the quantitative analysis of data required for practical applications in the clinic. As a consequence of these in vivo limitations, recent advances in the field of optical imaging have focused on developing methods for imaging micro-scopic events at the cellular and molecular level.

Endoscopy and surgery could benefit from the translation of optical imaging tech-niques to visualize tumor lesions or metastatic involvement intraoperatively and thereby provide real-time information to guide surgical resection (3). However, at present there are no clinically approved targeted probes for use with targeted fluorescence-reflectance imaging or fluorescence-mediated tomography. Further technical and theoretic challeng-es mean that to date, the research into developing hybrid systems that combine nuclear and anatomic methods with optical imaging cameras is limited (1,4). Currently intraop-erative methods to detect radionuclides are limited by the use of hand-held probes that do not provide any spatial information, whereas pure optical approaches are limited by the lack of clinically approved targeted agents. Because 2-dimensional imaging would re-quire large, expensive, and bulky equipment unsuitable for an operating suite, no meth-od is currently available to use the multiplicity of approved radiotracers in the clinic.

The emission of a continuum of ultraviolet and visible light from the decay of certain radionuclides in the condensed phase (now known as the Cerenkov effect) was first ob-served in 1926 and was characterized by Pavel A. Cerenkov in 1934 (5). Later, in 1958—and along with his colleagues Ilya Frank and Igor Tamm—Cerenkov was awarded the Nobel Prize in Physics, "for the discovery and the interpretation of the Cerenkov effect." Cerenkov radiation arises when charged particles, such as a β- (β$^-$

or β$^+$) or an α-particle, travel through an optically transparent, insulating material with a velocity that exceeds the speed of light, c, in the given medium (6). The Cerenkov effect is analogous to the sonic boom that occurs when a macroscopic object such as a jet plane or a whip exceeds the speed of sound in air. As the charged particle travels through

the medium, it loses kinetic energy by polarizing the electrons of the insulator (typically water). These polarized molecules then relax back to equilibrium through the emission of ultraviolet and visible light, and when the speed of the charged particle exceeds c, constructive interference occurs, giving the observed Cerenkov radiation (6,7).

Although the use of Cerenkov radiation for scintillation counting has been described (8–11), the use of inherent light emission of radionuclides for in vivo imaging is a new concept (12). In a recent paper, Robertson et al. were the first to characterize the use of Cerenkov radiation for the optical imaging of ^{18}F-labeled radiotracers in vivo (13). Further work by Cho et al. (14) and Spinelli et al. (15) verified the origins of visible light emission and paved the way for the development of Cerenkov luminescence imaging (CLI) as a novel in vivo imaging tool.

In this work, we provide further validation of the use of Cerenkov radiation from a much larger range of radionuclides including the positron emitters ^{18}F, ^{64}Cu, [89]Zr, and [124]I; β-emitter ^{131}I; and α-particle emitter [225]Ac. We report in vitro phantom studies that compare the relative intensity of the optical emission observed from these radionuclides and demonstrate the linear correlation between the observed light output and the measured PET signal. In addition, we also report the feasibility of using CLI for both the qualitative and the quantitative assessment of radiopharmaceutical uptake in tumors in vivo. Uptake of the novel monoclonal antibody (mAb)–based radiopharmaceutical [89]Zr-desferrioxamine B –[DFO]-J591 for in vivo immunoimaging of prostate-specific membrane antigen (PSMA) expression in a clinically relevant model of prostate cancer was observed by standard immuno-PET

and acute biodistribution studies. The results of these studies are correlated with the tumor uptake observed by CLI. These investigations reveal that optical imaging of Cerenkov radiation shows excellent promise as a potential new in vivo imaging modality for the rapid, low-cost, highthroughput screening of radiopharmaceuticals.

Materials and Methods

Radionuclides

The radionuclides ^{18}F, [89]Zr, and [124]I were produced in high radiochemical and radionuclidic purity via the ^{18}O-H_2O(p,n)[18]F, [89]Y(p,n)[89]Zr, and [124]TeO_2(p,n)[124]I transmutation reactions on an Ebco TR19/9 variable beam–energy cyclotron (Ebco Industries Inc.) in accordance with previously reported methods (16–20). [64]Cu was supplied by the Washington University School of Medicine (21). [131]I was purchased as a ^{131}I-NaI (aqueous) solution from MDS Nordion. [225]Ac was provided as a generous gift from Dr. Michael R. McDevitt and was obtained as a carrier-free product from elution of a [229]Th generator system (Oak Ridge National Laboratory) (22). For mAb radiolabeling studies, the [89]Zr-oxalate reagent was isolated in high radionuclidic and radiochemical purity greater

than 99.9%, with an effective specific activity of 195–497 MBq/μg (5.28–13.43 mCi/μg) (18).

Phantom Studies

For each radionuclide studied, phantoms of varying activity concentration (activity of 0–8.14 MBq [0–220 μCi] in 200 μL of water, for a concentration of 0–40.7 kBq/μL [0–1.1 μCi/μL]) and composed of 6 transparent plastic Eppendorf tubes were prepared by 5 serial 1:2 dilutions of a known amount of activity in deionized water. Phantoms were imaged at various times appropriate to the half-life ($t_{1/2}$) of the radionuclide under investigation using the Xenogen Ivis 200 device (Caliper Life Sciences). Where possible, PET images of the phantoms were also recorded at the same time points using a microPET Focus 120 scanner (Concorde Microsystems) (23).

Antibody Conjugation and 89Zr Radiolabeling

The IgG_1 mAb J591 was conjugated to the tris-hydroxamate, hexadentate chelate DFO (Calbiochem) using a 6-step procedure modified (24) from that described by Verel et al. (19) (supplemental materials).

Xenograft Models

All animal experiments were conducted in compliance with Institutional Animal Care and Use Committee guidelines and the Guide for the Care and Use of Laboratory Animals (25). All animal procedures were performed under anesthesia by inhalation of a 1%-22% isoflurane (Baxter Healthcare)–oxygen mixture. Full details are presented in the supplemental materials.

PET

PET experiments were conducted on a microPET Focus 120 scanner (23). PET images of the in vitro phantoms were recorded using the same methods and instrument parameters as described for the small-animal immuno-PET studies.

Mice were administered [89]Zr-DFO-J591 formulations (10.9–11.3 MBq [295–305 μCi], 60–62 μg of mAb, in 200 μL of sterile saline for injection) via retroorbital injection. Approximately 5 min before PET images were recorded, mice were anesthetized by inhalation of a 1%-22% isoflurane–oxygen gas mixture and placed on the scanner bed. PET images were recorded at various times between 24 and 96 h after injection. List-mode data were acquired for between 10 and 30 min using a γ-ray energy window of 350–750 keV and a coincidence timing window of 6 ns (the supplemental materials provide additional details).

Optical Imaging

Optical images were acquired using the Xenogen Ivis 200 optical imager. Cerenkov radiation was detected from each phantom containing various activities of the same radionuclide using the bioluminescence setting (integration time, 10, 20, 30, 40, 50, and 60 s; f/stop,1; binning, medium; field of view, B), with no light interference from the excitation lamp. Spectral analysis was obtained by measuring optical images either with or without the use of a narrow band filter (560, 580, 600, 620, 640, and 680, or open filter) of 20 nm in full width at half maximum (the supplemental materials provide additional details).

Acute Biodistribution Studies

Acute in vivo biodistribution studies were conducted at the end of the optical imaging and immuno-PET to validate the uptake and localization of ^{89}Zr-DFO-J591 observed in mice bearing dual subcutaneous LNCaP (50–250 mm^3) tumors (n = 3).

Statistical Analysis

Data were analyzed using the unpaired, 2-tailed Student t test. Differences at the 95% confidence level (P< 0.05) were considered to be statistically significant.

Results

Phantom Studies

The ability to visualize and quantify the Cerenkov radiation emitted from a range of positron, β-, and α-emitting radionuclides was first investigated using in vitro phantom studies. Standard solutions of decreasing activity concentration (ranging from 0 to 40.7 kBq/μL) of each radionuclide in water (200 μL) were prepared by 1:2 serial dilution and subjected to optical imaging at various times appropriate for the t$_{1/2}$ of the nuclide under investigation. For the positron-emitting radionuclides, the phantoms were also imaged using PET. Typical optical and PET images of the phantom are shown in Figures 1A and 1B, respectively. The phantom images recorded with the other radionuclides ^{18}F, ^{64}Cu, ^{89}Zr, ^{124}I, ^{131}I, and ^{225}Ac were qualitatively equivalent. However, for reasons of clarity and consistency with the in vivo studies, our analysis and discussion focus on ^{89}Zr. The data acquired from the optical and PET phantom studies were also quantitatively analyzed. Figure 2A shows a plot of the average (background-corrected) radiance (p/s/cm^2/sr) versus the ^{89}Zr activity concentration (kBq/μL). Background correction was applied by subtracting the radiance measured from a region of interest (ROI) of the optical images drawn over the sample containing no activity. Linear regression analysis reveals a strong, positive correlation between the light emission intensity and activity concentration, with a correlation coefficient of R = 0.98. Figure 2B displays a plot of the normalized radiance versus time, t/h, for the first two ^{89}Zr samples (Fig. 1, tubes 1 and 2). Exponential fitting of the data using the standard equation for first-order radioactive decay gave an

excellent correlation (R = 0.98), with a calculated t$_{1/2}$ (^{89}Zr radiance) equal to 79.1 ± 4.8 h. This experimentally measured t$_{1/2}$ is consistent with the known rate of decay of ^{89}Zr (t$_{1/2}$ = 78.41 h), which provides additional evidence that the source of the radiation arises directly from the radionuclide decay (16). Furthermore, the optical emission profile observed for ^{18}F, ^{64}Cu, ^{89}Zr, ^{124}I, ^{131}I, and ^{225}Ac was

found to be the same as previously reported for ^{18}F and is consistent with Cerenkov radiation (13–15).

To assess the potential for using the observed optical emission of radionuclides for quantitative analysis of the images, the relationship between optical ROI and PET volume of interest was examined. Figure 2C shows a plot of the average radiance (p/s/cm^2/sr) versus the mean activity measured by PET (presented in units of percentage injected dose per gram [%ID/g], which are commonly used for in vivo analysis of radiotracer uptake). A linear relationship (R = 0.98) was observed between the optical and PET signal intensities, suggesting that CLI is, in principle, quantitative. The relationship presented here represents an in vitro system for which the effects of depth- and medium dependent scattering are expected to be minimized. For in vivo imaging, tissue penetration and scattering of light in the ultraviolet and visible regions of the spectrum will complicate the quantification of Cerenkov emission data.

To assess the relative utility of different radionuclides for use in CLI, we investigated the relative light output from each of the available radionuclides. Figure 3 shows a plot of the ratio of the background-corrected average radiance to the activity concentration (in units of [p/s/cm^2/sr]/[kBq/μL]) versus the radionuclide. To facilitate comparison, the positron-emitting radionuclides have been arranged in order of increasing mean β+ kinetic energy/keV. The relationship between the number of positrons emitted in a given energy range and the theoretic number of photons produced in a medium of known
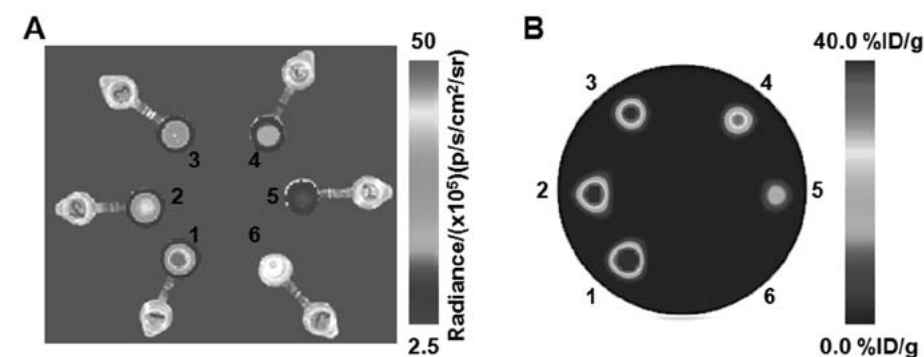

Figure 1. Phantom images recorded using optical (CLI) imaging (A) and PET (B) of 6 samples of ^{89}Zr activity in water. At time 0 h, the Eppendorf tubes labeled 1–6 corresponded to activity concentrations of 40.3, 32.6, 27.4, 20.4, 13.3 and 0.00 kBq/μL. Optical images were recorded by using an integration time of 30 s and f/stop 1.
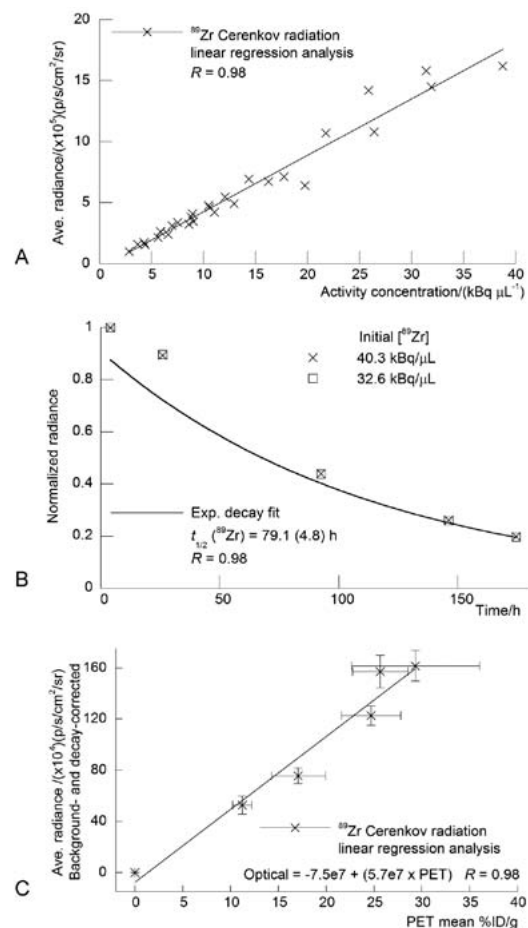
Figure 2. Quantitative analysis of the phantom studies. Positive correlation observed between measured average radiance (background-corrected in units of p/s/cm²/sr) and ^{89}Zr activity concentration (kBq/μL) (A), rate of decay observed in normalized radiance vs. time/h (B), and linear correlation observed between average radiance (background and decay-corrected in units of p/s/cm²/sr) vs. mean PET signal intensity (measured in units of %ID/g, commonly used for quantification of *in vivo* PET studies) (C). Ave. = average; Exp. = exponential.
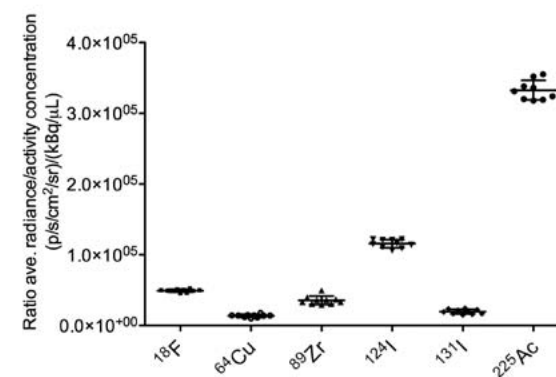

Figure 3. Plot of ratio of average radiance (p/s/cm²/sr)/activity concentration (μCi/μL) vs. radionuclide. Positron-emitting radionuclides are arranged in order of increasing average β⁺ kinetic energy (^{18}F: $E_{\beta+}$=249.8 keV [$I_{\beta+}$=100%]; ^{64}Cu: $E_{\beta+}$=278.2 keV [$I_{\beta+}$=17.6%]; ^{89}Zr: $E_{\beta+}$=395.5 keV [$I_{\beta+}$=22.7%]; ^{124}I: $E_{\beta+}$=820 keV [$I_{\beta+}$=22.7%]). For ^{131}I, $E_{\beta-}$=181.9 keV [$I_{\beta-}$ 100%]. ^{225}Ac decays by 100% α-particle emission with E_α in the range 5021–5830 keV (16). Ave. = average

[mean]=435 keV, $I_{\beta-}$=97.8%], ^{209}Pb ($t_{1/2}$=3.253 h, $E_{\beta-}$[mean]=197.5 keV, $I_{\beta-}$=100%], and ^{209}Tl ($t_{1/2}$=2.20 min., $E_{\beta-}$[mean]=656 keV, $I_{\beta-}$=100%] (28).

The decay of ^{225}Ac cannot be measured by current nuclear imaging modalities. Validation of the use of ^{225}Ac for optical imaging provides an example of the potential applications of dedicated CLI devices. A range of ^{225}Ac-labeled mAb-based agents has been developed (28–31). In an ongoing phase I clinical trial between

Memorial Sloan-Kettering Cancer Center (MSKCC) and the National Cancer Institute, ^{225}Ac conjugated to the humanized anti-CD33 mAb ^{225}Ac-HuM195 is under evaluation as a radioimmunotherapeutic agent for targeted therapy of leukemia and myelodysplastic syndrome (clinical trial NCT00672165). The ability to measure the tumor targeting of ^{225}Ac-labeled mAbs and potentially estimate in vivo dosimetry using optical imaging would represent a fundamental advance in imaging science.

Radiochemistry

To assess the potential of optical CLI of tumors in vivo, we developed the ^{89}Zr-labeled mAb ^{89}Zr-DFO-J591 (32–36). Several examples of the radiolabeling, characterization, and use of ^{89}Zr-DFO-mAbs for immuno-PET of various cancers have been reported (24,37–41). In these studies, the humanized mAb J591, which binds to an extracellular epitope of PSMA expressed in most prostate cancer cell lines, was functionalized with the trishydroxamate chelate DFO using bioconjugation methods modified (24) from the pioneering work of Verel et al. (19).

Full details of the mAb conjugation, identification, and ^{89}Zr radiolabeling and in vitro and in vivo characterization of ^{89}Zr-DFO-J591 will be reported elsewhere. The final radiochemical yield of the purified ^{89}Zr-DFO-J591 was 67%, and the product was formulated in 0.9% sterile saline with a radiochemical purity greater than 99% and a specific activity of 165.0 MBq/mg (4.47 mCi/mg) of mAb (Supplemental Figs. 1 and 2).

refractive index is well established (6,15,26). Despite the fact that the threshold for producing coherent Cerenkov radiation in water is 263 keV (6,7), 18F with a mean β+ kinetic energy of 249.8 keV and positron yield of $I_{\beta+}$= 100% gives a measured radiance for light output comparable to the higher-energy emitter ^{89}Zr ($E_{\beta+}$ = 395.5 keV; $I_{\beta+}$ = 22.7%). As expected for the positron-emitting radionuclides, the higher-energy decay of ^{124}I was found to give the most intense Cerenkov radiation.

^{225}Ac was found to give the most intense optical radiation (Fig. 3). ^{225}Ac is a pure (100%) α-emitter and its decay releases α-particles with energies in the range 5,021 to 5,830 keV. This energy range is considerably higher than the energy of the most energetic positrons studied in this work (^{124}I: $E_{\beta+}$[max.]=2137.6 keV). However, because of their relatively large size (mass) α-particles are known to travel at velocities below the threshold for Cerenkov radiation (27) . The origins of the optical emissions observed from ^{225}Ac remain uncertain, although it is possible that the optical emissions originate from a series of short-lived, β-emitting daughter nuclides including ^{213}Bi ($t_{1/2}$=45.59 min., $E_{\beta-}$

In Vivo Studies

The site-specific localization of ^{89}Zr-DFO-J591 in subcutaneous human xenograft LNCaP (PSMA-positive) tumors was used to assess the ability of optical CLI and immuno-PET to provide both qualitative and quantitative data on the biodistribution of a radiotracer in vivo. Temporal images of ^{89}Zr-DFO-J591 (10.9–11.3 MBq [295–305 µCi], 60–62 µg of mAb in 200 µL of sterile saline) tumor uptake recorded between 24 and 96 h after retroorbital administration using CLI and immuno-PET are

presented in Figures 4A and 4B, respectively. The mice were shaved to reduce signal scattering before imaging at 24 h (15). The images in Figure 4A demonstrate that optical imaging of Cerenkov radiation derived from the decay of an administered radiotracer can be achieved in vivo. In these studies each mouse was inoculated on both the right and the left flanks with LNCaP cells. Tumors grew on both flanks, but in each animal the growth of 1 tumor exceeded that of the other by between 3- and 4-fold, providing 2 different datasets classified as either small or large LNCaP tumors. Figure 4A also shows that differential uptake between the small and large tumors can be discerned by optical CLI. This result is, to the best of our knowledge, the first demonstration of specific
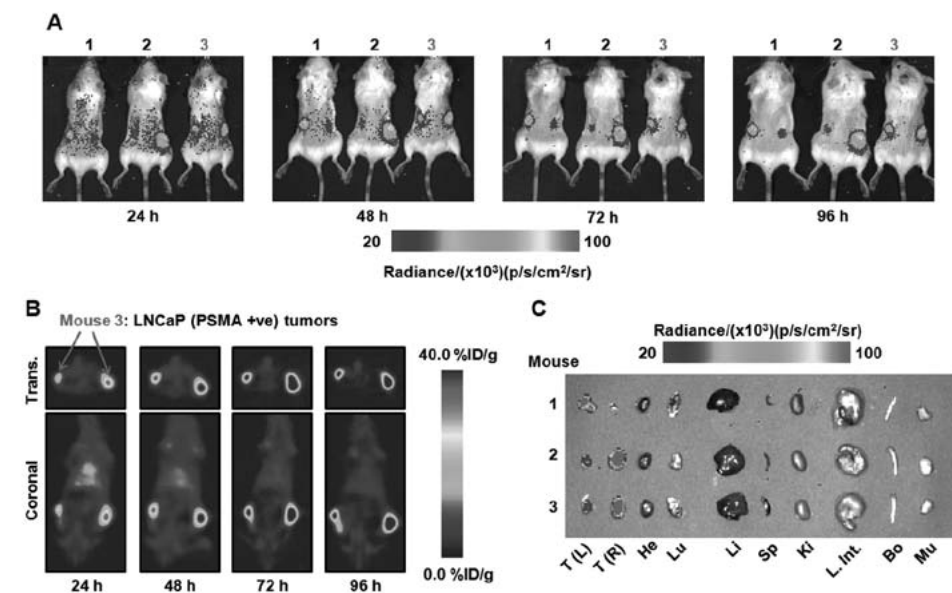

Figure 4. Temporal images of ^{89}Zr-DFO-J591 uptake (10.9–11.3 MBq, [295–305 µCi], 60–62 µg of mAb, in 200 µL 0.9% sterile saline) recorded in dual subcutaneous LNCaP (PSMA-positive) tumor-bearing Severe combined immune deficient mice between 24 and 96 h after administration. (A) signal observed in the optical spectrum from *in vivo* CLI of ^{89}Zr-DFO-J591 tumor uptake in 3 mice. (B) Corresponding coronal and transverse immuno-PET images recorded for mouse 3. (C) Optical image recorded of the organs after acute *ex vivo* biodistribution at 96 h. Transverse and coronal planar immuno-PET images intersect center of tumors. Upper and lower thresholds of CLI and immuno-PET images in A-C have been adjusted for visual clarity, as indicated by scale bars. Trans. = transverse; +ve = positive; T(L) = left tumor; T(R) = right tumor; He = heart; Lu = lungs; Li = liver; Sp = spleen; Ki = kidneys; L. Int. = large intestine; Bo = bone; Mu = muscle.

tumor imaging using the inherent Cerenkov radiation emitted from a metallolabeled immunoconjugate. Furthermore, qualitative analysis of the CLI pictures indicates that higher ^{89}Zr-DFO-J591 background activity is present at 24 h, with lower uptake in the tumors. Between 24 and 96 h, tumor uptake of ^{89}Zr-DFOJ591 continues to increase and activity in the background shows a concordant decrease (as deduced by observation of ROIs located over the mice but remote from the tumor locations).

The corresponding ^{89}Zr-DFO-J591 temporal immuno-PET images of a representative animal (mouse 3) recorded at the same times as the CLI pictures are shown in Figure 4B. Transverse and coronal slices are taken through the center of the tumors. For mouse 3, the LNCaP tumor located in the right flank was approximately 3 times larger in volume (250 mm^3) than the tumor in the left flank (80 mm^3). The first observation is that ^{89}Zr-DFO-J591 provides excellent contrast for the delineation of tumor-versus-background tissue uptake using immuno-PET. Furthermore, facile distinction between the radiotracer uptake and accumulation in the small and large tumors was observed, and tumor uptake continued to increase during the full time course of the immuno-PET experiments. These immuno-PET studies provide a reference point for the interpretation of the CLI data and confirm that the observed qualitative increase in optical intensity of the tumor ROIs over time is due to an increase in radiotracer accumulation. Full quantitative analysis is discussed in the next sections.

At the end of the imaging experiment (96 h), the mice were sacrificed and subjected to both optical imaging of the excised organs and acute ex vivo biodistribution studies to quantify the accumulation of ^{89}Zr radioactivity. An optical image of the excised organs from mice 1–3 is shown in Figure 4C. The organ image demonstrates that at the same optical emission settings and threshold values as used for the in vivo images, uptake in only the LNCaP tumors was observed. The lack of ^{89}Zr activity in the optical image of the background organs is consistent with the immuno-PET images recorded at 96 h, suggesting excellent clearance of ^{89}Zr-DFO-J591 from nontarget tissue.

Results from the acute biodistribution study at 96 h are presented as a bar chart in Figure 5. The data confirm that high uptake of ^{89}Zr-DFO-J591 in PSMA-positive tumors occurs within 96 h after administration. Differential radiotracer uptake and accumulation were observed between the large and small tumor groups. For the larger LNCaP tumors (average volume, 220 mm^3), radiotracer uptake reached 72.3 ± 4.6 %ID/g. However, for the smaller tumors (average volume, 65 mm^3), radiotracer uptake was still well above background tissue uptake but reached only 32.0 ± 5.4 %ID/g (P = 0.0007). The dependence of radiotracer accumulation on tumor size is likely due to enhanced vascularization and the increased number of available PSMA epitopes presented by the well-established tumors.
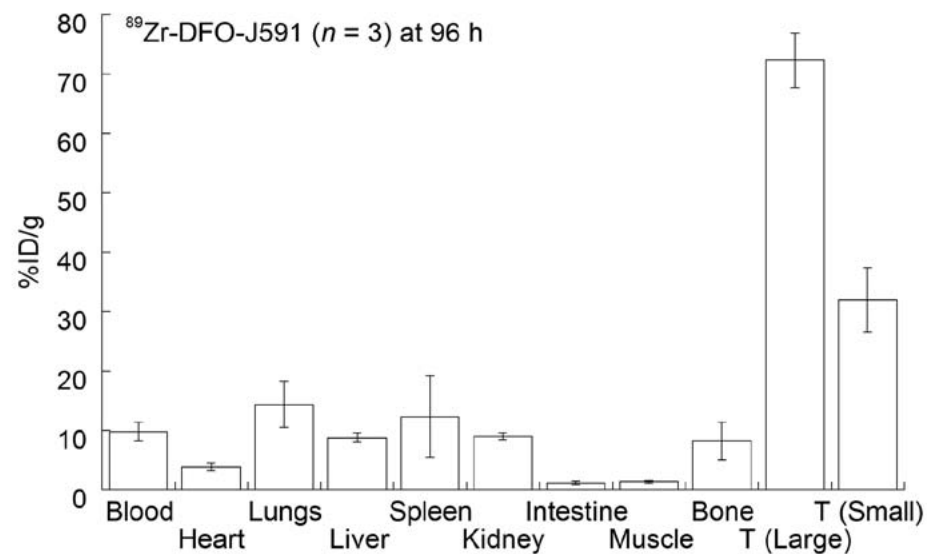
Figure 5. Bar chart showing selected tissue biodistribution data (%ID/g) for uptake of ^{89}Zr-DFO-J591 in male severe combined immune deficient mice at the end of optical and immuno-PET experiments (96 h post-injection). T = tumor

Overall, these biodistribution data are consistent with the optical and immuno-PET studies. For an imaging modality to be useful in a clinical setting, it is essential that the data obtained be at least semiquantitative. Figure 6 shows the time–activity curves derived from ROI and volume-of-interest analysis of the in vivo optical and immuno-PET images. The time–activity curves confirm that ^{89}Zr-DFO-J591 is efficiently removed from the blood pool and accumulated only to low levels in background tissue. The time–activity curves also show that ^{89}Zr-DFO-J591 uptake in the larger tumors increased between 24 and 96 h. For example, the immuno-PET tumor time–activity curve shows an increase in radiotracer accumulation from 16.7 ± 1.4 %ID/g at 24 h to 45.1 ± 10.3 %
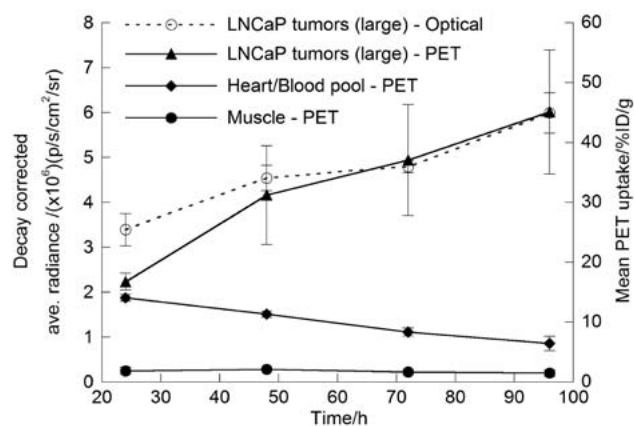
ID/g at 96 h, corresponding to a 2.5 ± 0.8-fold increase. ROI analysis of the optical images also showed the same increase in radiotracer uptake in the larger tumors over time. The measured, decay-corrected, average radiance for the larger tumors increased from 3.4 ± 0.35 to 6.0 ± 0.45 p/s/cm²/sr at 24 and 96 h, respectively. This change in measured tumor radiance corresponds to a 1.8- ± 0.3-fold increase over time, which is similar to changes observed from the immuno-PET studies. Indeed, accounting for the relative errors in the 2 measurements, the observed change in CLI intensity for ^{89}Zr-DFOJ591 tumor accumulation was the same as for immuno-PET.

Discussion

In 2009, Robertson et al. reported proof-of-concept studies that validated the use of Cerenkov radiation emissions in the ultraviolet and visible regions of the spectrum for in vivo optical imaging of ^{18}F-radiolabeled compounds (13). This new technique was termed CLI and represents a fundamental advance toward the development of hybrid nuclear–optical tomographic imaging devices. In this work, we explored the potential of imaging Cerenkov radiation with a wider range of radionuclides and provided the first examples of dual optical CLI and PET of in vivo tumor uptake using a metallolabeled antibody.

The in vitro and in vivo imaging studies presented in this work demonstrate not only that the inherent Cerenkov emissions of various clinically relevant radionuclides can be visualized but also that the data obtained correlate with the observed biodistribution of radiotracers. In addition, both qualitative and quantitative interpretation of the CLI data was found to give a strong correlation with immuno- PET and biodistribution studies. We anticipate that CLI of administered radiopharmaceuticals has a broad range of potential applications. In particular, the ability to simultaneously measure time-dependent changes in tumor uptake of radiotracers in multiple different tumor models or chemotherapeutic treatment regimes means that optical CLI offers the potential to conduct rapid, low-cost, high-throughput screening of novel radiotracers in vivo. In addition, intraoperative imaging of Cerenkov radiation is feasible with a highly sensitive camera in a dark room, the use of which can be achieved much more easily than with expensive nuclear medicine equipment. Notably, no additional development of optical agents is required because CLI can take advantage of many approved radiopharmaceuticals.

Therefore, the combination of endoscopic surgical methods with optical Cerenkov imaging has the potential to be used directly in the clinic for intraoperative visualization of tumor lesions and margins or metastatic involvement for Cerenkov radiation-guided surgery. Further studies using hybrid nuclear–optical imaging of radiopharmaceuticals are under way at MSKCC.

Figure 6. Time-activity curves showing ROI and volume-of-interest analysis of CLI and immuno-PET images for ^{89}Zr-DFO-J591 uptake in well-established (large) LNCaP tumors. Volume-of-interest analysis of immuno-PET images shows change in ^{89}Zr activity in heart-blood pool and muscle tissue.

Conclusion

Basic characterization of the inherent Cerenkov radiation emission from a range of positron-, β-, and α-emitting radionuclides commonly used as imaging and therapeutic isotopes in nuclear medicine is reported. Phantom studies confirm that the broad-spectrum optical emissions arise because of Cerenkov radiation in the condensed phase. The measured radiance was found to give a strong correlation with the known activity concentration, and the signal intensity was found to correlate with the known $t_{1/2}$ of the nuclides under investigation. In addition, in vitro studies comparing the optical signal intensity with that observed from the PET images of the positron-emitting nuclides revealed a linear correlation, indicating that CLI has the potential to provide quantitative data analysis of radiotracers.

In vivo studies looking at the uptake of ^{89}Zr-DFO-J591 in PSMA-positive LNCaP prostate tumors demonstrated that for the first time, to our knowledge, Cerenkov radiation emission can be used to quantify the tumor-specific uptake of a novel targeted, metallolabeled tracer. Furthermore, time–activity curves revealed that the intensity of the observed optical signal correlated with the quantitative immuno-PET and acute biodistribution studies. These results pave the way for further use and development of CLI as a novel optical imaging modality for the rapid, cost effective and high-throughput screening of radiopharmaceuticals. Studies aimed at using the Cerenkov radiation emitted by various radionuclides in the development of activatable reporter system probes are under way at MSKCC.

Acknowledgements

References

1. Weissleder R, Pittet MJ. Imaging in the era of molecular oncology. Nature. 2008;452(7187):580-589.
2. Pichler BJ, Kolb A, Nagele T, Schlemmer H-P. PET/MRI: Paving the way for the next generation of clinical multimodality imaging applications. J Nucl Med. 2010;51:333-336.
3. Kirsch DG, Dinulescu DM, Miller JB, et al. A spatially and temporally restricted mouse model of soft tissue sarcoma. Nat Med. 2007;13(7):992-997.
4. Grimm J, Kirsch DG, Windsor SD, et al. Use of gene expression profiling to direct in vivo molecular imaging of lung cancer. Proc Natl Acad Sci. 2005;102:14404-14409.
5. Cerenkov PA. Visible emission of clean liquids by action of γ-radiation. C R Dokl Akad Nauk SSSR. 1934;2:451-454.
6. Jelley JV. Cerenkov radiation and its applications. Br J Appl Phys. 1955;6:227-232.
7. Ross HH. Measurement of β−emitting nuclides using Cerenkov radiation. Anal Chem. 1969;41(10):1260-1265.
8. Plesums J, Bunch WH. Measurement of phosphorus following 32P cerenkov counting. Anal Biochem. 1971;42(2):360-362.
9. Simonnet F, Combe J, Simonnet G. Detection of 32P scintillating plastic vials. Appl Radiat Isotopes. 1987;38(4):311-312.
10. Hansen BS. Improved method for assaying pyrophosphate exchange measuring Cerenkov radiation. Anal Biochem. 1980;109(1):12-17.
11. Berger SL. The use of Cerenkov radiation for monitoring reactions performed in minute volumes: Examples from recombinant DNA technology. Anal Biochem. 1984;136(2):515-519.
12. Miyata M, Tomita H, Watanabe K, Kawarabayshi J, Iguchi T. Development of TOF-PET using Cherenkov radiation. J Nucl Sci Technol. 2006;43(4):339-343.
13. Robertson R, Germanos MS, Li C, Mitchell GS, Cherry SR, Silva MD. Optical imaging of Cerenkov light generation from positron-emitting radiotracers. Phys Med Biol. 2009;54:N355-N365.
14. Cho JS, Taschereau R, Olma S, et al. Cerenkov radiation imaging as a method for quantitative measurements of beta particles in a microfluidic chip. Phys Med Biol. 2009;54:6757-6771.
15. Spinelli AE, D'Ambrosio D, Calderan L, Marengo M, Sbarbati A, Boschi F. Cerenkov radiation allows in vivo optical imaging of positron emitting radiotracers. Phys Med Biol. 2010;55:483-495.
16. Holland JP, Williamson MJ, Lewis JS. Unconventional nuclides for radiopharmaceuticals. Mol Imaging. 2010;9(1):1-20.
17. Welch MJ, Redvanly CS, Editors. Handbook of Radiopharmaceuticals: Radiochemistry and Applications; Wiley, New York. 2003.

18. Holland JP, Sheh Y, Lewis JS. Standardized methods for the production of high specific-activity zirconium-89 Nucl Med Biol. 2009;36(7):729-739.

19. Verel I, Visser GWM, Boellaard R, Stigter-van Walsum M, Snow GB, van Dongen GAMS. 89Zr immuno-PET: Comprehensive Procedures for the production of 89Zr-labeled monoclonal antibodies. J Nucl Med. 2003;44:1271-1281.

20. Sheh Y, Koziorowski J, Balatoni J, Lom C, Dahl JR, Finn RD. Low energy cyclotron production and chemical separation of "no carrier added" iodine-124 from a reusable, enriched tellurium-124 dioxide/aluminum oxide solid solution target. Radiochim Acta. 2000;88(3-4):169-173.

21. McCarthy DW, Shefer RE, Klinkowstein RE, et al. Efficient production of high specific activity 64Cu using a biomedical cyclotron. Nucl Med Biol. 1997;24(1):35-43.

22. Miederer M, Scheinberg DA, McDevitt MR. Realizing the potential of the Actinium-225 radionuclide generator in targeted alpha particle therapy applications. Adv Drug Delivery Rev. 2008;60(12):1371-1382.

23. Kim JS, Lee JS, Im KC, et al. Performance measurement of the microPET Focus 120 scanner. J Nucl Med. 2007;48(9):1527-1535.

24. Holland JP, Caldas-Lopes E, Divilov V, et al. Measuring the pharmacokinetic effects of a novel Hsp90 inhibitor on HER2/neu expression in mice using 89Zr-DFO-trastuzumab. PLoS ONE. 2010;5(1):e8859.

25. Guide for the Care and Use of Laboratory Animals. Washington, DC: National Academy Press; 1996.

26. Levin CS, Hoffman EJ. Calculation of positron range and its effects on the fundamental limit of positron emission tomography system spatial resolution. Phys Med Biol. 1999;44:781-799.

27. Cherry SR, Sorenson JA, Phelps ME. Physics in Nuclear Medicine. 2003 3rd Edition, Saunders.

28. McDevitt MR, Scheinberg DA. Ac-225 and her daughters: the many faces of Shiva. Cell Death and Differentiation. 2002;9:593-594.

29. McDevitt MR, Ma D, Lai LT, et al. Tumor therapy with targeted atomic nanogenerators. Science. 2001;294(5546):1537-1540.

30. Jaggi JS, Henke E, Seshan SV, et al. Selective alpha-particle mediated depletion of tumor vasculature with vascular normalization. PLoS ONE. 2007;2(3):e267.

31. Ballangrud ÅM, Yang W-H, Palm S, et al. Alpha-particle emitting atomic generator (Actinium-225)-labeled trastuzumab (Herceptin) targeting of breast cancer spheroids: efficacy versus HER2/neu expression Clin Cancer Res. 2004;10:4489-4497.

32. Liu H, Moy P, Kim S, et al. Monoclonal antibodies to the extracellular domain of prostate-specific membrane antigen also react with tumor endothelium. Cancer Res. 1997;57:3629-3634.

33. Liu H, Rajasekaran AK, Moy P, et al. Constitutive and antibody-induced internalization of prostate-specific membrane antigen. Cancer Res. 1997;58:4055-4060.

34. Smith-Jones PM, Vallabahajosula S, Goldsmith SJ, et al. In vitro characterization of radiolabeled monoclonal antibodies specific for the extracellular domain of prostate-specific membrane antigen. Cancer Res. 2000;60(18):5237-5243.

35. Smith-Jones PM, Vallabhajosula S, Navarro V, Bastidas D, Goldsmith SJ, Bander NH. Radiolabeled monoclonal antibodies specific to the extracellular domain of prostate-specific membrane antigen: preclinical studies in nude mice bearing LNCaP human prostate tumor. J Nucl Med. 2003;44(4):610-617.

36. McDevitt MR, Barendswaard E, Ma D, et al. An {{alpha}}-Particle Emitting Antibody ([213Bi]J591) for Radioimmunotherapy of Prostate Cancer. Cancer Res. 2000;60(21):6095-6100.

37. Verel I, Visser GWM, Boellaard R, et al. Quantitative 89Zr immuno-PET for in vivo scouting of 90Y-labeled monoclonal antibodies in Xenograft-bearing nude mice. J Nucl Med. 2003;44:1663-1670.

38. Perk LR, Visser OJ, Stigter-van Walsum M, et al. Preparation and evaluation of 89Zr-Zevalin for monitoring of 90Y-Zevalin biodistribution with positron emission tomography. Eur J Nucl Med Mol Imaging. 2006;33(11):1337-1345.

39. Borjesson PKE, Jauw YWS, de Bree R, et al. Radiation dosimetry of 89Zr-labeled chimeric monoclonal antibody U36 as used for immuno-PET in head and neck cancer patients. J Nucl Med. 2009;50(11):1828-1836.

40. Aerts HJWL, Dubois L, Perk L, et al. Disparity between in vivo EGFR expression and 89Zr-labeled cetuximab uptake assessed with PET. J Nucl Med. 2009;50(1):123-131.

41. Dijkers ECF, Kosterink JGW, Rademaker AP, et al. Development and characterization of clinical-grade 89Zr-trastuzumab for HER2/neu immunoPET imaging. J Nucl Med. 2009;50(6):974-981.

5.2

Intra-operative imaging of PET radiotracers using Cerenkov luminescence emissions

Holland JP, Normand G, **Ruggiero A**, Lewis JS, Grimm J

Abstract

Imaging the location and extent of cancer provides invaluable information before, during, and after surgery. The majority of "image-guided" methods that use, for example, positron emission tomography (PET) involve preoperative imaging and do not provide real-time information during surgery. It is now well established that the inherent optical emissions (Cerenkov radiation) from various β-emitting radionuclides can be visualized by Cerenkov luminescence imaging (CLI). Here we report the full characterization of CLI using the positron-emitting radiotracer ^{89}Zr-DFO-trastuzumab for target-specific, quantitative imaging of HER2/neu-positive tumors *in vivo*. We also provide the first demonstration of the feasibility of using CLI for true image-guided, intraoperative surgical resection of tumors. Analysis of optical CLIs provided accurate, quantitative information on radiotracer biodistribution and tissue uptake that correlated well with the concordant PET images. CLI, PET, and biodistribution studies revealed target-specific uptake of ^{89}Zr-DFO-trastuzumab in BT-474 (HER2/neu positive) versus MDA-MB-468 (HER2/neu negative) xenografts in the same mice. Competitive inhibition (blocking) studies followed by CLI also confirmed the *in vivo* immunoreactivity and specificity of ^{89}Zr-DFO-trastuzumab for HER2/neu. Overall, these results strongly support the continued development of CLI as a preclinical and possible clinical tool for use in molecular imaging and surgical procedures for accurately defining tumor margins.

Introduction

Image-guided surgery provides the surgeon with unprecedented information as to the nature, location, and extent of diseased tissue. For example, in operative cancer patients, imaging modalities including computed tomography (CT) and magnetic resonance imaging (MRI), as well as the nuclear imaging techniques of c-camera imaging, single-photon emission computed tomography (SPECT), and positron emission tomography (PET), have been used to identify tumor masses and disease stage and facilitate minimally invasive surgical resection, with varying degrees of success (1). For women with breast cancer, primary forms of treatment include lumpectomy, mastectomy, and lum- pectomy combined with irradiation therapy (1,2).

The margin status of the resected tissue is an important prognostic factor in defining both the efficacy of surgery and the likelihood of tumor recurrence. In the clinic, margin status is usually assessed by a combination of gross specimen examination by surgeons and pathologists, typically using hematoxylin and eosin stains (3). Clinically, the occurrence of tumor-positive margins as defined by intraoperative pathology is very high, with reported rates of reexcision in the range of 48 to 59% (2,3). It is evident that there is a crucial requirement for developing novel methods to assist surgeons in defining tumor localization and margin status during the primary operation.

Vermeeren and colleagues recently demonstrated the effective use of a portable laparoscopic γ-probe coupled to a γ-camera for intraoperative detection of sentinel lymph nodes using ^{99m}Tc nanocolloids (4,5). Their studies also demonstrate the feasibility of operating on patients who have received a recent dose of radiolabeled agent. In contrast to this intraoperative technique, most "image-guided" surgery that employs PET/SPECT detection relies on preoperative imaging of the patient to identify the location of tumors, which provides the surgeon with the anatomic and potentially physiologic status of the lesions prior to surgery. However, in the surgical situation, these imaging modalities do not currently provide information on margin identification and status and, consequently, are of limited use for "guiding" intraoperative resection. Furthermore, these scanners are large and expensive and require trained personnel to run the acquisition.

What if the distribution of β-emitting radiotracers and radiotherapeutics could be imaged in real time, during the surgical procedure? This would allow the surgeon to use many of the various PET and radiotherapy agents that are already in clinical use, including radiolabeled monoclonal antibodies (mAbs), with high target specificity. In 2009, Robertson and colleagues introduced the concept of Cerenkov luminescence imaging (CLI), whereby the inherent optical emissions from various b-emitting radio- tracers can be visualized by use of a sensitive charge-coupled device (6).

Subsequently, we and others verified the origins and relative intensities of the optical emissions from a range of radionuclides, including ^{18}F, ^{64}Cu, ^{89}Zr, ^{124}I, ^{131}I, and ^{225}Ac (7–12). In preliminary studies, we characterized the ^{89}Zr (half-life = 78.41 hours, electron capture = 76.6%, β+ = 22.3%, Emax [β+] = 897 keV, E_{ave} [β+] = 396.9 keV, R_{ave} [β+] = 1.18 mm, Eγ = 908.97 keV, Iγ = 100%), radiolabeled mAb, and ^{89}Zr-DFO-J591, as the first radioimmunoconjugate for CLI of prostate-specific membrane antigen (PSMA)-expressing prostate xenografts *in vivo* (7,13). The advantages of using ^{89}Zr-radiolabeled mAbs for both PET and CLI include high target specificity, high *in vivo* stability, and the relatively long half-life of ^{89}Zr, which facilitates temporal imaging studies at time points beyond those attainable with ^{18}F, ^{64}Cu, ^{68}Ga, and ^{86}Y. In addition, we demonstrated that region-of-interest (ROI) analysis of *in vivo* CLI data is quantitative and correlates strongly with the measured PET signal (7).

In this work, we present a new application of the use of ^{89}Zr-DFO-trastuzumab PET radiotracer for target specific, quantitative CLI of HER2/neu-positive tumors *in vivo*.14 Changes in optical image data are correlated with the concordant PET image data, and the signal specificity is confirmed by comparison of the measured radiotracer uptake in BT-474 (HER2/neu positive) and MDA-MB-468 (HER2/neu negative) tumor models. In addition, competitive inhibition studies measured by CLI and PET also demonstrate that subtle changes in radiotracer distribution can be observed optically. Finally, we provide the first demonstration of the use of CLI for true image-guided, intraoperative surgical resection of tumors. The data presented strongly support the continued development of CLI as both a preclinical and a clinical tool for use in both molecular imaging and surgical procedures.

Materials and Methods

General details

All chemicals, unless otherwise stated, were purchased from Sigma-Aldrich (St. Louis, MO) and were used as received. Water (>18.2 MV/cm at 25uC; Milli-Q, Millipore, Billerica, MA) was purified by passing through a 10 cm column of chelex resin (Bio-Rad Laboratories, Hercules, CA) at a flow rate < 1.0 mL/min. All instruments were calibrated and maintained in accordance with previously reported routine quality control procedures (15). ^{89}Zr radioactivity measurements were made using a Capintec CRC-15R Dose Calibrator (Capintec, Ramsey, NJ) with a calibration factor of 465. For accurate quantification of radioactivities, experimental samples of positron-emitting radionuclides were counted for 1 minute on a calibrated Perkin Elmer Automatic Wizard^2 Gamma Counter (Perkin Elmer, Waltham, MA) using a dynamic energy window of 800 to 1,000 keV for ^{89}Zr (909 keV emission). ^{89}Zr radiolabeling reactions were monitored by using silica gel–impregnated glass fiber instant thin-layer chromatography (TLC) paper (Pall Corp., East Hills, NY) and analyzed on a radio-TLC plate reader (Bioscan System 200 Imaging Scanner coupled to a Bioscan Autochanger 1000 [Bioscan Inc., Washington, DC] using

Win-Scan Radio-TLC software version 2.2, LabLogic, Sheffield, United Kingdom). Solvent systems included diethylenetriamine pentaacetic acid in water (DTPA, 50 mM, pH 7) and phosphate-buffered saline. The BT-474 (HER2/neu positive) and MDA-MB-468 (HER2/neu negative) human breast cancer cell lines were obtained from the American Type Culture Collection (Manassas, VA), and cells were grown by serial passage using standard methods (14).

Radionuclides and Radiochemistry

^{89}Zr was produced in high radiochemical and radionuclidic purity via the ^{89}Y(p,n)^{89}Zr transmutation reaction on an EBCO TR19/9 variable beam energy cyclotron (Ebco Industries, Richmond, BC) in accordance with previously reported methods (16). Bioconjugation and ^{89}Zr radiolabeling of trastuzumab functionalized with the chelating ligand desferrioxamine B (DFO) were conducted in accordance with previously reported methods (14). The DFO-trastuzumab was radiolabeled to give ^{89}Zr-DFO-trastuzumab. After purification by using spin column size-exclusion chromatography (molecular weight cutoff > 30 kDa), ^{89}Zr-DFO- trastuzumab was formulated in sterile saline for injection with a radiochemical purity > 99% and a specific activity of 178 MBq/mg (4.8 mCi/mg). Isotopic dilution assays revealed that the DFO-trastuzumab conjugated had an average of 3.3 ± 0.2 chelates per mAb. In vitro cellular binding assays using BT-474 (HER2/neu positive) cells demonstrated that the ^{89}Zr-DFO-trastuzumab remained active with an immunoreactive fraction of 0.77 ± 0.06 (n = 3) (17).

Xenograft Models

All animal experiments were conducted in compliance with Institutional Animal Care and Use Committee guidelines and the National Institutes of Health (NIH) Guide for the Care and Use of Laboratory Animals (18). All animal procedures were performed under anesthesia by inhalation of 1 to 2% isoflurane (Baxter Healthcare, Deerfield, IL) and oxygen mixture. Animals were sacrificed by CO2 asphyxiation. Female athymic nu/nu mice (20–22 g, 6–8 weeks old) were obtained from Taconic Farms Inc. (Hudson, NY) and were allowed to acclimatize at the Memorial Sloan-Kettering Cancer Center (MSKCC) vivarium for 1 week prior to implanting tumors. Mice were provided with food and water ad libitum. BT-474 and MDA-MB-468 tumors were induced on the lower right and left flanks, respectively, by subcutaneous injection of 4.0×10^6 cells in a 100 μL cell suspension of a 1:1 v/v mixture of media with reconstituted basement membrane (BD Matrigel, Collaborative Biomedical Products Inc., Bedford, MA). Palpable tumors (50–150 mm^3) developed after a period of 10 to 14 days. The tumor volume (V/mm^3) was estimated using previously described methods (14). All surgical procedures were conducted under anesthesia, and the animals were sacrificed immediately at the end of the procedures without waking.

PET Imaging

PET imaging experiments were conducted on a microPET Focus 120 scanner (Concorde Microsystems, Knoxville, TN) (19). Mice were administered [89]Zr-DFO-trastuzumab formulations (4.07–4.26 MBq, [110–115 mCi], 23–24 mg of mAb, in 200 μL sterile saline for injection) via intravenous tail vein injection. For the competitive inhibition (blocking) studies, mice received a coinjection of [89]Zr-DFO-trastuzumab (3.15–3.52 MBq, [85–95 mCi]) with nonradiolabeled trastuzumab to give a total dose of 125 μg of trastuzumab per mouse. Approximately 5 minutes prior to recording PET images, mice were anesthetized by inhalation of 1 to 2% isoflurane-oxygen gas mixture and placed on the scanner bed. PET images were recorded at various time points between 3 and 144 hours postinjection. List-mode data were acquired for between 10 and 30 minutes using a γ-ray energy window of 350 to 750 keV and a coincidence timing window of 6 ns. For all static images, scan time was adjusted to ensure that a minimum of 20 million coincident events were recorded. Data were sorted into two-dimensional histograms by Fourier rebinning, and transverse images were reconstructed by filtered backprojection into a 128 x 128 x 63 (0.72 x 0.72 x 1.3 mm) matrix. The reconstructed spatial resolution for [89]Zr was 1.9 mm full-width half-maximum at the center of the field of view. Image data were normalized to correct for nonuniformity of response of the PET, dead-time count losses, positron branching ratio, and physical decay to the time of injection, but no attenuation, scatter, or partial-volume averaging correction was applied. An empirically determined system calibration factor (in units of [mCi/mL]/[cps/voxel]) for mice was used to convert voxel count rates to activity concentrations. The resulting image data were then normalized to the administered activity to parameterize images in terms of percent injected dose per gram (%ID/g). Manually drawn three-dimensional volumes of interest (VOI) were used to determined the average %ID/g (decay-corrected to the time of injection) in various tissues/phantom tubes. Images were analyzed using ASIPro VM software (Concorde Microsystems).

Optical Imaging

Optical images were acquired using the Xenogen Ivis 200 optical imager (Caliper Life Sciences, Alameda, CA). Cerenkov radiation was detected using the bioluminescence setting (integration times: 2, 3, 4, and 5 minutes; f/stop: 1; binning: 1, field of view B) with no light interference from the excitation lamp.

Animals were anesthetized and imaged at various time points between 3 and 144 hours postadministration of [89]Zr-DFO-trastuzumab. Images were collected using open filter for planar imaging. Images were collected and analyzed using Living Image 3.6 and 2.6 software (Caliper Life Sciences), respectively. The average radiance (p/s/cm^2/sr) was used for quantitative ROI analysis. Background correction was performed either through the use of dark images acquired at the equivalent instrument integration settings immediately before experimental image collection or by ROI analysis of a region in the same experimental image but remote from the area of interest. For quantitative comparison, ROI data were decay-corrected to the time of injection.

CLI-Guided Surgery

Surgical resection of the BT-474 (HER2/neu positive) tumor located on the lower right flank was performed at the end of the temporal CLI and PET imaging studies immediately prior to full biodistribution studies. Optical imaging was conducted following the same methods described above. Anesthesia was maintained throughout the entire procedure followed by CO2 asphyxiation immediately after the surgery.

Biodistribution Studies

In vivo biodistribution studies were conducted at the end of the optical and immuno-PET imaging to validate the uptake and localization of [89]Zr-DFO-trastuzumab observed in mice bearing dual subcutaneous BT-474 and MDA-MB-468 tumors (n = 4). Mice were anesthetized and then sacrificed by CO_2 asphyxiation at 144 hours postadministration. Thirteen tissue samples were collected, including the tumors, rinsed in water, dried in air for 5 minutes, weighed, and then stored at 4°C for 14 days to allow the activity to decay to a level suitable for counting on the γ-counter. Count data (counts per minute) were background and decay-corrected before a standard calibration curve was used for the numerical conversion to activity (kBq). The %ID/g for each tissue sample was then calculated by normalization to both the total amount of activity injected (kBq) and the organ mass (g).

Statistical Analysis

Data were analyzed using the unpaired, two-tailed Student t-test. Differences at the 95% confidence level (p < .05) were considered statistically significant.

Results

In previous studies, we provided the first pilot demonstration of quantitative CLI of the tumor uptake of an immuno-PET radiotracer, [89]Zr-DFO-J591, for imaging PSMA expression in prostate cancer xenografts (7). Here we describe the first use of CLI for image-guided surgical resection. In addition, we provide details of a full study demonstrating the ability of CLI to measure in a fully quantitative sense the target-specific tumor uptake of [89]Zr-DFO-trastuzumab (14,20–22) in BT-474 and MDA-MB-468 (HER2/neu negative) breast tumor models.

CLI and PET

Temporal CLIs and PET images recorded between 3 and 144 hours following intravenous administration of [89]Zr-DFO-trastuzumab in mice bearing subcutaneous human BT-474 (HER2/neu positive; lower right flank) and MDA-MB-468 (HER2/neu negative; lower left flank) xenografts are presented in Figure 1. The uncorrected optical

CLI data showing the radiotracer distribution in normal mice (left panel; mice 1–4) and trastuzumab-treated (block) mice (right panel; mice 5–8) are given in Figure 1A. Figure 1, B and C, shows representative maximum intensity projection (MIP) PET images recorded between 3 and 144 hours postadministration of [89]Zr-DFO-trastuzumab in normal (mouse 1) and trastuzumab-treated (mouse 7) animals, respectively.

Both the optical and PET images demonstrate that [89]Zr-DFO-trastumab uptake in BT-474 tumors can be visualized above the background. Furthermore, uptake is specific for the HER2/neu-positive tumors, which display an approximate fivefold higher optical signal than the radiotracer uptake observed in the HER2/neu-negative MDA-MB-468 xenografts. Interestingly, as with the PET data, the CLIs recorded at 3 to 48 hours show
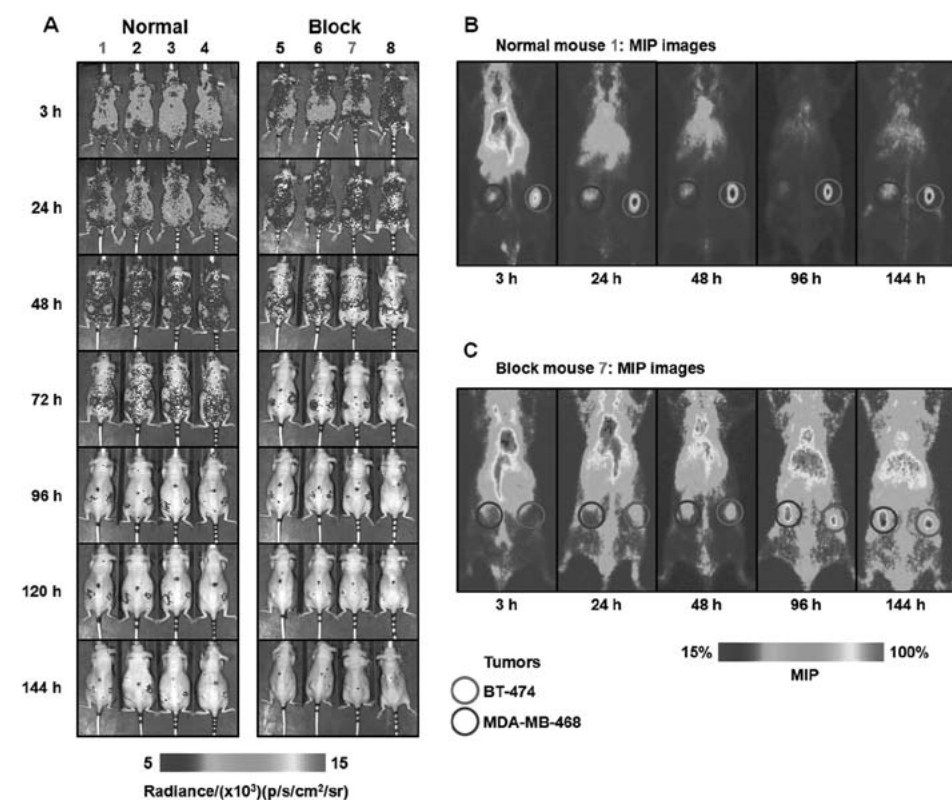
that background activity located primarily in the blood pool (heart, lungs, and liver) can be seen throughout the mouse. [89]Zr-DFO-trastumab uptake in these BT-474 tumor models is known to increase for up to 72 hours in an exponential manner consistent with the expected *in vivo* pharmacokinetics of a radiolabeled IgG1 immunoglobulin (14). As the radiotracer is extracted from the circulation by specific targeting to the HER2/neu antigen, tumor activity increases and blood pool activity decreases with a concordant lowering of optical signal intensity in the background tissues. In addition, by the 72- to 144-hour time points, the [89]Zr-radionuclide decays through 1 to 2 half-lives. Radioactive decay has the effect of lowering the overall signal intensity observed from the mice. At longer time points, the optical signal from background tissue and MDA-MB-468 tumors decreased to levels below the noise. In contrast, owing to the higher radiotracer uptake, Cerenkov emission intensity from the BT-474 tumors remained visible, with improved tumor contrast. In this respect, qualitative analysis of the CLI data was found to be entirely consistent with the changes in radiotracer uptake in tumor and background tissues observed by PET imaging (see Figure 1B).

The optical images also demonstrated the ability of CLI to distinguish between normal and trastuzumab-treated mice (Figure 1, A [right panel] and C). Administration of a blocking dose of trastuzumab competed effectively with the [89]Zr-DFO-trastuzumab for the available HER2/neu antigen, thereby reducing radiotracer uptake in the BT-474 xenografts to values comparable to the uptake in the MDA-MB-468 tumors. Radiotracer uptake in the HER2/neu-negative and the blocked HER2/neu-positive tumors was confirmed previously to be consistent with the "enhanced permeation and retention" mechanism (14). Again, the CLI data were found to be qualitatively consistent with the radiotracer biodistribution observed by PET.

To demonstrate the feasibility and accuracy of using CLI for quantitative analysis of radiotracer distribution, ROI analysis of the two-dimensional optical images was compared to the tissue uptake as measured from VOI analysis of the PET data. Time-activity curves (TACs) showing the average and maximum radiance (in units of p/s/cm²/sr) signal intensity measured from the CLI data of [89]Zr-DFO-trastuzumab uptake in the BT-474 and MDA-MB-468 xenografts for both the normal and blocking experiments are given in Figure 2, A and B, respectively. Corresponding mean and maximum (%ID/g) tumor TACs derived from the PET images of the same mice at equivalent time points are presented in Figure 2, C and D. Quantitative analysis is consistent with the qualitative assessment of the CLIs and PET images. At all time points □ 24 hours, radiotracer uptake in the BT-474 tumors in mice 1 to 4 was higher than that observed in either the MDA-MB-468 tumors (mice 1–8) or the blocked BT-474 tumors (mice 5–8) (see supplementary Tables S1 to S3 for full statistical analysis of the data).

The correlations observed between the quantitative CLI and PET data for the average radiance versus mean %ID/g and the maximum radiance versus maximum %ID/g for all tumors (mice 1–8) at 3, 24, 48, 96, and 144 hours postinjection are shown in Figure
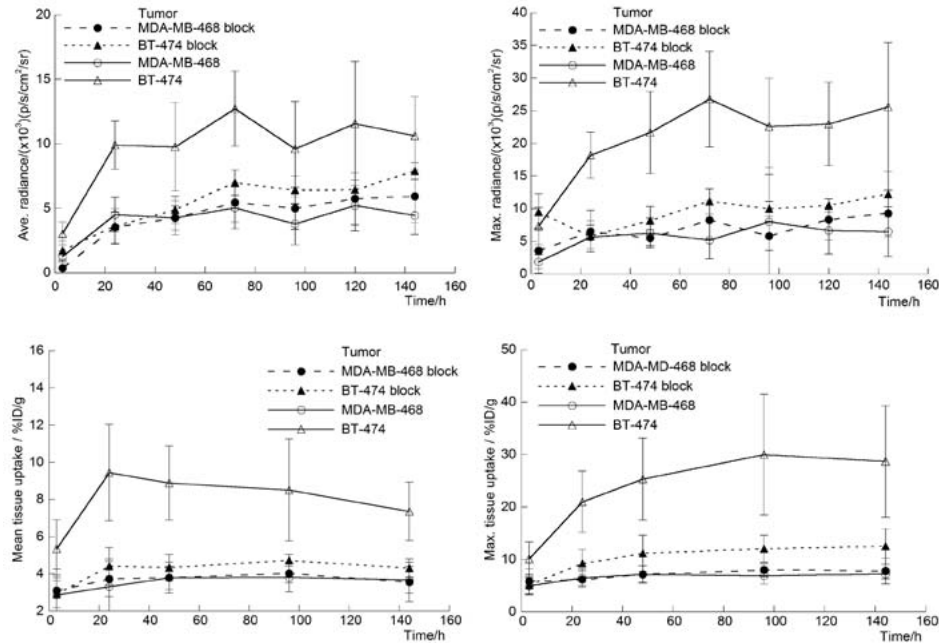

Figure 1. Temporal images of 89Zr-DFO-trastuzumab uptake (4.07–4.26 MBq [110–115 mCi], 23–24 mg mAb; 200 mL sterile saline) recorded in dual BT-474 (HER2/neu positive; lower right flank) and MDA-MB-468 (HER2/neu negative; lower left flank) tumor-bearing mice between 3 and 144 hours postadministration. A, Optical CLI signal observed for 89Zr-DFO-trastuzumab tumor uptake in four normal mice (left panel) and four mice treated with a blocking dose (125 mg/mouse) of nonradiolabeled trastuzumab (see Figure S1 for control optical images). Corresponding temporal maximum intensity projection (MIP) PET images of two representative mice from the (B) normal (mouse 1) and (C) blocking (mouse 7) groups. The upper and lower thresholds of the CLIs and PET images have been adjusted for visual clarity, as indicated by the scale bars. For the MIP images, the higher and lower intensity thresholds were set at 100% and 15%, respectively.

Figure 2. Time-activity curves (TACs) showing change in 89Zr-DFO-trastuzumab accumulation in BT-474 and MDA-MB-468 tumors in both normal and trastuzumab-treated mice. TACs are derived from region-of-interest (ROI) and volume-of-interest (VOI) analysis of the CLIs and PET images, respectively. (A) Average and (B) maximum radiance (p/s/cm2/sr) versus time for the optical CLI data. (C) Mean and (D) maximum %ID/g tumor uptake of 89Zr-DFO-trastuzumab as measured from the PET image data.

3, A and B, respectively. Both plots show strong positive correlation between the optical CLI and PET data with correlation coefficients of R = .82 and R = .89 for the average and maximum data, respectively. Interestingly, in comparison to the mean PET tumor uptake ‛data, the average CLI data (see Figure 3A) appears to slightly overestimate the amount of activity present, giving a linear fit with a gradient of 1.15 x PET signal. In contrast, for the maximum data (see Figure 3B), CLI appears to underestimate the activity present with a gradient of 0.75 x PET signal. This underestimation of the maximum data from CLI is likely due to light attenuation and scattering from the subcutaneous tumor (vide infra). Overall, these data demonstrate that, in principle, given careful calibration of the instrumentation, CLI can provide fully quantitative data on radiotracer uptake in subcutaneous xenograft models.

Biodistribution Data

At the end of the imaging experiment (144 hours), the mice were sacrificed and the organs collected for ex vivo biodistribution studies to quantify the accumulation of ^{89}Zr radioactivity (Figure 4). Biodistribution data are consistent with those reported previously (14,20) and demonstrate that ^{89}Zr-DFO-trastuzumab uptake in BT-474 tumors is very high (47.2 ± 6.3%ID/g) versus MDA-MB-468 (7.2 ± 1.4%ID/g; p = .008), blocked
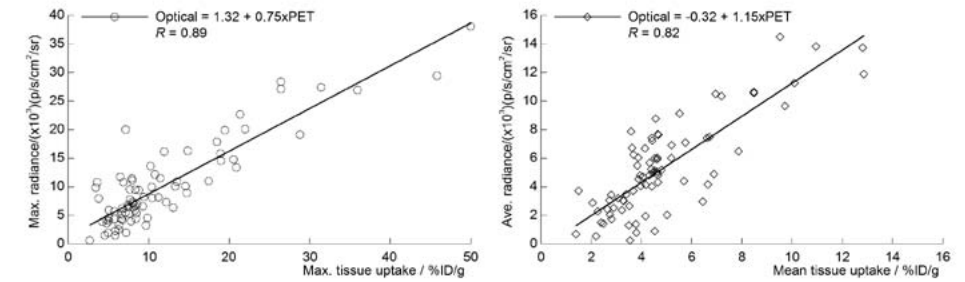

Figure 3. Scatterplots showing the correlation between the observed background and decay-corrected CLI optical signal intensity and the quantitative decay-corrected PET image data for (A) the average radiance and mean %ID/g and (B) the maximum radiance and maximum %ID/g. Each scatterplot contains image data recorded at 3, 24, 48, 96, and 144 hours postinjection of the radiotracer for all normal and trastuzumab- treated (block) groups of mice (total n 5 8 mice; 8 BT-474 and 8 MDA-MB-468 tumors; 5 time points).

BT-474 (21.9 6 7.5%ID/g; p = .005), and blocked MDA-MB-468 (6.5 ± 0.4%ID/g; p = .007) tumors. Full biodistribution data are presented in supplementary Table S4. These ex vivo data support the conclusions from the imaging studies and provide further validation of the quantitative accuracy of the CLI and PET image data.
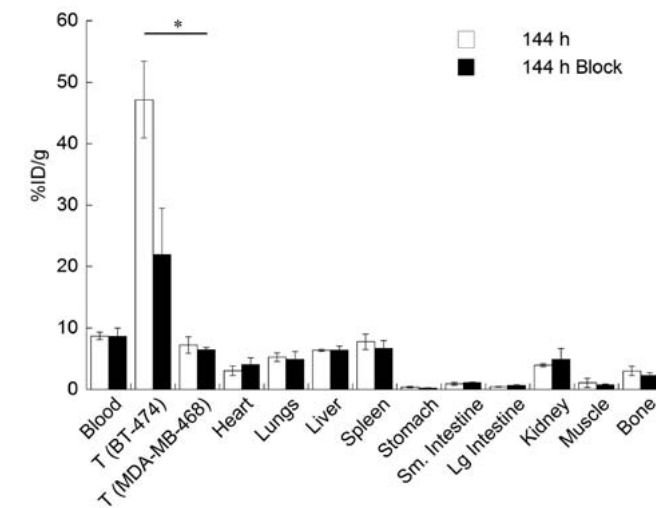

Figure 4. Bar chart showing selected tissue biodistribution data (%ID/g) for the uptake of ^{89}Zr-DFO-trastuzumab in female, athymic nu/nu mice at the end of the optical CLI and PET imaging experiments (144 hours postinjection). *p < .05.

Intraoperative CLI-Guided Surgery

Figure 5 shows a series of CLIs recorded before, during, and after surgical resection of the BT-474 (HER2/neu positive) tumor located on the lower right flank at 144 hours postadministration of ^{89}Zr-DFO-trastuzumab. All images are presented with identical upper and lower radiance thresholds as indicated by the scale bar. A background image

of the surgical workspace and scanner bed is presented as a control in Figure 5A, demonstrating no background CLI. The optical CLI signal observed in the preoperative anesthetized mouse prior to surgical incision shows clear delineation of the BT-474 tumor (see Figure 5B). Note that prior to exposing the tumor mass, the average radiance of the BT-474 tumor was approximately 1×10^4 p/s/cm²/sr. The intraoperative image recorded after surgical incision and exposure of the tumor (red circle) is shown in Figure 5C. As expected, the optical signal intensity showed a marked increase to the average tumor radiance of approximately 1.4×10^4 p/s/cm²/sr. This increased radiance is due to decreased photon attenuation and scattering by removal of the skin. Figure 5D shows the complete loss of optical signal intensity emitted from the mouse on the lower right flank (formerly the location of the BT-474 tumor) and translocation of the signal with the tumor mass (placed in the upper left corner). As a further control, Figure 5E demonstrates that the optical signal is associated with the tumor mass now separated from the mouse. Finally,
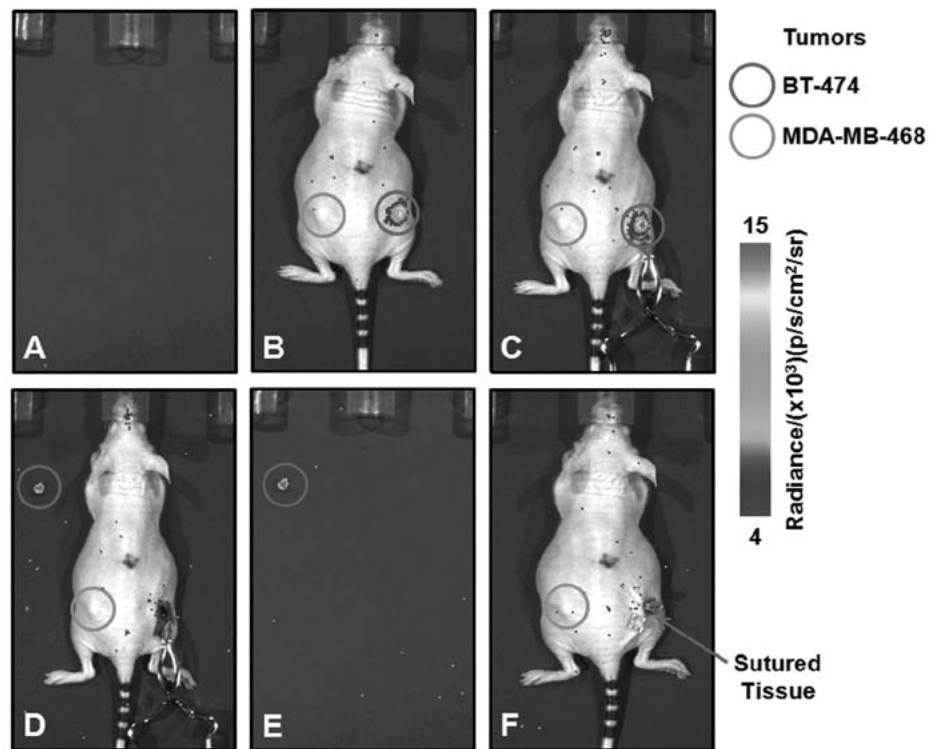

Figure 5. Intraoperative optical CLI of mouse 4 during surgical resection of the BT-474 (HER2/neu positive) tumor at 144 hours postadministra- tion of 89Zr-DFO-trastuzumab. A, Background CLI of the scanner bed recorded immediately prior to com- mencing surgery. B, Preoperative opti- cal CLI of mouse 4 prior to surgical incision. C, Intraoperative optical CLI of the exposed tumor immediately prior to resection. Note the increased intensity of the CLI signal owing to reduced attenuation and scattering from removal of the skin. D, Resected tumor (upper left corner) and the exposed incision site showing the complete loss of CLI signal in the exposed region of the mouse. E, CLI of the excised BT-474 tumor alone. F, Postoperative CLI of the mouse after closing the incision site with sutures. All CLIs are shown at the same radiance scale for direct quantitative comparison.

the postoperative optical image of mouse 4 after closing up the surgical field demonstrates the loss of optical signal in the former location of the BT-474 tumor (see Figure 5F). The entire procedure, including surgical resection and acquisition of all images, was completed in , 40 minutes. Overall, these pre-, post-, and intraoperative optical images demonstrate to our knowledge for the first time the feasibility of developing CLI as a novel surgical tool for improving surgical identification of active tumor lesions showing positive radiotracer uptake and for supporting the surgeon.

Discussion

The studies presented here build on our previous work, in which we demonstrated the potential of using the prompt optical Cerenkov emissions for noninvasive, quantitative *in vivo* imaging of radiolabeled antibodies (7). The phenomenon of Cerenkov radiation from b-particle-emitting radionuclides is well established (6–11,23). Rather than presenting a further demonstration of the origins of the optical emissions, we sought to demonstrate the potential use of CLI for quantitative imaging of radiotracer distribution, and further explore how this new imaging modality may be developed and applied for preclinical and clinical applications.

The *in vivo* imaging and biodistribution studies confirm that accurate qualitative and quantitative information about radiotracer uptake and subcutaneous tumor localization can be obtained from temporal CLI data. Further, we provide a thorough comparison between the TAC data derived from the optical and PET imaging, which confirmed the linearity between the measured light emission intensity and the coincident positron emission data. The observed qualitative and quantitative differences between 89Zr-DFO-trastuzumab uptake in the BT-474 tumors in mice 1 to 4 and the other three tumor models demonstrate that CLI is sensitive enough to distinguish (with statistical significance) between subcutaneous tissues, with an image contrast ratio on the order of 2:1 target-to-background uptake. Given the encouraging results presented here, it seems likely that novel uses of quantitative CLI can be developed using many other common radiotracers and radiotherapeutics, including immuno-PET, and other small molecule agents, such as 18F-fluorodeoxyglucose (6–11).

The image-guided surgery demonstrates that CLI can be used as a very efficient method for identifying small tumor masses with high sensitivity, defining the localization or extent of tumor lesions with accurate delineation of tumor margins, and monitoring the progress of or guiding surgical resection. It is of interest to note that from ex vivo analysis, the absolute amount of 89Zr activity in the BT-474 tumor following tumor resection was only 20.4 kBq (0.55 mCi). Although, in these studies, we did not explicitly investigate the absolute lower limit of activity concentration required for *in vivo* delineation of subcutaneous tissue, our observations do demonstrate the high degree of sensitivity of CLI, which further supports the development of novel optical intraoperative or even laparoscopic or endoscopic tools based on CLI for clinical application.

Other intraoperative imaging methods used clinically, in, for example, sentinel lymph node detection, include visual staining with patent blue and γ-probe detection of ^{99}mTc nanocolloids (4,5). However, each of these methods has its limitations. Patent blue is known to migrate very rapidly, providing only a transient window of opportunity for visualizing lesions. The use of γ-probe imaging is limited by the requirement to use large amounts of radioactivity and by the low spatial resolution of c-ray detection. In contrast to PET and CLI, γ-ray detection is also nonquantitative. Optical imaging by CLI has the potential to circumvent many of these problems by providing almost real-time, quantitative information on radiotracer uptake with high sensitivity while limiting the radiation dose to the patient and surgical teams. Importantly, many clinically used advanced radiotracers approved by the Food and Drug Administration, such as labeled antibodies, can be used without the need for bulky and expensive equipment. Instead, a relatively inexpensive optical device based on CLI detection could be used. This unique combination of optical imaging from radiotracers makes intraoperative CLI a highly attractive approach.

As a result of the unique imaging characteristics of Cerenkov radiation, CLI has the potential to find future use in a wide range of preclinical and clinical applications. These applications include but are not restricted to the optimization of radiopharmaceutical design or target identification via high-throughput *in vivo* screening; the development of low-cost radiotracer imaging equipment that might be used as an alternative to PET in certain circumstances; the use of prompt optical Cerenkov luminescence emissions in a technique analogous to autoradiography; *in vivo* Cerenkov luminescence tomography (11); the use of broad-spectrum Cerenkov emissions as an internal excitation source for fluorescent markers or photoexcitable/cleavable reporter systems; coregistered three-dimentional CLI/PET as a validation tool of bioluminescent reconstruction algorithms; and, as demonstrated here, CLI as the basis of new optical laparoscopic tools for intraoperative, image-guided surgery. In combination with the high target specificity provided by ^{89}Zr- radiolabeled mAbs, it is conceivable that a patient could be imaged by PET at 24 to 72 hours postadministration of the radiotracer to locate tumor lesions, enter surgery approximately 24 hours after the first PET image with CLI used to define accurate tumor margins, and then undergo postoperative PET imaging to confirm the efficacy of the surgical procedure.

Conclusions

In this work, we presented experimental confirmation of the potential of using Cerenkov radiation from β-particle-emitting radiopharmaceuticals as a qualitative and quantitative tool for assessing radiotracer distribution *in vivo*. Changes observed in the CLI data measured with respect to time, tumor model, and radiopharmaceutical formulation were fully consistent with the corresponding PET data recorded in the same mice. An excellent correlation was found between the average and maximum ROI data

between the optical and PET images. Further, all image data were corroborated by quantitative ex vivo assessment of radiotracer biodistribution.

We also present the first demonstration of the use of CLI as a tool facilitating image-guided surgical identification and resection of tumors based on the optical signature of localized radiotracers. Overall, these studies pave the way for further use and development of CLI as a novel optical imaging modality for both preclinical and clinical applications.

Acknowledgments

References

1. Fisher B, Anderson S, Bryant J, Margolese RG, et al. Twenty-year follow-up of a randomized trial comparing total mastectomy, lumpectomy, and lumpectomy plus irradiation for the treatment of invasive breast cancer. N Engl J Med 2002;347:1233-41

2. Balch GC, Mithani SK, Simpson JK, Kelley MC. Accuracy of intraoperative gross examination of surgical margin status in women undergoing partial mastectomy for breast malignancy. Am Surg 2005;71:22-7

3. Chagpar A, Yen T, Sahin A, Hunt KK, et al. Intraoperative margin assessment reduces reexcision rates in patients with ductal carcinoma in situ treated with breast-conserving surgery. Am J Surg 2003;186:371-7

4. Vermeeren L, Meinhardt W, Bex A, van der Poel HG, et al. Paraaortic sentinel lymph nodes: toward optimal detection and intraoperative localization using SPECT/CT and intraoperative real-time imaging. J Nucl Med 2010;51:376-82

5. Vermeeren L, Valdes Olmos RA, Klop WMC, Balm AJM, et al. A portable g-camera for intraoperative detection of sentinel nodes in the head and neck region. J Nucl Med 2010;51:700-3

6. Robertson R, Germanos MS, Li C, Mitchell GS, et al. Optical imaging of Cerenkov light generation from positron-emitting radiotracers. Phys Med Biol 2009;54:N355-N65

7. Ruggiero A, Holland JP, Lewis JS, Grimm J. Cerenkov luminescence imaging of medical isotopes. J Nucl Med 2010; in press

8. Cho JS, Taschereau R, Olma S, Liu K, et al. Cerenkov radiation imaging as a method for quantitative measurements of beta particles in a microfluidic chip. Phys Med Biol 2009;54:6757-71

9. Spinelli AE, D'Ambrosio D, Calderan L, Marengo M, et al. Cerenkov radiation allows in vivo optical imaging of positron emitting radiotracers. Phys Med Biol 2010;55:483-95

10. Liu H, Ren G, Miao Z, Zhang X, et al. Molecular optical imaging with radioactive probes. PLoS ONE 2010;5:e9470

11. Li C, Mitchell G, Cherry S. Cerenkov luminescence tomography for small animal imaging. Optics Letters 2010;in press

12. Holland JP, Williamson MJ, Lewis JS. Unconventional nuclides for radiopharmaceuticals. Mol Imaging 2010;9:1-20

13. Holland JP, Divilov V, Bander NH, Smith-Jones PM, et al. ^{89}Zr-DFO-J591 for immunoPET imaging of prostate-specific membrane antigen (PSMA) expression *in vivo*. J Nucl Med 2010; in press

14. Holland JP, Caldas-Lopes E, Divilov V, Longo VA, et al. Measuring the pharmacokinetic effects of a novel Hsp90 inhibitor on HER2/*neu* expression in mice using ^{89}Zr-DFO-trastuzumab. PLoS ONE 2010;5:e8859

15. Zanzonico P. Routine quality control of clinical nuclear medicine instrumentation: a brief review. J Nucl Med 2009;49:1114-31

16. Holland JP, Sheh Y, Lewis JS. Standardized methods for the production of high specific-activity zirconium-89 Nucl Med Biol 2009;36:729-39

17. Lindmo T, Boven E, Cuttitta F, Fedorko J, et al. Determination of the immunoreactive fraction of radiolabeled monoclonal antibodies by linear extrapolation to binding at infinite antigen excess. J Immunol Methods 1984;72:77-89

18. National Institutes of Health. Guide for the care and use of laboratory animals. Washington, DC: National Academy Press; 1966.

19. Kim JS, Lee JS, Im KC, Kim SJ, et al. Performance measurement of the microPET Focus 120 scanner. J Nucl Med 2007;48:1527-35

20. Dijkers ECF, Kosterink JGW, Rademaker AP, Perk LR, et al. Development and characterization of clinical-grade ^{89}Zr-trastuzumab for HER2/neu immunoPET imaging. J Nucl Med 2009;50:974-81

21. Dijkers EC, Oude Munnink TH, Kosterink JG, Brouwers AH, et al. Biodistribution of ^{89}Zr-trastuzumab and PET imaging of HER2-positive lesions in patients with metastatic breast cancer. Clin Pharmacol Ther 2010

22. Oude Munnink TH, Korte MAd, Nagengast WB, Timmer-Bosscha H, et al. ^{89}Zr-trastuzumab PET visualises HER2 downregulation by the HSP90 inhibitor NVP-AUY922 in a human tumour xenograft. Eur J Cancer 2010;46:678-84

23. Cherry SR, Sorenson JA, Phelps ME. Physics in Nuclear Medicine. 2003;3rd Edition. Saunders.

6

Discussion

In this thesis we have performed investigations on different topics from novel nanotechnology platform to reporter gene imaging, from cell tracking by quantitative MRI to Cerenkov radiation. These topics were all connected by the *"fil rouge"* of molecular imaging (MI). In fact, by using multiple modalities from PET to optical imaging to quantitative MRI we explored the potential of the molecular imaging suite in addressing the major topics in imaging sciences: a) development and evaluation of novel and innovative probes for targeted imaging and therapy (**chapter 3**); b) optimization of reporter gene imaging and direct labeling for cell tracking by PET and MRI (**chapter 4**); c) assessment and evaluation of novel approaches for multimodal optical imaging and their use in the intraoperative or endoscopic settings (**chapter 5**).

Molecular imaging for novel probe development and testing

The lecture by Richard Feynman "there is plenty of room at the bottom" in 1959 is credited as the start of the interest of nanotechnology and its application for imaging and therapy (1). He discussed "the problem of manipulating and controlling things on a small scale," including placing "the mechanical surgeon inside the blood vessel" to observe, report, and perform the surgery. In the field of nanomedicine we are now successfully approaching solutions to this challenge (2, 3). The appeal of nanomaterial-based probes in targeted imaging and therapy is based on two factors. First, the ability to control the synthesis of the agents in a manufacturing process to make multifunctional and multivalent molecules, to alter molecules' pharmacokinetics, making them suitable for human applications in terms of safety and potency. Second, the sizes and shapes of the novel nanomolecules which are quite different from conventional protein-based agents, have unique advantages as a large surface to volume ratio and the possibility of containment for various cargo. For example, single wall carbon nanotubes (SWCNT) have a mass similar to a typical large protein (of 100-150 kDa) but more than 15 times the surface area available for ligand attachment or cell interaction than a large protein. Because of the non-biological origin of these materials, different sizes and shapes, their tissue distribution and excretion of nanomaterials is very different from the known probes and have been extensively debated (4). Therefore, there is an urgent need to investigate the in vivo behaviour of these platforms. In **chapter 3.1**, we designed SWCNTs decorated with various ligands (by covalent functionalization) such that the renal clearance of these materials in mice could be monitored by using three different imaging techniques (microscopy, in vivo optical imaging and PET imaging). By both experimental and theoretical approaches, we investigated how SWCNTs can align with flowing blood and be rapidly excreted through the renal filter. These findings have implications for our fundamental understanding of renal physiology and our knowledge of the ability of chemically functionalized SWCNTs to translocate biological barriers (5). In fact, the glomerular filter is a multicompartment structure composed of endothelial cells, the glomerular basal membrane and podocyte foot processes. Similar to transport across any membrane, there was thought to be a maximum size limit for molecules that could cross this structure (6). Until recently, the threshold - in terms of molecular weight - was

believed to be around 50 kDa (4). We observed that chemically functionalized SWCNTs (average length: 200–500 nm), of molecular weights of up to 500 kDa are eliminated by rapid translocation through the glomerular filter following intravenous administration, without signs of degradation. More importantly, we showed that no active transport mechanism (secretion) is responsible for this overwhelming glomerular translocation and that SWCNTs follow rapid, "first-pass" pharmacokinetics that eliminates most of the injected dose from the body within minutes. Only a small fraction (~15% of injected dose) is reabsorbed into the tubule cells of the kidneys and presumably, though not shown experimentally, recycled into the bloodstream, leading to slower, second-phase, excretion rates. Moreover, the theoretical analysis illustrates the importance of SWCNT's shape and aspect ratio, in allowing alignment with flowing blood and hence, orientation of fibrils perpendicular to the glomerular filter. Previous investigations of tissue distribution and blood clearance kinetics of the same chemically functionalized single and multiwalled carbon nanotubes (7) following intravenous administration had shown the rapid renal clearance and translocation across the glomerular filter (8). However, these results had elicited along with excitement some skepticism because other studies using carbon nanotubes modified with polymeric molecules or with different surface chemistries reported different and contradictory observations such as liver accumulation and slow hepatobiliary excretion (9). Rapid elimination from blood circulation and urinary excretion is desirable from a imaging point of view (especially for radionuclide imaging), allowing the probe accumulation only in the site of the potential target and giving a very low background (presence of the probe in the circulation or non-target sites). Also, it is suitable for therapeutic purposes as the cargo properties allow the delivery of a higher payload of drugs or radiotherapeutics.

Since the real appeal of these novel constructs is inherent to targeted approaches, their potential was assessed by making them specific towards the neoplastic vasculature with the antibody E4G10, as described in **chapter 3.2** (10-14). By using a quantitative optical imaging device (Fluorescence Molecular Tomography, FMT) the targeting potential was assessed and the number of VE-cad epitopes per endothelial cell estimated. Then, E4G10-SWCNT were designed for imaging and therapy. The beauty of this approach is related to the high aspect ratio and to the periodic structure of SWCNT, which make these nanomaterials amenable to being simultaneously appended with multiple copies of reactive primary amines, radiometal chelates (DOTA or DFO) and antibodies. By amplifying the number of chelates per SWCNT, we have demonstrated a dramatic increase of specific activity of radiolabeling of SWCNT-(DOTA) relative to IgG constructs. Each of these SWCNT molecules had ~100 DOTA or DFO chelates appended per SWCNT. In contrast, an IgG might only accommodate 5–10 DOTA moieties per molecule before losing the ability to target and binding efficiency (15). PET imaging showed specific tumor accumulation of the targeted construct (versus untargeted) at the tumor site, also confirmed by blocking studies with cold antibody. However, the possibility of obtaining higher specific activity at the site of interest is much more relevant in the design of constructs for therapeutic purposes. Therefore, the therapeutic version

of this construct was radiolabeled with the alpha particle emitting radionuclide (^{225}Ac). Alpha particles are particulary suitable for vasculature targeting as track lengths (~50–80 µm) appropriately matches the vessel dimensions (typical tumor vasculature diameter: 100 µm), and a single traversal through a cell of a high linear energy transfer (LET) alpha particle can be acutely cytotoxic (16-18). With this approach, we observed increased survival of animals and arrest of tumor growth after only one treatment relative to the control groups.

Besides the production and testing of novel imaging platforms, the most intruiguing aspect of MI is the possibility to develop and suggest novel approaches to adequately evaluate the response to cancer treatment, which is one of the most striking challenges of medical imaging. The RECIST guidelines, published in 2000 and revised in 2009, have become the most widely accepted criteria for response evaluation for clinical trials and practice in most solid tumors (19-21). RECIST are based on uni-dimensional (1D) measurements (maximum diameter of target lesions) and their relative changes during therapy. Briefly, they provide a standardized and practical method to assess response OR define progression in solid tumors, however, pitfalls and limitations of RECIST have been noted in various clinical scenarios (22). Novel approaches based on the tridimensional (instead of unidimensional) evaluation of the tumor has been suggested, successfully performed by using semi-automated or automated softwares but yet not completely validated (23, 24).

Some of the pitfalls and limitations arose with the development of specific targeted therapies (25, 26). Clinical observations indicate that traditional RECIST-based criteria, originally developed to assess response to cytotoxic chemotherapeutic agents, may not be sufficient to fully characterize tumor response and progression in genomically defined subsets of patients treated with specific targeted therapies. Functional and molecular imaging target of response to treatment are urgently needed. The further evolution of RECIST into PERCIST (27), which include PET criteria have been discussed; also an approach based on the the dynamic evaluation of contrast enhancement has been suggested in the clinical arena (28). In MI, several probes like annexin V have been tested to monitor tumor apoptosis upon treatment (29). In **chapter 3.3**, we sought to provide a "proof-of-concept" by using an FDA approved antibody to monitor response assessment by PET. Capromab Pendetide or ^{111}In-7E11 (ProstaScint; Cytogen Corp.) is a monoclonal antibody targeting the prostate specific membrane antigen (PSMA) and also one of the earliest monoclonal antibodies FDA approved for imaging (SPECT) purposes. However, the use of ^{111}In-7E11 for clinical diagnosis has been considered limited (in comparison to other PSMA antibodies, as J591) since its intracellular binding site is accessible only upon membrane disruption in dead, dying, or apoptotic cells within tumor sites. Moreover, we envisioned to make use of the presupposed limitation of 7E11 to monitor the changes in epitope presentation after treatment by PET imaging. By in vitro, in vivo, and ex vivo investigations, we tested the hypothesis that the effects of different treatment options available for PC could be monitored by observing the increase

in 7E11 uptake secondary to cell membrane disruption during treatment. In addition, being this antibody already available for clinical use, we envisioned a potential and easier clinical translation. Thus far, no clinically used antibodies have been suggested for imaging treatment response in prostate cancer, although other agents have shown some potential (30). For example, ^{99m}Tc-annexin V has been proposed to image early apoptosis in murine tumors after chemotherapy (31). The loss of cellular membrane integrity has been imaged by using macromolecules that can be exchanged between the extra- and intracellular compartment, such as ^{99m}Tc-pyrophosphate (32) or ^{99m}Tc-glucarate (33). Moreover, we sought to overcome the limitation of SPECT imaging by designing a novel radiolabeled version with ^{89}Zr, allowing PET imaging, gaining higher sensitivity and better spatial and temporal resolution (34). Our in vitro and microscopy studies, demonstrated a gradual and statistically significant increase in 7E11 cell positivity during treatment, as a result of membrane disruption and cell death (as confirmed by 7AAD and caspase staining). Then, immunoPET imaging after injection of ^{89}Zr-7E11 reported higher uptake in treated tumors versus control, demonstrating an early response to treatment. Importantly, this study tested the proof-of-concept that an intracellular epitope can be the target of the imaging of response assessment as it becomes available on cell membrane permeabilization after treatment.

Optimization of reporter gene imaging and direct labeling for cell tracking in PET and MRI

Cell-based therapies hold great promise and interest for cancer treatment and regenerative medicine. The convergence of the imaging and molecular/cell biology disciplines in the mid 1990s is at the heart of this success story and it is the wellspring for further advances in this new field. Molecular imaging, in its many forms, has rapidly become a necessary tool for the validation and optimization of cell engrafting strategies in preclinical studies. These include a suite of radionuclide, magnetic resonance and optical imaging strategies to evaluate non-invasively the fate of transplanted cells. In **chapter 4**, we explored the two different techniques available for cell tracking, namely reporter gene-based approaches and the passive labeling. Reporter gene approaches have the intriguing potential to provide unique insights into the mechanisms of cell-based therapies. Namely, this system identifies with exquisite specificity only viable cells (which actively contain the gene product) and allows long term tracking of transduced SC (circumventing issues of probe dilution with cellular proliferation). There are several approaches (discussed in **chapter 4.1**), from luciferase/luciferine (suitable only for *in vitro* assays and small animal imaging) to the most advanced thymidine kinase gene (HSV1-tk, suitable also for large animals or human use). The latter, introduced by the pioneering work of researchers at Memorial Sloan-Kettering Cancer Center (35, 36) is currently the most commonly used PET radiotracer-based reporter gene in cell tracking studies. The reporter gene paradigm requires often the appropriate combination of reporter transgene and a reporter probe, such that the reporter gene product interacts with an imaging probe and when this event occurs the signal may be detected and quantified. It has been successfully

used in association with several probes such as ^{18}F-FIAU, ^{124}IFIAU,^{18}F-FEAU and ^{18}F-FHBG. Theoretically, it should be a "zero background" technique as the signal is present and amplified only in the site where the reporter gene is expressed, but in reality notable levels of background radioactivity following injection of radiolabeled nucleosides are observed in the abdomen owing to both renal and hepatobiliary clearance of such agents. Besides this, other factors might play a role, as discussed in **chapter 4.2**. We tested the hypothesis that radionucleoside analogues can translocate from the bloodstream to the intestinal mucosa, where they can be taken up, phosphorylated and trapped by the commensal intestinal flora contributing to the high and early intestinal background observed in radionucleoside imaging. We observed that the presence or absence of bacteria in the intestinal lumen does not affect intestinal background radioactivity. Then, we aimed to reduce the intestinal background by increasing the intestinal excretion of the probes and gaining a better tumor-to-background ratio. The combination of liquid diet and osmotic laxative lowered intestinal radioactivity levels and increased (2.2-fold) the HSV1-*tk* transduced xenograft-to-intestine ratio for ^{18}F-FEAU.

As mentioned, this approach guarantees the theoretical long term expression of the reporter gene in the proliferating population and provides information regarding the viability status of implanted cells. Albeit, some concerns exist (which delay a broad clinical translation). First, the non-physiological expression of reporter gene proteins may perturb the cellular and therapeutic functions. Secondly, some issues may arise from the transduction technique adopted. In fact, adenoviral transduction is hampered by episomal gene expression and by immunogenicity (leakiness of immunogenic adenoviral proteins that can lead to an immune response) (37, 38). On the other hand, the lentiviral transduction guarantees the integration of the reporter gene in the host cell chromatin allowing stable expression in dividing cells (39) and circumventing immunogenicity (40). The integration of the reporter gene within the genome has raised concerns about the risk of mutagenesis and potential oncogenicity (41). Conversely, passive labeling is associated with a more acceptable safety profile, but very limited information on the cell viability status. Fluorescent, radioactive or paramagnetic molecules can be loaded into cells and visualised with the correspondent technique. In the last decade the most successful and clinically translatable approach has been the use of iron oxides for MRI imaging of implanted cells. Iron oxides are superparamagnetic compounds which perturb the magnetic field inducing changes in the relaxivity of tissues and allow the visualisation by MRI. A few *in vitro* studies suggested that the evaluation of relaxivities by R2 (1/T2) and R2* (1/T2*) parametric mapping can be a reliable and reproducible quantification method of superparamagnetic iron oxides (SPIO) or SPIO-labeled cells per voxels (42-44). Most importantly, variation of R2 and R2* according to the compartimentalization have been described. Intriguingly, R2 measurements are higher for the free iron than for the cell-bound iron (43, 45). From these assumptions we aimed in **chapter 4.3** and **chapter 4.4** to perform quantitative MRI of passive labeled cells (by Gd or iron oxides) aiming to complement and potentially correlate our findings with the unique information provided by a reporter gene approach (Luciferase).

In **chapter 4.3,** we investigated *in vitro* and *in vivo* the R1, R2 and R2* characteristics of cells labeled with either Gd-liposomes or SPIOs. Particularly, we observed how the compartmentalization of the label influences the relaxivity values. Intriguingly, Gd-labeled cells presented a characteristic behaviour: their signal is "quenched" (on T1-w images) immediately after injection and then undergoes a "dequenching" upon cell proliferation (label dilution) or cell death. We observed that both ΔR1 (decrease) *and* ΔR2 (increase) are affected by compartmentalization, causing the typical Gd signal "quenching" in viable cells. Instead, non-viable cells, allowing both an efflux of Gd and/or influx of water molecules more easily, exhibited an increased ΔR1/ΔR2 ratio. The SPIO labeled cells caused a persistent signal void, independently of their viability status. However, the scientific literature on MRI quantitative mapping for quantification of labeled cells in realistic settings (e.g. beating heart) has been quite limited. Therefore, in **chapter 4.4**, 2e sought to use R2 mapping as a means to detect *in vivo* changes associated with probe dilution and potential decompartmentalization of SPIO as a result of cell proliferation and cell death, respectively. We employed a double inversion recovery BBFSE sequence and tested its robustness in a reproducibility experiment. The signal was quite homogenous and the technique was proven to be robust and reproducible. Luciferase expressing mesenchymal stem cells were labeled with SPIO and implanted in the heart. Bioluminescence showed an initial increase of the optical signal (peak on day 7), most probably related to cell proliferation, followed by a decrease in signal strength. By using MRI to monitor cell proliferation, we and others previously reported that under *in vitro* conditions, cell proliferation/division is associated with a R2 decrease (T2 increase). On MRI, we observed a 2-fold significant R2 increase from day 3 to 5 after injection, which corresponded to the increasing optical bioluminescence signal (cell proliferation). However, we reported decreasing R2 values already from day 5 onwards, while bioluminescence data still suggested proliferation. Overall we found no significant correlation between bioluminescent signal profiles and MRI signal evolution. We argued that the processes happening *in vivo* (such as cell redistribution in the injection site, re-absorption of the injection medium) obscured the detection of potential changes associated with probe dilution and cell death. In addition, the presence of endogenous cells (e.g. macrophages) plays a role in the potential uptake of the SPIO released in the extracellular matrix or in the phagocytosis of dead cells and act as a confounding factor. Our study was the first investigation to demonstrate the difficulty to assess quantitatively *in vivo*, the intriguing properties of SPIO labeled cells observed *in vitro* by MRI. Infact, cell proliferation, cell migration, cell death, extracellular SPIO dispersion or aggregation exhibit different relaxivities. In the in vivo setting these process happen simultaneously, making quantification challenging if not impossible.

Assessment and evaluation of novel approaches for multimodal PET/optical imaging and their potential use in the intraoperative or endoscopy setting

Among the different MI techniques, optical imaging is certainly a field that found already a rapid translation from the preclinical to the clinical arena, for its potential in

endoscopy and intraoperative evaluation. In surgery palpation and visual appearance is the only way to differentiate between tumor and normal tissue. In the era of image-guided surgery, great work has been done in the field of optical imaging, to better evaluate neoplastic masses, metastasis and obtain adequate tumor-free margins (46). Particularly, the properties of light emitted from a light source are exploited to image anatomic or chemical characteristics of tissue. Imaging of optical contrast can be performed using either the properties intrinsic to the tissue or using ligands conjugated to an optically active reporter to target a recognized disease biomarker (47). In the last 2 years, the optical imaging community witnessed a revamp of an old and well described phenomenon. The direct emission of a continuum of ultraviolet and visible light from the decay of certain radionuclides was first observed in 1926 and was characterized in 1934 by Pavel A. Cerenkov who received the nobel prize in Physics in 1958, "for the discovery and the interpretation of the Cerenkov effect" (5). Although the use of Cerenkov radiation for scintillation counting has been described (48, 49), the use of inherent light emission of radionuclides for *in vivo* imaging is a new concept (12). Conventional optical imaging (besides bioluminescence) requires either excitation by an external light source or by a biological process. Cerenkov Luminescence imaging (CLI) produces the light from the radioactivity, so no external illumination is needed. In **chapter 5.1** and **5.2,** we explored the potential of CLI with a wider range of radionuclides and provided the first examples of dual optical (CLI) and PET of in vivo tumor uptake using a radiolabeled antibody. Qualitative and quantitative interpretation of the CLI data was found to give a strong correlation with immuno-PET and biodistribution studies. We envisioned that CLI of radiopharmaceuticals has a broad range of potential applications. First, radioactive agents are traditionally studied by PET, SPECT or gamma-cameras, which are expensive, difficult to maintain and not widely available to many researchers. Our results clearly show that commercially available optical imaging instruments can be used to study radioactive probes (β+/ β– emitter), in addition to bioluminescence and fluorescence probes. Second, optical imaging systems have high throughput capabilities being able to image up to five animals simultaneously, whereas small-animal PET and SPECT systems can image only one mouse at a time. In view of the very low cost, wide accessibility and high throughput features of optical imaging instruments compared with PET and SPECT, radioactive probe development will probably be dramatically accelerated by the use of this approach (50). Moreover, the combination of optical imaging and nuclear medicine is a new path for the imaging of medical isotopes. Infact, intraoperative imaging of Cerenkov radiation is feasible with a highly sensitive camera in a dark room, the use of which can be achieved much more easily than with expensive nuclear medicine equipment. Notably, no additional development of optical agents is required because CLI can take advantage of many approved radiopharmaceuticals. Therefore, the combination of endoscopic surgical methods with optical Cerenkov imaging has the potential to be used directly in the clinic for intraoperative visualization of tumor lesions and margins or metastatic involvement for Cerenkov radiation-guided surgery. Preliminary studies on the potential use for endoscopy have been recently published by Gambhir group and are promising (51).

In **chapter 5.2**, we specifically explored this last aspect by performing PET and CLI of a breast cancer cells xenograft after injection of ^{89}Zr trastuzumab. We showed how CLI facilitated image-guided surgical identification and resection of tumors based on the optical signature of localized radiotracers. We showed that CLI is a very efficient method to identify small tumor masses with high sensitivity, to define the localization or extent of tumor lesions with accurate delineation of tumor margins, and to guide surgical resection. Intriguingly, from ex vivo analysis, we observed that the absolute amount of radiotracer activity following tumor resection was very low.

Interesting, application have risen from the use of Cerenkov radiation, as the possibility to use radioactive probes as an internal source of light able to excite fluorophores (52, 53) or induce the activation of light sensitive probes "without light" (54). This approach might open important opportunity in the design and production of probes able to release their content (as paramagnetic compounds or drugs) upon excitation of light coming from a cerenkov radiation emitter.

Finally, it is an intriguing feature of radionuclide and as Pavel A. Cerenkov stated during the nobel lecture "There can be no doubt that the usefulness of this radiation will in the future be rapidly extended" (55).

Conclusion

Preclinical research in molecular imaging has resulted in the indentification of a huge number of molecular targets and the development of novel imaging probes and corresponding advancement in imaging technologies. Clinical translation has been quite limited with most current applications in PET/SPECT and a relatively small number of applications in MRI/MRS, optical and ultrasound imaging. Current clinical trends are calling for new strategies able to implement early detection of diseases through improved imaging and screening approaches, to develop patient-specific treatment selection (personalized medicine), to deliver specific treatment (targeted-therapy) and to accurately monitor response to treament.

The progress to date and the further evolution of molecular imaging involves the cross-talk between a broad spectrum of biomedical disciplines, as clearly shown in this thesis. These includes physics and engineering for device design and development; chemistry and material science for development of novel imaging probes; molecular pharmacology for pharmacodynamic and pharmacokinetic assessment; cellular and molecular biology for target assessment and complex cell manipulation (reporter gene imaging); "omics" sciences and high throughput screening technologies to assess targets and new drugs; mathematics and bioinformatics for image reconstruction and data modeling. It is clear that new generations of medical imaging professionals should be regarded not only as the final users of these advancements but should play an active role at all stages

of the process. The introduction of molecular imaging training in the core curriculum of Radiology specialty in Europe and the development of sub-specialty MI societes within clinical radiology society is definitely a step forward that will increase radiologist involvement in imaging probe and techniques development, therefore speeding up the development of diagnostic an therapeutic agents and ultimately improve patient care.

References

1. Feynman RP, Robbins, J. & Dyson, F. J. . The Pleasure of Finding Things Out: The Best Short Works of Richard P. Feynman. Cambridge, MA: Perseus Books, 2009.

2. Haberzettl C. Nanomedicine: destination or journey? Nanotechnology 2002; 13.

3. Whitesides G. The once and future nanomachine. Sci. Am. 2001; 285:78–83.

4. Kostarelos K. Carbon nanotubes: Fibrillar pharmacology. Nat Mater; 9:793-795.

5. Kostarelos K, Lacerda L, Pastorin G, et al. Cellular uptake of functionalized carbon nanotubes is independent of functional group and cell type. Nat Nanotechnol 2007; 2:108-113.

6. Haraldsson B, Nystrom J, Deen WM. Properties of the glomerular barrier and mechanisms of proteinuria. Physiol Rev 2008; 88:451-487.

7. Singh R, Pantarotto D, Lacerda L, et al. Tissue biodistribution and blood clearance rates of intravenously administered carbon nanotube radiotracers. Proc Natl Acad Sci U S A 2006; 103:3357-3362.

8. Lacerda L SA, Singh R. Dynamic Imaging of functionalized multi-walled carbon nanotube systemic circulation and urinary excretion. Adv. Mater 2008; 20:225-230.

9. Liu Z, Tabakman S, Welsher K, Dai H. Carbon Nanotubes in Biology and Medicine: In vitro and in vivo Detection, Imaging and Drug Delivery. Nano Res 2009; 2:85-120.

10. Corada M, Liao F, Lindgren M, et al. Monoclonal antibodies directed to different regions of vascular endothelial cadherin extracellular domain affect adhesion and clustering of the protein and modulate endothelial permeability. Blood 2001; 97:1679-1684.

11. Liao F, Doody JF, Overholser J, et al. Selective targeting of angiogenic tumor vasculature by vascular endothelial-cadherin antibody inhibits tumor growth without affecting vascular permeability. Cancer Res 2002; 62:2567-2575.

12. Corada M, Zanetta L, Orsenigo F, et al. A monoclonal antibody to vascular endothelial-cadherin inhibits tumor angiogenesis without side effects on endothelial permeability. Blood 2002; 100:905-911.

13. May C, Doody JF, Abdullah R, et al. Identification of a transiently exposed VE-cadherin epitope that allows for specific targeting of an antibody to the tumor neovasculature. Blood 2005; 105:4337-4344.

14. Lamszus K, Brockmann MA, Eckerich C, et al. Inhibition of glioblastoma angiogenesis and invasion by combined treatments directed against vascular endothelial growth factor receptor-2, epidermal growth factor receptor, and vascular endothelial-cadherin. Clin Cancer Res 2005; 11:4934-4940.

15. Nikula TK, Bocchia M, Curcio MJ, et al. Impact of the high tyrosine fraction in complementarity determining regions: measured and predicted effects of radioiodination on IgG immunoreactivity. Mol Immunol 1995; 32:865-872.

16. McDevitt MR, Sgouros G, Finn RD, et al. Radioimmunotherapy with alpha-emitting nuclides. Eur J Nucl Med 1998; 25:1341-1351.

17. Nikula TK, McDevitt MR, Finn RD, et al. Alpha-emitting bismuth cyclohexylbenzyl DTPA constructs of recombinant humanized anti-CD33 antibodies: pharmacokinetics, bioactivity, toxicity and chemistry. J Nucl Med 1999; 40:166-176.

18. Singh Jaggi J, Henke E, Seshan SV, et al. Selective alpha-particle mediated depletion of tumor vasculature with vascular normalization. PLoS One 2007; 2:e267.

19. Therasse P, Arbuck SG, Eisenhauer EA, et al. New guidelines to evaluate the response to treatment in solid tumors. European Organization for Research and Treatment of Cancer, National Cancer Institute of the United States, National Cancer Institute of Canada. J Natl Cancer Inst 2000; 92:205-216.

20. Eisenhauer EA, Therasse P, Bogaerts J, et al. New response evaluation criteria in solid tumours: revised RECIST guideline (version 1.1). Eur J Cancer 2009; 45:228-247.

21. Suzuki C, Jacobsson H, Hatschek T, et al. Radiologic measurements of tumor response to treatment: practical approaches and limitations. Radiographics 2008; 28:329-344.

22. Nishino M, Jagannathan JP, Krajewski KM, et al. Personalized Tumor Response Assessment in the Era of Molecular Medicine: Cancer-Specific and Therapy-Specific Response Criteria to Complement Pitfalls of RECIST. AJR Am J Roentgenol; 198:737-745.

23. Zhao B, Oxnard GR, Moskowitz CS, et al. A pilot study of volume measurement as a method of tumor response evaluation to aid biomarker development. Clin Cancer Res; 16:4647-4653.

24. Mozley PD, Schwartz LH, Bendtsen C, Zhao B, Petrick N, Buckler AJ. Change in lung tumor volume as a biomarker of treatment response: a critical review of the evidence. Ann Oncol; 21:1751-1755.

25. Choi H, Charnsangavej C, de Castro Faria S, et al. CT evaluation of the response of gastrointestinal stromal tumors after imatinib mesylate treatment: a quantitative analysis correlated with FDG PET findings. AJR Am J Roentgenol 2004; 183:1619-1628.

26. Choi H, Charnsangavej C, Faria SC, et al. Correlation of computed tomography and positron emission tomography in patients with metastatic gastrointestinal stromal tumor treated at a single institution with imatinib mesylate: proposal of new computed tomography response criteria. J Clin Oncol 2007; 25:1753-1759.

27. Wahl RL, Jacene H, Kasamon Y, Lodge MA. From RECIST to PERCIST: Evolving Considerations for PET response criteria in solid tumors. J Nucl Med 2009; 50 Suppl 1:122S-150S.

28. Tateishi U, Miyake M, Nagaoka T, et al. Neoadjuvant Chemotherapy in Breast Cancer: Prediction of Pathologic Response with PET/CT and Dynamic Contrast-enhanced MR Imaging--Prospective Assessment. Radiology; 263:53-63.

29. Kuge Y, Sato M, Zhao S, et al. Feasibility of 99mTc-annexin V for repetitive detection of apoptotic tumor response to chemotherapy: an experimental study using a rat tumor model. J Nucl Med 2004; 45:309-312.

30. De Saint-Hubert M, Prinsen K, Mortelmans L, Verbruggen A, Mottaghy FM. Molecular imaging of cell death. Methods 2009; 48:178-187.

31. Mandl SJ, Mari C, Edinger M, et al. Multi-modality imaging identifies key times for annexin V imaging as an early predictor of therapeutic outcome. Mol Imaging 2004; 3:1-8.

32. Khaw BA. The current role of infarct avid imaging. Semin Nucl Med 1999; 29:259-270.

33. Perek N, Sabido O, Le Jeune N, et al. Could 99mTc-glucarate be used to evaluate tumour necrosis? In vitro and in vivo studies in leukaemic tumour cell line U937. Eur J Nucl Med Mol Imaging 2008; 35:1290-1298.

34. Rahmim A, Zaidi H. PET versus SPECT: strengths, limitations and challenges. Nucl Med Commun 2008; 29:193-207.

35. Tjuvajev JG, Finn R, Watanabe K, et al. Noninvasive imaging of herpes virus thymidine kinase gene transfer and expression: a potential method for monitoring clinical gene therapy. Cancer Res 1996; 56:4087-4095.

36. Tjuvajev JG, Avril N, Oku T, et al. Imaging herpes virus thymidine kinase gene transfer and expression by positron emission tomography. Cancer Res 1998; 58:4333-4341.

37. Gray SJ, Samulski RJ. Optimizing gene delivery vectors for the treatment of heart disease. Expert Opin Biol Ther 2008; 8:911-922.

38. Krishnan M, Park JM, Cao F, et al. Effects of epigenetic modulation on reporter gene expression: implications for stem cell imaging. FASEB J 2006; 20:106-108.

39. Ma Y, Ramezani A, Lewis R, Hawley RG, Thomson JA. High-level sustained transgene expression in human embryonic stem cells using lentiviral vectors. Stem Cells 2003; 21:111-117.

40. Toelen J, Deroose CM, Gijsbers R, et al. Fetal gene transfer with lentiviral vectors: long-term in vivo follow-up evaluation in a rat model. Am J Obstet Gynecol 2007; 196:352 e351-356.

41. Mikkers H, Berns A. Retroviral insertional mutagenesis: tagging cancer pathways. Adv Cancer Res 2003; 88:53-99.

42. Boutry S, Forge D, Burtea C, et al. How to quantify iron in an aqueous or biological matrix: a technical note. Contrast Media Mol Imaging 2009; 4:299-304.

43. Kuhlpeter R, Dahnke H, Matuszewski L, et al. R2 and R2* mapping for sensing cell-bound superparamagnetic nanoparticles: in vitro and murine in vivo testing. Radiology 2007; 245:449-457.

44. Peldschus K, Schultze A, Nollau P, et al. Quantitative MR imaging of targeted SPIO particles on the cell surface and comparison to flow cytometry. Magn Reson Imaging; 28:599-606.

45. Kotek G, van Tiel ST, Wielopolski PA, Houston GC, Krestin GP, Bernsen MR. Cell quantification: evolution of compartmentalization and distribution of iron-oxide particles and labeled cells. Contrast Media Mol Imaging; 7:195-203.

46. Keereweer S, Kerrebijn JD, van Driel PB, et al. Optical image-guided surgery--where do we stand? Mol Imaging Biol; 13:199-207.

47. Frangioni JV. New technologies for human cancer imaging. J Clin Oncol 2008; 26:4012-4021.

48. Plesums J, Bunch WH. Measurement of phosphorus following 32 P Cerenkov counting. Anal Biochem 1971; 42:360-362.

49. Hansen BS. An improved method for assaying pyrophosphate exchange measuring Cerenkov radiation. Anal Biochem 1980; 109:12-17.

50. Lucignani G. Cerenkov radioactive optical imaging: a promising new strategy. Eur J Nucl Med Mol Imaging; 38:592-595.

51. Kothapalli SR, Liu H, Liao JC, Cheng Z, Gambhir SS. Endoscopic imaging of Cerenkov luminescence. Biomed Opt Express; 3:1215-1225.

52. Dothager RS, Goiffon RJ, Jackson E, Harpstrite S, Piwnica-Worms D. Cerenkov radiation energy transfer (CRET) imaging: a novel method for optical imaging of PET isotopes in biological systems. PLoS One; 5:e13300.

53. Liu H, Zhang X, Xing B, Han P, Gambhir SS, Cheng Z. Radiation-luminescence-excited quantum dots for in vivo multiplexed optical imaging. Small; 6:1087-1091.

54. Ran C, Zhang Z, Hooker J, Moore A. In vivo photoactivation without "light": use of cherenkov radiation to overcome the penetration limit of light. Mol Imaging Biol; 14:156-162.

55. Cerenkov P. Nobel Lecture -11 December 1958 http://nobelprize.org/nobel_prizes/physics/laureates/1958/cerenkov-lecture.html. In.

7

Samenvatting
Acknowledgements
List of Publications
Portfolio
Curriculum Vitae

Samenvatting

Molecular Imaging (MI) is zich aan het ontwikkelen tot een nieuwe subspecialisatie binnen de radiologie. De recente intrede van onderzoek met moleculaire beeldvorming in de radiologische gemeenschap is het gevolg van gelijktijdige ontwikkelingen binnen de disciplines van cellulaire en moleculaire biologie, genomics en proteomics, nanotechnologieën en toenemende verfijning van al onze beeldvorming technologieën, in combinatie met een grote diversificatie vannieuwe contrastmiddelen en sondes. MI is het onderzoeksveld dat zich bezighoudt, , op een macroscopisch niveau van resolutie, met het *in vivo* karakteriseren en meten van biologische processen, welke zich op een cellulair en moleculair niveau afspelen. Het zich snel ontwikkelende gebied van MI belooft verbeteringen in de specificiteit en kwantificatie voor screening en vroegtijdige diagnose, gerichte en gepersonaliseerde therapie en vervroegde follow-up van behandeling. Het begrijpen van de huidige beperkingen van beeldvormende technieken en de uitdagingen van de huidige klinische geneeskunde samen met een directe kennis van de beloften en hindernissen van nieuwe beeldvormings platformen en technologieën draagt zeker bij aan vooruitgang in de ontwikkelingen binnen het veld. Het doel van dit proefschrift was om inzicht in de verschillende mogelijkheden van MI te verkrijgen. **Hoofdstuk 1** betreft een algemene introductie tot het onderwerp van dit proefschrift en **in hoofdstuk 2** treft u de motivatie tot het creeren van dit proefschrift. Alle belangrijke beeldvormende technieken en mogelijke toepassingen worden verkend en besproken in **hoofdstuk 3, 4 en 5**.

Hoofdstuk 3 geeft een overzicht van de rol van MI bij het beoordelen van nieuwe probes voor beeldvorming en therapie. Nanopartikels en specifiek gerichte probes worden steeds belangrijker in biomedisch onderzoek om ons begrip van zowel de mechanismen die betrokken zijn bij pathologische omstandigheden als van de interacties tussen nanodeeltjes en het omringende biologische milieu te bevorderen. Vanuit een meer praktische zin, zijn draadvormige nanomaterialen ontworpen als transporteurs van therapeutische en / of diagnostische middelen met zeer gewenste controle over hun weefsel navigatie in vivo, hun afgifte van de agentia en klaringsprofiel. In **hoofdstuk 3.1** is het mechanisme van klaring van een dergelijk type draadvormige nanostructuur (singlewalled carbon nanotubes (SWCNTs) onderzocht. Aan de SWCNTs zijn verschillende liganden covalent gekoppeld, waardoor de klaring van de materialen via de nieren in muizen bestudeerd kan worden met behulp van drie verschillende beeldvormende technieken, te weten PET, optische beeldvorming en microscopie. De gemiddelde lengte van SWCNT, welke een gefunctionaliseerde constructie zou opleveren met een moleculgewicht van ~ 350-500 kD, werd bepaald op 200-300 nm. Het SWCNT construct werd snel (t1 / 2 ~ 6 min.) en intact uitgescheiden via de nieren door glomerulaire filtratie met gedeeltelijke tubulaire reabsorptie en tijdelijke translocatie in de proximale tubulaire celkernen. De directionele absorptie werd in vitro bevestigd bevestigd met behulp van gepolariseerde niercellen.

Het onderzoek biedt mechanistische verklaringen, zowel experimenteel als theore-

tisch, hoe SWCNTs in lijn met de bloedstroom gebracht kunnen worden en snel via de nieren worden uitgescheiden. Deze bevindingen hebben gevolgen voor ons fundamentele begrip van de nierfysiologie en onze kennis van het vermogen van chemisch gefunctionaliseerde SWCNTs om zich door biologische barrières verplaatsen. In **hoofdstuk 3.2** hebben we SWCTs verder gefunctionaliseerd, waardoor ze als gerichte middelen (beeldvorming en behandeling) voor de monomere vorm van E-cadherine, een molecuul betrokken bij bij de bloedvatnieuwvorming (neoangiogenesis), kunnen dienen. Het vermogen van deze constructen om zich op tumoren te richten en hun farmacokinetische profielen werden beoordeeld door middel van optische beeldvorming (fluorescent molecular tomography en FMT) en via een PET-camera in LS174T tumor-dragende muizen. Door middel van het labelen van specifiek gerichte SWCNT met de de α-emitter [225]Ac werden de effecten van de versterking van de specifieke activiteit onderzocht in een therapie studie.

PET-beeldvorming liet specifieke accumulatie van het construct in de tumor en zien, ten opzichte van ongerichte SWCNT, verder aangetoond middels blocking studies met koude antilichamen. Met deze aanpak namen we, na slechts 1 behandeling, niet alleen een verhoogde overleving van dieren waar, maar ook een stabilisatie van tumorgroei ten opzichte van de controlegroep.

In **hoofdstuk 3.3** hebben we een nieuw MI-middel, bestaande uit [89]Zr-gelabelde monoklonaal antilichamen, ontwikkeld en getest voor gerichte beeldvorming van het prostaatspecifieke membraan antigeen (PSMA) met een PET-camera. PMSA is een prototype van een transmembraanmarker die tot overexpressie gebracht wordt in prostaatkanker. We onderzochten de mogelijkheden die [89]Zr-DFO-7E11 biedt om de respons van de tumor op therapie af te bakenen; [89]Zr-DFO-7E11 bindt zich uitsluitend aan de intracellulaire epitoop van PSMA, die alleen beschikbaar komt na verstoring van de celmembraan in dode of stervende cellen. Bevindingen die in vitro, in vivo en ex vivo zijn gedaan geven aan dat [89]Zr-DFO-7E11 een hoog weefselcontrast tussen tumor en achtergrond vertoont in immuno-PET en gebruikt kan worden als middel voor het controleren en kwantificeren, met hoge specificiteit, van "tumor response" in PSMA-positieve prostaatkanker.

Hoofdstuk 4 onderzocht een ander belangrijk gebied van de MI: "cell tracking" en het potentieel ervan voor regeneratieve geneeskunde. In **hoofdstuk 4.1** wordt een overzicht gegeven van de MI aanpak en recente ontwikkelingen van het vervolgen van cellen in het hart. In **hoofdstuk 4.2** introduceerden we de belangrijkste beperking van beeldvorming door middel van een PET-gebaseerde reportergen, bestaande uit hoge achtergrond radioactiviteit. Deze hoge achtergrond radioactiviteit is gerelateerd aan de suboptimale farmacokinetiek van probes, zoals 18F-FHBG, ^{18}F-FEAU en [124]I-FIAU die vaak gebruikt worden voor HSV1-tk PET-beeldvorming. Onze hypothese was inherent aan de mogelijkheid dat opname van de probes door de darmbacteriën (die thymidine kinase tot expressie brengen) kunnen bijdragen aan de achtergrond radioactiviteit. We hebben ook verschillende strategieën onderzocht voor het terugdringen van de achtergrond in PET-

reportergen gebaseerde -beeldvorming via het verhogen van de intestinale klaring van deze probes. De combinatie van een vloeibaar dieet en een osmotisch laxans verlaagde de intestinale radioactiviteit en verhoogde (2,2-voudig) de HSV1-tk getransduceerde xenograft-tot-darm-ratio voor 18F-FEAU.

In **hoofdstuk 4.3** onderzochten we, in vitro en in vivo, of eventuele verschillen in R1, R2 of R2* relaxatiesnelheid kunnen dienen als een maat voor levensvatbaarheid van mesenchymale stamcellen gelabeld met Gd-liposomen of ijzeroxide nanodeeltjes. Wij hebben het gedrag, de voor- en nadelen van deze twee benaderingen voor cellabeling bepaald. Na injectie, werden er geen substantiële kwantitatieve of visuele verschillen tussen levende en dode SPIO-MSC's gedetecteerd. Bovendien, zorgden SPIO-MSC's voor een aanhoudende signaalverlies in vivo, hetgeen de specificiteit van dit contrastmiddel sterk vermindert. In vivo persistentie van SPIO deeltjes werd ook bevestigd door histologische kleuring. Er werd een groot verschil gevonden tussen SPIO- en Gd-gelabelde cellen in de nauwkeurigheid van MR relaxometrie om te differentiëren tussen levende en dode cellen. Gd-liposomen zorgen voor een meer nauwkeurige en specifieke beoordeling van het al dan niet in leven zijn van de cellen dan SPIO-deeltjes. Levende Gd-cellen kunnen op de MRI-beelden zelfs op het oog onderscheiden worden van dode Gd-cellen.

In **hoofdstuk 4.4**, hebben we, door middel van kwantitatieve MRI van het hart (in vivo) en bioluminescentie, onderzocht of veranderingen van relaxatiesnelheid (R2) in verband gebracht kunnen worden met celvermeerdering, cel overleving en dood van mesenchymale stamcellen gelabeld met ijzer-oxide die in het hart waren geïmplanteerd. We zagen geen statistisch significante correlatie tussen de veranderingen in de bioluminescente optische signaal geassocieerd met celproliferatie en celdood en de veronderstelde (gebaseerd op in vitro studies) veranderingen in de relaxatietijden geassocieerd met ijzer-oxide verdunning (proliferatie) en afgifte in de extracellulaire matrix bij celdood. We concludeerden dat celproliferatie, celmigratie, celdood, extracellulaire SPIO dispersie of aggregatie verschillende relaxatietijden vertonen. Tenzij, er is maar een goed gedefinieerd proces gebeurt in een beperkt volume van belang in vivo Kwantificering is zeer complex, tenzij er, in een beperkt volume, slechts één van meerdere voornoemde processen een rol speelt.

Hoofdstuk 5 onderzoekt de mogelijkheid van een "nieuwe" multimodale strategie waar MI technieken zich op richten. In **hoofdstuk 5.1** hebben we gerapporteerd over het gebruik van de inherente optische emissies tijdens het verval van radiofarmaca voor Cerenkov-luminescentie-beeldvorming (CLI) van tumoren in vivo. De resultaten zijn gecorreleerd aan die van de overeenkomstige immuno-PET studies. Deze studies vormen de eerste kwantitatieve beoordeling van CLI voor het meten van de opname van radiotracers in vivo. We hebben aangetoond dat er een lineaire correlatie bestaat tussen de waargenomen lichtopbrengst en het gemeten PET signaal zowel in in vitro, in vivo als in ex vivo monsters. Veel radionucliden die gebruikt worden voor tomografische nucleaire beeldvorming en stralingstherapie hebben het potentieel om te worden gebruikt in CLI.

De waarde van de CLI ligt in het feit dat via deze methode ook radionucliden gebruikt kunnen worden die niet geschikt zijn voor beeldvorming met de huidige nucleaire beeldvormende technieken omdat ze geen positronen of γ-stralen uitzenden.

Bovendien is Cerenkov straling veelbelovend als een potentiële nieuwe in vivo beeldvormende modaliteit voor een snelle, goedkope, highthroughput screening van radiofarmaca.

In **hoofdstuk 5.2** bieden we de eerste demonstratie van het gebruik van de CLI voor echte beeld-geleide, intra-operatieve chirurgische resectie van tumoren. De gepresenteerde resultaten ondersteunen de verdere ontwikkeling van CLI voor zowel moleculaire beeldvorming als chirurgische interventie in preklinische en klinische toepassingen.

We rapporteerden de volledige karakterisering van CLI door middel van de positron-emitterende radiotracer 89Zr-DFO-trastuzumab voor target-specifieke, kwantitatieve beeldvorming van HER2/neu-positive mammatumoren in vivo. De beeld-geleide operatie toont aan dat CLI gebruikt kan worden als een zeer efficiënte methode voor het identificeren van kleine tumormassa's met een hoge gevoeligheid, het bepalen van de lokalisatie en de omvang van tumorlaesies met nauwkeurige afbakening van de tumor marges, en het toezicht op de voortgang en het aansturen van chirurgische resectie. Het is interessant op te merken dat uit ex vivo analyse van de gereseceerde tumor bleek dat de absolute hoeveelheid 89Zr activiteit in de tumor erg laag was.

De resultaten van dit proefschrift worden verder besproken en samengevat in **hoofdstuk 6** en **hoofdstuk 7**. De tot dusver geboekte vooruitgang en de verdere ontwikkeling van moleculaire beeldvorming betreft een samenkomst van een breed spectrum van biomedische disciplines, zoals duidelijk blijkt uit dit proefschrift. Deze omvat natuurkunde en techniek voor ontwerp en ontwikkeling van het apparaat, chemie en materiaalkunde voor de ontwikkeling van nieuwe probes voor medische beeldvorming, moleculaire farmacologie voor farmacodynamische en farmacokinetische toetsing; cellulaire en moleculaire biologie voor het definiëren en beoordelen van de aangrijppunten en voor complexe cel manipulaties (reportergen-beeldvorming); "omics" wetenschappen en "high throughput screening" technologie om aangrijppunten en nieuwe geneesmiddelen te beoordelen; wiskunde en bio-informatica voor beeldverwerking en beeld data analyse. Het is duidelijk dat nieuwe generaties van medische beeldvorming professionals, niet alleen als eindgebruikers van deze ontwikkelingen moeten worden beschouwd, maar dat ze een actieve rol binnen alle fasen van het proces moeten spelen.

Acknowledgments

List of publications

Original articles

- ***Ruggiero A**, Guenoun J, Doeswijk G, Houston G, Krestin GP, Bernsen MR, Kotek G.*
  In vivo mapping of iron oxide labeled mesenchymal stem cells implanted in the heart with bioluminescence validation.
  To be submitted: Contrast Media and Molecular Imaging

- *Guenoun J*, **Ruggiero A***, Koning GA, Doeswijk G, Krestin GP, Bernsen MR.* In vivo quantitative assessment of Gadolinium or iron-labeled cell viability using MRI and BLI
  equal contribution; submitted: Contrast Media and Molecular Imaging

- ***Ruggiero A**, Holland JP, Hudolin T, Shenker L, Koulova A, Bander NH, Lewis J, Grimm J*
  Targeting the internal epitope of prostate-specific membrane antigen with [89]Zr-7E11 immunoPET imaging. *J Nucl Med. 2011 Oct;52(10):1608-15*

- *Holland JP,Normand G, **Ruggiero A**, Lewis JS, Grimm J*
  Intra-operative imaging of PET radiotracers using Cerenkov luminescence emissions. *Mol Imaging. 2011 Jun;10(3):177-86)*

- ***Ruggiero A**, Villa CH, Holland JP, Sprinkle SR, May C, Lewis JS, Scheinberg DA, McDevitt MR* Imaging and treating tumor vasculature with targeted radiolabeled carbon nanotubes. *International Journal of Nanomedicine 2010:5 783–802*

- ***Ruggiero A**, Villa C, Bander E, Rey DA, Bergkvist M, Batt CA, Manova-Todorova K, Deen WM, Scheinberg DA, McDevitt MR.* Paradoxical glomerular filtration of carbon nanotubes. *Proc Natl Acad Sci U S A. 2010 Jul 6;107(27):12369-74*

- ***Ruggiero A**, Holland JP, Lewis JS, Grimm J* .Cerenkov luminescence imaging of medical isotopes *J Nucl Med. 2010 Jul;51(7):1123-30*

- ***Ruggiero A**, Brader P, Serganova I, Zanzonico P, Hricak H, Lipman N, Blasberg RG.* Different strategies for reducing intestinal background radioactivity associated with imaging HSV1- tk expression using established radionucleoside probes. *Mol Imaging 2010 Feb;9(1):47-58*

Review articles

- ***Ruggiero A**, Thorek DLJ, Guenoun J, Krestin GP, Bernsen.* MR Cell tracking in cardiac repair: what to image and how to image. Eur Radiol. 2012 Jan;22(1):189-204.

Books and Chapters

- *Bernsen MR, **Ruggiero A**, van Straten M, Kotek G, Haeck J, Wielopolski PA, Krestin GP*
  Molecular Imaging in Oncology: Technology and Probe Design: CT and MRI *Molecular Imaging in Oncology – Springer in press 2012*

Poster and oral communications at Meetings

- ***Ruggiero A**, Guenoun J, Doeswijk GN, Krestin GP, Kotek G; Bernsen MR.*
  Longitudinal Monitoring of Stem Cell Fate in the Myocardium by Quantitative MRI. *RSNA Annual Meeting; Chicago (USA), November 25-30 December 2012.*

- *Smit H, **Ruggiero A**, Doeswijk G, Milanesi M, Houston G, Bernsen M, Krestin GP, Klein S, Kotek G.* T1 mapping of labeled stem cells injected in rat myocardium with a modified CINE-IR protocol. *International Society for Magnetic Resonance in Medicine (ISMRM) meeting 2012. Melbourne, (Australia) May 5-11 2012.*

- ***Ruggiero A**, Guenoun J, Kotek G, Krestin GP, Bernsen MR.* Cell tracking in cardiac repair: what to image and how to image. Educational exhibit. *RSNA Annual Meeting; Chicago (USA), 27 November-2 December 2011.*

- *Guenoun J, **Ruggiero A**, Doeswijk G, Koning GA, Krestin GP, Bernsen MR* In Vivo Assessment of Gd- or SPIO-labeled Cell Graft Viability: A Bimodal Approach Combining MRI and Bioluminescence Imaging. *RSNA Annual Meeting; Chicago (USA) 27 November-2 December 2011*

- ***Ruggiero A**, Guenoun J, Doeswijk G, Krestin GP, Bernsen MR, Kotek G*
  In vivo R2 mapping of SPIO-labeled MSC viability in the rat heart with bioluminescence validation. *European Molecular Imaging Meeting; Leiden, The Netherlands. June 19-21 2011*

- *Guenoun J, **Ruggiero A**, Doeswijk G, Koning GA, Krestin GP, Bernsen MR*
Optimizing the cell labeling strategy with cationic Gd-liposomes, allowing in vitro and longitudinal in vivo follow up of Gd-labeled MSCs. *European Molecular Imaging Meeting. Leiden, The Netherlands. June 19-21 2011*

- *Guenoun J, **Ruggiero A**, Doeswijk G, Kotek G, Krestin GP, Bernsen MR*
In vivo assessment of Gd- or SPIO-labeled cell graft viability: a bimodal approach combining MRI and bioluminescence imaging. *European Molecular Imaging Meeting. Leiden, The Netherlands. June 19-21 2011*

- ***Ruggiero A**, Holland JP, Lewis JS, Grimm J* Cerenkov optical imaging of radioisotopes. *European Congress of Radiology (ECR). Vienna (Austria), 3-7 March 2011.*

- *McDevitt MR, **Ruggiero A**, Holland JP, Villa C, Sprinkle S, Lewis JS, Scheinberg D*
Amalgamating nanomaterials, radionuclides, and antibodies to image tumor vasculature. *Annual Translational and Molecular Imaging Symposium. The New York Academy of Medicine; New York (USA) April 16, 2010*

- ***Ruggiero A**, Brader P, Serganova I, Zanzonico P, Hricak H, Blasberg RG*
The role of intestinal microflora in nucleoside analog HSV1-TK microPET imaging, different strategies in reducing intestinal background radioactivity. *Society of Nuclear Medicine Annual Meeting. Toronto (Canada) June 13-17 2009*

- ***Ruggiero A**, Brader P, Serganova I, Zanzonico P, Hricak H, Blasberg RG*
High microPET background radioactivity in nucleoside analog HSV1-TK imaging: no role of bacteria but simple strategies reduce it. *World Molecular Imaging Congress 2009. WMIC 0330. Montreal (Canada) 24-26 September 2009*

- *Scheinberg C, Villa CH, McDevitt MR, Escorcia F, **Ruggiero A,** Bander E*
Cancer targeted multi-functional, alpha emitting, carbon nanotubes. *215th Electrochemical Society (ECS) Meeting. 15 May 2009 San Francisco. USA.*

Portfolio
Completed Courses (ECTS = European Credit Transfer System; 1 ECTS is equivalent to 20 hours of study)

Title	Institution	Location	Dates	ECTS	Notes
Special Meeting of NCI for R25T grant	National Cancer Intitute (NCI)	Bethesda Hyatt, Washington, DC, USA	March 16, 2008	1	12 hrs
Write winning grants workshop	MSKCC	New York, NY, USA	March 2008	2	40hrs
Rarc New Investigator Orientation	MSKCC/Cornell	New York, NY, USA	February 7, 2008	0,5	10 hrs
Basic Mouse Hands on	MSKCC/Cornell	New York, NY, USA	February 18, 2008	0,5	10 hrs
Xenograft Lecture	MSKCC/Cornell	New York, NY, USA	March 5, 2008	1	20 hrs
Mouse injection Tail I.V. /retroorbital	MSKCC/Cornell	New York, NY, USA	August 8, 2008	0,5	10 hrs
Hazardous Material Training	MSKCC/Cornell	New York, NY, USA	February 12, 2008	0,5	10 hrs
Rodent breeding	MSKCC/Cornell	New York, NY, USA	February 27, 2008	0,5	10 hrs
Radioisotope guidelines	MSKCC/Cornell	New York, NY, USA	February 13, 2008	0,5	10 hrs
Molecular Imaging Lecture Series	Department of Radiology - MSKCC	New York, NY, USA	Jan 29- May 13, 2008	1,5	28 hrs (14 lectures)

Title	Institution	Location	Dates	ECTS	Notes
R25T Program Molecular Imaging Research Meetings	Department of Radiology- MSKCC	New York, NY, USA	February 8, 2008 – March 19, 2010	4	80 hrs
Student supervision and mentoring	MSKCC – Dr. Jan Grimm Lab	New York, NY, USA	June 2009- March 2010	4	80 hrs
Responsible Research Course	MSKCC	New York, NY, USA	September – December 2009	2	5 h ½ + personal study (40 h)
Radiation Protection Course	ErasmusMC	Rotterdam	September – October 2010	2	40 hrs
Animal Training	LUMC	Leiden,	December 2010	6	120 hrs
In Vivo Imaging 'From Molecule to Organism'	ErasmusMC	Rotterdam	October 25-29, 2010	2	40 hrs
Course Biomedical Research Techniques	ErasmusMC	Rotterdam	October 11-15, 2010	2	40 hrs
Translational Imaging Workshop by AMIE 'From mouse to man	ErasmusMC	Rotterdam	January 25-28, 2011	2	40 hrs
Translational Imaging Workshop by AMIE 'From mouse to man	ErasmusMC	Rotterdam	6-9 March 2012	2	80 hrs (Speaker; lecture preparation)

*MSKCC (Memorial Sloan-Kettering Cancer Center, New York, USA); *Cornell (Cornell University, New York, USA)

Curriculum Vitae

Personal Information

    Name: **Alessandro Ruggiero**
    Nationality: **Italian**

    Place and date of Birth: **Brindisi (Italy), 02 September 1979**

Professional Experience and Education

- *May 2012-present:* Clinical Radiology. Department of Radiology. Addenbroke's Hospital. Cambridge University Hospital. Cambridge, United Kingdom.

- *April 2010-April 2012*: Molecular Imaging Research. Department of Radiology, Molecular Imaging Lab. Erasmus MC University Medical Center. Rotterdam, The Netherlands.

- *January 2008-April 2010*: Molecular Imaging Research. Department of Radiology and Nuclear Medicine. Memorial Sloan-Kettering Cancer Center. New York, NY, United States of America.

- *November 2004-November 2008*: Radiology Residency. Department of Radiology, Campus Bio-Medico University of Rome. Rome, Italy.

- *July-October 2003:* Intensive Care Unit Internship. Saint Bartolomews Hospital and Homerton Hospital. London, United Kingdom.

- *October 1998-October 2004*: Medical School at Campus Bio-Medico University of Rome. Graduated with Summa cum laude.

- *November 1992 – June 1998*. Scientific Liceum. Liceo Scientifico "Enrico Fermi". Brindisi, Italy.

Honors and Awards

- *Molecular Imaging Training for Oncology 2008-2010*. National Institute of Health (NIH)/National Cancer Institute (NCI) R25T Training Grant. European Society of Radiology (ESR) and Memorial Sloan-Kettering Cancer Center, New York, USA.

- *Erasmus Exchange Project 2003*. Campus Bio-Medico University of Rome and Queen Mary University of London. London. Intensive Care Unit Internship. Saint Bartolomews Hospital. Homerton Hospital. London, United Kingdom.